Geoelectrical characterisation of Alpine orogenic belts in the Iberian Peninsula using the magnetotelluric method

Hoël Seillé

Universitat de Barcelona

Departament de Dinàmica de la Terra i de l'Oceà

Geoelectrical characterisation of Alpine orogenic belts in the Iberian Peninsula using the magnetotelluric method

Memoria presentada por

Hoël Seillé

para optar al título de Doctor del programa de doctorado de Ciencias de la Tierra de la Universitat de Barcelona, bajo la dirección del **Dr. Jaume Pous.**

Junio de 2016

Director y tutor de tesis	Doctorando
Dr. Jaume Pous	Hoël Seillé

Acknowledgements

First of all I would like to thank my supervisor Jaume Pous for giving me the opportunity to pursue a PhD. I appreciate his scientific advice, guidance and encouragements over all these years, allowing me to grow into an independent geoscientist. He also gave me the opportunity to work on several projects and participate in a number of field works all across Spain.

I want to thank my friends and colleagues from the University of Toulouse for giving me the passion for Earth Sciences, in particular Cliff, Flo and Ju. I also want to thank all my friends and colleagues from the University of Barcelona, with whom I shared a lot during all these years in the campus and in the field: Ane, Anna, Cris, Eloi, Ivan, Gonzalo, Lena, Manu, Marta and many more. I am also grateful to all the people I have met during my professional stay in Milan, from whom I learnt a lot about geophysics and its industry: Christophe, David, Graeme, Jérémie, Marilou, Romain, Skander, Stefano and more.

Finally I would like to thank my family for their love and support.

Barcelona, 22 June 2016

Abstract

The Iberian Peninsula is considered as a “micro-continent”, located between the Eurasian and the African plates. Several ranges formed during the Alpine orogeny, in the borders of the plate or intraplate. As part of this thesis the first magnetotelluric (MT) data was collected across the intraplate Iberian fold and thrust belt and the first long-period magnetotelluric was collected across the Cantabrian Mountains, located in the northern boundary of the Iberian plate. This MT data was used to image the electrical conductivity distribution of the crust beneath these two orogens. The analysis of the MT data revealed the presence of three-dimensional structures in both studied areas and therefore 3-D inversion algorithms were used to obtain the final resistivity models.

In the Cantabrian Mountains the correlation between the geoelectric image, the existing geophysical models and the surface geology provided a deeper understanding of the lithospherical processes. The final model shows excellent correlation with the superficial geology, depicting the main faults and lithologies at depth. The Duero Basin sediments are well delineated. A thickness of 2.5 to 3.5 km was deduced, and is in agreement with the seismic studies and well log data. Conductive zones in the Palaeozoic basement are related to enhanced permeability along the main Alpine faults. These conductive zones detected in the model do not reach more than 10 km in the southern part of the Cantabrian Mountains and 15 km in the northern part, and are therefore concentrated in the upper crust. The hydration/serpentinization of the upper mantle within the mantle wedge and beneath the Moho of the Cantabrian Margin is imaged as a zone of low resistivities.

In the Iberian Chain the 3-D inversion model indicates that several Alpine thrusts are imaged as dipping conductors, which are limited to the upper crust. Two of them are the North Iberian Thrust and the Serranía de Cuenca Thrust, which bound to the north and to the south respectively the basement involved areas of the Iberian Chain. Both faults do not reach more than 15 km depth, suggesting that they are linked to the thrust system detachment at 10–15 km depth. This indicates that the Cenozoic thrust system causing the crustal thickening of the Iberian Chain is concentrated in the upper crust, which confirms the previous geological hypothesis proposed by Guimerà and Alvaro (1990). The 3-D inversion model is consistent with the collocated seismic image. A statistical analysis of the correlation between seismic velocity and electrical resistivity along a NE-SW profile is carried out for the upper crust and shows a clear correlation between both parameters. An increase in both seismic velocity and electrical resistivity is observed and is related to the depth at which the geological formations are located.

Resumen

La Península Ibérica es un micro continente situado entre las Placas Euroasiática y Africana. Existen varios orógenos alpinos situados en el borde de placa y en su interior. En esta tesis se han realizado perfiles de magnetotelúrica a través de dos de estos orógenos: la Cordillera Cantábrica y la Cadena Ibérica. A partir de los datos de magnetotelúrica se han obtenido las imágenes de resistividad eléctrica a escala litosférica en la Cordillera Cantábrica y a escala cortical en la Cadena Ibérica. En ambos casos el análisis de la dimensionalidad de la estructura geoeléctrica ha puesto de relieve un comportamiento 3-D. Por tanto se han realizado en cada caso inversiones 3-D conjuntas de las cuatro componentes del tensor de impedancias y de la función de transferencia geomagnética.

En la Cordillera Cantábrica, la correlación de la distribución de resistividad eléctrica con otros modelos geofísicos y la geología de superficie ha conducido a una mejor comprensión de los procesos litosféricos de formación de la cordillera. El modelo de resistividades obtenido da una imagen de las principales fallas y estructuras en profundidad. La Cuenca del Duero está formada por sedimentos con un espesor variable, entre 2.5 a 3.5 km. El basamento paleozoico resistivo presenta zonas de conductividad elevada relacionadas con las fallas alpinas que no superan los 10 km de profundidad en la parte más meridional de la Cordillera y los 15 km en la parte septentrional de la misma, lo que indica que se sitúan en la corteza superior. La hidratación /serpentinización en la cuña del manto del margen cantábrico aparece reflejada por una zona de elevada conductividad eléctrica.

En la Cadena Ibérica el modelo de inversión 3D obtenido revela la geometría de los cabalgamientos alpinos mediante zonas de elevada conductividad. Los dos principales son el Cabalgamiento Frontal Noribérico y el de la Serranía de Cuenca que limitan, al Norte y al Sur respectivamente, el basamento de la Cadena Ibérica. Ambas fallas no superan los 15 km de profundidad, indicando que el sistema de cabalgamientos cenozoico causante del engrosamiento de la cadena se concentra en la corteza superior. Se ha realizado un análisis estadístico de la correlación entre el modelo de resistividades obtenido y un modelo de velocidades sísmicas existente. El resultado indica una coincidencia entre un aumento de velocidades sísmicas y un aumento de resistividad eléctrica relacionado con la localización de las formaciones geológicas a distintas profundidades.

Contents

List of figures

1 Introduction

This thesis is about the characterization of the crustal structure of two alpine orogens in the Iberian Peninsula, the Cantabrian Mountains and the Iberian Chain, using the magnetotelluric method. This work focuses on the analysis, modelling and interpretation of the magnetotelluric data acquired across these two orogens.

1.1 Motivations and objectives

1.1.1 Structure of the Iberian Peninsula and its alpine orogens

The present lithospheric structure of the Iberian Peninsula developed from the succession of geodynamic processes that took place since the Permian and Triassic time. The basement of the Iberian plate, mostly constituted by Palaeozoic and Precambrian rocks deformed during the Variscan orogeny (Perez-Estaún, 2004), started to stretch during the extensional processes related to the break-up of Pangaea and the consequent opening of the Atlantic Ocean (Ziegler, 1990). Later on during the Early Cretaceous, the opening of the northern part of the Atlantic Ocean reached the Iberian plate causing the separation of the Eurasian and Iberian plates through the Bay of Biscay, which led to the individualization of Iberia as a microplate (Franke, 1989; Rosenbaum et al., 2002). This extensional process permitted the development of rift basins in the borders and in the interior of the Iberian Plate. Finally, in Late Cretaceous to present time, the North-South convergence of Africa and Europe caused the partial closure of the Bay of Biscay and the formation of the Cantabrian-Pyrenean Mountains in the north of the Iberian plate, followed by the formation of the Betics-Rif Chain in the south. The motion of the different tectonic plates is responsible for the creation of zones of intense deformation, which are generally concentrated along the plate boundaries. However, intraplate deformation also occurred in the Iberian plate (Dercourt et al., 1986; Vergés and Fernandez, 2006; De Vicente et al., 2008), provoking significant intraplate compressional structures (Central System and Iberian Chain).

As a result of this complex geodynamic history, the Iberian Peninsula is characterized by different geological units: in the west of the Iberian Plate, the Variscan Iberian Massif, which is mainly constituted by outcrops of a Precambrian-Palaeozoic Basement, while the eastern part shows thick Mesozoic sedimentary sequences inverted during the Alpine orogeny. The Variscan basement was also involved in the Alpine Orogeny, generally by the inversion of Mesozoic normal faults. Cenozoic foreland basins bound the orogens: the Duero Basin, located between the Cantabrian Mountains and the Central System, the Ebro Basin between the Pyrenees and the Iberian Chain and the Guadalquivir Basin north of the Betic Chain. The magnetotelluric profiles studied during this thesis cross the Cantabrian Mountains and the Iberian Chain, which involve outcropping formations that are Cenozoic in the basins and vary from Palaeozoic to Mesozoic in the orogens.

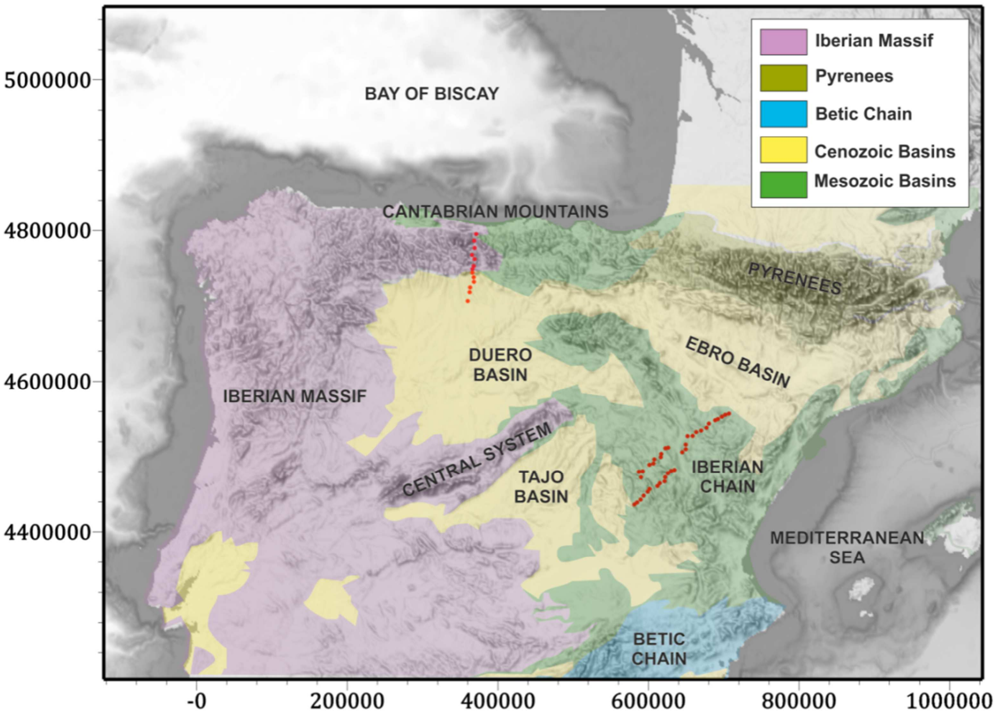

Figure 1-1: Geological map of the Iberian Peninsula. Red points: MT sites.

1.1.2 Present geophysical/geological knowledge of the Iberian Peninsula

The crustal structure of the Iberian Plate is well defined from several seismic, gravity and magnetotelluric surveys. It has been extensively explored using seismic data since the late 1970s. The crustal imbrication beneath the Pyrenees, reaching thicknesses of 45-50 km, has been documented from wide-angle (Daignières et al., 1982, Gallart et al., 1981) and deep multichannel seismic profiles (Choukroune et al., 1989). The seismic exploration of the Valencia Trough using marine multichannel profiles and wide angle profiles (Watts et al., 1990, Torne et al., 1992, Gallart et al., 1995, Dañobeitia et al., 1992) has revealed the strong variation in crustal thickness as a result of the rifting process that affected the zone, with Moho depths around 35 km in NE Iberia, thinning to 15-18 km beneath the centre of the Valencia Trough and thickening again towards the Balearic promontory. The crustal structure beneath central Iberian Massif was already explored by early seismic profiles (Banda et al., 1981), but the recent IBERSEIS and ALCUDIA experiments have allowed to define precisely its geometry and velocity structure, which is characterized by a subhorizontal Moho located close to 32 km depth (Simancas et al., 2003, Carbonell et al., 2004, Ehsan et al 2014, Ehsan et al, 2015). Although scarce seismic information is available for the Iberian Chain, Zeyen et al. (1985) showed an average crustal thickness of 30-32 km, with a local thickening beneath the central northern part of the chain. Diaz and Gallart (2009) compiled the results from deep seismic profiles beneath the Iberian plate and its surrounding areas, providing a crustal thickness map of the region.

Magnetotelluric profiles have provided crustal resistivity images of the main orogens and related foreland basins in the Iberian Peninsula. The Alpine orogens investigated are the Pyrenees (e.g. Pous et al.1995; Ledo et al., 2000; Campanya et al., 2012), the Cantabrian range (e.g. Pous et al., 2001) and Betic Mountains (e.g. Pous et al., 1999, Marti et al, 2009; Rosell et al., 2011; Ruiz-Constan et al, 2012), while Monteiro Santos et al. (1999), Almeida et al.(2005), Pous et al. (2004), Muñoz et al.(2008), Pous et al. (2011) have investigated the Iberian Variscan Massif. As the electrical resistivity is a physical parameter independent of the elastic seismic parameters a combination of both geophysical methods has contributed to clarify ambiguities in the interpretations (e.g. Carbonell et al., 2004).

This thesis is part of the Topo-Iberia project, a multi-disciplinary national Spanish project that involves several institutions with the aim of defining the whole structure of the Iberian 'micro-continent'. This thesis focuses on the use of one of the disciplines, the magnetotelluric method, applied to the investigation of two orogens of the Iberian Peninsula.

1.1.3 Approach employed: the magnetotelluric method

The magnetotelluric method was first proposed by Tikhonov (1950) and Cagniard (1953). This passive electromagnetic method allows to determine the electrical conductivity of the subsurface as a function of depth. Over the years this geophysical exploration technique started to gain importance and became the most used method for deep EM exploration in the academic community. The development of the instrumentation, improvements of modelling and inversion algorithms (2-D and 3-D) and the increase of computing capabilities have led to its use on a regular basis to build reliable electrical conductivity models for geodynamic studies and for natural resources exploration.

The MT method is a pretty flexible and robust method. Data acquisition can be performed by small teams in a short amount of time with a relative small budget. Compared to other geophysical methods it can be performed under almost all geographical conditions and in several geological environments. Over the last decades, a continuous increase in the use of the MT method for geothermal, oil, gas and mining exploration industry has been observed. In addition, its sensitivity to the electrical conductivity, which is independent from other geophysical parameters, has turned the MT method into a powerful exploration technique, especially when it is integrated with other geophysical methods.

In the scope of this thesis the MT method has been useful to study the two orogens at crustal scale. It has been able to detect interconnected fluids, discriminate between different geological formations, map faulted areas and detect lithospheric conductivity anomalies related to tectonic processes. These results, associated to geological observations and geophysical models allowed us to obtain an image of the structure of the lithosphere beneath both orogens and to interpret them geodynamically.

An important decision that has to be taken during an MT study is the number of spatial dimensions that have to be considered to accurately model the geology. The Earth is intrinsically three-dimensional. When assumptions of one or two dimensions are not taken properly incorrect or biased models can be obtained. In this thesis the dimensionality analysis of the conductivity structure was rigorously studied and as a consequence 3-D modelling was the more suitable approach to explain both datasets with precision. We therefore employed 3-D inversions for the two areas of study.

It is well known that all the geophysical methods suffer of an inherent ambiguity, or non-uniqueness, in the determination of the structure and composition of the subsurface. The different sensitivity and/or resolution of all geophysical techniques can be used to reduce this ambiguity when an integration using different geophysical methods is applied. In this thesis the complementarity and relations between the MT models and other existing models was considered.

1.1.4 Aims of the thesis

This thesis focuses on two areas of the Iberian plate, the Cantabrian Mountains and the Iberian Chain. The Iberian Chain is an intraplate mountain chain where geophysical studies are scarce and no relevant information on the major crustal structures has been obtained so far. The Cantabrian Mountains, formed at the northern boundary of the Iberian plate, are the western prolongation of the Pyrenees. Although well constrained from a number of geophysical, geological and petrophysical studies (Gallastegui, 2000; Pedreira, 2015; Pulgar, 1996), the understanding of the electrical conductivity distribution will provide new insights. In this context the **aims** of this thesis are:

Characterization of the crustal structure below the Duero Basin and the Cantabrian Mountains. An MT N-S oriented profile across the Cantabrian Mountains and the north part of the Duero Basin was acquired between 2009 and 2011 in the scope of this thesis. The profile consists of 13 MT soundings, 6 of them including long period data. The main aim of this study is to provide a new geoelectric model of the Cantabrian Mountains that: (1) satisfies and integrates all the geological and geophysical studies available for the area; (2) reproduces the complex magnetotelluric responses observed. The methods adopted here allowed us to build a 3-D geoelectrical model of the area integrated with the previous seismic and geological observations, in an effort to achieve a deeper understanding of the crustal structure and the geodynamical evolution of this orogen.

Characterization of the crustal structure of the Iberian Chain. Two MT profiles consisting of 38 soundings were acquired across the central part of the Iberian Chain between 2011 and 2013 in the scope of this thesis. The first goal of this study is to provide the first geophysical image of the crustal structure of the Iberian Chain. The integration of the 3-D geoelectrical model obtained with a recent refraction/wide-angle reflection seismic profile and gravity modelling carried out by the Institute of Earth Sciences (CSIC) allowed us to obtain a constrained crustal model of the Iberian Chain. The geological interpretation of this new integrated modelling permits to confirm previous geological assumptions and raise new questions about the geodynamical evolution of this orogen.

1.2 Structure of the thesis

The thesis is divided in six chapters:

Chapter 1. Introduction and Motivations: Illustrates the motivations, problematics and the main objectives of this thesis.

Chapter 2. Geological overview: This chapter gives an overview of the geological and geodynamical processes that gave rise to the Alpine belts in the Iberian Peninsula. A geological and geophysical review of the Cantabrian Mountains and the Iberian Chain areas are presented and specific objectives for each area are addressed.

Chapter 3. Introduction to the magnetotelluric method: The third chapter gives an overview of the magnetotelluric method. The theory of the method, data acquisition, data processing and the multidimensional modelling are discussed.

Chapter 4. Results for the Cantabrian Mountains: This chapter presents the results obtained from the 2-D and 3-D inversion of the magnetotelluric transect through the Cantabrian Mountains. The methodology adopted for the data analysis and inversion is presented. The comparison between both inversions and the requirement for a 3-D inversion is discussed. The 3-D model obtained is then integrated with the geophysical and geological observations and ultimately geologically interpreted.

Chapter 5. Results for the Iberian Chain: This chapter presents the results from the geoelectrical modelling of the crustal structure of this intraplate orogen. The 3-D inversion of the MT data is presented, along with the interpretation obtained integrating the MT model and the seismic results.

Chapter 6. Discussion and conclusions: In this chapter the main contributions of the thesis are discussed and summarized.

2 Geological Setting

2.1 Introduction

The Iberian Peninsula is located at the westernmost part of the Alpine-Himalayan Belt between the Eurasian and African plates. The Alpine-Himalayan Belt extends from the Iberian Peninsula to New Zealand (Figure 2-1). The Iberian microplate belongs nowadays to the Eurasian plate but behaved as an independent plate in Early Cretaceous during the opening of the Bay of Biscay (Srivastava et al., 1990). The Alpine orogeny started in Late Cretaceous, with deformation occurring in the borders of the Iberian plate and in the interior of the plate, giving rise to the current mountain ranges in the Peninsula and their associated foreland basins.

This thesis will focus on the characterization of the lithospherical structure of two orogens of the Iberian Peninsula: the Cantabrian Mountains, a thrust and fold belt located along the northern coast of Iberia, and the Iberian Chain, an intraplate thrust belt located within the Iberian plate.

In this chapter an overview of the structure of the Iberian Plate will be given followed by a specific description of the two orogens studied from a geological and geophysical point of view. Finally, the objectives of this thesis for each area of investigation are presented.

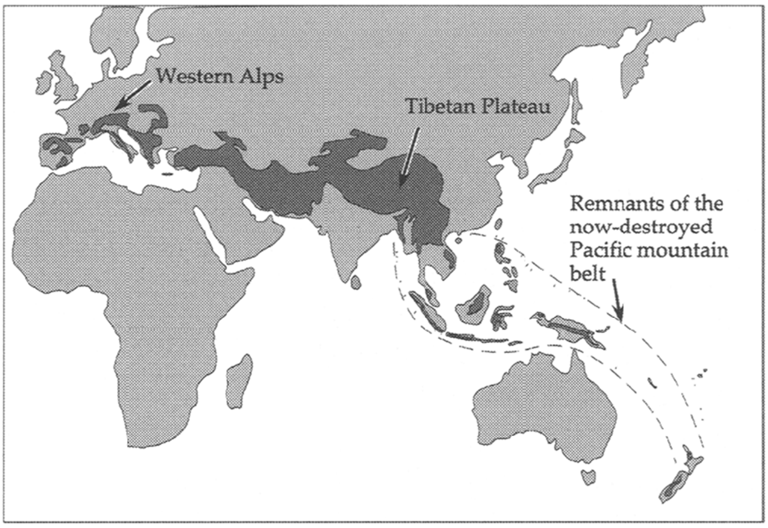

Figure 2-1: Sketch of the Alpine-Himalayan orogenic belt (Lister et al., 2001).

2.2 Structure of the Iberian Plate

The major part of the Western and Central Europe is constituted by a pre-Mesozoic basement, formed by Superior Protozoic to Carboniferous rocks, deformed and partially metamorphized and intruded during the Variscan orogeny that took place at the end of Palaeozoic. The Variscan orogeny resulted from the collision of two continents, Laurentia to the NW and Gondwana to the SE, at the end of the Carboniferous (Matte, 2001) forming the supercontinent called Pangaea. Figure 2-2 shows the tentatively paleo-geographical maps from Ordovician to Carboniferous describing the Variscan orogeny (Matte, 2001).

This Palaeozoic mountain system extended for more than 8000 km long and 1000 km broad, from the Caucasian Mountains in the East to the Southern Appalachians in the West. The European Variscan Orogen shows a complex sinuous pattern having an arc-shape in the SW part of Europe (Figure 2-3). It is known as the Iberican-Armorican Arc, located in the NW part of the Iberian Peninsula (Franke, 1989; Matte, 2001). The European Variscan Orogen is still visible and well conserved in the Iberian Peninsula.

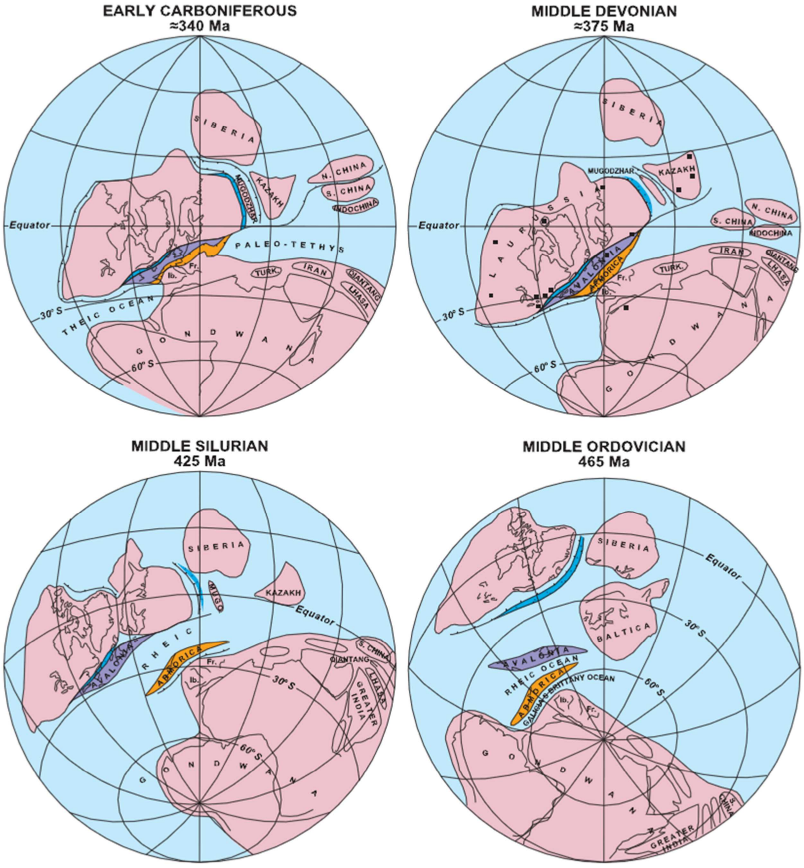

Figure 2-2: Tentatively paleo-geographical maps from Ordovician to Carboniferous describing the Variscan orogeny (Matte, 2001).

Palaeozoic outcropping is mainly present in the occidental part of the Iberian Peninsula, in the Iberian Massif. In the Cantabrian Mountains the MT profile carried out is located in Palaeozoic rocks, while the MT profiles crossing the Iberian Chain are located in Mesozoic rocks (Figure 1-1). However, Palaeozoic outcroppings are visible in the Iberian Chain, mainly because of the posterior Tertiary contraction that involved the Variscan basement. In the NW part of the Iberian Peninsula different characteristics of the Variscan collisional orogeny can be observed: an internal area characterized by metamorphism and intrusive bodies (Asturo Occidental-Leonesa Zone) and an external zone with thin-skinned tectonics, with thrusts and folds structures and absence of metamorphism (Cantabrian Zone).

At the end of the Variscan Orogeny, in Permian Times (280 Ma), the supercontinent Pangea started to suffer an extensional process that lasted until the Late Cretaceous (80 Ma). This distensive episode created a divergent margin between Africa-Europe and America (Figure 2-2).

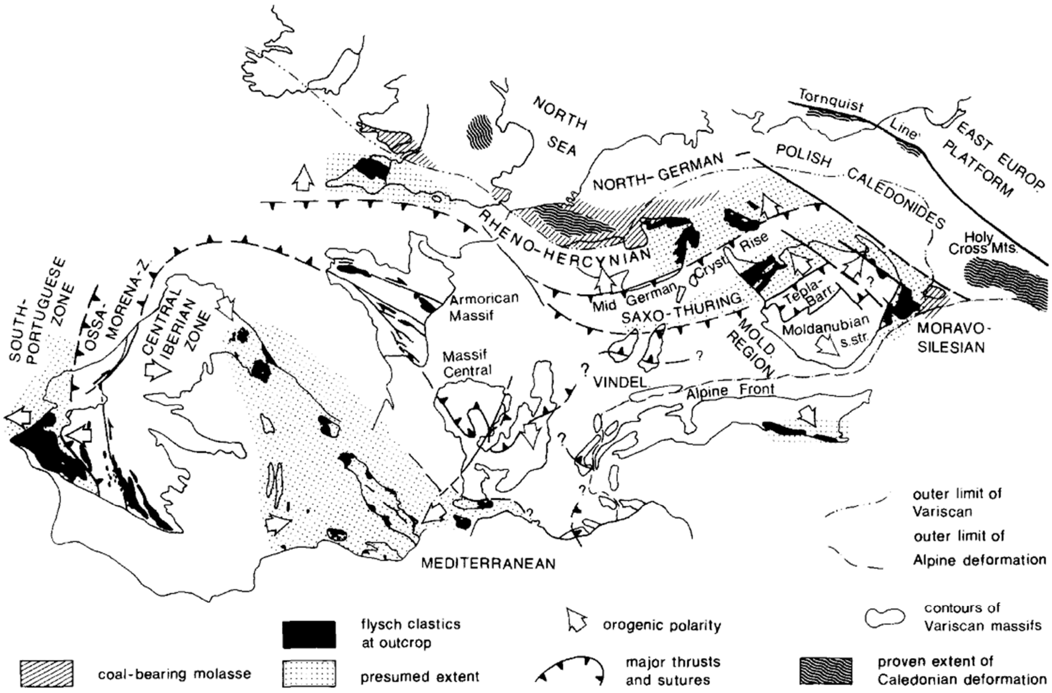

Figure 2-3: Main structural elements in the Variscan Belt of Europe during the Early Carboniferous (Franke, 1989).

The oceanization of these rifts started in the Jurassic (180Ma). At that point the behaviour of the Iberian Plate is independent from Eurasia to the North and Africa to the South. Considering Eurasia as stable, the movement of Africa to the East is due to the opening of the Atlantic Ocean (Srivastava et al., 1990). Opening of the North Atlantic Ocean provoked the motion of the Iberian plate to the SE, accompanied by a counter-clockwise rotation, dragged by the eastward movement of Africa (Malod y Mauffret, 1990). This rotation of the Iberian plate provoked the opening of the Bay of Biscay, splitting the Cantabrian and Armorican margins, which later on behaved as passive margins (Figure 2-4a). The Bay of Biscay opening is done from west to east from the Aptiense until the Campamiense. In the eastern part the continental crust is thinned, while in the most western part oceanic crust formation occurred (Malod et al., 1982). During this extensional process rift basins developed in the borders and in the interior of the Iberian plate. The most important rift systems that developed in northern Iberia are the Pyrenean rift and the Iberian rift, where Mesozoic sediments deposition occurred.

In Late Cretaceous (Figure 2-4b) the opening of the South Atlantic Ocean provoked the northward drift of the African plate and, as a consequence, the beginning of the convergence between the Eurasian and Iberian plates and the end of the Mesozoic extension. This convergence led to the partial closure of the Bay of Biscay and the development of the Cantabrian-Pyrenean Mountains. The Mesozoic basins of the Pyrenean rift were inverted and formed part of the Pyrenean orogen. To the west a limited subduction took place along the Cantabrian Margin with the associated uplift of the Cantabrian Mountains.

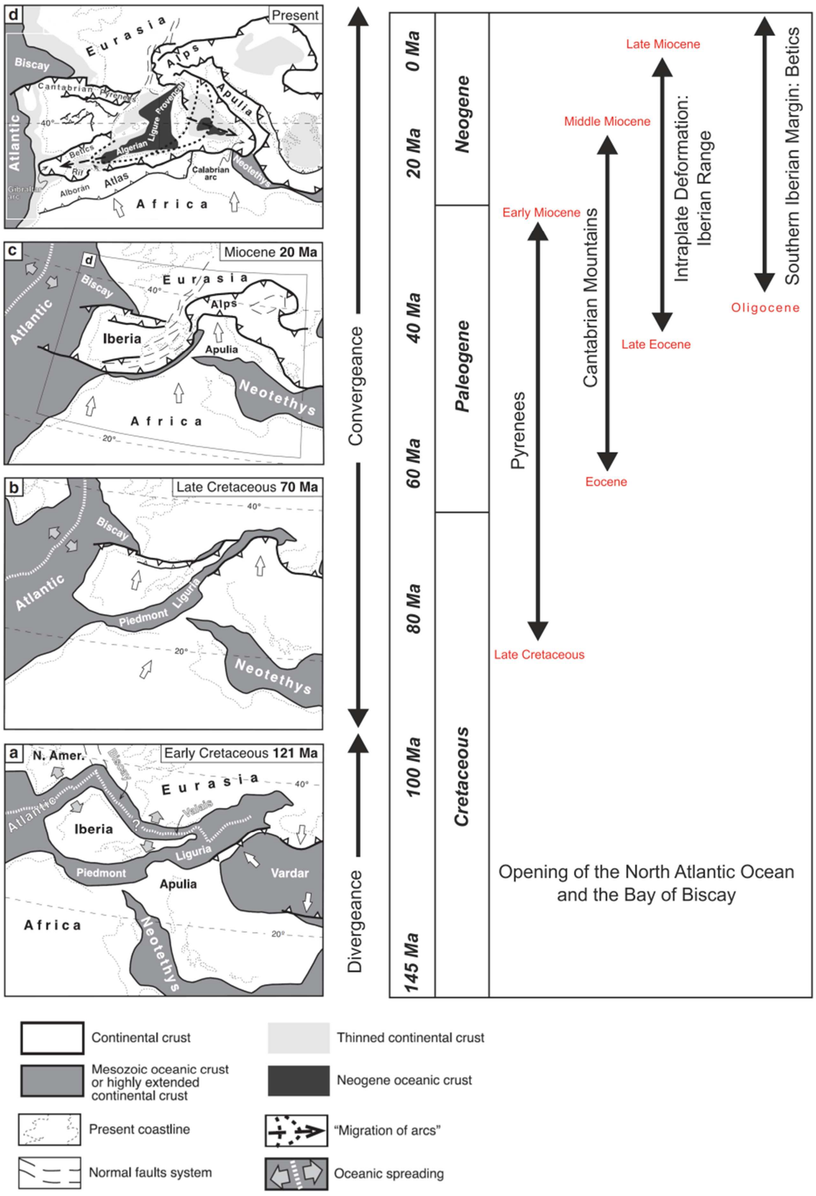

Figure 2-4: Left: a-c) Palaeographic evolution of the Iberian Plate, between Early Cretaceous and Miocene. d) Present tectonic map of the Iberian plate and surrounding areas (modified from Quintana et al., 2015). Right: Evolution of the principal orogens of the Iberian Plate (Quintana et al., 2015, and reference therein).

In the Oligocene, the convergence of the African and Iberian plates started to be mostly accommodated by the Betic-Rif orogenic system and the intraplate orogens (Verges and Fernandez, 2012) (Figure 2-4c). The contractive event occurring in North Iberia ended in the middle Miocene (Verges and Fernandez, 2012). Intraplate shortening took place with the formation of the Iberian fold-and-thrust belt (Iberian Chain) and the Central System from late Eocene to end of Miocene (Guimerà et al., 1995, 2004; de Vicente et al., 2007). The Iberian Chain shortening is about half of that of Pyrenees (Guimerà et al., 2004; Muñoz-Jimenez and Casas-Sainz, 1997; Sibuet et al., 2004). Since early Miocene the convergence between Eurasia and Africa became slow, leading to an extensional event that gave rise to the Alboran Basin and the Gibraltar Arc (Rosembaum et al., 2002; Figure 2-4d).

2.3 Regional geophysical background

2.3.1 Crustal thickness inferred from seismic studies

The structure and thickness of the crust in the Iberian Peninsula has been estimated by several regional seismic studies. Diaz and Gallart (2009) compiled crustal depth thicknesses along published deep seismic soundings (DSS) profiles in the whole Iberian Peninsula. The resulting map is shown in Figure 2-5a. The crustal thickening reaches a maximum of 50 km beneath the Pyrenean Range, extending westwards along the Cantabrian Mountains to a crustal thickness of about 42 km. The Iberian Chain has a crustal root reaching 40 km in its SE part. In the rest of the Iberian Peninsula crustal thickness between 30 km and 35 km are reported with the exception of the Betics Chain with a crust of 38 km thick.

A recent regional study using P-receiver functions (PRF) was carried out by Mancilla and Diaz (2015) (Figure 2-5b). It covers the whole Iberian Peninsula and northern Morocco. The receiver function technique consists in measuring ground motion at a seismic station when distant teleseismic signal arrives. Comparing to the previous studies, these techniques allowed to obtain a regular grid of crustal depth estimations, because of the high coverage of seismic stations deployed in the whole Peninsula, although with less resolution.

Consistent results between active and passive sources show a thickened crust beneath the Pyrenees/Cantabrian Mountains and the Betics (around 45). In the Iberian Chain the Moho is found at a depth around 40 km. However, some differences appear in some parts of the Pyrenean-Cantabrian orogen and in the Betics. In the Cantabrian Mountains the base of the crust differs more than 10 km between active and passive sources. The complex lithospheric structure and the lateral variations in the crustal thickness beneath northern Iberia could explain those differences (Mancilla and Diaz, 2015).

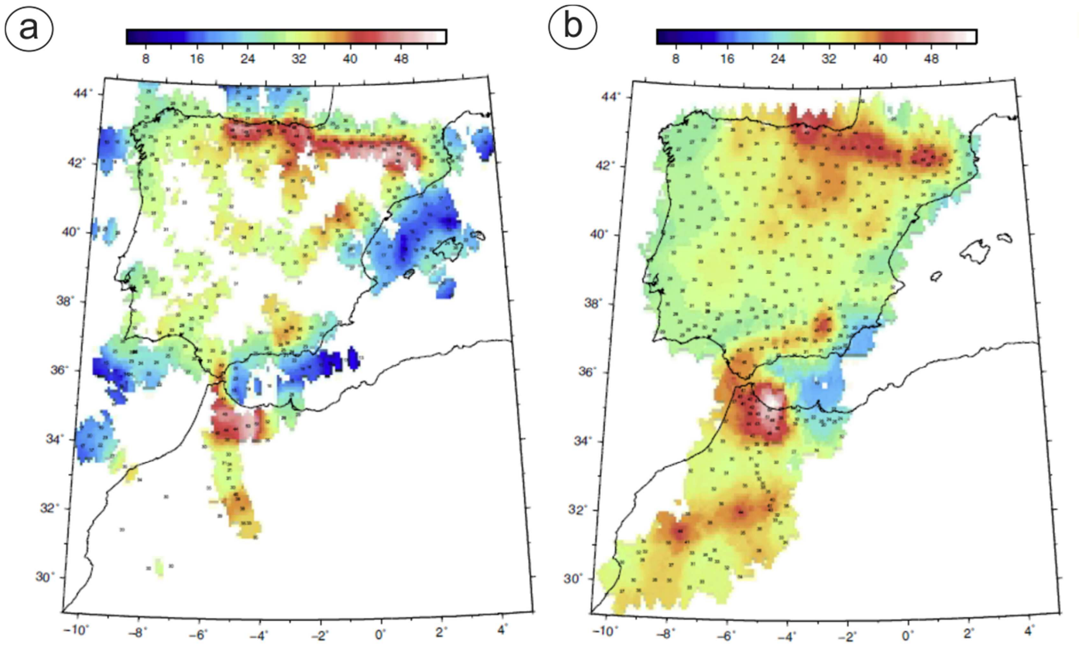

Figure 2-5: Crustal depth thicknesses. a): based on deep seismic soundings (active source). b): based on receiver function data (passive source) (Diaz and Gallart, 2009; Mancilla and Diaz, 2015). Colour scale in km depth.

2.3.2 Crustal and lithospheric thicknesses inferred from potential field data

Torne et al. (2015) present the results of the combination of potential field data with steady state thermal analysis carried out for the entire Iberian Peninsula. Figure 2-6a shows the Bouguer anomaly map and Figure 2-6b the crustal thickness obtained from combining elevation and geoid data. Although there is a general agreement with the DSS and PRF values, significant differences appear beneath the Cantabrian Mountains, probably due to the complex crustal structure of this area, as previously mentioned (Figure 2-6b and Figure 2-5).

The combination of elevation and geoid data gives the lithospheric thickness (Figure 2-6c). It points to a thick lithosphere (>150km) beneath the Pyrenees, while in the Iberian Chain, the Betics, and the Cantabrian Mountains the lithospheric thickness is between 140 and 150 km (Torne et al., 2015) and beneath the Duero Basin around 130 km. However, Pedreira et al. (2015) and Carballo et al. (2015) studies point to a deeper lithosphere beneath the Cantabrian Mountains, reaching 170 to 180 km.

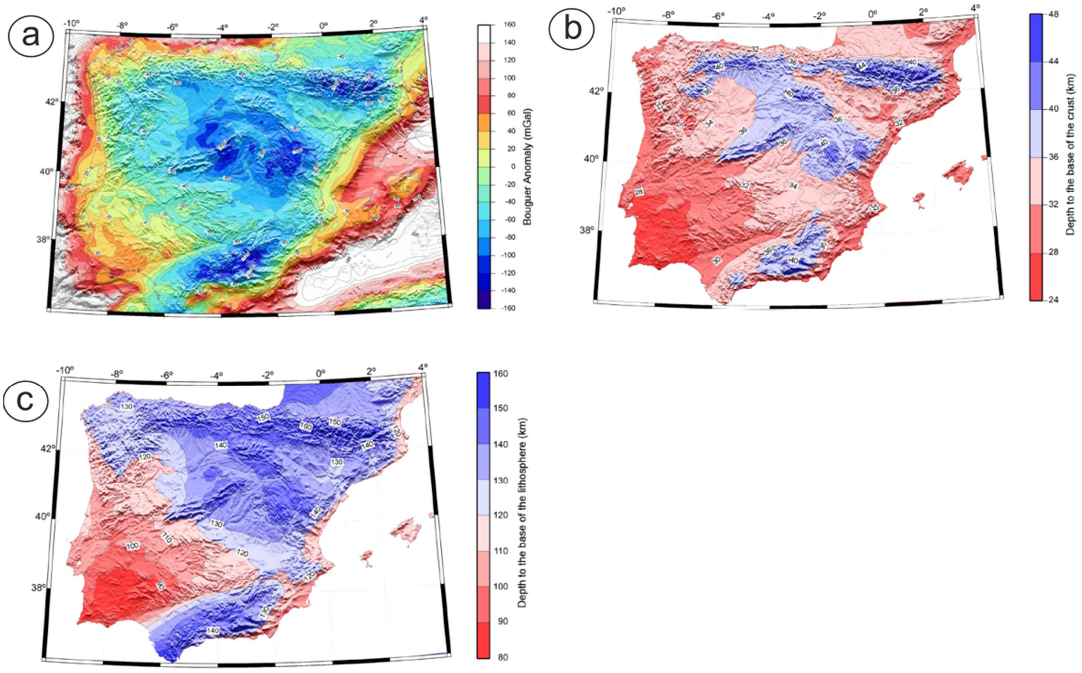

Figure 2-6: a): Bouguer anomaly map (Torne et al., 2015 from Ayala (2013)). Crustal (b) and lithospheric (c) thicknesses obtained from combining elevation and geoid data (Torne et al., 2015).

2.3.3 Seismicity

The borders of the Iberian plate are active, especially in the contact with the African plate in the south and the Eurasian plate in the north. Figure 2-7 shows the seismicity of the Iberian region projected on a map of active faults (Stich et al., 2006).

Activity is concentrated in the borders, but some activity is also evidenced intraplate, in particular in the Iberian Chain, where earthquakes with magnitudes greater than 3 have been recorded. The few earthquakes observed in the Cantabrian Mountains are concentrated north of the Venteniella-Ubierna strike-slip fault, oriented NW-SE, at depths between 5 and 15 km as well as in the Basque Cantabrian Basin.

These data correlate well with the active tectonic areas. It should be pointed out that the magnetotelluric method is sensitive to electrically conductive fluids, and therefore, it has the capacity of mapping faults, although it is not possible to differentiate between active and passive faults based only on the electrical conductivity (Simpson and Bahr, 2005).

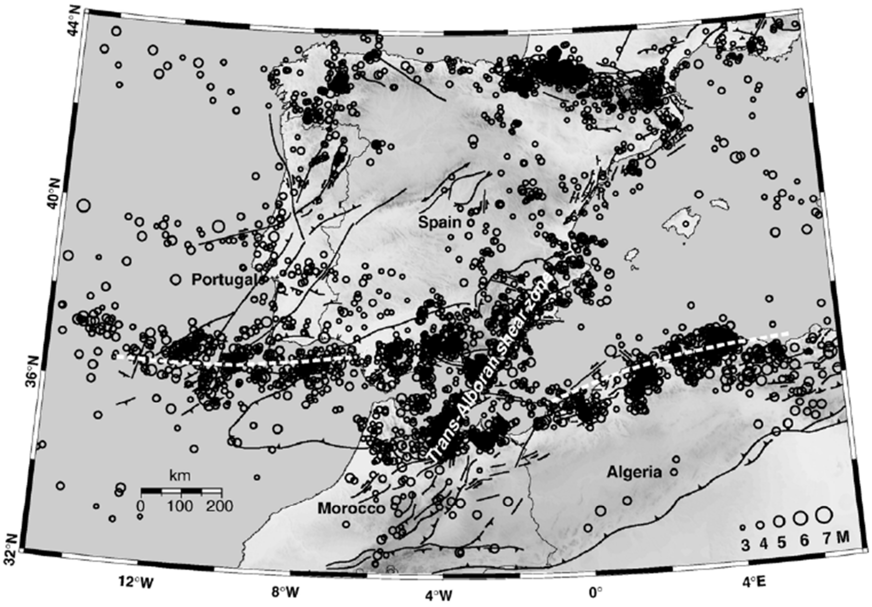

Figure 2-7: Seismicity observed in the Iberian Peninsula and northern Morocco (after Stich et al., 2006).

2.3.4 GPS data

Deformation of Earth’s surface in terms of slip and strains rates can be quantified using global positioning system (GPS) geodesy techniques. Velocity map shown in Figure 2-8 was derived from GPS measurements obtained between 1998 and 2005 (Stich et al., 2006). Considering the European plate as stable, we can see that stations located NE of the Iberian Peninsula almost do not move, suggesting that this region is attached to the Eurasian plate (Stich et al., 2006). In the southern part of the Iberian Peninsula westwards velocities are observed.

The *CANT* GPS station, located in the Cantabrian Mountains, shows south-eastwards displacement at a relative velocity of 1.22 mm/yr. (Stich et al., 2006), suggesting a NW-SE active tectonics in the Cantabrian Mountains, which is also pointed out by the earthquake epicentres alignments (Figure 2-7). The *EBRE* GPS station located NE of the Iberian Chain, in the Ebro Basin, shows a SSE directed displacement with a relative velocity of 1.15 mm/yr. (Stich et al., 2006).

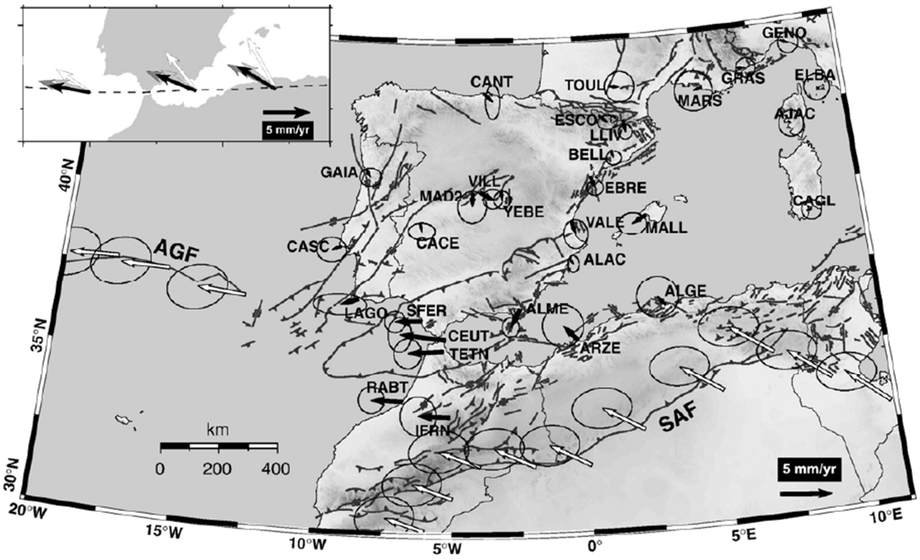

Figure 2-8: GPS velocity fields for the Iberian plate and surrounding areas. Black arrows show the horizontal motion relative to the stable European plate (Stich et al., 2006).

2.3.5 Integrated geophysical studies

Large scale integrated studies (Quintana et al., 2015; Carballo et al., 2015) have obtained overall images of the crust and upper mantle along 2-D transects of the whole Iberian Plate.

Quintana et al. (2015) used results from previous studies to calculate the displacement transfer during the Alpine Orogeny in the entire plate. They conclude that the total alpine shortening of the Iberian plate is between 267 and 292 km. A mid-crustal detachment could exist in the entire Iberian Plate allowing the displacement transfer from the Betics and Cantabrian Mountains to the intraplate ranges.

Carballo et al. (2015), combining potential fields, thermal elevation, seismic and petrological data, obtained the lithospheric thickness along a NS transect crossing the whole Iberian plate. The lithospheric thickness and the interpreted composition allowed to reproduce well the P and S-wave velocities. This study pointed to a deep Lithosphere Asthenosphere Boundary (LAB) beneath the Cantabrian Mountains (around 180 km) with a hydrated upper mantle composition. Beneath the Duero Basin, the Central system and the Tajo Basin, the lithosphere thickness is estimated around 130 km, getting thicker in the south beneath the Betic Chain, where the LAB depth estimation is 160 km.

2.4 Cantabrian Mountains: Geological Setting

2.4.1 Geological structure of the Cantabrian Mountains

The Cantabrian Mountains, which extend for more than 250 km along the northern border of the Iberian Peninsula, constitute the western prolongation of the Pyrenees. To the south, the range is flanked by the Tertiary Duero foreland basin and, to the north, it overlies the northern Iberian continental margin and the Bay of Biscay abyssal plain. The range evolved from different tectonic regimes in Palaeozoic, Mesozoic and Cenozoic times. Figure 2-9 shows the geological map of the studied area, along with the location of the MT sites recorded in this thesis.

During the Palaeozoic, the NW Iberian Peninsula constituted part of the continental margin of Gondwana and the collision with Laurentia gave rise to the European Variscan belt. The Variscan Iberian Massif outcrops in the central and western parts of the Cantabrian Mountains, constituted by Palaeozoic and Precambrian rocks (Figure 2-9a). The main zone of the Iberian Massif recognized in the Cantabrian Mountains is the Cantabrian zone CZ (or the Asturian Massif, Figure 2-9b). It is the most eastern zone of the Iberian Massif, and represents the foreland fold-and-thrust belt of the Variscan orogeny.

The Variscan orogen was then eroded, followed by the Mesozoic extension related to the opening of the Atlantic Ocean and the Bay of Biscay. Several sedimentary basins between Eurasia and Iberia developed, giving rise to the Parentis and Basque-Cantabrian basins, located in the present-day extremity of the Bay of Biscay. The Mesozoic extension ended up in the mid to Late Cretaceous with formation of oceanic crust in the centre of the Bay of Biscay (west of 6ºW, Sibuet et al., 2004). The Bay of Biscay is flanked by two passive margins, the North-Iberian (or Cantabrian) continental margin to the south and the Armorican margin to the north. The Basque-Cantabrian Basin (BCB) is located east of the CZ (Figure 2-9b) and presents several thousand meters of Mesozoic sediments. The transition from the BCB to the CZ is diffuse, defining gradually the limit of the basin deposits that lies unconformably on the Variscan basement (Pedreira et al., 2007).

In Late Cretaceous-Cenozoic times, the Alpine Orogeny began and Iberia and Eurasia started to converge. It resulted in the inversion of the Mesozoic basins and the development of the Pyrenean-Cantabrian mountain belt as a doubly-vergent orogen all along northern Iberia. This belt is characterized by the northwards subduction of the Iberian crust beneath the Eurasian plate for the Pyrenees (Muñoz, 2002) and beneath the Iberian margin for the Cantabrian Mountains (Pulgar et al., 1996).

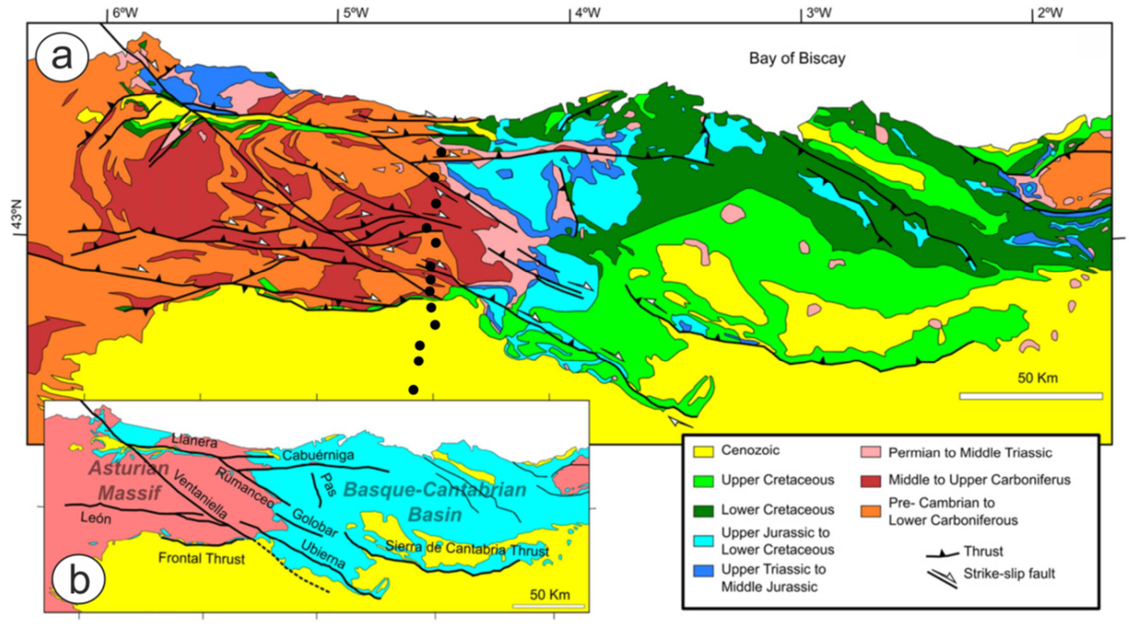

Figure 2-9: a) Geological map of the Cantabrian Mountains (modified from Tavani, 2012). Black points are the MT sites. b) Tectonic map of the area, with the name of the main faults.

The central Cantabrian Mountains formed as a regional uplift of the Palaeozoic basement over a north dipping thrust ramp connected to a flat midcrustal detachment (Alonso, 1996). Even if the northward subduction of the Iberian plate along an E-W strike is shared from eastern Pyrenees to the western part of the Iberian Peninsula, the Cantabrian Mountains show along strike differences in the style and trend of deformation. WNW-ESE striking anticlines and synclines are running parallel to main extensional faults (Ventaniella, Ubierna, Golobar and Rumaceo faults, see Figure 2-9b). The Ventaniella-Ubierna faults system is the longest of them, being a 300 km-long right-lateral strike-slip shear zone (Boillot and Malod, 1988; Tavani, 2012) oriented WNW-ESE (Figure 2-9b). In the northern part of the Cantabrian Mountains the structural trend changes. The most important E-W striking structures are the Llanera and Cabuerniga faults. The Cenozoic sediments of the Duero Basin are located south of the Cantabrian frontal thrust. The N-S oriented MT profile carried out crosses most of these tectonic structures.

2.4.2 Previous data: Seismic velocity structure

The present day knowledge of the structure of the Cantabrian Mountains lithosphere as described before has mainly been driven by the seismic experiments carried out in the last decades. The deep seismic reflection profile on land ESCIN-2 (Pulgar et al., 1996, 1997), the wide-angle reflection profile offshore ESCIN-4 (Fernandez Viejo et al, 2000) and the onshore refraction Profile 5 (Fernandez Viejo, 1997; Fernandez Viejo et al., 1998, 2000), permitted to obtain a detailed image of the lithosphere beneath the Duero Basin, the Cantabrian Mountains and the Bay of Biscay. Location of NS oriented profiles is shown in Figure 2 10a.

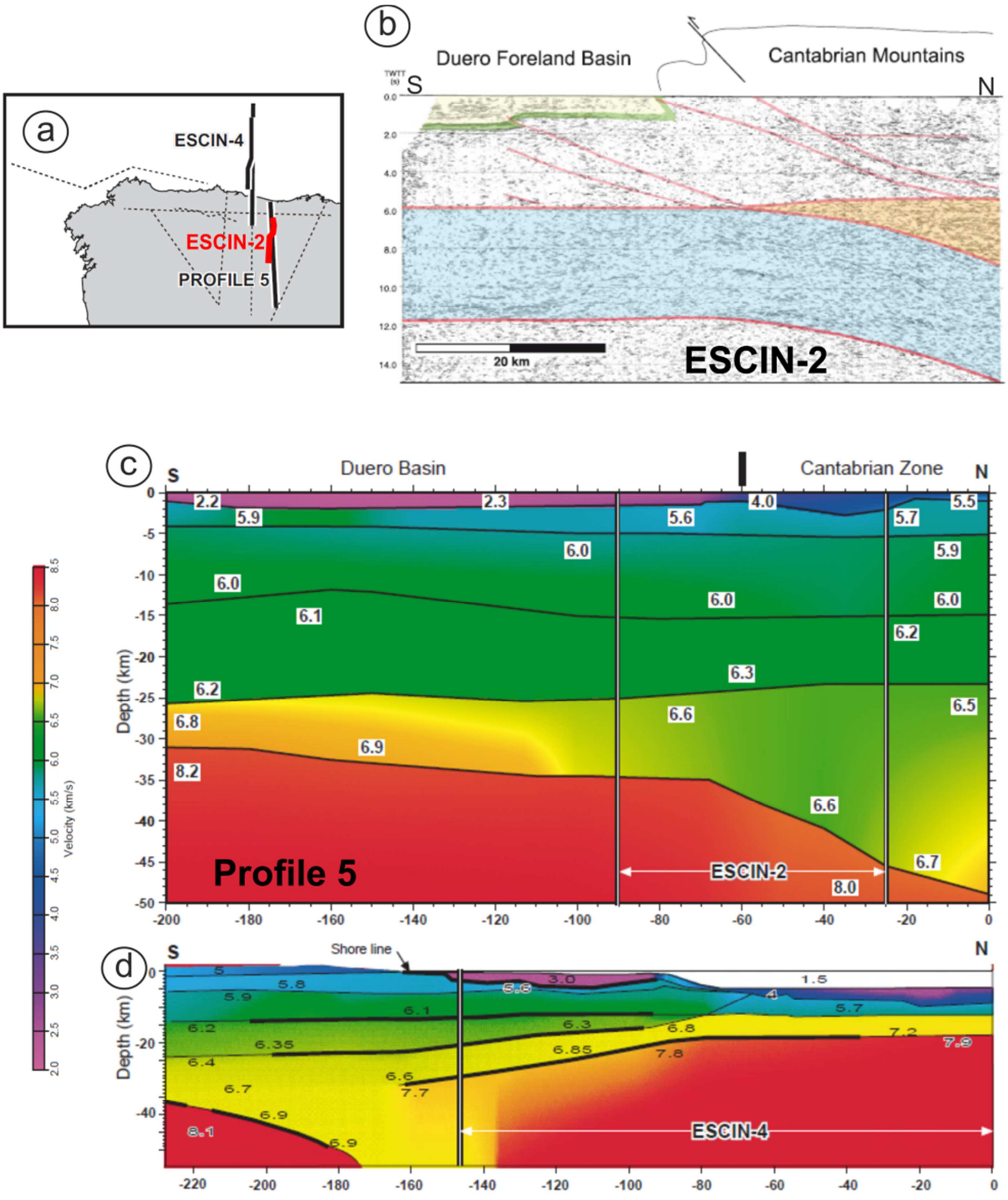

Figure 2-10: Seismic models in the Cantabrian Mountains area. a): location of the profiles. b): ESCIN-2 unmigrated profile (TWT in s), showing the main reflectors interpreted by Pulgar et al. (1996). c): P-wave velocity model of profile 5 (Fernandez Viejo et al., 1998). d): P-wave velocity model of profile ESCIN-4 (Fernandez Viejo et al, 2000).

Crustal P-wave velocities range from 5 km/s in the upper crust to 6.9 km/s in the lower crust, with some lateral variations in the lower crust attributed to different water content (Pedreira et al., 2015). P-wave velocities of the Iberian mantle are in 8.1 km/s. The ESCIN-4 wide-angle seismic experiment revealed a lower crustal layer along the margin with velocities of ~6.6 km/s beneath the coastline, increasing up to ~7.2–7.3 km/s to the north of the continental slope. Upper mantle shows anomalous low velocity values (7.7 – 7.9 km/s). It was interpreted as upper mantle hydration/serpentinization (Roca et al., 2011, Pedreira et al., 2015). All these profiles exhibit coherent features, with a Moho depth of 34 km below the Duero Basin. The north-dipping behaviour of the Iberian Moho subducting beneath the Margin, as observed in the Pyrenees, is revealed by both the reflection seismic and the wide angle records. The Moho reaches a depth of 55 km at 20 km south of the coastline. Below the coast line, the Moho is detected at a depth of 30 km shallowing to 18 km below the Bay of Biscay abyssal plain. This reflection in this case is attributed to the Cantabrian Margin Moho (Pulgar et al., 1996, 1997).

Gallastegui (2000) constructed a NS transect integrating all the geophysical results (Figure 2-11. It shows the complex imbrication between the Iberian and Cantabrian crusts related to the northward subduction of the middle and lower Iberian crust. This important crustal thickening is accompanied by the deformation of the Cantabrian Mountains, along with several north dipping thrusts that cross the upper crust and converge to a flat mid-crustal detachment located at 14 - 15 km depth (Figure 2-11; Gallastegui, 2000).

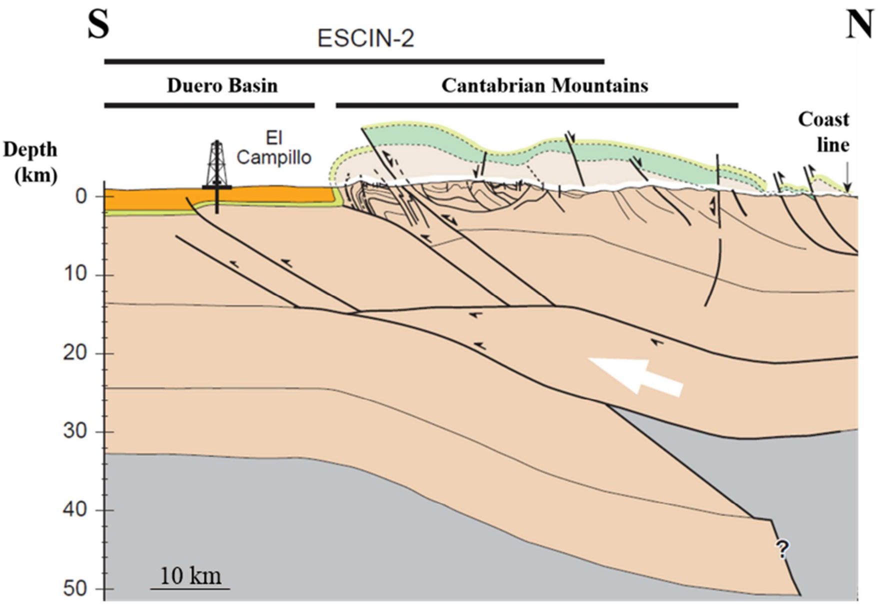

Figure 2-11: N-S crustal transect of the Cantabrian Mountains (modified from Gallastegui, 2000).

2.4.3 Previous data: Magnetotelluric data

A broad band MT transect (Figure 2-12), close to the current MT profile, has been carried out in 2001 (Pous et al. 2001). It is coincident with the seismic profile ESCIN-2 (Figure 2-10b).

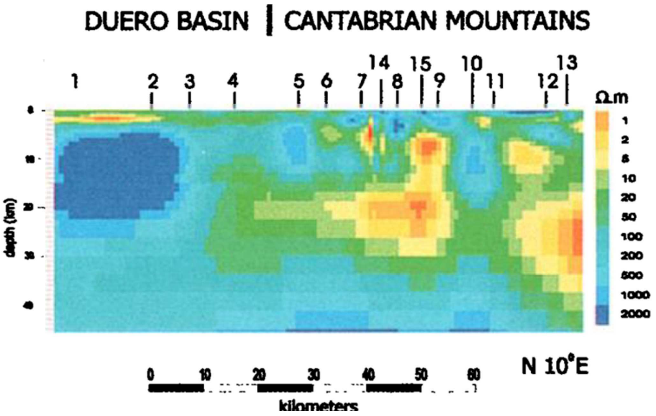

Figure 2-12: 2-D resistivity model obtained by Pous et al. (2001).

Main conclusions rising from this study were high conductivities related to the Duero Basin sediments and the presence of north-dipping conductors associated with alpine faults, one of them being interpreted as the sole detachment of the Cantabrian Mountains (Figure 2-12). A deep conductor located north of the profile beneath the coastline was tentatively explained as partial melting, as it has been interpreted further to the east in the Pyrenees (Pous et al 1995; Ledo et al. 2000; Campanya et al., 2012). This MT broad band dataset has been interpreted using a 2-D approach. By contrast the present dataset contains long period data and a 3-D inversion had to be carried out after the dimensionality analysis.

2.4.4 Geodynamical evolutionary model

Pedreira et al. 2015 presents a tentative evolutionary model (Figure 2-13) of the studied area during the Alpine orogeny. This model explains the underthrusting and indentation to the south of the lower crust of the oceanic/continental margin, which is responsible for the uplift of the Cantabrian Mountains and the formation of a crustal root at 55 km depth. This evolutionary model from the end of the extension in Late Cretaceous to the present day is similar to the one proposed by Gallastegui (2000).

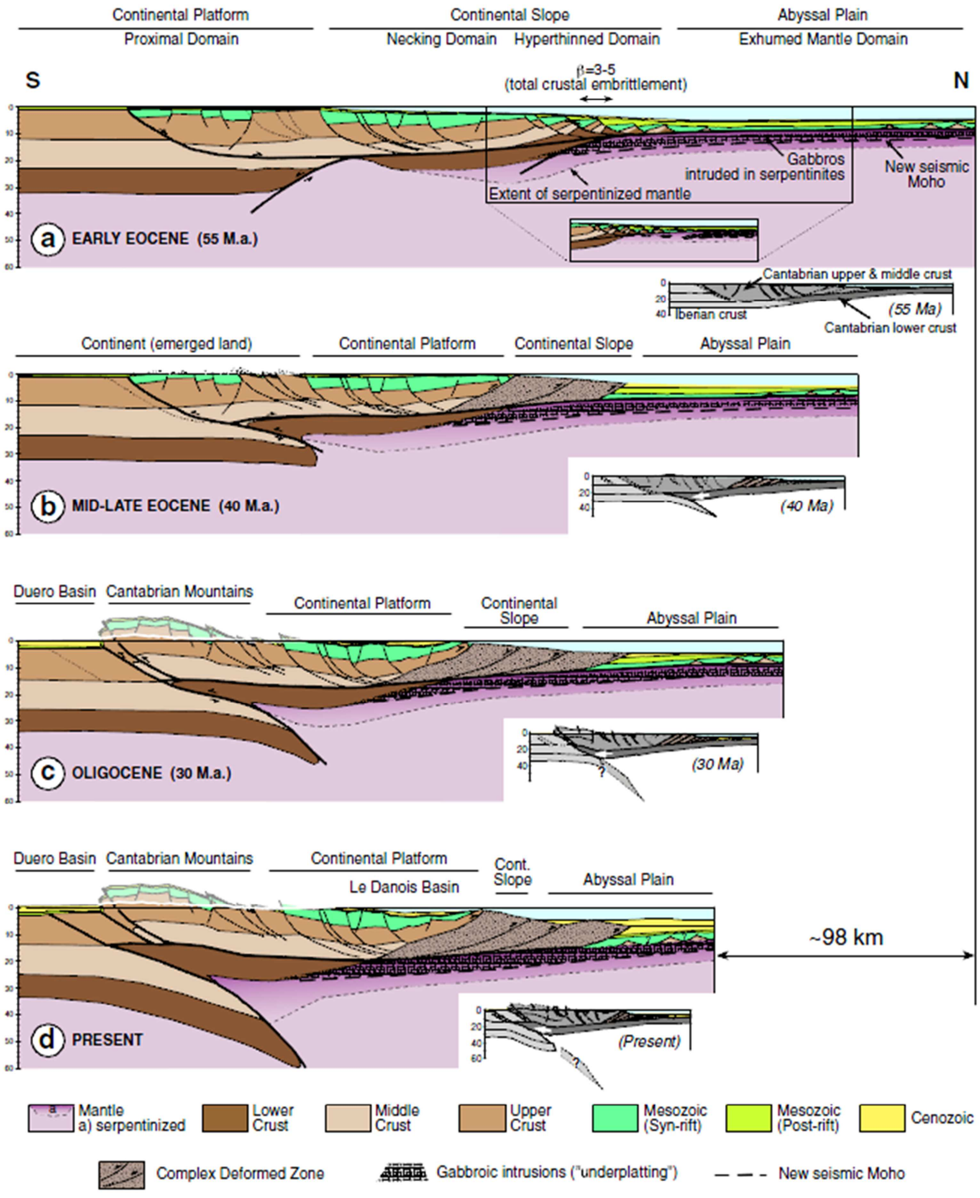

Figure 2-13: Schematic Alpine tectonic evolution for the N-S transect from Pedreira et al. (2015).

During the Late Cretaceous the North-Iberian margin is under extension, with upper crustal normal faults that root in a mid-crustal extensional detachment. In the continental slope, lower crustal rocks are exhumed through the normal faults, providing a path for the seawater into the mantle and serpentinize it (Figure 2-13a). In the Middle Eocene, the compressional stage started, provoking the underthrusting of the lower continental crust of the margin accompanied by its indentation into the Iberian crust, splitting it along the former extensional detachment. The indentation provoked the subduction of the Iberian lower crust to the north (Figure 2-13b). In the Oligocene, the lower crustal indentor progressed towards the south, uplifting the Variscan basement (Figure 2-13c). The weak hydrated mantle of the margin could not indent and therefore began to accrete against the subducting Iberian crust, forming the mantle wedge (Figure 2-13d).

This geodynamical model explains the low velocities found in the mantle wedge (serpentinization), and the shortening inferred from section balancing, about 100 km, as proposed by Gallastegui (2000).

2.4.5 Summary and objectives in the scope of this thesis

A good geological and geophysical knowledge of the lithospheric structure and the geodynamical evolution of the Cantabrian Mountains and the Duero Basin have been achieved. Recompilation of the results obtained so far indicates that the Alpine contraction provoked the northwards subduction of part of the Iberian continental crust beneath the Cantabrian Margin, leading to the uplift of the Cantabrian Mountains. Seismology and GPS studies indicate active tectonics along WNW-ESE to NW-SE directions.

The MT study presented in this thesis deals with a different physical parameter, the electrical conductivity, to bring new insights about the mechanisms responsible for the formation of the Cantabrian Mountains. The new MT transect differs from the previous one of Pous et al. (2001). The new data was acquired using new instrumentation that included long period data. The modelling of the complex crustal structure of the Cantabrian Mountains has to be approached using advanced MT dimensionality analysis and inversion techniques to achieve more accurate and reliable results.

Main objectives of this study from the new acquired MT transect across the Cantabrian Mountains are:

- Obtention of a 3-D inverse model able to fully reproduce the complex MT responses observed in the acquired data.
- Imaging the orientation and extension in depth of the main faults observed in surface and quantify which part of the crust was affected by the Alpine contraction.
- Determining the geometry of the subducted Iberian crust along the N-S transect by means of the interpretation of the conductivity anomalies.
- Providing insights to clarify the serpentinization occurring in the mantle wedge, as it has been previously interpreted.
- Achieving a deeper understanding of the crustal structure and the geodynamical history of the area.

2.5 Iberian Chain: Geological Setting

2.5.1 Geological structure of the Iberian Chain

The Iberian Chain is the major intraplate thrust-belt of the Iberian Peninsula. It developed during the Cenozoic as a consequence of the contractive inversion of the Iberian Mesozoic rift basins (Salas et al, 2001). The current structure of this part of the Iberian Peninsula is mainly the result of the geodynamic evolution occurring during the Mesozoic and the Cenozoic. The range is flanked to the NE by the Tertiary Duero Basin, and to the SW by the Tertiary Tajo Basin (Figure 2-14).

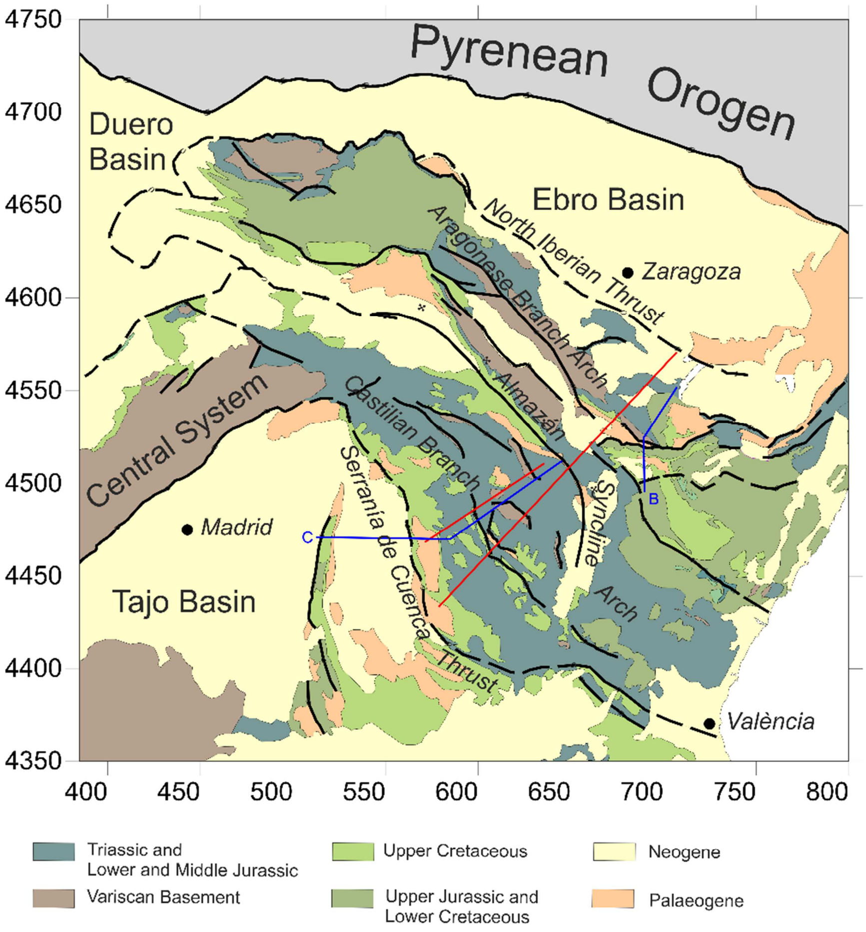

Figure 2-14: Simplified geological map of the Iberian Chain and surrounding Tertiary basins (modified after Guimerà, 2004, 2013). Red lines are two MT profiles carried out in this thesis. UTM coordinates (30T, ED50) are shown in km. Blue lines represent the two geological sections shown in Figure 2-15.

The Variscan basement crops out extensively in the Variscan Iberian Massif (in the western half of the Iberian Peninsula) and also within some areas of the Iberian Chain (Figure 2-14). The Variscan basement was strongly eroded during the latest Palaeozoic and a generalized planation surface was developed over it.

As a consequence of the extension period related to the opening of the Atlantic Ocean the Iberian Basin was formed as an intracratonic basin during the Mesozoic. It contains thick sequences of Upper Permian and Mesozoic continental and shallow marine clastic rocks, carbonates and minor evaporites. Large lateral thickness changes are observed in the Mesozoic sedimentary sequence of the Iberian Chain, indicating deposition in tectonically active basins (Guimerà et al., 2004).

The contractive event happening in the Iberian Plate started to affect the Iberian Basin during the Eocene (Guimerà and Álvaro, 1990), forming the Iberian Chain. It formed as a double-vergent intraplate thrust-belt, with a NW-SE main trend (Guimerà and Álvaro, 1990). It results from the contractional inversion of the Iberian Mesozoic basins, also involving the Variscan basement between the North Iberian and the Serranía de Cuenca Thrusts (Figure 2-14 and Figure 2-15) (Guimerà et al., 2004; Salas et al., 2001). In the areas where the basement has been involved in the inversion, two big arches (the Castilian Branch Arch and the Aragonese Branch Arch) can be distinguished, separated by the Almazán Syncline. Both arches are crustal scale structures. The Cenozoic thrust system has been proposed to involve only the upper crust with 10 -12 km deep detachment level (Guimerà and Alvaro, 1990) or the whole crust (Salas and Casas, 1993 and Anadón and Roca, 1996). Guimerà et al. (2004) proposed, based on the fact that the Pyrenees and the Betics were active simultaneously in Oligocene, that the deformation of the Iberian Chain could be related to either of them, or both of them, by means of a mid-crustal detachment.

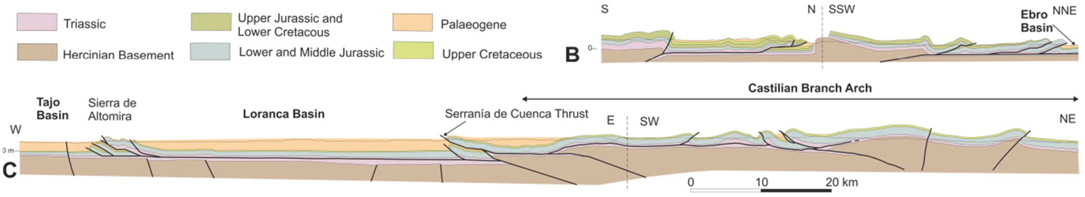

Figure 2-15: Geological sections across the central Iberian Chain (B: After Guimerà, 2004; C: after Guimerà and Álvaro (1990) and Muñoz Martín and de Vicente (1998). For location, see Figure 2-14.

Cenozoic shortening in the Iberian Chain is estimated to vary between 41 km (19%) in the NW across the Cameros area and 37 km (14%) in the central parts, along the sections shown in Figure 2-15 (Guimerà, 2013). The Cenozoic shortening is responsible for the uplift of the Mesozoic and Lower Cenozoic rocks and the generation of the present day topography of the Iberian Chain (Guimerà and González, 1998, Guimerà, 2013). The crustal thickening exceeds 40 km beneath the Iberian Chain (Salas and Casas, 1993).

In the eastern coastal areas of the Iberian Peninsula, the topography is strongly influenced by the late Oligocene-to-Present development of the Western Mediterranean. NE-SW extensional faults related to the crustal thinning between the Balearic Islands and the Iberian Peninsula are preserved on-shore, producing a descending topographic gradient from the elevated inner parts of Iberia to the Mediterranean coast (Seillé et al., 2015).

2.5.2 Previous data: Seismic velocity structure

A refraction/wide-angle reflection seismic profile crossing the Iberian Chain confirms the existence of a moderate crustal thickening beneath the central part of the profile (Gallart et al., 2004; Seillé et al., 2015), where Moho depths exceeding 40 km is documented. The profile samples the area with a Bouguer gravity low in the range of -100 to -140 mGal (Figures 2-16 and 2-17).

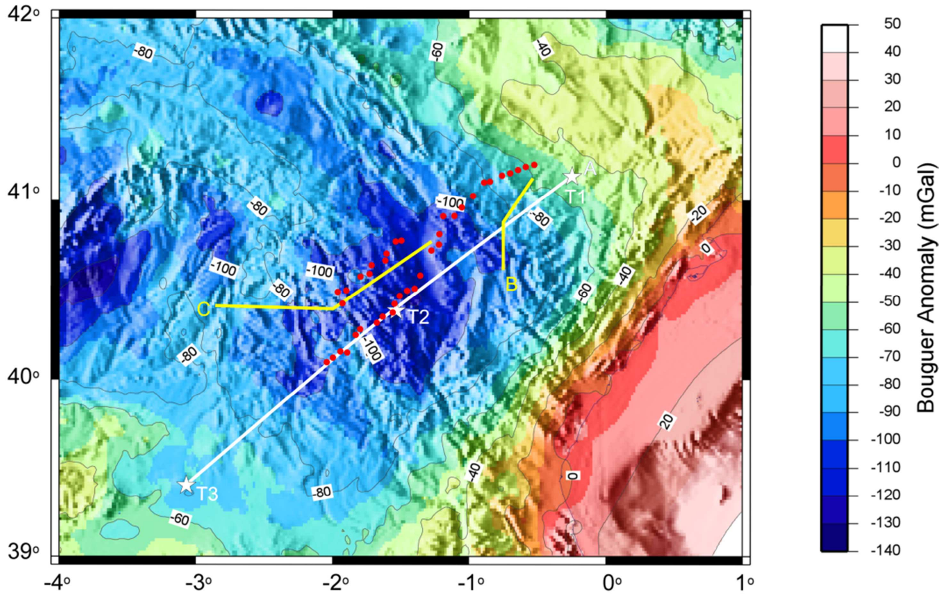

Figure 2-16: Bouguer anomaly map of the study area (Seillé et al., 2015). The map has been calculated using the geodetic reference system GRS80 and a reference density of 2670 kg/m3. Colour key shows Bouguer Anomaly. Contours every 10 mGal. Shading indicates elevation. White thick lines show the location of seismic profile. Yellow thick lines represent the geological cross-section shown in Figure 2-15. Red dots show MT sites.

The uppermost sedimentary layer has velocities ranges from 4.2 to 5.1 km/s (Figure 2-17). The basement depth ranges between 3 and 5 km along the profile and it is defined with velocities between 5.1 and 5.4 km/s. A local thickening is present in the model, reaching depths of 7-8 km. The model has a middle crust layer with velocities ranging between 6.3 and 6.45 km/s and showing smooth vertical gradients (Seillé et al. 2015).

The main result inferred from the velocity-depth modelling is the presence of a 100 km wide crustal thickened area located NE of shot T2 (Seillé et al., 2015). The top of the transitional zone associated with the Moho evolves from 30 km at the SW part of the profile to a maximum depth of about 40 km at offsets close to 200 km, then thin again to 30 km at the NE edge of the profile. The thickened area, located up to 70 km NE of shot T2, is consistent with results arising from passive seismic experiments (Mancilla and Diaz, 2015), as well as with the gravity minimum observed in the Bouguer anomaly map (Figure 2-16). In addition the model shows a local rise of the Moho boundary at distances of 110-150 km from the SW edge.

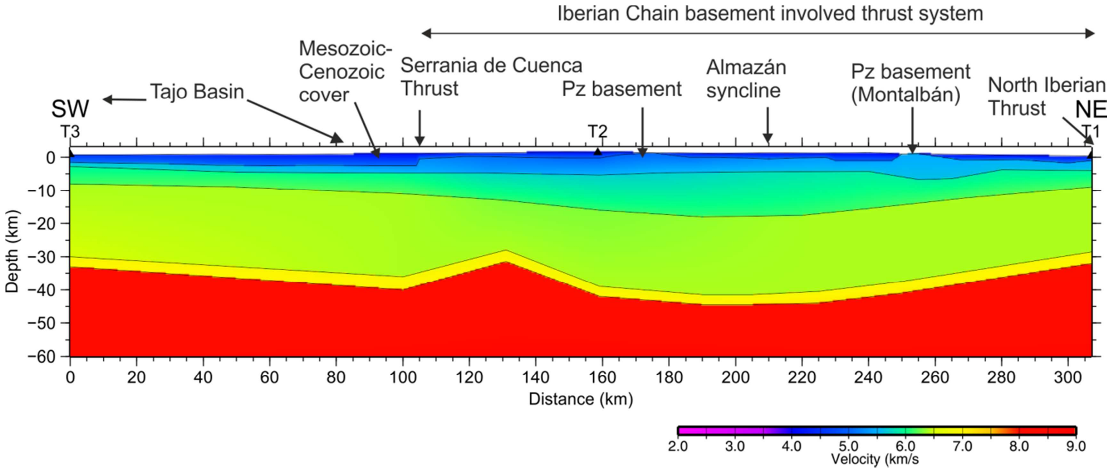

Figure 2-17: Velocity-depth model along the profile (Seillé et al., 2015). Colour scale shows the corresponding P-wave velocities. Note the thickening of the upper crust beneath the Iberian Chain basement involved thrust system. T1, T2 and T3 are the shots location.

2.5.3 Summary and objectives in the scope of this thesis

The MT data was acquired along two parallel profiles oriented NE-SW, one of them being coincident with the trace of the seismic profile. Integration of the results of the seismic velocity model with the results of the 3-D MT resistivity model will give the first geophysical image of the Iberian Crust.

Main objectives of this study involving the 3-D inversion of the two acquired MT profiles across the Iberian Chain are:

- Obtaining a 3-D resistivity model able to accurately reproduce the MT data acquired.
- Characterisation and mapping of the orientation, dipping and extension at depth of the faults involved in the Tertiary contraction.
- Elucidating if the Cenozoic thrust system involves only the upper crust (Guimerà et al., 2004) or the whole crust (Salas et al., 1993).
- Integration of the 3-D resistivity model with the existing seismic velocity, in order to obtain a first constrained image of the crustal structure of the Iberian Chain.

3 The Magnetotelluric Method

3.1 Introduction

The magnetotelluric method (MT) is a geophysical technique used for imaging the electrical conductivity in the Earth's crust and upper mantle. It is a passive electromagnetic method which uses the propagation of the natural electric and magnetic fields in the conductive subsurface. Simultaneous measurements of electric and magnetic varying fields in orthogonal directions at the surface of the Earth allow to infer the subsurface electrical conductivity variations from hundreds of meters to hundreds of kilometres depth. Recent publications include in details all aspects of the MT method (Simpson and Bahr 2005; Berdichevsky and Dmitriev, 2010; Chave and Jones, 2012).

3.2 Electrical properties of the earth

The electrical resistivity, or its reciprocal the electrical conductivity, is the most variable geophysical property. Variation of ten orders of magnitude can be encountered in the Earth and several orders of magnitude can appear for the same rock formation. The electrical resistivity of the typical subsurface rocks generally varies between 10^{-2} Ωm and 10^{6} Ωm. The electrical resistivity of common materials of the lithosphere is shown in Figure 3-1.

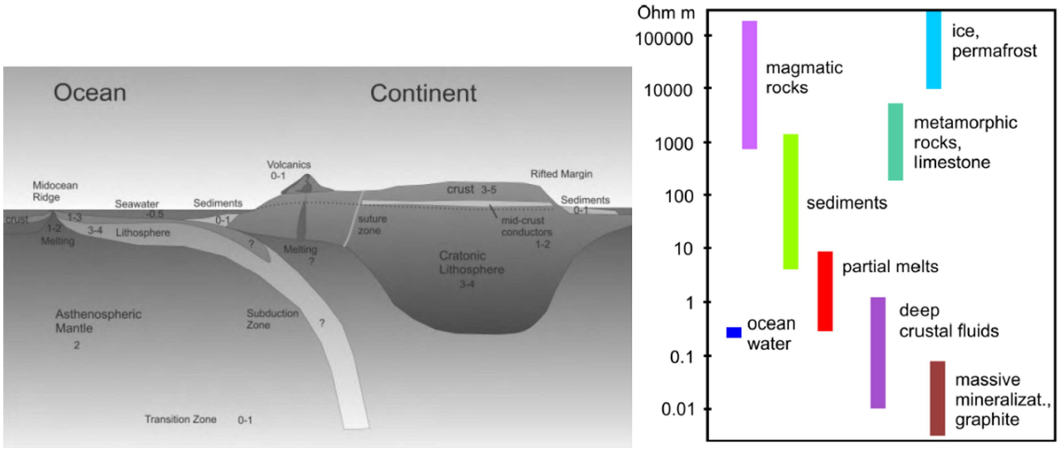

Figure 3-1: Electrical resistivity of common materials of the lithosphere (left: Chave and Jones, 2012, in log resistivity).

Transmission of electrical currents occurring in rocks and minerals is done via three types of conduction: electrolytic, electronic and semi-conduction.

Electrolytic conduction occurs in solution containing dissolved ions. The conductivity depends on the rock porosity, pore connectivity (or permeability), fluid content and fluid saturation. Pores in the rock matrix are generally filled with saline water, which increases the bulk conductivity of the medium. Porosity, fluid conductivity and saturation are empirically related through the Archie's law (Archie, 1942):

$$\rho_B = \rho_F \theta^{-m} S^{-n} \tag{3.1}$$

Where ρ_B is the bulk resistivity, ρ_F is the pore fluid resistivity, θ the porosity, S the pore saturation, n the saturation exponent and m is an exponent controlling pore geometry. Typical values for m are between 1 and 2. In crack-like pores it is closer to 1, while for spherical pores it is closer to 2.

Considering a sedimentary rock such as calcareous sandstone with a porosity of 20%, a m value of 2, fully filled by meteoric water with electrical resistivity of 0.5 Ωm, the bulk resistivity of the sediments is ρ_m= 12.5 Ωm. Accordingly, typical values for sedimentary rocks can be around 10 Ωm. This value generally increases with depth, as a consequence of the rock compaction and porosity reduction. On the other side, crystalline or metamorphic rocks generally present very low porosity and have very high bulk resistivity. For a fixed salt concentration of the fluid, the fluid conductivity increases with temperature until 300-400ºC due to increased ionic mobility (Bedrosian, 2007). At great crustal depths several metamorphic processes release free water, and, associated with presence of high heat flow (i.e. high temperatures), the melting point of the crustal rocks is lowered causing partial melting. Presence of melts in the rocks matrix increases the electrical conductivity. Partial melting in the crust was observed for example in Southern Tibet (Unsworth et al., 2005).

Metallic ore minerals are responsible for electronic conduction. The transport of charges is carried out by the electrons contained in the metallic minerals. Electronic conduction due to presence of graphite can be observed in the crust and has been detected by EM studies (e.g. Pous et. al, 2004).

Semi-conduction occurs at greater depths, in the upper mantle. Increase of temperature, pressure and oxygen fugacity controls the charge carrier transport, increasing the bulk conductivity of the mantle rocks. Semi conduction dominates in the mantle minerals such as olivine (Chave and Jones, 2012).

3.3 Sources

The most important part of the magnetic field on the surface of the Earth is generated by magneto-hydrodynamic processes in the outer core of the Earth. However, what is of special interest for MT investigations are the fastest and lower amplitude variations which have an external source.

Sources of the electromagnetic fields studied in MT are generated by two different types of natural phenomena, depending on the signal frequency. Figure 3-2 shows the power spectrum of the natural magnetic field, and their associated sources.

Electromagnetic fields with frequencies higher than 1 Hz (period shorter than 1 s) have its origin in the thunderstorm activity, propagating within the waveguide bounded by the Earth´s surface and the ionosphere.

The second type of natural source is characterized by frequencies below 1 Hz (period greater than 1 s) and is of interest to study the Earth at lithospheric scale. These electromagnetic fluctuations are generated by the interaction between the solar wind and the magnetosphere. The amount of solar wind produced by the sun activity is responsible for the intensity of the EM field variations. Low solar activity decreases the amplitude of the signal, affecting the quality of the data.

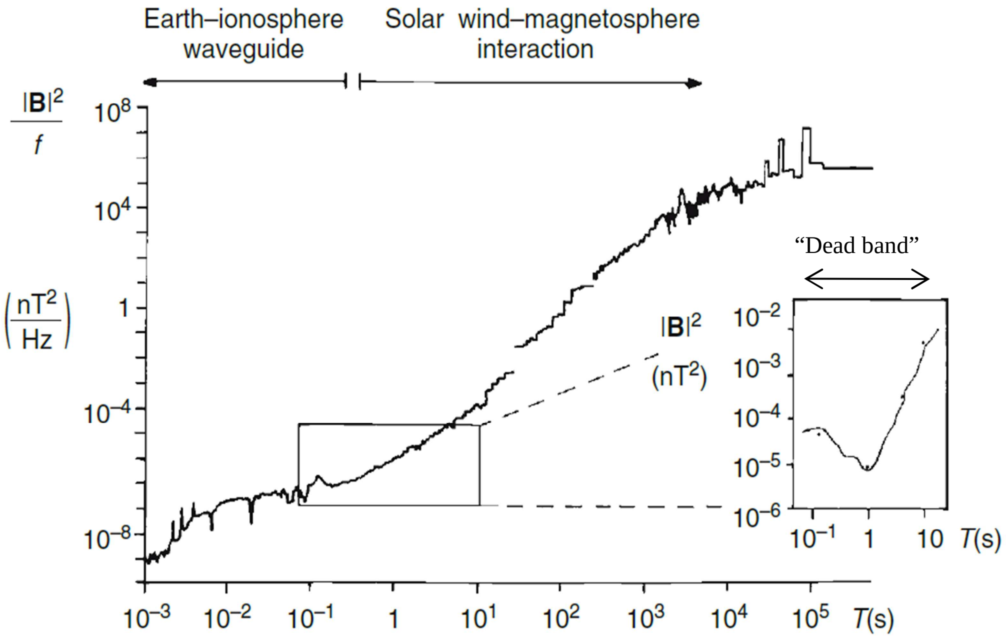

Figure 3-2: Power spectrum of the natural magnetic variations (modified from Simpson and Bahr (2005) after Junge, 1996).

Around 1 Hz a minimum in the intensity of the source of the electromagnetic field is observed, because of the intensity of both sources below and above 1Hz. This zone is called "dead band", which is generally affected by poor quality data (Figure 3-2).

Electromagnetic fluctuations due to the interaction of the magnetosphere and the solar wind are of special interest for lithospheric scale studies. In this context a high sun activity is of our interest in order to obtain good quality data. Figure 3-3 shows the solar activity for the last 50 years, along with the acquisition periods of the MT data recorded in this thesis.

The campaign realized in 2009 in the Cantabrian Mountains suffered from a low solar activity, which decreased the signal to noise ratio. On the other hand a high solar activity was registered during the campaigns realized between 2011 and 2014, which allowed to obtain good quality data.

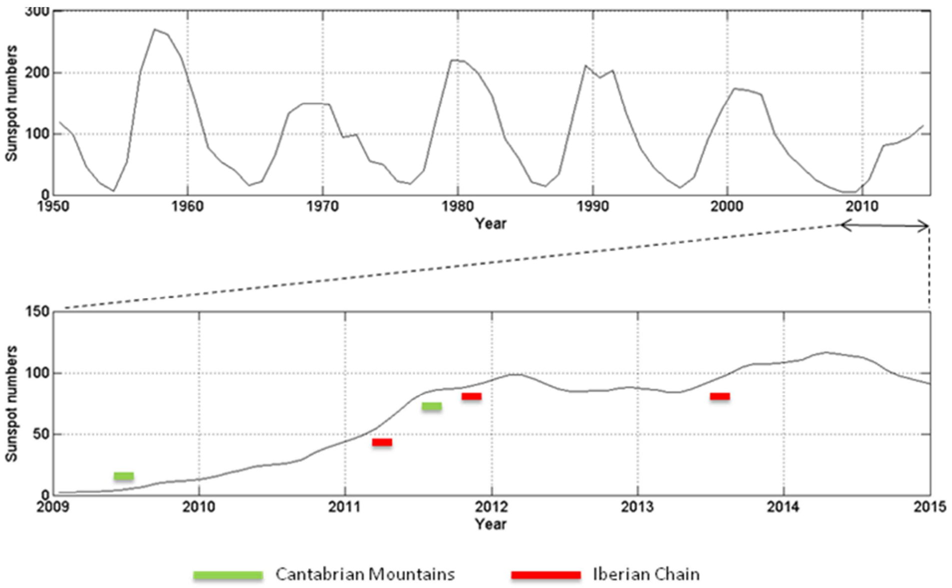

Figure 3-3: (Top) Cycle of solar activity from 1950 to 2015. (Bottom) Cycle of solar activity from 2009 to 2015 with the periods of data acquisition in this thesis (Source: WDC-SILSO, Royal Observatory of Belgium, Brussels).

3.4 Data acquisition

The acquisition of MT data is done according to the field layout shown in Figure 3-4. The electric and magnetic field variations are recorded simultaneously in orthogonal directions, generally along the magnetic north and its orthogonal direction. Vertical magnetic field is also recorded in order to obtain the complete magnetic field. Five channels are then recorded: Ex, Ey, Hx, Hy and Hz.

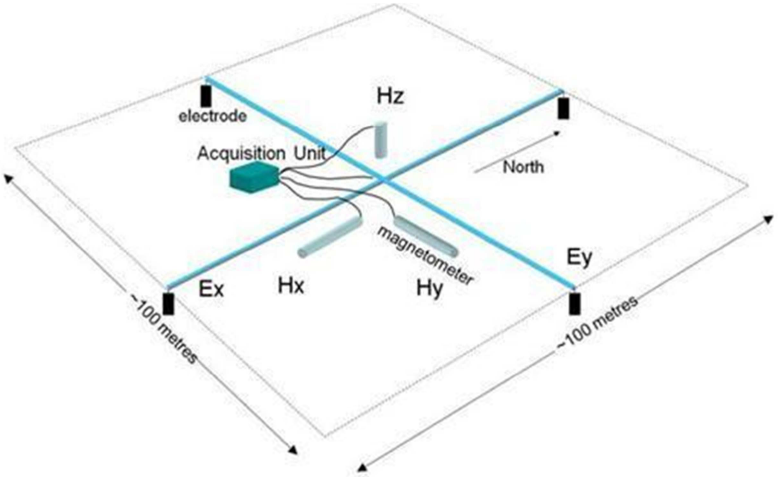

Figure 3-4: Magnetotelluric layout (after http://www.moombarriga.com.au/).

Two pairs of electrodes in forms of dipoles of length between 50 and 100 meters cross each other orthogonally. The fluctuations of the electric field for each pair of electrodes are recorded from the electric potential differences between each electrode. Two orthogonal magnetometers are disposed horizontally in the same directions as the electrical dipoles, and one magnetometer vertically. They record the fluctuations of the magnetic field over time. Depending on the type of recording system used, the magnetometers are induction coils that record separately the magnetic field in each direction (N-S, E-W and vertical), or a fluxgate magnetometer that records the magnetic field in the three directions.

The equipments used in this thesis for data recording are the ADU-07 equipment with induction coils as magnetometers and the LEMI-417 equipment with a fluxgate magnetometer. Differences between magnetometers involve different sensibility to the period of the fluctuations of the magnetic field. For long periods, generally higher than 1000 s, the fluxgate magnetometer is more sensitive. The fluxgate is measuring the magnetic field (B) while the induction coil measures dB/dt.

Figure 3-5 shows the frequency spectrum and noise level for these two types of magnetometers indicating the effectiveness of each one depending on the period. For periods longer than 100 s (0.01 Hz), the noise level of the fluxgate magnetometer is below the induction coils. All the data are recorded in a datalogger for its posterior analysis.

With the ADU equipment the measurements are recorded in different runs, which differ in the sampling rate and recording time. High frequencies sampling (e.g. 8 kHz, 2 kHz) are recorded during minutes while lower frequency (e.g. 128 Hz) require hours or days depending on the depth of investigation. The LEMI-417 equipment records electromagnetic field fluctuations continuously on the same frequency (e.g. 4Hz, 1 Hz) during weeks, in order to record periods greater than 1000 s.

Once the data have been acquired a quality control is carried out in order to check how the time series are affected by external interferences due to man-made noise or technical failures (such as electric line cut off or motion of the magnetometers). Correlated noise (powerlines, pipes lines, railways, towns, electrical fences) and uncorrelated noise (wind moving the magnetometers, animals digging…) disturb the natural EM signal (see section 3.6).

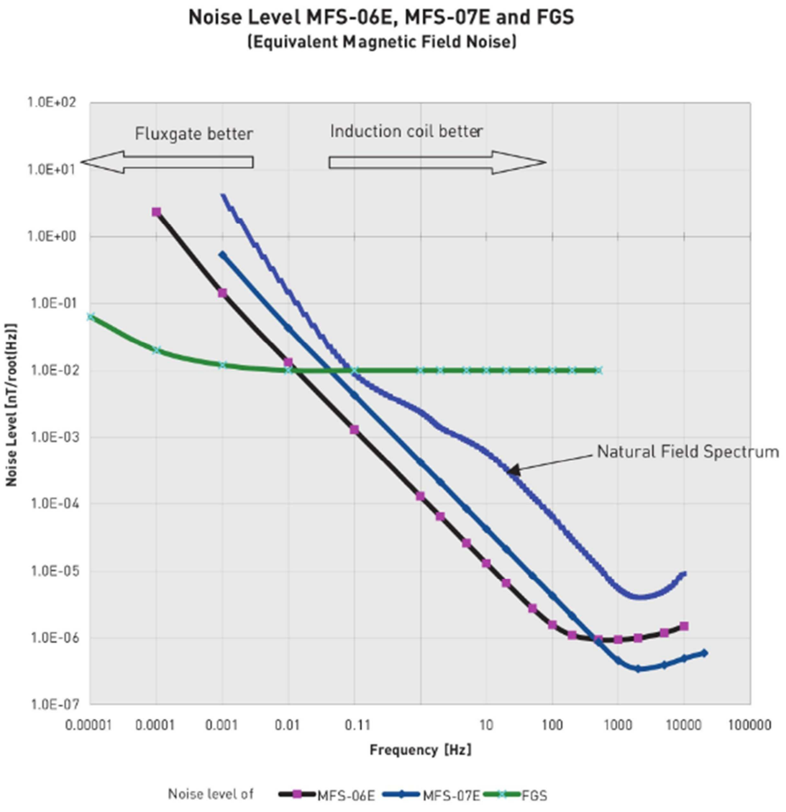

Figure 3-5: Frequency spectrum analysing the noise level for various induction coils (MFS-06E, MFS07E) and a fluxgate magnetometer (FGS) (http://www.geo-metronix.de/).

3.5 Magnetotelluric Theory

The generated natural electromagnetic fields propagate in the form of plane wave vertically incident on the surface of the conductive Earth. This assumption is valid only if the measurements are not contaminated by man-made noise or natural noise and when they are performed away from the equatorial and auroral electrojets.

This incident plane wave reaches the surface of the Earth inducing electric and magnetic fields in the earth under Faraday's and Ampere's laws. The measurements made on the surface of the Earth are the sum of this primary and the secondary fields induced by the conductive Earth.

The electromagnetic fields convolved with the Earth are measured in the surface: horizontal electric fields (E_x and E_y) and horizontal and vertical magnetic fields ($H_x, H_y$and H_z). Hence, the electrical nature of the Earth can be determined through the transfer function of the measured input and output signals as a function of frequency. It takes the form of a complex tensor 2 x 2 (equation 3.2):

$$\begin{pmatrix} E_x \\ E_y \end{pmatrix} = \begin{pmatrix} Z_{xx} & Z_{xy} \\ Z_{yx} & Z_{yy} \end{pmatrix} \cdot \begin{pmatrix} H_x \\ H_y \end{pmatrix}$$
$$H_z = \begin{pmatrix} T_x & T_y \end{pmatrix} \cdot \begin{pmatrix} H_x \\ H_y \end{pmatrix} \tag{3.2}$$

Where Z_{ij} are the elements of the impedance tensor and T_i the elements of the geomagnetic transfer function (VTF). The fields distribution depends on its frequency and on the electrical conductivity of the conductive medium traversed. Electromagnetic fields are more attenuated in a conductive medium than in a resistive one and low frequency signals penetrate deeper than high frequency signals. Electromagnetic fields at different frequency thus contain information on the variation of the electrical conductivity with depth. The skin-depth principle resumes in a simply manner the relationship between the frequency of an electromagnetic wave and its depth of attenuation depending on the resistivity of the medium:

$$\delta \cong 503\sqrt{\rho \cdot T} \tag{3.3}$$

where δ is the skin depth in meters, ρ the resistivity in Ωm and T the period in seconds. The skin depth is the depth to which the amplitudes are attenuated the factor 1/e of their values on the surface when the Earth is a homogeneous medium of resistivity ρ.

It has been shown that the simultaneous recording of the horizontal components of the electric field and the three components of the magnetic field permits to determine the electrical conductivity distribution of the subsurface with depth. Being based on the propagation of the electromagnetic fields through a conductive medium (the Earth), the MT method follows Maxwell's equations:

$$\begin{gathered} \nabla \times \mathbf{E} = -\frac{\partial \mathbf{B}}{\partial t} \\ \nabla \times \mathbf{H} = \left(\mathbf{J} + \frac{\partial \mathbf{D}}{\partial t}\right) \\ \nabla \cdot \mathbf{D} = d \\ \nabla \cdot \mathbf{B} = 0 \end{gathered} \tag{3.4}$$

where **E** is the electric field intensity (in V/m), **B** the magnetic induction vector (in T), **D** the electric displacement vector (in C/m^2), **H** the magnetic field intensity (in A/m), **J** the electric current density (in A/m^2) and d the electric charge density (in C/m^3). $\mathbf{E}$, $\mathbf{B}$, $\mathbf{D}$ and $\mathbf{H}$ represent the electromagnetic field. These 5 vectorial magnitudes are not independent and are related through the constitutive relations:

$$\begin{aligned} \mathbf{D} &= \varepsilon\mathbf{E} \\ \mathbf{B} &= \mu\mathbf{H} \\ \mathbf{J} &= \sigma\mathbf{E} \end{aligned} \tag{3.5}$$

where ε is the electrical permittivity (in F/m), μ the magnetic permeability (in H/m) and σ the electrical conductivity (in S/m). For the majority of rocks and material studied in MT the variations in electrical permitivities and magnetic permeabilities are negligible and therefore these parameters are considered to be equal to their free-space values ($\varepsilon = \varepsilon_0 = 8.85 \times 10^{-12}$ F/m and $\mu = \mu_0 = 4\pi 10^{-7}$ H/m).

Considering electromagnetic induction in the Earth the following assumptions are used:

- Far-field approximation: natural EM sources are generated far away from the Earth's surface, implying that they can be treated as uniform, plane-polarized EM waves reaching the Earth's surface with near-vertical incidence.
- Quasi-static approximation: for the period range used in MT (10^{-4}– 10^{4} s) and the electrical conductivity of Earth materials the time-varying displacement currents are negligible compared with the time varying conduction currents.

Taking into account these assumptions the solutions for E and B of the Maxwell's equations are:

$$\begin{aligned} \mathbf{E} &= \mathbf{E}_0 e^{i\omega t - kz} \\ \mathbf{B} &= \mathbf{B}_0 e^{i\omega t - kz} \end{aligned} \tag{3.6}$$

where $\mathbf{E}_0$and $\mathbf{B}_0$ are the amplitudes at the Earth surface, k the wavenumber and ω the angular frequency. These relationships show the sinusoidal time variation and the exponential decay in the vertical direction of the EM fields.

3.6 Data processing

The electromagnetic fields are measured at each MT site in the time domain as time series of the electric and magnetic fields fluctuations in orthogonal directions. In order to obtain the transfer functions that links the electromagnetic fields recorded on the surface to the electrical conductivity distribution of the subsurface, the temporal series have to be processed. Robust processing codes used during this thesis are the one of Egbert and Booker (1986) and Varentsov (2006). The first step in the processing is the visual inspection of the time series.

Secondly the time series of each channel are transformed to frequency domain using the Fourier transformation. The horizontal components of electromagnetic fields **E** and **H** are related by the complex impedance tensor, which is a complex tensor 2 x 2 defined by the equations:

$$\begin{aligned} E_x &= Z_{xx}H_x + Z_{xy}H_y \\ E_y &= Z_{yx}H_x + Z_{yy}H_y \end{aligned} \tag{3.7}$$

The components $Z_{ij}$of the tensor are obtained resolving these equations. This is a set of 4 equations (2 real and 2 imaginary) with 8 unknowns (4 real and 4 imaginary). This discrepancy is resolved using the fact that **Z** varies very slowly with the frequency (Vozoff, 1972). **Z** is then computed as average over frequency bands. A value of **Z** is calculated for a given number of frequencies per decade, generally between 6 and 10 (Simpson and Bahr, 2005).

Transfer functions are obtained multiplying equations 3.7 by the conjugate complex value of the horizontal magnetic fields $H_x$and H_y, in order to obtain a system of 8 equations and 8 unknowns. The conjugates of the magnetic fields are used because noise is generally present primarily in the electric field (Vozoff, 1972). Solutions of these equations are:

$$\begin{aligned} Z_{xx} &= \frac{\langle E_x H_x^* \rangle \langle H_y H_y^* \rangle - \langle E_x H_y^* \rangle \langle H_y H_x^* \rangle}{\langle H_x H_x^* \rangle \langle H_y H_y^* \rangle - \langle H_x H_y^* \rangle \langle H_y H_x^* \rangle} \\ Z_{xy} &= \frac{\langle E_x H_x^* \rangle \langle H_x H_y^* \rangle - \langle E_x H_y^* \rangle \langle H_x H_x^* \rangle}{\langle H_y H_x^* \rangle \langle H_x H_y^* \rangle - \langle H_y H_y^* \rangle \langle H_x H_x^* \rangle} \\ Z_{yx} &= \frac{\langle E_y H_x^* \rangle \langle H_y H_y^* \rangle - \langle E_y H_y^* \rangle \langle H_y H_x^* \rangle}{\langle H_x H_x^* \rangle \langle H_y H_y^* \rangle - \langle H_x H_y^* \rangle \langle H_y H_x^* \rangle} \end{aligned} \tag{3.8}$$

$$Z_{yy} = \frac{\langle E_y H_x^* \rangle \langle H_x H_y^* \rangle - \langle E_y H_y^* \rangle \langle H_x H_x^* \rangle}{\langle H_y H_x^* \rangle \langle H_x H_y^* \rangle - \langle H_y H_y^* \rangle \langle H_x H_x^* \rangle}$$

Where AB* is the cross power of A and B and A* the complex conjugate of A. Once Z_{ij} values are known they can be replaced in the equations (3.7) to meet the predicted values of *Ex* and Ey. Consistency between the observed and predicted data gives us important information about the quality of the data and the presence of noise for which a coherency function is defined (Vozoff, 1972). A coherency of 1 indicates a perfect correlation.

The impedance tensor is generally represented as apparent resistivity and phases depending on the frequency, which are calculated through the following relationships:

$$\rho_{aij}(\omega) = \frac{1}{\mu_0 \omega} \left| Z_{ij}(\omega) \right|^2$$
$$\Phi_{ij} = tan^{-1} \left(\frac{ImZ_{ij}(\omega)}{ReZ_{ij}(\omega)} \right) \tag{3.9}$$

The vertical magnetic fields are generated by lateral conductivity gradients. The geomagnetic transfer function is introduced and is defined by the relation between the vertical magnetic field H_z and the horizontal magnetic fields H_x and H_y:

$$H_z = T_x H_x + T_y H_y \tag{3.10}$$

The complex geomagnetic transfer function is (T_x, T_y), which is generally displayed as induction arrows. They are vectors represented on a xy plane.

Given that the vertical magnetic fields are generated by lateral conductivity gradients, the induction arrows can be used to infer lateral variations in conductivity. In this thesis the Wiese convention has been adopted, where the real induction arrows point away from the conductive zones. Their distribution can give qualitative indications on the dimensionality of the data: in a 2-D case the real induction vectors are perpendicular to the geoelectric strike.

Generally, MT signals are superimposed with several types of other EM signal that act as noise sources (Junge 1996; Szarka 1988). The uncorrelated noise is related to instrumental noise such as variations in the contact potential of the electrodes, temperature dependence of the magnetometers or motion of the magnetometers. In that case the noise present in the electric and magnetic channels is independent. Correlated noise is defined as man-made noise, such as electrified railways, power lines, electrical fences... These sources are similar to near field controlled source signals. The correlated noise, characteristic of near field sources, is characterized by 45º slope of the apparent resistivity curve and zero phases for low frequencies, as shown in Figure 3-6 (Junge, 1996).

Egbert and Booker (1986) showed that a robust algorithm for time series data processing was able to remove partially the coherent and incoherent noise. On the other hand, down-weighting of outliers during the processing improve the transfer functions obtained.

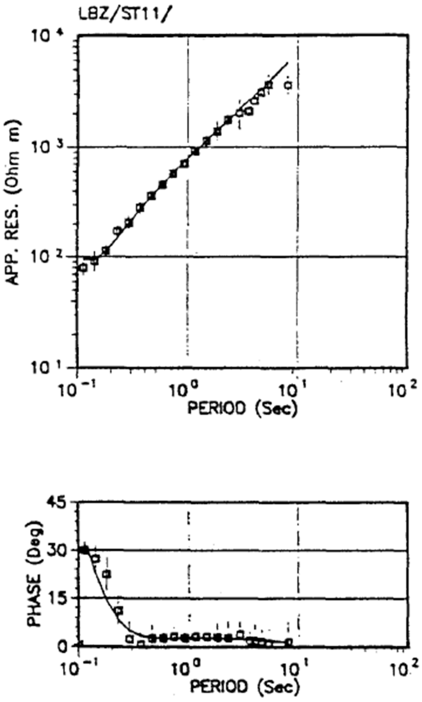

Figure 3-6: Apparent resistivity and phase at an industrial MT site in China (dots) along with the responses (continuous line) of a simple 1-D model obtained using controlled source with transmitter-receiver separation of 18 km (after Qian and Pedersen, 1991).

The best way to remove noise present in the magnetic field and thus improving the transfer function estimation is the remote reference technique introduced by Gamble et al. (1979). This technique uses remotely record of magnetic fields at an additional location, which is generally picked because of its low EM noise. Magnetic remote reference is used because the natural magnetic field is coherent over large spatial scales and because it is less affected by noise than the electric fields. Noise components that are not correlated between the MT site and the remote station can be identified and removed.

3.7 Impedance tensor and the geoelectric dimensionality

This section shows the different configurations of the impedance tensor depending on the dimension of the conductivity structure of the subsurface. The approaches used to evaluate the dimensionality, the Bahr decomposition (Bahr, 1988), the Groom-Bailey decomposition (Groom and Bailey, 1989) and the phase tensor (Caldwell et al., 2004) are discussed.

3.7.1 One-dimensional case (1-D)

The one-dimensional case, 1-D, is referred to an electrical conductivity distribution that only varies in one direction, usually the vertical direction. In the real world that case can be observed at very shallow depth, or in basin environments, where the sediments are deposited horizontally and uniformly in form of horizontal and parallel layers. In this situation the impedance tensor is defined as (Cagniard, 1953):

$$Z_{1D} = \begin{bmatrix} 0 & Z_0 \\ -Z_0 & 0 \end{bmatrix} \tag{3.11}$$

Figure 3-7 shows for a three layer model the different effect of conductive and resistive layers on the MT responses. A middle layer of varying resistivity (10 Ωm, 400 Ωm, 1000 Ωm and 10000 Ωm) located at 5 km depth, 25 km thick, is embedded in a homogeneous half-space of 100 Ωm. At high frequencies, the apparent resistivity has the value of the first layer and phases equal to 45º, corresponding to a homogeneous model. Going to longer periods (i.e. to greater depths), the apparent resistivity curve goes to the value of layer 2 and finally reach asymptotically the value of the last layer.

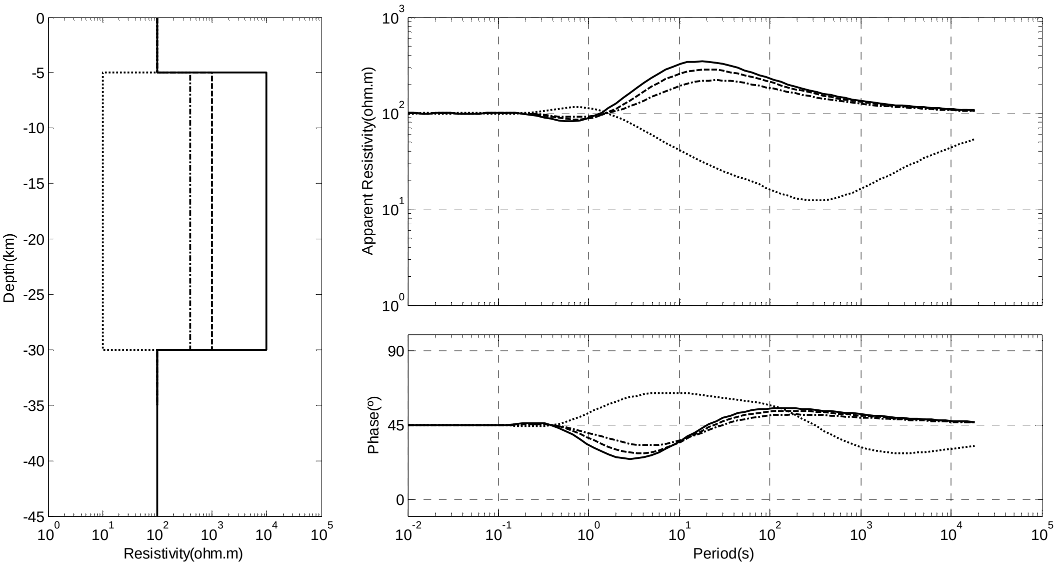

Figure 3-7: 1-D models and their associated responses where the resistivity of the intermediate layer varies (10, 400, 1000 and 10000 Ωm) embedded in a medium of 100 Ωm.

The model with a conductive middle layer (10 Ωm) has a greater effect on apparent resistivity compared to the models with a resistive middle layer (400 Ωm, 1000 Ωm or 10000 Ωm). The conductive medium strongly attenuates the EM signals causing an important change on the impedance computed in surface. On the other hand the EM signals travelling through the resistive middle layer have low attenuation. Then in surface the responses have little change and it becomes difficult to discriminate between different high resistivity values.

Figure 3-8 illustrates the ambiguity of the MT method, showing the responses of a three layer model where the second layer has different thickness and conductivity but maintaining the same conductance. The conductance of a layer is the product of the conductivity and the thickness. In all cases the second layer has a conductance of 1000 Siemens. The different curves are very similar and cannot be easily distinguished one from another.

As shown in Figure 3-8 only the conductance of the conductive layer could be determined through inversion. This non-uniqueness inherent to the MT method itself becomes more important if noise is present in the data. Large error bars increase the possible models able to fit the data. This non-uniqueness can be overcome using additional information such as geological, geophysical or well-log data.

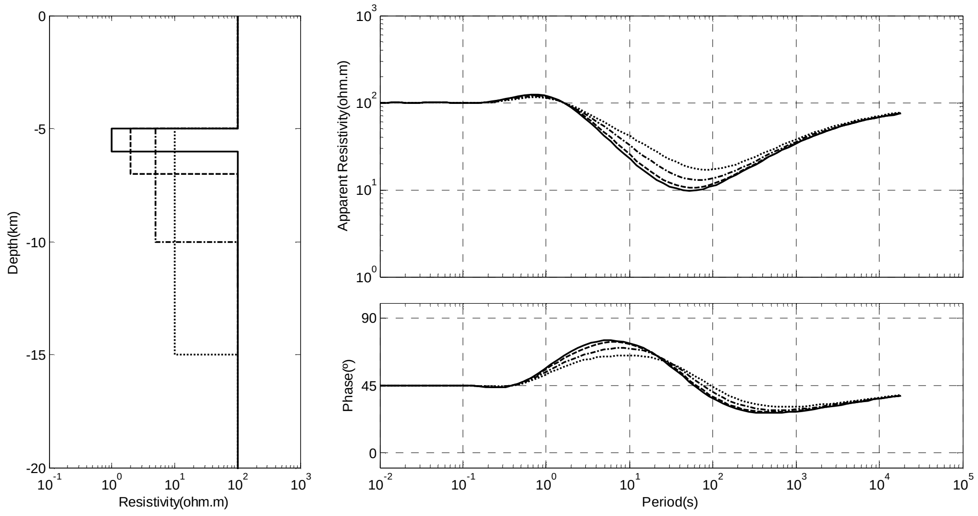

Figure 3-8: 1-D models and their associated responses where the conductance of the intermediate layer is constant (1000 Siemens) but with different thicknesses and resistivity values.

3.7.2 Two-dimensional case (2-D)

The two-dimensional case, 2-D, has an electrical conductivity distribution that varies with depth and one of the horizontal directions. In the other direction, the strike direction, the electrical conductivity remains constant. In this case, when the axes *x* or *y* are aligned orthogonally and parallel to the geological strike direction the impedance tensor has the form:

$$Z_{2D} = \begin{bmatrix} 0 & Z_{xy} \\ Z_{yx} & 0 \end{bmatrix} \tag{3.12}$$

When the x and y axes are not aligned with the strike direction the diagonal elements of the impedance tensor are not null. In that case it is possible to rotate the impedance tensor to minimize the diagonal elements, until reaching the case that satisfies equation 3.12, having the rotation angle equal to the strike direction (with an ambiguity of 90º). The off-diagonal components are associated to two principal modes. If x is the strike direction the electric field polarized perpendicular to the strike direction (Transverse Magnetic, TM mode or **B** polarization) corresponds to Z_{yx} and the electric field parallel to the strike direction (Transverse Electric, TE mode or **E** polarization) which corresponds to Z_{xy}.

Figure 3-9 shows the case of a profile across a vertical contact of two different resistivities (Simpson and Bahr, 2005). Apparent resistivity and phases at two periods (0.1 s on the top and 10 s on the bottom) for the TE mode (Z_{xy}) and the TM mode (Z_{yx}) are shown as a function of distance along the profile. The TE mode apparent resistivity varies smoothly across the contact, while the TM mode apparent resistivity is discontinuous. The TM mode behaviour is due to the boundary conditions. The electric current density perpendicular to the discontinuity must be conserved and following Ohms law, $(J_y = \sigma . E_y)$ the electric field E_y must be discontinuous, as observed for the TM mode. Consequently, the TM mode is more suitable to resolve lateral conductivity variations than the TE mode.

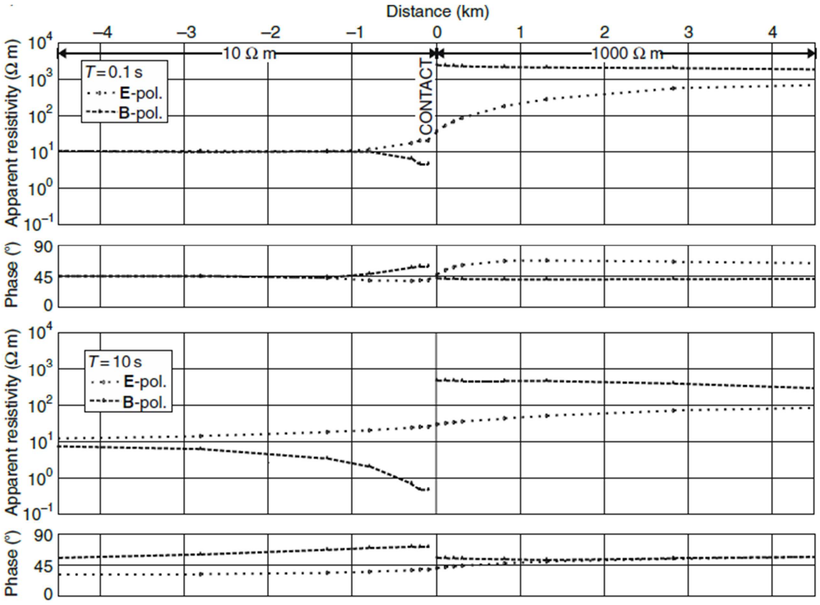

Figure 3-9: Apparent resistivity and phase as a function of distance across a vertical contact separating resistivity of 10 Ωm (left) and 1000 Ωm (right), for T=0.1 s and T=10 s (Simpson and Bahr, 2005).

3.7.3 Tri-dimensional case (3-D)

In the tri-dimensional case, 3-D, the electrical conductivity varies in all directions, and the impedance tensor takes the form:

$$Z_{3D} = \begin{bmatrix} Z_{xx} & Z_{xy} \\ Z_{yx} & Z_{yy} \end{bmatrix} \tag{3.13}$$

In this case the four components of the impedance tensor are not null. Four apparent resistivities and four phases are then considered.

3.7.4 Galvanic distortion

The galvanic distortion is caused by charges accumulation at superficial small-scale heterogeneities (with dimensions of the dipole length and less) beneath the MT sounding. These charges accumulation can strongly distort the electric field, yielding to distortion of the impedance tensor and different magnetotelluric responses from the one that would have been obtained without these heterogeneities.

In a 2-D case, the rotation of the impedance tensor to the geoelectric strike allows to eliminate part of the galvanic distortion. Only one element of the distortion matrix cannot be recovered. It is a real scaling factor that enhanced or diminished the impedance magnitude, causing a shift in the apparent resistivity curves, called “static shift”. This effect is recognized when analysing the apparent resistivity curves behaviour. Several methods are commonly applied to overcome this problem:

- Manual adjustment of the apparent resistivity curves, based on well log data, geological constraints or simply by comparison with the surrounding MT sites in order to guess real resistivity at high frequency (Jones, 1988).
- Calibration of the apparent resistivity curves by means of TDEM soundings when available (Meju, 2004).
- Inversion of the impedance phases only. However, apparent resistivity contains critical information about the subsurface resistivity that needs to be included in the inversion process.
- “Inversion for static shift”: This allows to obtain compensated static shift on average. However this assumption is justified for a large number of sites.

In the 3-D case the galvanic distortion cannot be removed. Soyer et al., (2008) assumes that modelling very shallow structures close to the MT sites and fitting the data could reproduce the galvanic distortion. Recently, Adeeva et al. (2015) proposed a new approach which includes the elements of the distortion matrix as unknowns in the inversion, but assuming a minimum distortion. Romero-Ruiz (2015) has developed a stochastic method that using specific constraints allow to recover the distortion parameters in many 3D regional cases.

3.7.5 Bahr dimensionality parameters

Bahr (1988) suggested a decomposition method to determine the 2D geoelectric strike direction and classify the dimensionality and galvanic distortion.

This method supposes multi-dimensionality heterogeneities superposed on a regional 2-D structure. In order to separate local heterogeneities from regional underplaying 2-D structure, the data have to be rotated to the geoelectric strike. For data aligned along the strike direction, the observed tensor Z can be decomposed as follows:

$$\mathbf{Z} = \mathbf{C} \cdot \mathbf{Z}_{2D}$$

$$\begin{pmatrix} Z_{xx} & Z_{xy} \\ Z_{yx} & Z_{yy} \end{pmatrix} = \begin{pmatrix} C_1 & C_2 \\ C_3 & C_4 \end{pmatrix} \cdot \begin{pmatrix} 0 & Z_{2D,xy} \\ Z_{2D,yx} & 0 \end{pmatrix} \tag{3.14}$$

where $\mathbf{Z}_{2D}$ is the impedance tensor corresponding to the regional 2D structure and **C** the galvanic distortion matrix which is assumed to be frequency independent. In this situation it is easy to see that the tensor elements in the columns of the impedance tensor have the same phase:

$$\frac{Re(Z_{xx})}{Im(Z_{xx})} = \frac{Re(Z_{yx})}{Im(Z_{yx})} \quad and \quad \frac{Re(Z_{yy})}{Im(Z_{yy})} = \frac{Re(Z_{xy})}{Im(Z_{xy})} \tag{3.15}$$

The rotation angle that satisfies this condition is referred as the *phase sensitive strike*. Thus, if aligned with the geoelectric strike, ρ_{xy} curve should be parallel to ρ_{yy} curve, displaced on the logarithmic scale by a scalar factor. Similar behaviour is observable for ρ_{yx} and ρ_{xx}.

Bahr also defined a rotationally invariant parameter, the *phase sensitive skew* η. It defines a measure of departure from ideal 1-D or 2-D behaviour of the data, as described in equation 3.14. Data presenting *phase sensitive skew* $\eta > 0.3$ is considered to be 3-D (Bahr, 1988).

3.7.6 Groom and Bailey decomposition

Considering a regional 2-D case a decomposition of the observed impedance tensor **Z** was proposed by Groom and Bailey (1989), where the frequency independent distortion matrix **C**, is factorised as:

$$\mathbf{C} = g\, \mathbf{T} \cdot \mathbf{S} \cdot \mathbf{A} \tag{3.16}$$

the product of three matrices, twist $\mathbf{T}$, shear $\mathbf{S}$, anisotropy $\mathbf{A}$ and a scalar g. The measured impedance tensor is:

$$\mathbf{Z} = \boldsymbol{\beta}_{\boldsymbol{\theta}} \cdot g\, \mathbf{T} \cdot \mathbf{S} \cdot \mathbf{A} \cdot \mathbf{Z}_{2D} \cdot \boldsymbol{\beta}_{\boldsymbol{\theta}}^{\mathbf{T}} \tag{3.17}$$

where $\mathbf{Z}_{2\mathrm{D}}$, is the regional impedance tensor and $\boldsymbol{\beta}_{\boldsymbol{\theta}}$ the matrix rotation to the strike Θ. $\mathbf{T}$, $\mathbf{S}$ and $\mathbf{A}$ matrices take the form:

$$\mathbf{T} = \frac{1}{\sqrt{1+t^2}} \begin{pmatrix} 1 & -t \\ t & 1 \end{pmatrix}$$

$$\mathbf{S} = \frac{1}{\sqrt{1+e^2}} \begin{pmatrix} 1 & e \\ e & 1 \end{pmatrix} \tag{3.18}$$

$$\mathbf{A} = \frac{1}{\sqrt{1+s^2}} \begin{pmatrix} 1+s & 0 \\ 0 & 1-s \end{pmatrix}$$

t, e and *s* being the twist, shear and anisotropy parameters, which are generally represented as angles: Φ_t=arctan(t) ,Φ_e=arctan(e) and Φ_s=arctan(s).

In a 2D case g and $\mathbf{A}$ cannot be determined independently from equation 3.17 and therefore they are included in a new tensor $\mathbf{Z'}_{2D} = g\mathbf{A}\mathbf{Z}_{2D}$, and the decomposition equation takes the form:

$$\mathbf{Z} = \boldsymbol{\beta}_{\boldsymbol{\theta}} \cdot \mathbf{T} \cdot \mathbf{S} \cdot \mathbf{Z'}_{2D} \cdot \boldsymbol{\beta}_{\boldsymbol{\theta}}^{\mathbf{T}} \tag{3.19}$$

Equation 3.19 is a system of 8 equations (real and imaginary parts of the impedance tensor $\mathbf{Z}$) and 7 unknowns (real and imaginary parts of the regional tensor $\mathbf{Z'}_{2\mathrm{D}}$, twist, shear and rotation angle). This new system of equations is resolvable by least-square fitting. McNeice and Jones (2001) implemented the method allowing to determine $\mathbf{T}$, $\mathbf{S}$ and $\boldsymbol{\beta}_{\theta}$ for several frequencies and several sites simultaneously. This analysis finds a unique strike for a complete dataset and determines which sites or frequency ranges are not compatible with the strike. However this analysis does not resolve for the static shift issue and it is only valid for a regional 2-D case.

3.7.7 Phase tensor

The above decomposition methods assume 1-D or 2-D regional conductivity structure superimposed by near-surface heterogeneities which produce galvanic distortion. Caldwell et al. (2004) presented a method that does not require any dimensionality assumption. The complex impedance tensor is defined by its real and imaginary parts, as $\mathbf{Z}=\mathbf{X}+i\mathbf{Y}$ (Caldwell et al., 2004). The phase tensor is defined as (Caldwell et al., 2004):

$$\mathbf{\Phi} = \mathbf{X}^{-1}\mathbf{Y} = \begin{bmatrix} \Phi_{xx} & \Phi_{xy} \\ \Phi_{yx} & \Phi_{yy} \end{bmatrix} \tag{3.20}$$

which is unaffected by galvanic distortion (Caldwell et al., 2004), so the regional and observed phase tensors are identical.

As a 2x2 tensor, the phase tensor is represented as an ellipse, whose axes are equal to the magnitude of the maximum and minimum phase tensor elements, and ϕ_{max} and ϕ_{min} (Figure 3-10).

Caldwell defines the skew angle β:

$$\beta = \frac{1}{2} tan^{-1}\left(\frac{\Phi_{xy} - \Phi_{yx}}{\Phi_{xx} - \Phi_{yy}}\right) \tag{3.21}$$

For a 1-D case the phase tensor is plot nearly as a circle, because ϕ_{min} and ϕ_{max} are almost equal. Moreover the β skew angle is zero.

For a 2-D case the phase tensor is symmetric and $\beta=0^o$. The angle α is related to the geoelectrical strike direction for undistorted data. The axes of the ellipses are parallel or perpendicular to the strike of the 2D structure (Caldwell et al., 2004).

In a 3-D case the direction of the major axis is given by the angle $\alpha - \beta$. The skew angle β measures the deviation from two-dimensionality, i.e. the asymmetry in the regional MT response (Figure 3-10). Values of $\beta \neq 0$ imply 3-D regional conductivity structure. However a “quasi-2D” regional impedance tensor can be considered if $|\beta| < 3^o$, as suggested by Caldwell et al. (2004).

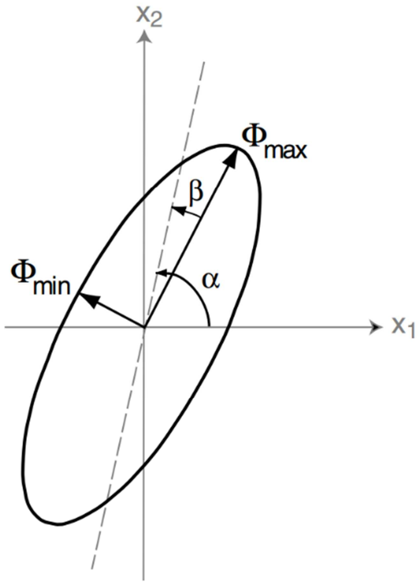

Figure 3-10: Graphical representation of the phase tensor (Caldwell et al., 2004). Major and minor axes of the ellipse are defined by the rotationally invariants ϕ_{min} and ϕ_{max}, and by the angle α, which defines the orientation of the major axis in the symmetric case (grey line). When non symmetric as represented here, the orientation of the ellipse is rotated by an angle β away from its symmetric position, and the direction of the major axis is given by the angle α-β.

Thus, the phase tensor analysis gives useful information about the dimensionality of the data. Because it is unbiased by galvanic distortion it can be useful to determine variations in the conductivity distribution (Heise et al., 2008). Direction of the major axis indicates the preferred flow direction of the regional induction currents, allowing to determine quantitatively the dimensionality as a function of the sites and the frequencies.

3.8 Modelling of MT data

In the framework of this thesis we used different 2-D and 3-D inversion algorithms. The 2-D inversion code used for the inversion of the data in the Cantabrian Mountains is the non-linear conjugate gradient (NLCG) algorithm (Rodi and Mackie, 2001), implemented in the WinGLink commercial software. The implementation of this algorithm in 3-D (Mackie and Madden, 1993; Rodi and Mackie, 2012) was used for the 3-D inversion of the Iberian Chain data. The 3-D data-space inversion (Siripunvaraporn and Egbert, 2000; Siripunvaraporn et al., 2005b, 2009) was used for the 3-D inversion of the data of the Cantabrian Mountains.

The forward problem is the practice of calculating what should be the observed responses of a given model, it has a unique solution. The inverse problem consists in determining the distribution and values of a given physical parameter by comparing the measurement to the predictions of a model. The results of an inverse problem are non-unique since different models can adjust equally the observed data, especially if the data have large errors.

In the inverse problem the unknowns are the number M of resistivity cells **m**= $[m_1,\ m_2, \dots, m_M]$, in which the model is discretised, and the measurements are the number N of observed data $\mathbf{d} = [d_1,\ d_2, \dots, d_N]$. **d** is the complex impedance tensor and geomagnetic transfer functions (3-D case) or the TM and TE modes of apparent resistivity and phases and tipper (2-D case) for each frequency.

In order to obtain a model whose responses reproduce as close as possible the observed data, the least-square method is employed in order to minimize the misfit function which account for the residual between observed and calculated data (Rodi and Mackie, 2012):

$$\Phi(m) = \sum_{i=1}^{N} C_d^{-1}(d_i - F_i(m))^2 \tag{3.22}$$

Where *F(m)* denotes the model responses and C_d the data covariance matrix. The data covariance matrix is defined as the observed errors associated to the data, but an error floor parameter is generally introduced in the inversion process. Errors below the error floor value will be raised to the error floor value. This value is generally chosen depending on the fitting required and on the confidence the user has with the data. Too low error floors could bias the inversion, forcing it to fit noisy data or data of non-adequate dimensionality (Booker, 2014; Siripunvaraporn, 2005b).

The misfit function could be reduced without any restrictions. However, due to the non-uniqueness of the method a model structure penalty function term is introduced in the objective function (Rodi and Mackie, 2012):

$$\Omega(m) = (m - m_0)^T C_m^{-1}(m - m_0) \tag{3.23}$$

where C_m is the model covariance matrix and m_0 the prior model. This function penalizes a model m that go away from the prior model m_0.

The purpose of the inversion is then to minimize the total objective function, which is the sum of the two functions:

$$\Psi(\mathrm{m}) = \Phi(\mathrm{m}) + \lambda\Omega(\mathrm{m}) \tag{3.24}$$

The Lagrange multiplier λ, known as the regularizer, controls the weight that is given to each one of the functions during the minimization of the objective function. A high value of λ will penalize the data misfit and give more weight to produce a model that do not go away from the prior model, generally leading to a smooth model. On the contrary, a low value of λ penalizes the smoothness in order to reduce the data misfit. In general a compromise has to be found between these two functions in order to obtain a smoothed model but fitting satisfactorily the data. During the inversion process an eye has to be kept on the elements of the objective function in order to check which term is driving the inversion.

The WS3DINV algorithm (Siripunvaraporn et al., 2005a, 2009) is based in the Occam approach (Constable et al., 1987), while the NLCG algorithm (Mackie and Madden, 1993; Rodi and Mackie, 2001; Rodi and Mackie, 2012) is based on the non-linear conjugate gradient modelling approach. Both algorithms allow for the inversion of the full impedance tensor and the vertical transfer function. A complete review of the 3-D MT inversion algorithms can be found in Siripunvaraporn (2012). 3-D MT inversions become more and more popular thanks to the current increase of the computation capacity of computers, workstations and clusters. However, depending on the size of the dataset (number of sites, number of frequencies) and the size of the mesh used, which can be drastically increased if topography and/or bathymetry have to be accurately modelled, the computation capacity is still a major bottleneck.

4 The Cantabrian Mountains crustal structure revealed by magnetotelluric soundings

4.1 Magnetotelluric data

A north south profile was carried out across the Cantabrian Mountains and the Duero Basin. It consists of thirteen magnetotelluric sites, with an approximate length of 100 km. The acquisition was done during two campaigns carried out in 2009 and 2011 in the frame of TOPOIBERIA project.

The five components of the electromagnetic field were recorded in N-S and E-W directions (x is north and y is east) with periods ranging from 0,001 s to 10000 s for six MT sites (long period LMT) and from 0,001 s to 1000 s for eight MT sites (broadband BBMT). The recording time was between 2 and 3 days for the BBMT data and 2 weeks for the LMT data. The space between sites is between 5 and 10 km (Figure 4-1). The BBMT data were processed using the standard robust processing algorithm (Egbert and Booker, 1986) and the LMT data using the code of Varentsov (2006). Good quality data was obtained for the whole period range (Figure 4-2) with only some exceptions in some sites in the interval 1-10 s.

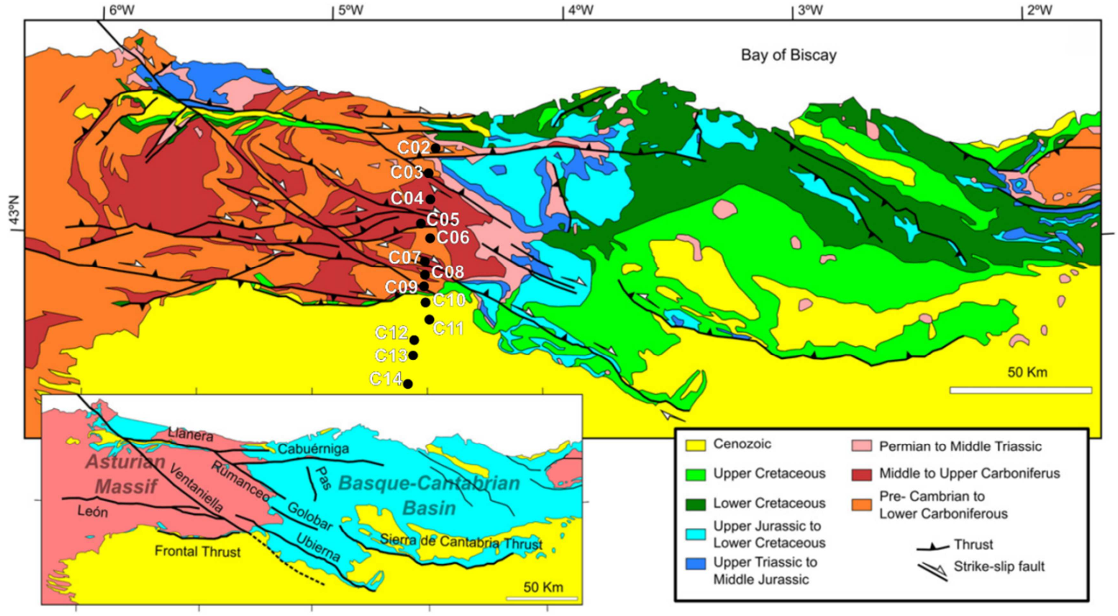

Figure 4-1: Geological map of the Cantabrian Mountains (modified from Tavani, 2012). Black points are the MT sites.

4.2 Data Analysis

Main issue arising from merging two datasets acquired with different instruments is the possible static shift that can affect both impedance tensors independently. Consistency between apparent resistivity and phase of the magnetotelluric data is expected for 1-D (Parker and Booker, 1996) and 2-D data. In order to test the consistency across the whole frequency range and to check the correct merging of these two datasets the D+ smoothing solution (Parker and Booker, 1996), was applied. The conclusion is that no major discrepancies were found in all the merged sites. Figure 4-2 shows the result of the merging carried out for the sites 03 and 05.

Application of the D+ algorithm to the BBMT sites showed that phases and apparent resistivities are in general consistent with each other. Some discrepancies appeared around 10 s, probably due to poor data quality in this frequency range as a consequence of the low solar activity during the field campaigns (Fig. 3-3).

Quality control of the data was carried out. Suspicious behaviour of the apparent resistivity, phase or tipper data were excluded from dimensionality analysis and inversion. Typical near-field effects affecting the data (such as apparent resistivity curves with slopes higher than 45°

and phases close to 0°) were excluded from the inversion process. Furthermore, points with large error bars or considered as outliers were also removed.

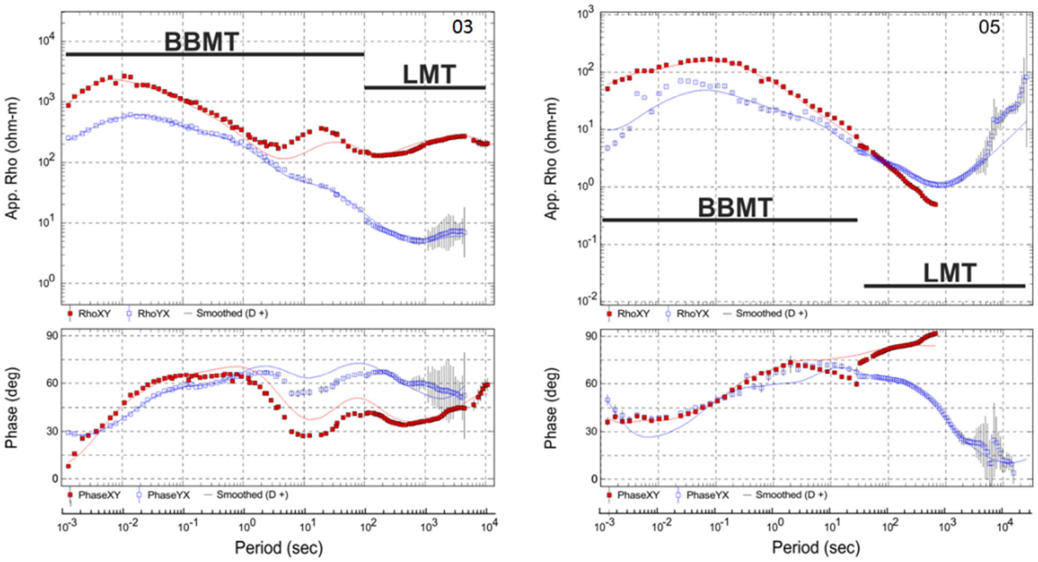

Figure 4-2: Apparent resistivity and phase data for sites 03 (left) and 05 (right). High frequency data range was obtained using BBMT instruments, while the long period data was obtained using LMT instruments. Continuous lines represent the smoothed curves using the D+ solution, with 10% error for the apparent resistivity and the phase respectively.

Figure 4-3 shows the apparent resistivity and phases of all sites. Data are shown with a rotation of –N80°E, a dominant direction appearing from the dimensionality analysis carried out in section 4.3. This rotation allows us to better describe the data behaviour in terms of the TE and TM modes. We split the dataset between the sites located in the Cantabrian Mountains and those located in the Duero Basin. Regional differences characterizing the data behaviour can be observed. In the Cantabrian Mountains, the apparent resistivity of the TE mode shows a minimum between 100 s and 1000 s. By contrast, the TM mode presents different behaviour along the profile, as expected for this mode, which is more sensitive to across strike conductivity heterogeneities. In the Duero Basin the sites show a similar behaviour for both modes, suggesting a relative 1D behaviour beneath the Duero Basin. Sites 04 and 05 of the Cantabrian Mountains show a shift in the TE apparent resistivities compared to adjacent sites without affecting the phases, suggesting static shift effects. For the majority of sites the TE apparent resistivity drops to values around 10Ωm between 100 s and 1000 s, however, in these two sites the TE apparent resistivity drops to 1 Ωm.

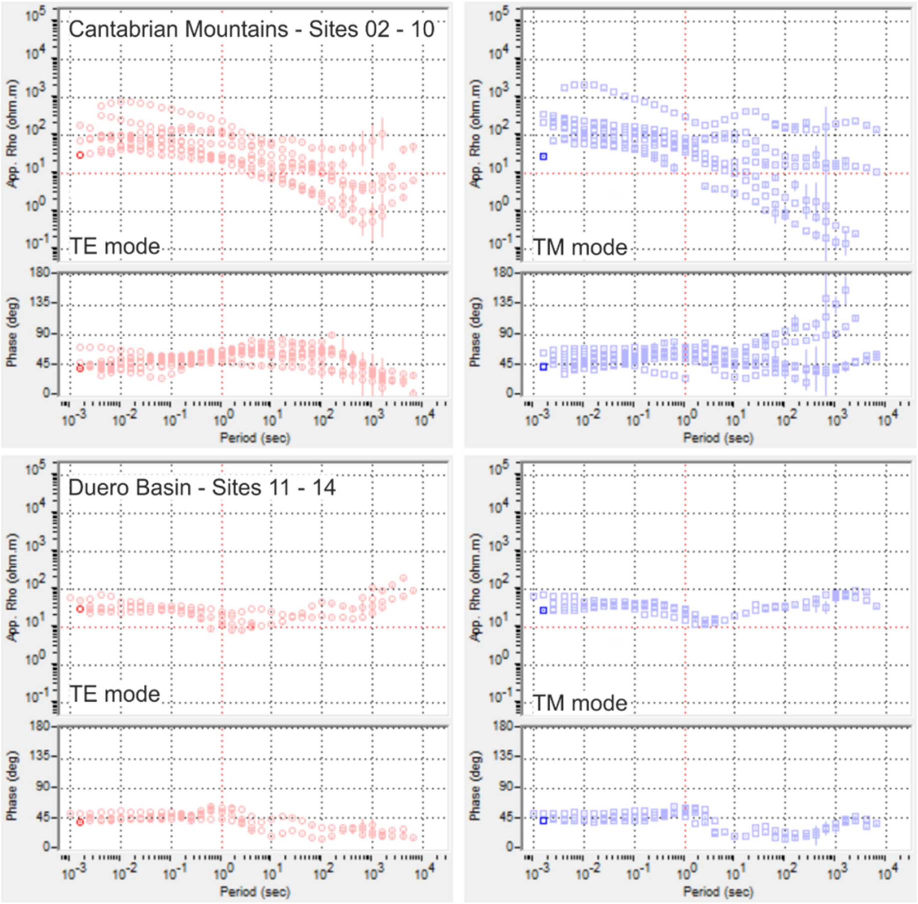

Figure 4-3: Apparent resistivity and phase data for all sites. Data rotated to -80°. Sites located in the Cantabrian Mountains (top) and sites located in the Duero Basin (bottom). TE mode (left) and TM mode (right) are shown (see text for details).

We can also notice the presence of phases greater than 90° in the TM mode for three sites, 05, 06 and 07, accompanied by very low values of apparent resistivity (between 1 and 0.1 Ωmat 1000 s). Phases greater than 90° were observed in several geological settings, where different physical or geological causes were invoked. Electrical anisotropy (Heise and Pous, 2001; Heise and Pous, 2003) or presence of 3-D conductive bodies (Lazaeta and Haak, 2003; Ichihara and Mogi, 2009) could be responsible for the phases observed here. The presence of graphite was invoked by Heise and Pous (2003) and Pous et al. (2004) to explain this behaviour (TM phases > 90° for long period, and apparent resistivities dropping to low values). However, no evidence of electrical anisotropy can be inferred from local geology in the Cantabrian Mountains. Current channelling and/or 3-D conductive body (L-shaped body, Ichihara and Mogi, 2009) is the most probable explanation of this behaviour affecting sites 05, 06 and 07, which are located close to complex imbrications of WSW-ENE and NW-SE oriented faults (see Figure 4-1).

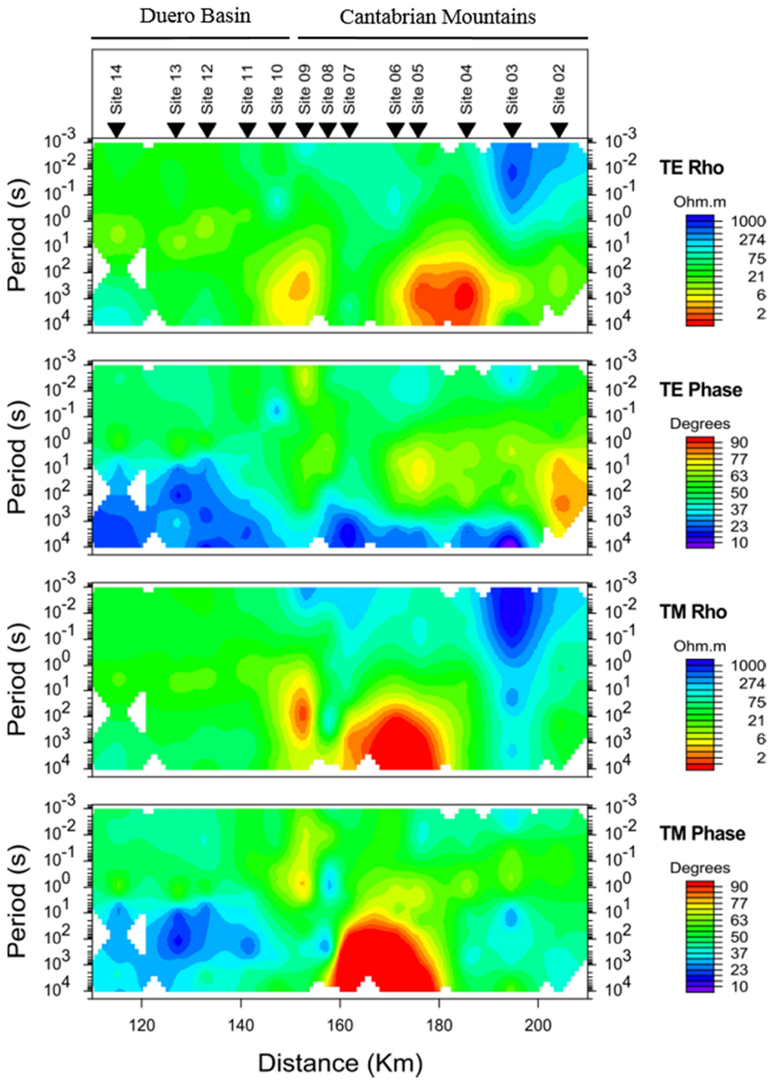

Figure 4-4: Pseudo sections of apparent resistivities and phases of TE and TM modes. Rotation –N80°E.

Figure 4-4 shows the pseudo sections for TM and TE modes. As discussed before the TM mode is more sensitive to conductivity variations along the direction perpendicular to the strike. Therefore, it is more suitable to highlight conductivity heterogeneities along the profile. On the other hand the TE mode is expected to be more regular and with a smoothed conductivity variation along the profile (see chapter 3). These differences, based on differences in sensitivity of each mode along and perpendicular to the strike direction, can be observed in the pseudo sections. At long periods the phase pseudo sections reveal a high resistivity beneath the Duero basin, for both modes, whereas in the Cantabrian Mountains they are more heterogeneous and with lower resistivity at long periods. The TE phase shows a resistive behaviour (low phases) for all stations at long periods. By contrast the TE apparent resistivity shows variations, suggesting static shift effect in this mode at sites 04 and 05. The TM phase presents variations along the profile, with some noticeable anomalies beneath some stations. This behaviour is, to some extent, similar to the apparent resistivity. Accordingly, only the TE mode of sites 04 and 05 was corrected of static shift. The apparent resistivities were displaced vertically upwards by a decade, in order to match with the surrounding sites at long period. The impedance tensor was conveniently corrected in order to use the corrected data both for the 2-D and the 3-D inversions.

4.3 Dimensionality analysis and geoelectric strike estimation

Dimensionality of the subsurface has to be assessed in order to choose the appropriate modelling method to explain the data. The main goal is to determine if the data can be explained by a 2-D approach, considering structures infinite along strike (and thus to determine the geoelectric strike), or if 3-D modelling is required by the data. A regional two-dimensional behaviour of the geological structures of the Cantabrian Mountains is observed on surface, with a strike roughly oriented E-W. However, several tectonic features suggest other orientations, especially the strike-slip faults that are oriented NW-SE (e.g. the Venteniella-Ubierna fault). The dimensionality analysis and geoelectric strike estimation is carried out to determine the principal direction of the regional structures, and to determine which sites and which frequency ranges may be affected by 3-D structures.

4.3.1 Induction arrows

The geomagnetic transfer function, or vertical transfer function (VTF) represented as induction arrows is an indicator of lateral variations of electrical conductivity as a function of frequency. In Figure 4-5 the real induction arrows of all sites and all frequencies are shown, in the Wiese convention (pointing away from conductive zones). This pseudo section is constructed so that the vertical axis is north-south oriented, the east pointing to the right. Outliers and noisy tipper data were removed before to the data representation.

As observed, there is a general orientation N-NE (S-SW) at long periods (between 100 s and 10000 s). At shorter periods (1s – 100s) the vectors point to different directions, suggesting the presence of several off-profile structures along the profile.

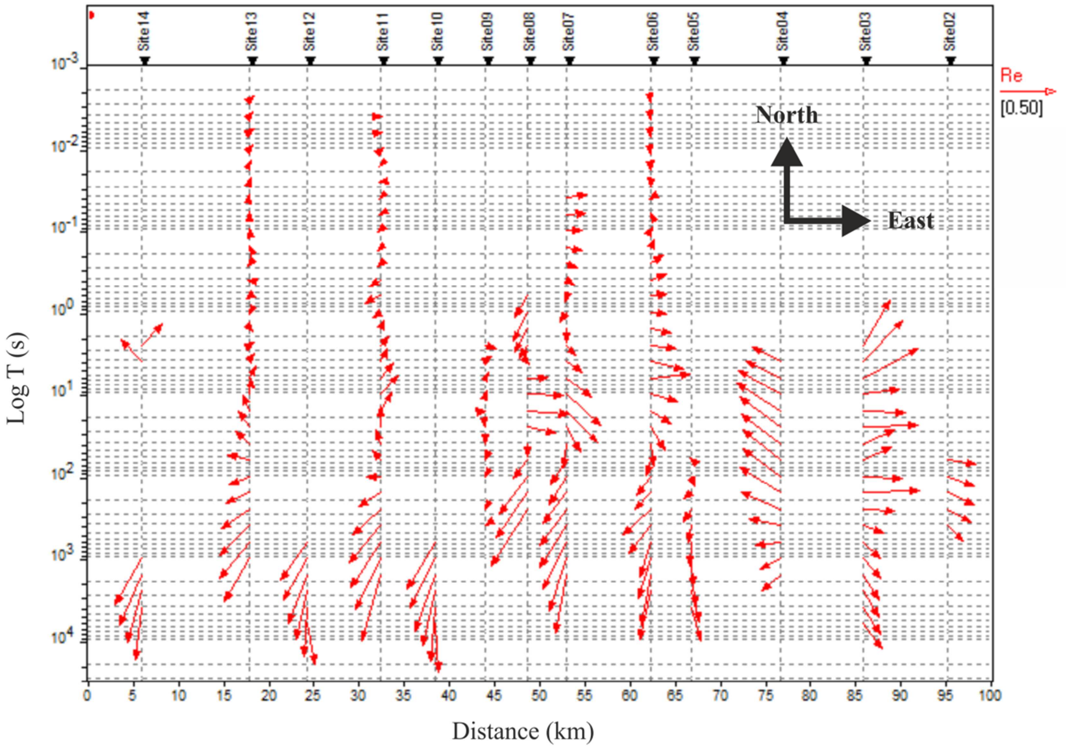

Figure 4-5: Real induction arrows for all sites and frequencies, in Wiese convention (pointing away from conductors).

Note the possible conductive area between sites 03 and 04. In the period range 1 s - 1000 s both sites show arrows pointing in opposite ways, to the east in site 03 and to the west-northwest in site04. This behaviour suggests the presence of a near-vertical conductive body between both sites that could be oriented NW-SE. Deflection of the arrows southwards at longer periods is due to the effect of the conductive Atlantic Ocean.

Another interesting feature at sites 06, 07 and 08, is the change in direction of the arrows from east to west when increasing period. A simple way to explain this feature would be the presence of a conductive body dipping eastwards beneath these sites, in addition to the influence of the conductive ocean at longer periods.

The effect of the Atlantic Ocean was tested through forward modelling of a 100 Ωm homogenous half-space including a detailed sea of 0.33 Ωm. The real arrows responses of such model point to the south, even if with smaller magnitude compared with the observed arrows. This indicates that the Ocean has an effect on the data, which diminishes gradually to the south. In general the higher amplitude and the different orientation of the real observed arrows reveal the presence of several conductive bodies at different depths and with different orientations.

In conclusion, a predominant NE/SW to NS direction is observed at long periods (> 300 s), which suggests a regional strike direction NW/SE to EW at great depths. For shorter periods (< 300 s) some sites present arrows that change direction with increasing period, indicating possible changes of strike with depth, 3-D and/or oblique conductive structures. This is especially clear beneath sites 05, 06, 07 and 08.

4.3.2 Phase tensor

The phase tensor provides useful information about the dimensionality of the data. When it is represented as an ellipse, its major and minor axes indicate the strike direction of the geoelectrical structures (Caldwell et al., 2004). If the structure is 1-D, currents do not have a preferred flowing direction and the phase tensor is represented as a circle. The skew angle $|\beta|$ represents the asymmetry of the phase response produced by tri-dimensional structures (section 3.7.7). Figure 4-6 shows the phase tensor ellipses of the observed data. The colour used to fill the ellipses is the $|\beta|$ value.

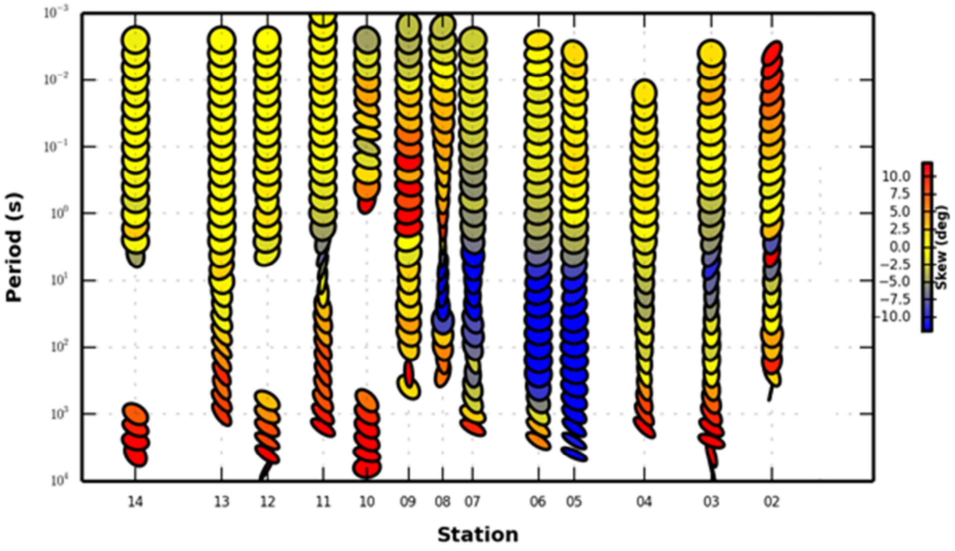

Figure 4-6: Phase tensor ellipses of the observed data, filled with the skew angle beta. Vertical axis of the plot is north-south oriented.

For periods between 0.001 s and 1 s, the ellipses show a relative 1-D behaviour in most of the sites, having the major ellipse axis roughly equal to the minor one. From 10 s to 10000 s the major axis of the ellipses starts to be orientated along WNW-ESE and NW-SE directions.

Caldwell et al. (2004) estimate skew angles less than 3° to validate a 2-D approach. Even if some flexibility can be taken using this criterion, high skew angle beta should be an indication of strong 3-D effects and these data should be excluded in a 2-D inversion. At periods lower than 100 s, $|\beta|$ is less than 4^{o} for the majority of the sites (with the exception of site 09) indicating a 2D structure until the corresponding period. By contrast, from 100 s to longer periods $|\beta|$ is higher than 8^{o}, indicating a 3-D regional structure at greater depths. Sites 05, 06 and 07 with phases greater than 90° have a high skew angle ($|\beta| > 6°$) from 10 s to longer periods.

4.3.3 Bahr

The Bahr (1988) approach decomposes the data into local non-inductive responses (caused by multi-dimensional heterogeneities) and a regional 2-D structure. Two parameters are extracted from this analysis, the *phase sensitive skew* and the *phase sensitive strike* (section 3.7.5).

Figure 4-7shows the phase sensitive skew for all sites as a function of period. Bahr suggested that a *phase sensitive skew* higher than 0.3 does not satisfy the assumption of a regional 2-D impedance tensor. Figure 4-7 shows low values of the *phase sensitive skew* at periods less than 100 s and greater than 0.3 at long periods (T > 1000 s), which indicates a 3-D regional structure at greater depths, as pointed out by the phase tensor behaviour. Again sites 05, 06 and 07 with high *phase sensitive skew* are an exception coinciding with the high values of the phase tensor *skew* β (Figure 4-6).

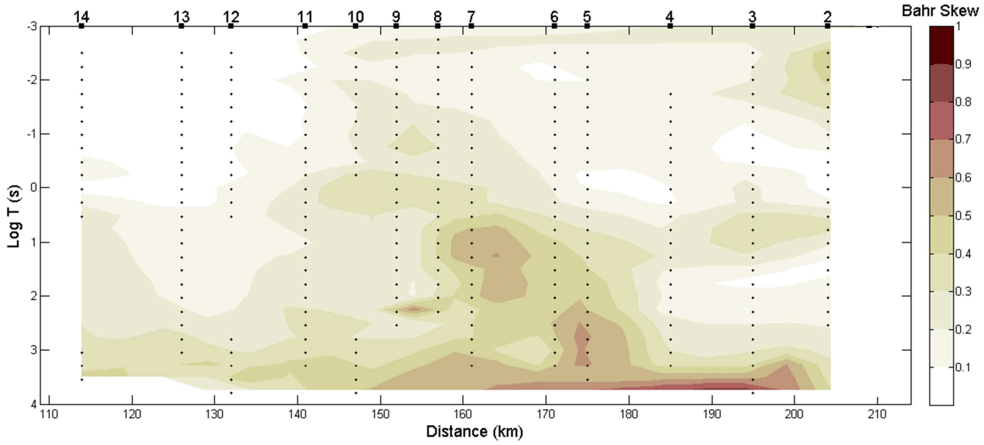

Figure 4-7: Phase sensitive skew (Bahr, 1988) for all sites and all frequencies. Black dots represent the data used for the gridding of the contour map.

The strike estimation using the *phase sensitive strike* of the Bahr method was also carried out. We considered for the *phase sensitive strike* analysis only the data having a *phase sensitive skew* less than 0.3. This analysis was carried out for several period ranges and is presented as rose diagrams in Figure 4-8. At short periods (between 1 and 10 s) the strike angle is scattered, indicating shallow structures with different orientations. For the period range between 10-100 s there is a dominant direction between 0-10°, although a direction of -20°/-30° is also present for a minor number of periods. For the period range 100-300 s only few values were considered as many data in this frequency range have *skew* values greater than 0.3. However, a clear direction 0-10° is observed with again a second -20°/-30° direction. Considering the whole period range, the same characteristics appear with a maximum for a strike angle 0-10° and a secondary angle -20°/ -30°. Separating the analysis by tectonic units (the Cantabrian Mountains and the Duero Basin) for the whole period range a dominant direction of 0-10° is present for the Cantabrian Mountains and a dominant direction of -30° for the Duero Basin. In both areas, however, the second direction is present (fig. 4-8).

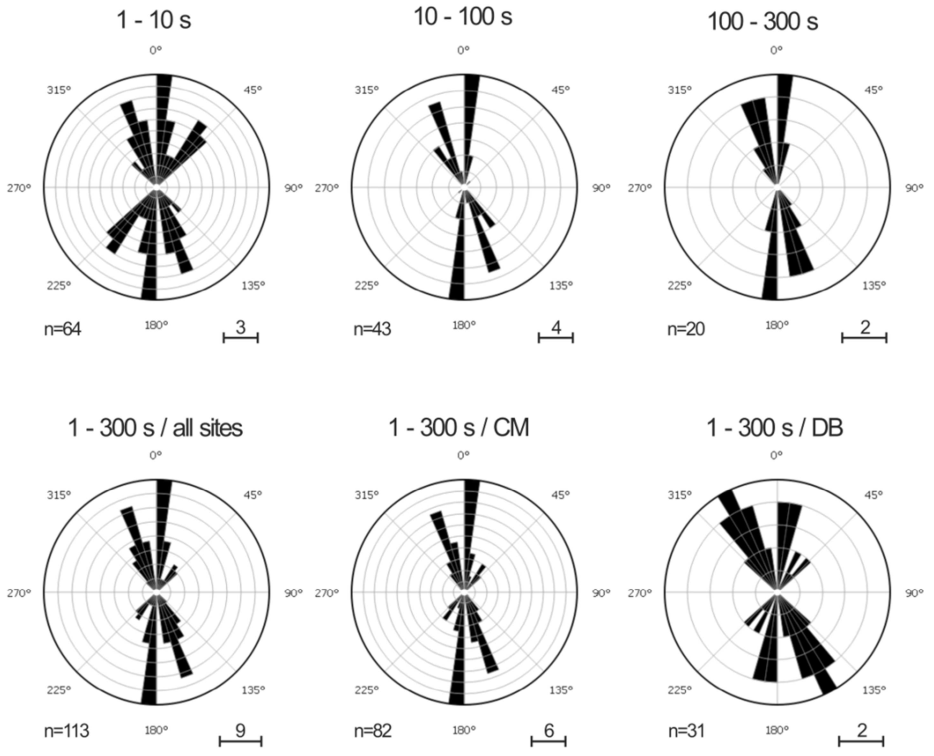

Figure 4-8: Phase sensitive strike of Bahr (1988). Only the data that presents phase sensitive skew < 0.3 was used for this analysis. The rose diagrams show the results for short, intermediate and long period bands (top), for all the sites for the entire period range (bottom left), and for the sites located in the Cantabrian Mountains (CM) and in the Duero Basin (DB) (bottom); n represents the number of frequencies used.

The method of Bahr suggests the presence of 3-D effects at long periods (for T > 100 s) along the whole profile. A dominant direction for the strike was estimated between 0 and 10°, although an alternative strike angle of -20°/-30° could be considered. The ambiguity of 90º in the strike angle is solved taking into account the main direction of the induction arrows as well as the geological structure. These observations match with the phase tensor analysis, where the ellipses are roughly oriented EW for periods less than 100 s. Estimation of the data affected by 3-D effects is also coherent between both methods (see Figure 4-6 and Figure 4-7).

4.3.4 Groom and Bailey

Additionally, we carried out the multisite/multiperiod analysis (McNeice and Jones, 2001) based on the Groom and Bailey (1989) tensor decomposition implemented in the code STRIKE (McNeice and Jones, 2001). This algorithm searches for a unique geoelectric strike direction suitable for all sites and the whole data range.

The Groom and Bailey method makes the assumption of two-dimensional data. In order to maintain as much as possible this assumption we removed the data with 3-D effects prior to the strike analysis. These data were chosen in base of the phase tensor and Bahr analysis. High beta values (Figure 4-6) coincide with high *phase sensitive skew* values (Figure 4-7). We did not consider the data with |β| values greater than 4° and *phase sensitive skew* values greater than 0.3.

The strike direction was calculated between 0.1s and 300 s for all the sites. Using an error floor of 8% for the impedance tensor, the smallest error was achieved for a strike direction of N10°E. Because of the 90° ambiguity existing for the impedance tensor, the choice of the real geoelectric strike was made based on the induction arrows and taking into account the geological information. Roughly, NS oriented arrows and EW oriented tectonic structures suggest that the true strike for the considered data and periods less than 300 s is N100°E.

4.3.5 Conclusions

The dimensionality analysis was carried out using three approaches: the phase tensor, Bahr method and Groom and Bailey method. All approaches gave similar results:

- *Phase sensitive skew* (Bahr, 1988) and the phase tensor skew (Caldwell et al. 2004) coincide in pointing to 3-D effects at long periods (higher than 300 s) for the whole profile, and localised 3-D effects at intermediate periods (higher than 5 s) beneath sites 05, 06 and 07.
- The Bahr (1988) and Groom and Bailey (1989) approaches gave similar results pointing to a 2-D preferred strike direction of N100°E, for the period range between 1 and 300 s.

The dimensionality analysis concludes that a 2-D approach considering a geoelectric strike of N100° is valid considering only a limited period range (T < 300 s). At long periods, clear indications of 3-D regional structure appear. The phase tensor analysis shows at long periods a NW-SE orientation of the ellipses, which is coherent with the NE-SW orientation of the real induction arrows for most sites from 100 s to 10000 s, suggesting deep regional elongated structures in a NW-SE direction. It should be pointed out that the surface geology shows the presence of several strike-slip faults oriented NW-SE, some of them being hundreds of kilometres long.

Consequently, we will carry out a 2-D inversion on the limited dataset (periods less than 300 s and periods that presented 3-D effects) assuming a strike of N100°E, followed by a 3-D inversion of the whole dataset.

4.4 2-D inversion

The 2-D inversion was carried out using the non-linear conjugate gradient (NLCG) algorithm (Rodi and Mackie, 2001). In accordance with the dimensionality analysis the data were rotated to –N80°E, the XY polarization being the TE mode and the YX polarization the TM mode. The apparent resistivity of the TE mode for the site 04 and 05 were manually shifted upwards by one decade, as explained in section 4.3.

4.4.1 Starting model

The mesh used for the 2-D inversion is large enough laterally and in depth to account for the boundary conditions necessary to satisfy the computation of the Maxwell’s equation during the forward modelling. The Atlantic Ocean to the north was included in the initial mesh and fixed to a value of 0.33 Ωm. The starting model resistivity was set to 100 Ωm. Excepting the ocean all the model was free of change during the inversion process.

Several tests were carried out to define the mesh discretization used for the inversion. Horizontally we opted for a mesh that is fairly equidistant in the central part of the mesh, with a logarithmic decrease of the cell size close to the sites. Outside of the core area the cell size increases exponentially taken into account the exponential decay of the EM fields. Vertically we used a fine mesh in the upper part of the model. The cell size increases logarithmically from 50m on the top until reaching a cell size of 2000 m thick at 10 km depth. This cell size is kept constant until a depth of 80 km, where it increases again in an exponential way until the bottom of the mesh.

4.4.2 Inversion settings

The error floor is an error value assigned to all data whose error is less than the error floor. The error floor used during the inversion was in accordance with the strike analysis carried out using the Strike program (McNeise and Jones, 2001) based on Groom and Bailey (1989). The estimated strike that satisfied all the data was obtained using an error of 8% on the impedance tensor, which correspond to an absolute error of 4.57° for the phase and a relative error of 16.64% for the apparent resistivity. Finally, we choose an error floor of 5% for the phase, 20% for the apparent resistivity, for both modes and of 0.04 for the tipper.

The NLCG (Rodi and Mackie, 2001) uses a regularization operator, following the Tikhonov regularization (Tikonov and Arsenin, 1977). It minimizes the misfit between observed and computed data keeping a smoothly varying resistivity volume. Several values of the Laplacian regularizer were tested in order to obtain an optimal value with an adequate compromise between roughness of the model and data misfit. Figure 4-9 shows the trade-off curve (L-curve). The corner of the L-curve defines the optimal regularizer value, which is 2 in this case.

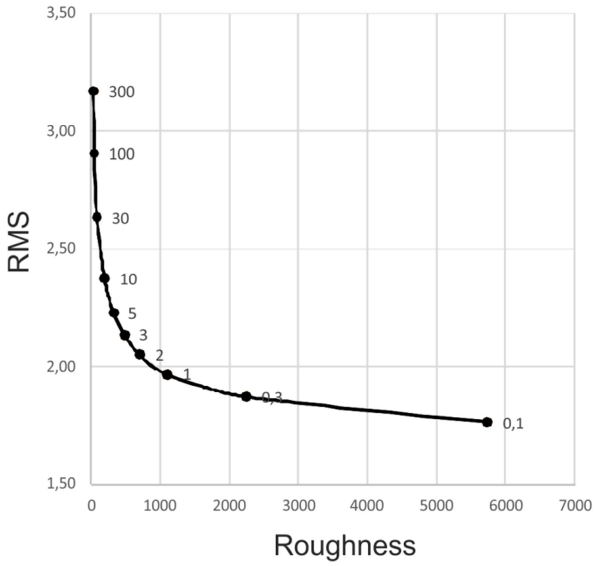

Figure 4-9: L-curve. A value of 2 was chosen for the subsequent 2-D inversion.

4.4.3 Single inversions

Inverting each data component independently allows to retrieve information about the resolvability of each kind of data. Figure 4-10 shows the result of the following independent inversions: tipper, TM mode, TE mode and joint inversions of TM mode and tipper and TE mode and tipper.

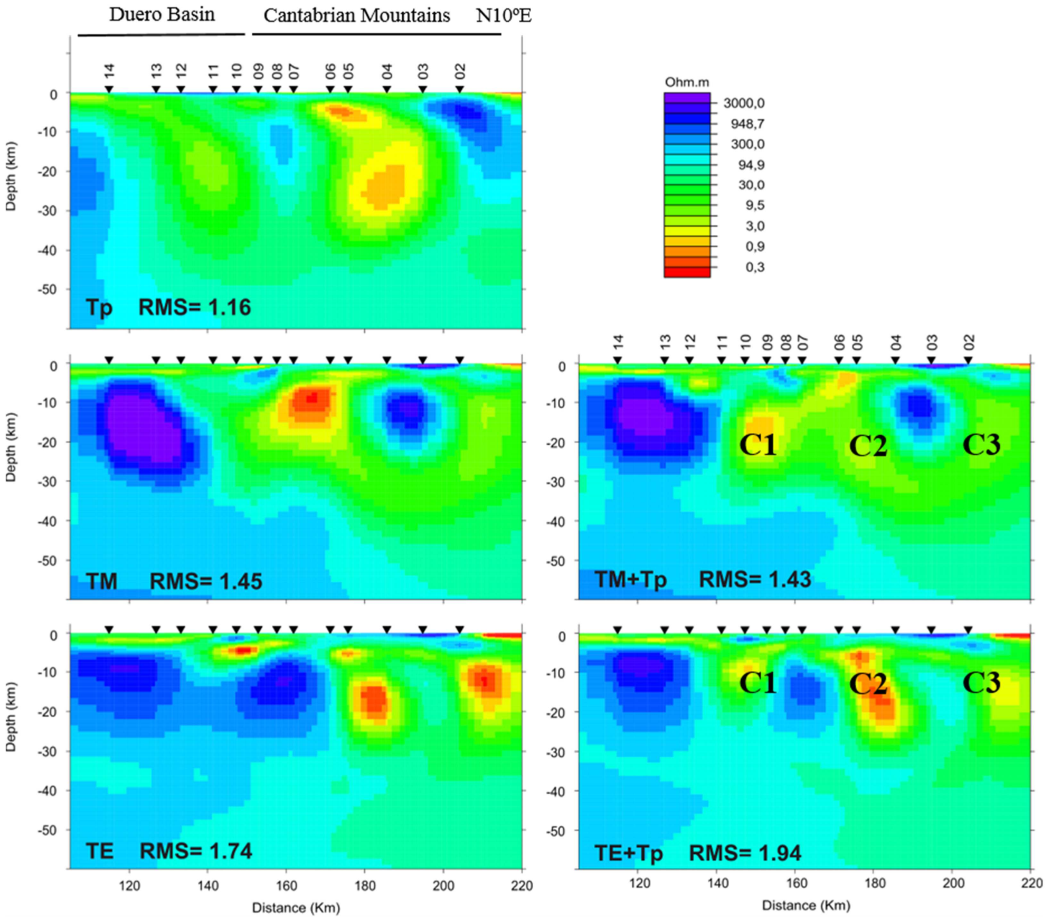

Figure 4-10: Resistivity models from independent inversions.

The TM and TE inversions show different features, mainly between sites 6 and 11. A better agreement is visible when the tipper data is jointly inverted with each mode. Three conductive anomalies between 10 and 20 km depth are observed in the TE and TM mode inverted jointly with the tipper, C1, C2 and C3. In the TM mode a relative deep resistive structure dipping north is observed. The TE mode also shows the same behaviour, even if not so well depicted. This feature could correspond to the downgoing Iberian crust subducing below the Iberian Margin, as observed in the seismic models.

4.4.4 Final inversion

Finally, a joint inversion of the three kinds of data, TM and TE modes and tipper was carried out using the same inversion parameters. The period range used for the inversion was from 0.001 s to 300 s. The final model reached a final RMS of 2.03. The model is presented in Figure 4-11.

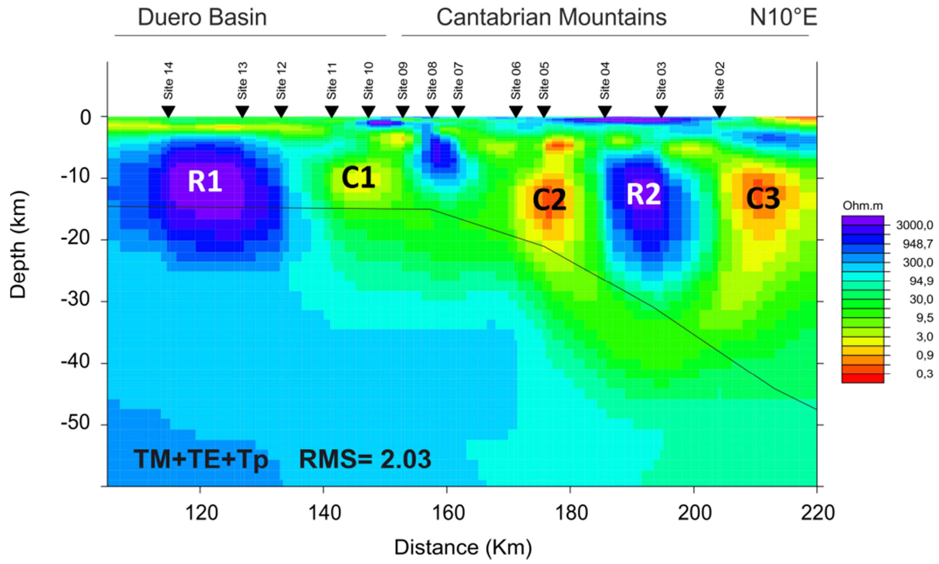

Figure 4-11: 2-D resistivity model obtained by the joint inversion of the TM, TE and tipper data. Black line represents the top of the subducting middle Iberian crust from Gallastegui (2000).

Fitting of the data is good as it can be observed in the comparison between the observed and calculated pseudo sections (Figure 4-12).

The final model (see Figure 4-11) presents several conductive and resistive anomalies. In the south part of the model, from site 14 to site 11 a shallow conductor (C1) is observed, overlying a very resistive block (R1) that expands to the bottom of the model. This feature corresponds to the Duero basin conductive sediments lying on the resistive basement of the Iberian crust. From site 10 to the north, the Cantabrian Mountains is characterized by a heterogeneous distribution of conductive and resistive anomalies (C2/R2/C3). Between 0 and 10 km depth there are several north dipping conductive anomalies. At mid-crustal and lower crustal depths two conductive anomalies are present. The first conductive anomaly, C2, beneath sites 05 and 06, extends from 10 km to 20 km depth. The second conductive anomaly, C3, beneath site 02, extends from 10 km to 25 km depth.

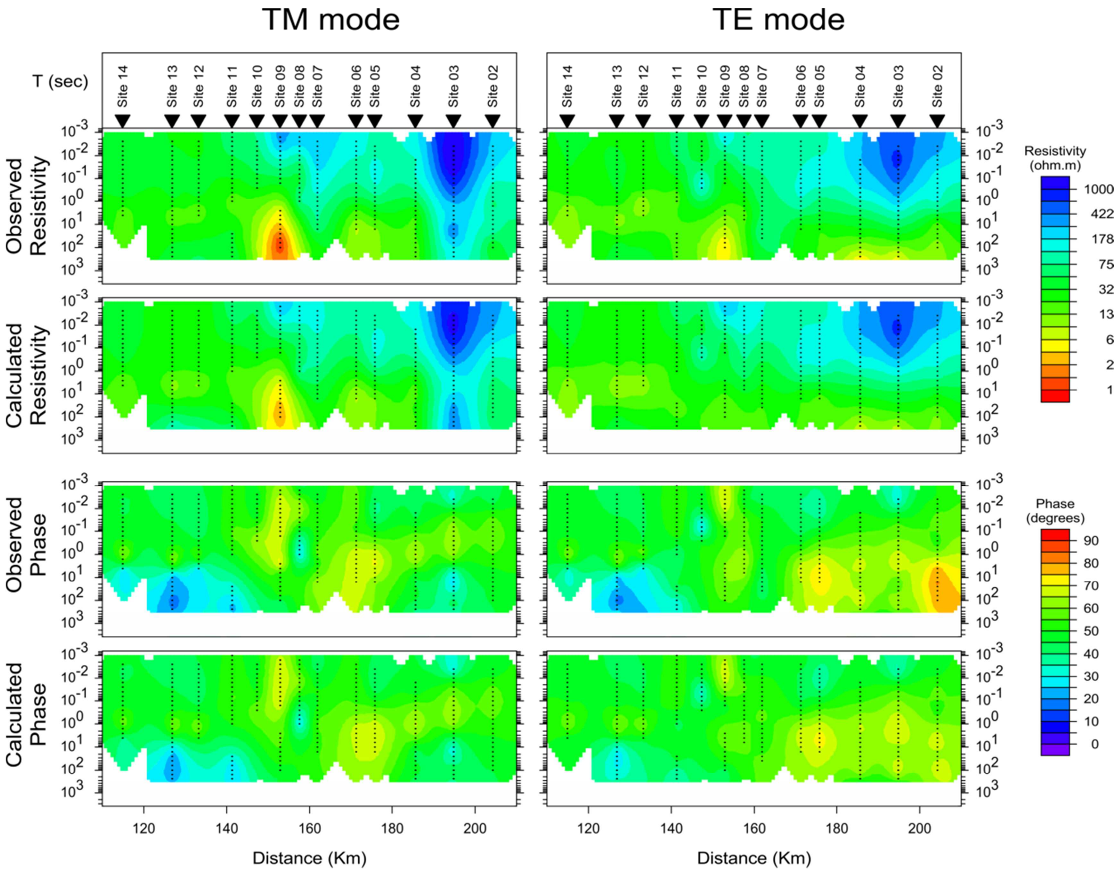

Figure 4-12: Pseudo sections of data and responses of inverse 2-D modes. Black points represent the data considered for the 2-D inversion. Data with 3D effects were not used in the inversion.

4.4.5 Constrained inversions

The sensitivity to the resistive middle and lower Iberian crust has been noticed in the unconstrained inversions, especially constrained by the TM mode data. It is modelled as a resistive feature dipping north, at a position that matches with the slab imaged by the seismic.

Sensitivity of the magnetotelluric data can be improved incorporating constraints in the inversion (McGary et al., 2014; Matsuno et al., 2010; Evans et al., 2014). In a similar context these authors introduced in the starting model a resistive subducting crust, or slab, constrained by seismic results. At the interface between the slab and the surrounding cells a relaxation in the smoothing constrain used in the inverse codes is introduced during the inversion, thus allowing great changes of resistivity across that boundary. In the software package WinGLink this feature is defined as a *tear zone*. A cell that is part of the *tear zone* will have its boundaries free of smoothness constraint. It should be noted that the slab was not kept fixed during the inversion.

Two approaches were tested: We incorporated in the initial model of the inversion a slab of resistivity 2000 Ωm constrained from the seismic results, embedded in a homogeneous half-space of 100 Ωm. (1) we run a classic inversion and (2) we run an inversion imposing a *tear zone* at the interface between the resistive slab and the homogeneous background.

In order to keep consistency between both results the same inversion parameters were used. Figure 4-13a shows the starting model, where the structural model from Pedreira et al. (2015) is superimposed (Fig 2-12). Figure 4-13b shows the results of the constrained inversion without *tear zone* and Figure 4-13c with the *tear zone*.

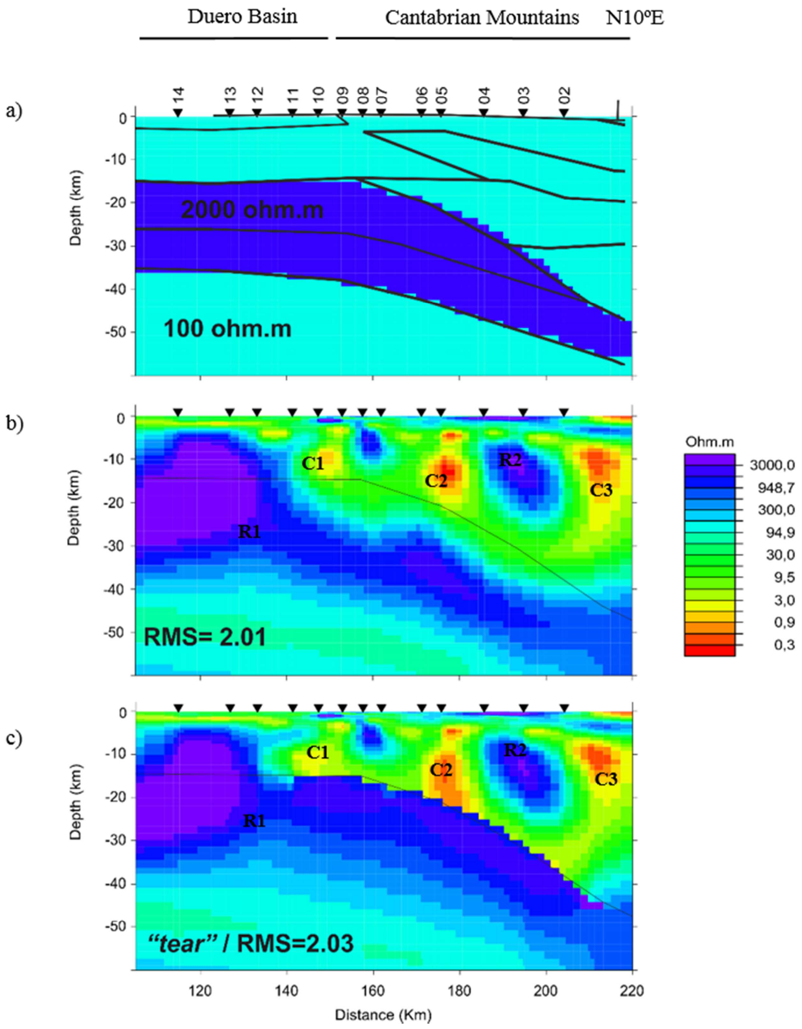

Figure 4-13: a): Initial model used for the constrained inversions. Black lines are the structural model from Pedreira et al., 2015. b): Results for the 2-D inversion using the constrained starting model. c): Results of the 2-D inversion applying a tear zone at the top of the resistive slab.

Both inversions reached the same RMS and the models present the same features. These results show us that the three models (unconstrained model, Figure 4-11, and constrained models, Figure 4-13b and Figure 4-13c are equally feasible as all fit equally the data. The presence of a resistive Iberian crust dipping north was already seen in the unconstrained inversion (Figure 4-11). This non-uniqueness is due to the limitations of the MT method itself. First, in the unconstrained inversion the least-square inversion scheme does not resolve for sharp boundary structures, as it occurs in this case. The model will be blurred with depth and laterally. Second the bottom of a conductor cannot generally be resolved by the MT data (Simpson and Bahr, 2005). The moderate conductor located between -15 km and -25 km depth beneath sites 10 to 8 is not constrained because located just beneath a strong conductor.

In spite of the limited period range (0.1 s to 300 s) used in this 2-D inversion, we can conclude that the presence of a resistive Iberian crust dipping north is possible and suggested by the data, but it cannot be defined with precision with the unconstrained inversion. The link between conductors C2 and C3 with the slab interface probably does not exist. In the unconstrained inversion, the position of the conductor C2 is 5 km above the slab and the *tear zone,* breaking the smoothness across the adjacent cells, has the tendency to induce the inversion to place anomalies at the boundaries where the *tear zone* is defined.

4.5 3-D inversion

As pointed out the data presenting 3-D effects were removed from the 2-D inversion. This mainly concerns long period data (T > 300s), which restricts the 2-D inversion to more superficial structures. 3-D effects are a consequence of the complexity of the tectonics of the area. It was also noticed that two main different directions are present in the 2-D data. The 3-D structures and changes in the strike direction cannot be resolved by the 2-D approach. Accordingly we proceed with a 3-D inversion of this dataset.

3-D inversion of a unique MT profile not only is sensitive to the resistivity distribution beneath the profile but also provides resolution on the off-profile structures affecting data along a profile (Siripunvaraporn et al., 2005b, Patro and Egbert, 2011; Xiao et al., 2012; Brasse et al., 2015). The L-shaped conductive feature (Ichihara and Mogi, 2009) was the most probable explanation to explain the phases greater than 90°of sites 05, 06 and 07 located close to complex imbrications of faults with different orientations. We decided not to include these phases in the first steps of the inversion. Taking into account that the data consist of a unique profile this behaviour could lead the inversion to create resistivity artefacts off-profile and bias the inversion. As it will be explained these data will be include in a later stage of the inversion.

3-D inversions allow to explore a large range of solutions compared to 2-D inversions. However, because of the increased computational cost of 3-D inversions the model discretization has to be coarser and the number of periods used has to be reduced. As a consequence, along profile resolution is reduced compared with 2-D inversions.

Here we used the WSINV3DMT code developed by Siripunvaraporn et al. (2005a, 2009) for the 3-D inversion. This code allows for the inversion of the impedance tensor components (Z) and for the vertical transfer function data (VTF).

4.5.1 Starting Model description

The starting model was a uniform 100 Ωm half space, including the Atlantic Ocean to the north following the bathymetry (ETOPO1, Amante and Eakins, 2009). The seawater resistivity was set to 0.33 Ωm and was fixed during the inversion. Model grid dimensions are N_x=66, N_y=32 and N_z=60, plus 7 air layers, for a total number of cells of 126,720. Figure 4-14 shows the mesh in the core area along with the sites position. Vertically, the first layer is 30 m thick, increasing to a larger size at depth. Horizontally, in the core area the cells have dimensions of 1.75 km x 1.75 km. The cell size is then increased logarithmically in both directions to avoid the boundary effects. The total mesh dimension is 1546 km x 1602 km x 947 km. The MT sites that were not located in cell centres were slightly displaced. This displacement did not exceed 500 m.

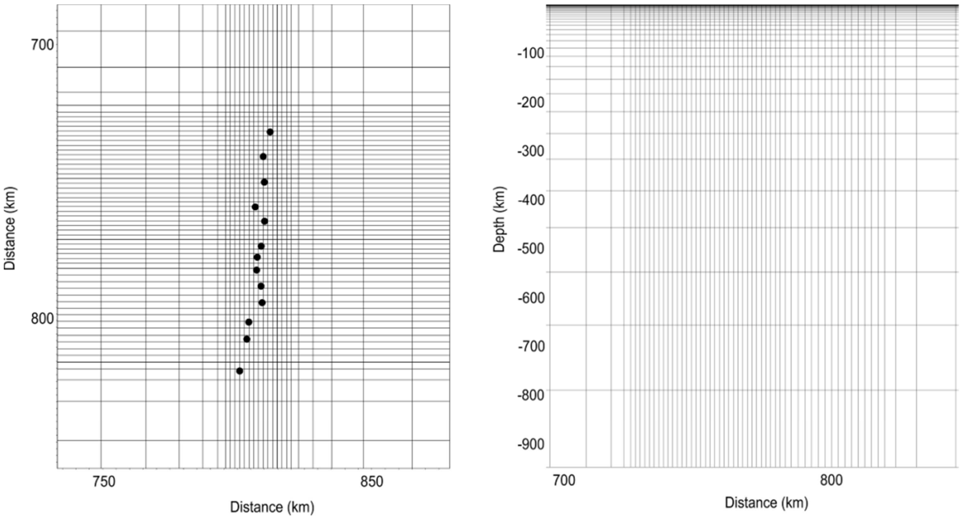

Figure 4-14: 3-D mesh. Left: plane view of the core area, black points are the MT sites. right: Section view of the mesh, centred on the core area.

4.5.2 Inversion parameters

Thirteen stations were used during the inversion, with 12 periods between 0.25 s and 6309 s, having 2.5 periods per decade. Noisy data were excluded from the inversion. An error floor of 5% for the impedance tensor ($0.05*\left|Z_{xy}Z_{yx}\right|^{1/2}$) and 15% for the vertical transfer function (VTF) ($0.15*\left(\left|T_{zx}\right|^2+\left|T_{zy}\right|^2\right)^{1/2}$) was applied. The inversion algorithm used allows for smoothing penalty along the three directions of the space. We realized several tests where anisotropic smoothing was applied, in both directions E-W and N-S. However these tests always led to similar models or unsatisfactorily models from a roughness point of view. The default smoothing was then applied, with the length scale parameters of $\tau=5$, $\delta_x = \delta_y = \delta_z = 0.1$. The Lagrange multiplier parameters were set as default, with an initial value $\lambda=1$ and a step =0.5.

4.5.3 Inversion strategies

The inversion was carried out using two simultaneous inversion strategies.

First, we decided to invert only the off-diagonal part of the impedance tensor. The resulting model was re-inverted adding the VTF data until reaching convergence. In a last stage the model obtained was re-inverted including the diagonal components of the impedance tensor, along with the off-diagonal terms that presented phases > 90º. This strategy was carried out based on the data that wanted to be considered. The VTF data was included in a second stage because it is more sensitive to horizontal structures and resistivity contrast than to depths or absolute values of resistivity (Siripunvaraporn et al, 2009). Then, adding the VTF data in a later stage keeps the shape of the structures and mainly enhances or reduces the conductivity contrasts in the 3-D model to fit the VTF data. Furthermore, the analysis of the data showed that the diagonal elements of the impedance tensor were not of high quality. This strategy allowed to obtain a model that was primarily driven by the data of better quality (first the off-diagonal terms, then the VTF), to prevent noisy data fitting. This conclusion was observed during the inversion process, allowing to conclude that there is good agreement between the Z and the VTF data. When the full impedance tensor and the VTF were inverted simultaneously from a starting homogeneous model the inversion was not able to converge to the RMS obtained applying this strategy without having much more iterations and leading to models that resulted to be rough, geologically unfeasible or with unreasonable conductivity values.

Secondly, independently of the type of data used, we adopted a multistage inversion scheme to decrease effectively the data misfit. This strategy was used by Patro and Egbert (2011), Xiao et al. (2012), Boonchaisuk et al. (2013). It consists in running the inversion for several iterations until a minimum RMS is achieved. When the inversion starts to diverge the resulting model is used as new starting and prior model for a new round of iterations. This process is repeated until a satisfactory convergence is reached. This strategy permits to reach a better data misfit. However, since the inversion algorithm penalises deviations from the prior model, the resulting model does not represent a true minimum structure model respect to the original prior model, which is homogeneous (Patro and Egbert, 2011). Nevertheless, the model obtained after few restartings was geologically plausible and this strategy did not cause the inclusion of unnecessary or rough structures in the model.

The combination of these two strategies was found to be optimum for the inversion of this dataset.

4.5.4 Inversion process and results

The inversion was run on a Linux operating system with a machine of 128 GB Ram. Each iteration lasts about 4 hours. The inversion process carried out reached a final RMS of 1.94 after a total of 17 iterations, after restarting the inversion five times. Figure 4-15 shows the statistics through the inversion process.

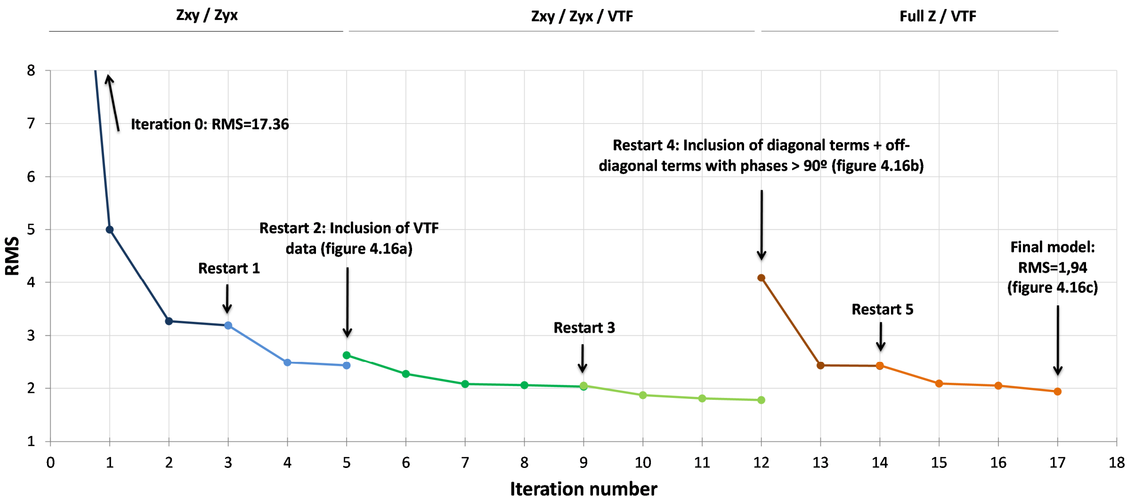

Figure 4-15: Evolution of the data misfit as a function of iteration number during the inversion. Intermediary models are shown in figure 4.16.

In order to illustrate the expected behaviour in the subsequent restarting inversions Figure 4-16 shows the intermediate models. The models are shown along a N10ºE oriented cross section through the 3D inverse model. The model obtained when inverting only the off-diagonal elements of the impedance tensor is shown Figure 4-16a. The model obtained when inverting the off-diagonal elements of the impedance tensor jointly with the VTF data starting from model shown in Figure 4-16a is shown in Figure 4-16b. Finally, the model that fits the full impedance tensor and the VTF starting from model shown in Figure 4-16b is shown in

Figure 4-16c. We can see that the main structures constituting the model are already present at the end of the inversion that only includes the off-diagonal elements of the impedance tensor (iteration five or start of restart 2; Figure 4-16a).

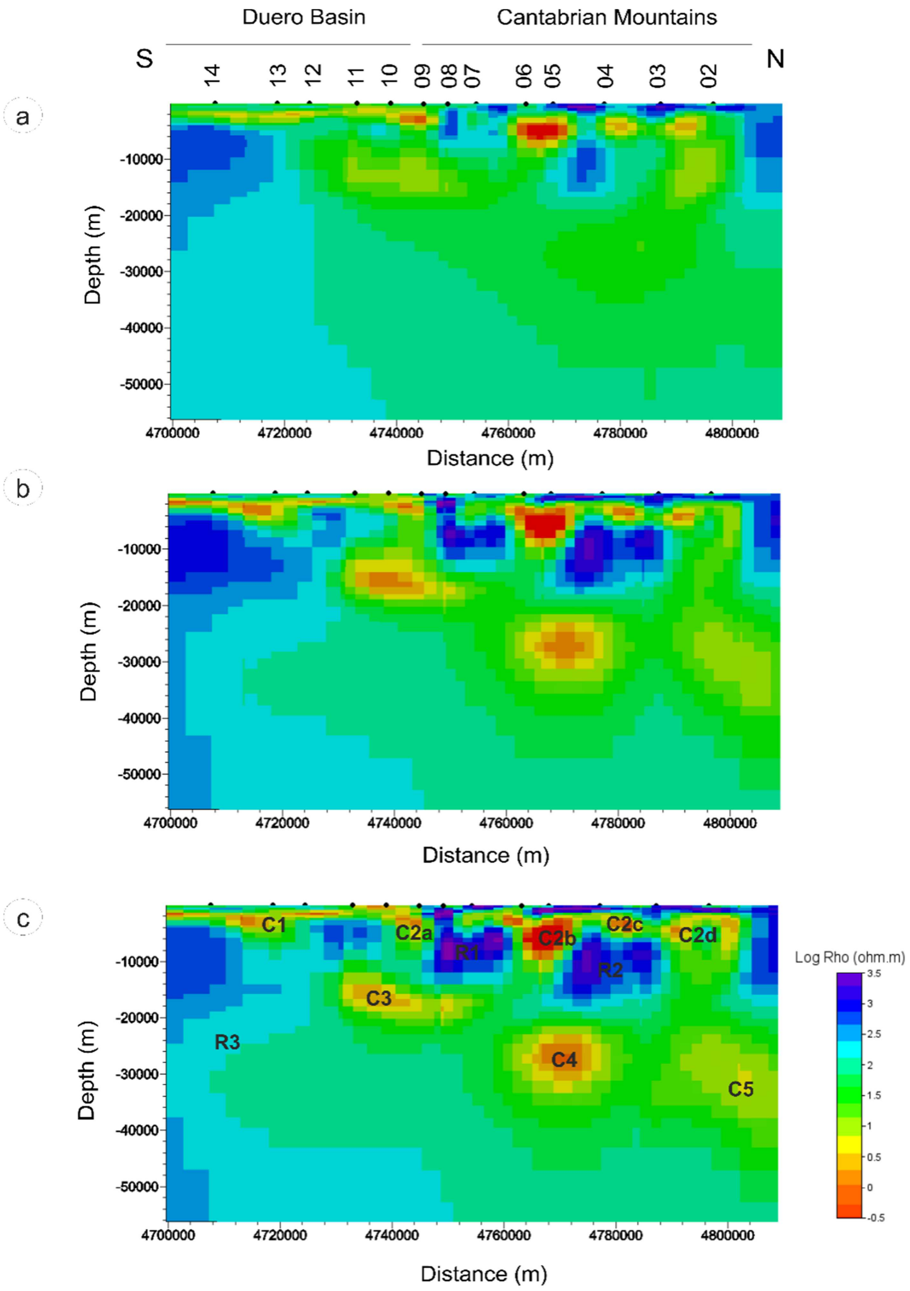

Figure 4-16: Intermediary models along a N10ºE profile across the 3-D inverse models. a) model obtained after five iterations, inverting only the off-diagonal elements of the impedance tensor, RMS=2.44. b) model obtained after twelve iterations, inverting the off-diagonal elements of Z and the VTF, RMS=1.78. c) model obtained after seventeen iterations, inverting the full impedance tensor and the VTF, RMS=1.94. See text and figure 4-15 for details.

Adding the VTF at restart 2 increased the resistivity contrasts, as expected, maintaining the main structures. The small increase of the RMS in restart 2 (Figure 4-15) is due to the inclusion of the VTF data. The small difference confirms that VTF data are compatible with the off-diagonal elements of the impedance tensor. At the end of restart 2, the RMS achieved was very good (RMS = 1.78). At that point we included the diagonal terms of Z and the off-diagonal terms of Z that presented phases > 90º (long period of polarization XY for sites 05, 06 and 07). The large increase of the RMS (Figure 4-15, iteration 12) was mainly due to the inclusion of the off-diagonal data with phases greater than 90º. However, as expected, the structures of the model did not change and the full data was able to be fitted in few iterations, pointing to compatibility between all the elements of Z and the VTF.

We also noticed that the inversion had the tendency to slightly modify the sea resistivity, even having fixed it during the inversion. For this reason the original distribution of the sea was re-introduced between each restart, leading to a slight increase in the RMS respect to the previous iteration (Figure 4-15).

Impedance and VTF tensors misfit:

The fit of the full Z and the VTF is satisfactory (RMS = 1.94) taking into account the error floor used. Figure 4-17 shows the fitting of apparent resistivity, phase and VT for four selected sites. In appendix 1 all the sites along with the responses of the final model are shown.

Figure 4-18 shows the real induction arrows data and responses of the final model. Figure 4-19 shows the pseudosections of data and responses for comparison. All these ways of assessing the data fitting show a very good agreement between data and responses.

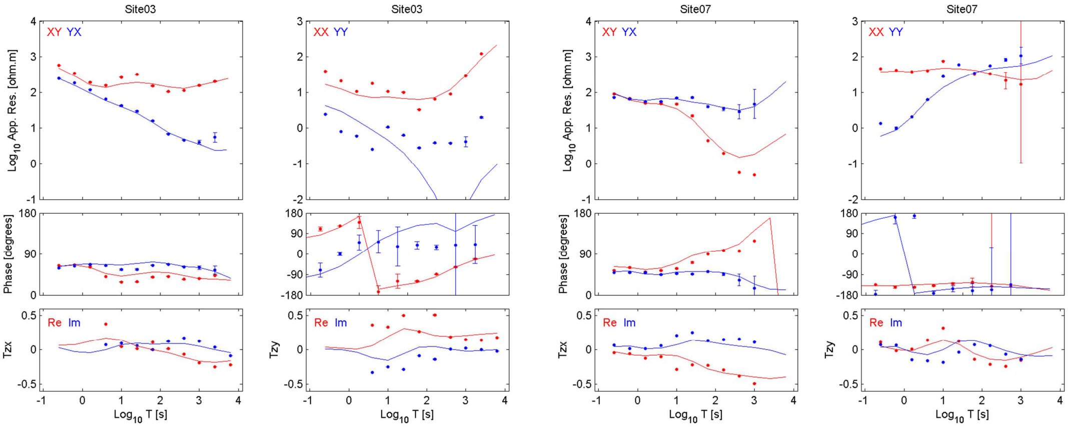

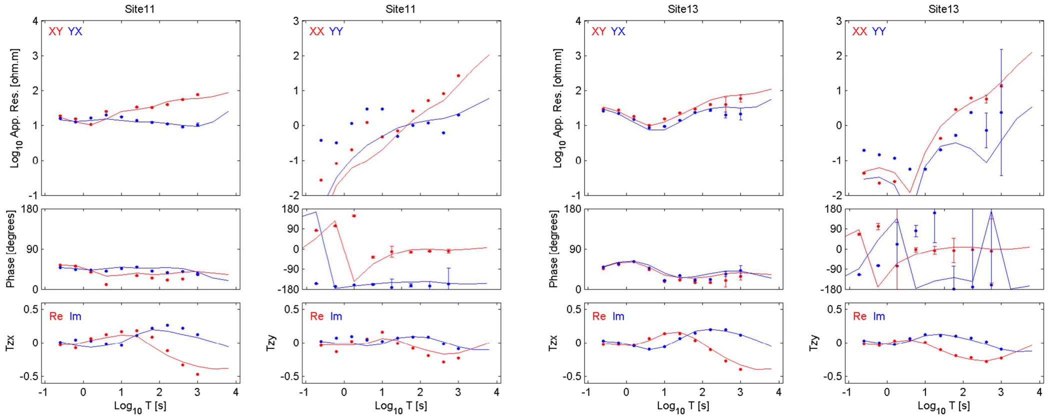

Figure 4-17: Four selected sites (03 / 07 / 11 / 13). Data (points) and responses (continuous line) of the 3-D inverse model.

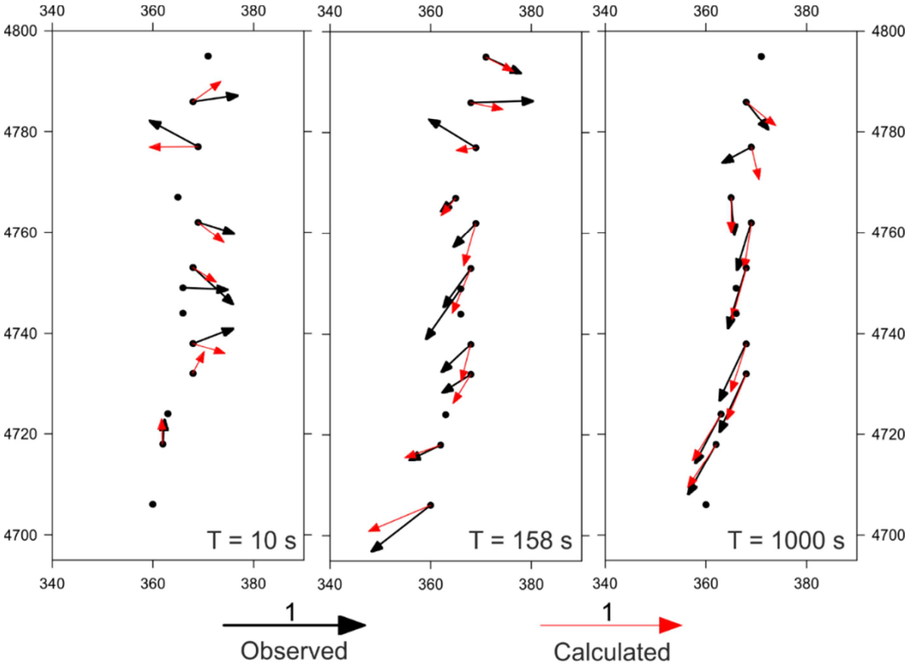

Figure 4-18: Real induction arrows for three selected periods (10 s, 158 s and 1000 s). Observed (black arrows), calculated (red arrows).

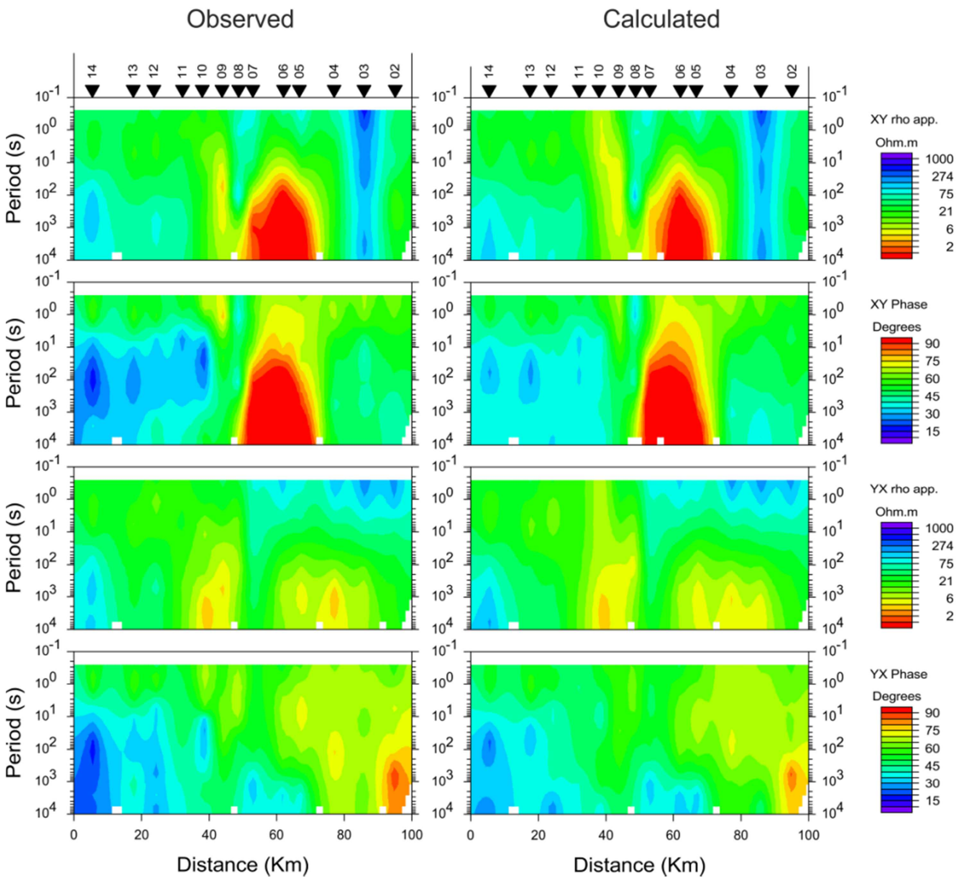

Figure 4-19: Pseudo sections of apparent resistivity and phase of the off-diagonal data used for the inversion (left) and the calculated data of the final 3-D model (right).

Phase tensor misfit:

Even if the impedance tensor and the VTF were inverted, comparing the observed and calculated phase tensors permits to assess the misfit achieved during the modelling. This method was introduced by Heise et al. (2007), where responses of a 2-D model were compared to the observed data to depict the departure of the 2-D responses due to 3-D structure. The phase tensor includes all the components of the impedance tensor. The coordinate invariants of the phase tensor as introduced by Caldwell et al. (2004) should be coherent between the observed data and the calculated responses. The phase tensor ellipses whose axes are defined by the maximum (Φmax) and minimum (Φmin) tensor values are filled with the skew angle beta, which is a measure of the tensor's asymmetry and then of the departure from 2-D behaviour in the data.

Figure 4-20 shows the observed and calculated phase tensor ellipses. Note the calculated phase tensor ellipses orientation is reproduced by the 3D inverse model, especially the deflection of the ellipses to a NW-SE direction at long period. The phase tensor skew values are well reproduced, with an increase of the phase tensor skew at long period and in the centre of the profile.

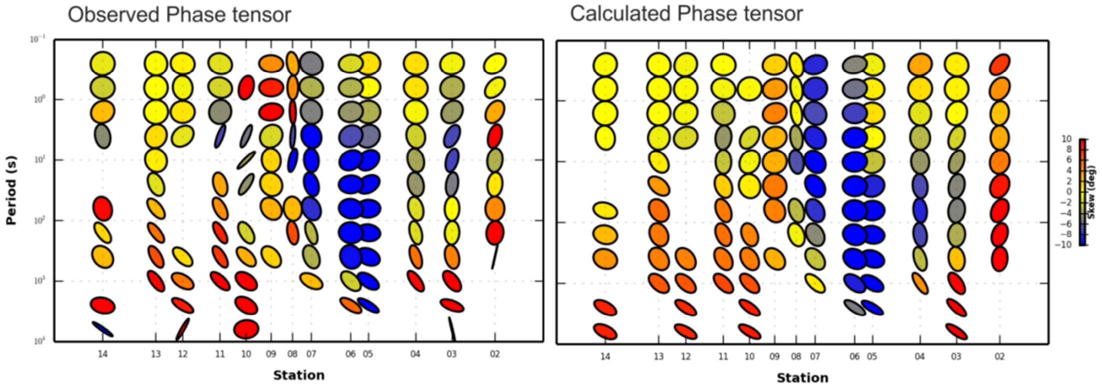

Figure 4-20: Phase tensor fitting. The ellipses are filled with the skew angle beta. Vertical axis of the plot is north-south oriented. Top: observed phase tensor. Bottom: predicted phase tensor.

4.5.5 Model description

Figure 4-21 shows the N-S sections (X planes) of the core area of the model. This representation allows to see variations along the E-W direction and highlights which parts of the model are better constrained by the data. Note that the parts of the model that are not directly located beneath sites can suffer some ambiguity. The off-profile structures introduced by the inversion are not well constrained, especially at shallow depths. The Figure 4-21 shows consistency along the different planes. However, there is a discrepancy in the southern part of the model between plane 13, in the W, and plane 19 in the E. In the eastern planes (planes 18 and 19) the conductor C3 merges with the conductor C1 (conductors are labelled in Figure 4-16c) due to a new conductor dipping north and linking them (Figure 4-21). This new conductor is located outside of the data coverage and therefore we chose not to consider it. The presence of the shallow and thick conductive sediments of the Duero Basin east of the southern sites probably affects them and could provoke an artefact during the 3D inversion of a unique profile.

In order to ensure the robustness of the model and discuss only those features located beneath the sites (discarding off-profile resistivity structures) we decided to choose a cross section through the 3D inverse model that better coincide with the direction of the MT profile, which is N10°E.

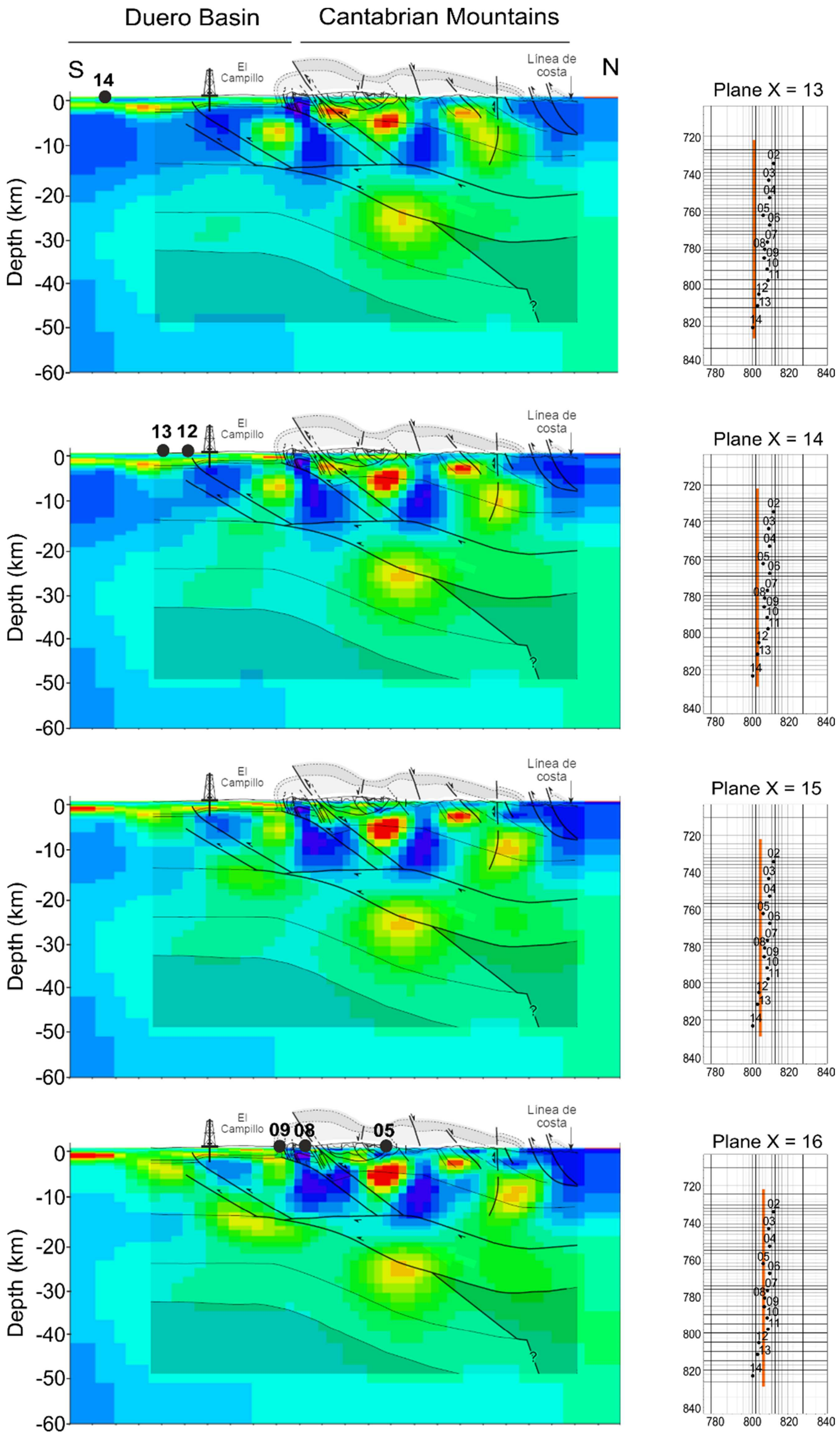
Duero Basin
Cantabrian Mountains
S
14
El Campillo
Linea de costa
N
Depth (km)
0
-10
-20
-30
-40
-50
-60
Plane X = 13
13 12
Plane X = 14
Plane X = 15
09 08
05
Plane X = 16
720
740
760
780
800
820
840
780
800
820
840
02
03
04
05
06
07
08
09
10
11
12
13
14

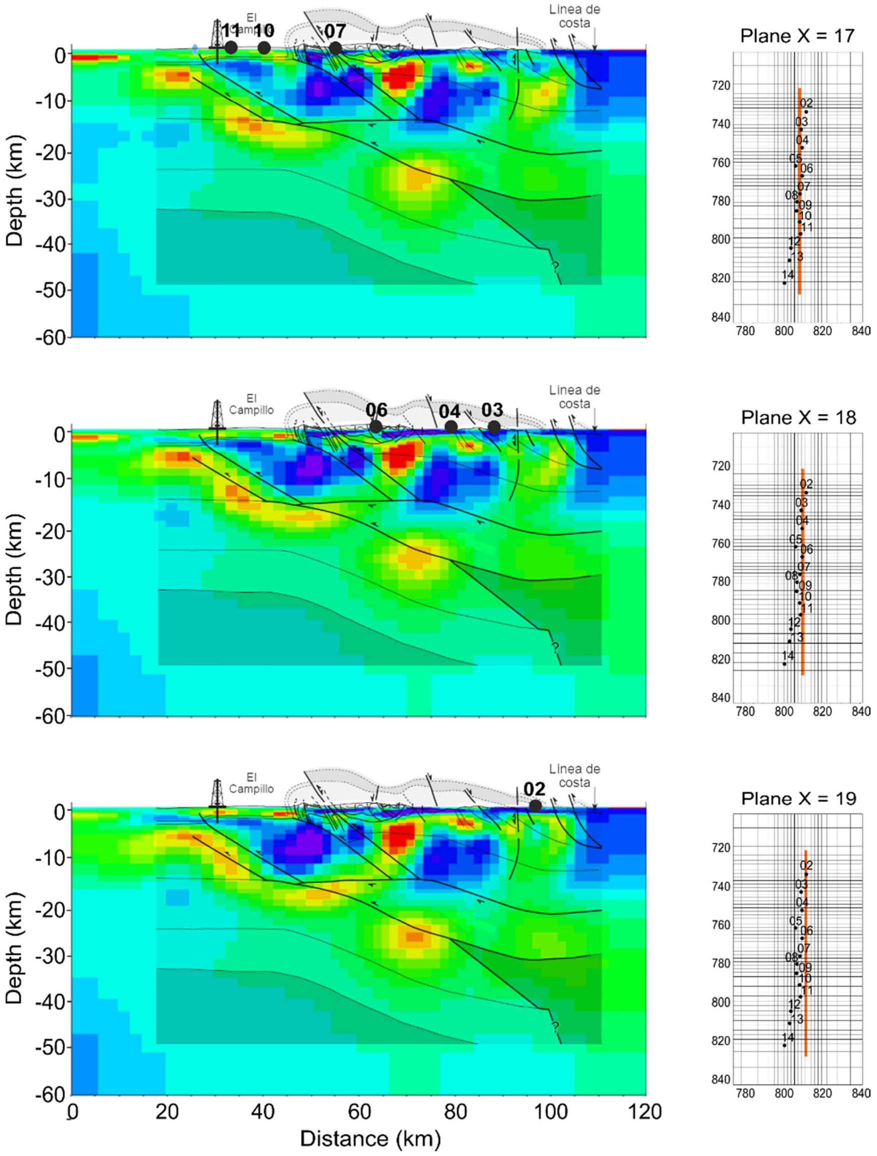

Figure 4-21: 3-D inverse model. The NS oriented planes (X planes) of the core area of the model are shown on the left, with their location on the mesh (on the right). Each plane is separated from the other ones by 1.75 km. Superimposed on the MT model: crustal-scale cross section by Gallastegui (2000), based on the surface geology, the results of the ESCIN-2 seismic reflection profile and gravity modelling. This section is approximately coincident with the alignment of MT sites.

The final model along a N10°E oriented line cross section is shown in Figure 4-16c. Several conductive anomalies are highlighted. The anomalies are labelled in the cross section and in the depth slices (Figure 4-22).

- A shallow conductor C1 (1 - 20 Ωm), which is 2 to 2.5 km thick beneath sites 10 to 12, and gets thicker to the south being 3.5 km thick beneath site 13.

- Several shallow conductors labelled C2 (1 - 20 Ωm), which extend from the surface to different depths, with a maximum at 10-15 km depth for the conductor C2d. The depth slices show that these anomalies have different orientations (the C2d and C2c and C2b conductors are oriented E-W, NW-SE and E-W to NE-SW respectively), generally following the trace of the faults in surface (depth slice 19 in Figure 4-22).
- A conductor C3 (3 - 10 Ωm) elongated subhorinzontally in N-S direction, located at 15 km depth beneath site 11 to 08.
- A conductor C4 (1 - 10 Ωm), located between 20 and 30 km depth, beneath sites 04 to 06. As visible on depth slice 32 (Figure 4-22), this conductor is oriented EW.
- A conductive anomaly C5 (5 - 20 Ωm).
- A shallow high resistive anomaly, R1 (> 300 Ωm), extending to 12 km depth beneath sites 06 to 09. This resistive anomaly is oriented E-W to NW-SE (depth slices 19 and 24 in Figure 4-22).
- A resistive anomaly R2 (> 300 Ωm) extending to 16 km depth beneath sites 03 to 05. This anomaly is oriented approximately E-W (depth slices 24 and 27 in Figure 4-22).
- A resistive anomaly R3 (> 100 Ωm), present in the whole model. Located at 3 km depth in the southern part of the profile until the bottom of the model, it dips to the north to be located at 40 km in the northern part of the profile beneath conductor C5.

In the shallow part (depth slice 19 in Figure 4-22) the anomalies are oriented following the orientation of the main faults, E-W to NW-SE in the north, NE-SW and E-W to the south. Deeper, as observable in depth slice 32 the anomalies are mainly oriented E-W, while in depth slice 42 the resistive anomaly R3 and its contact with the northern more conductive zone (centre of profile) take an approximate NW-SE orientation. This observation is in agreement with the dimensionality analysis carried out in the previous part of this chapter. The phase tensor ellipses at long period are elongated along a NW-SE direction, and the induction arrows point to the S, SSW and SW. This behaviour is now visible in the final model. At shorter periods we noticed that some alternative strike directions were present in the data, which is now reflected in the model with the orientation of the anomalies.

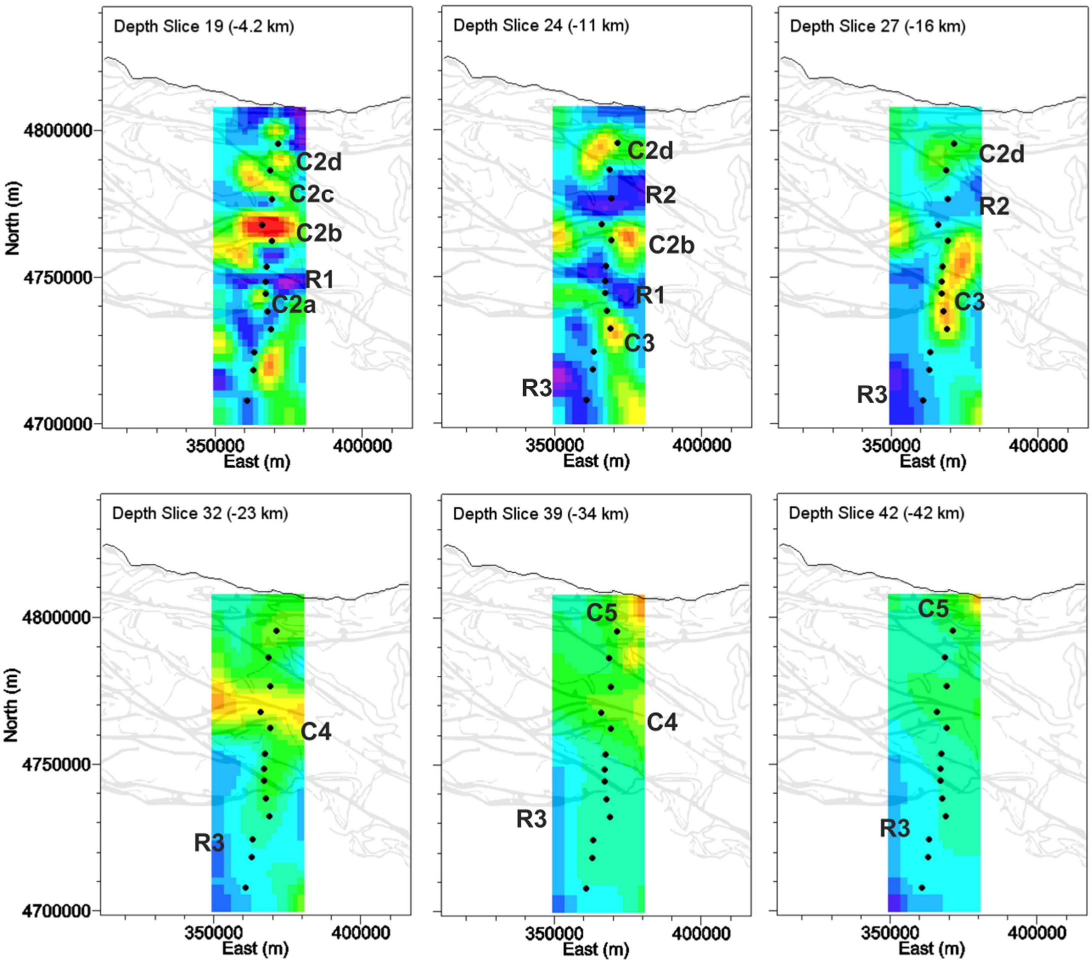

Figure 4-22: Depth slices of the final 3-D model superimposed on the structural map of the area (from Tavani et al., 2012).

4.5.6 Sensitivity tests

Main structures have to be tested for their robustness prior to the interpretation. It is important to note that during the inversion work several inversion parameters were tested and all of them converged to similar results. This repeatability already gave us confidence on the robustness of the model.

A simple way to test if a model feature is required by the data is to remove it from the model and compare the responses of the perturbed model with the responses of the inverse model. If they are the same, within the measurement errors, then the structure is not required by the data and could be an artefact of the inversion. When differences are observed the structure is needed and can be considered as robust.

Three structures of interest were tested: the conductor C3, C4 and C5. In all the cases we removed the conductive anomaly and replace it by a resistivity of 300 Ωm. The areas removed for each test are shown in Figure 4-23.

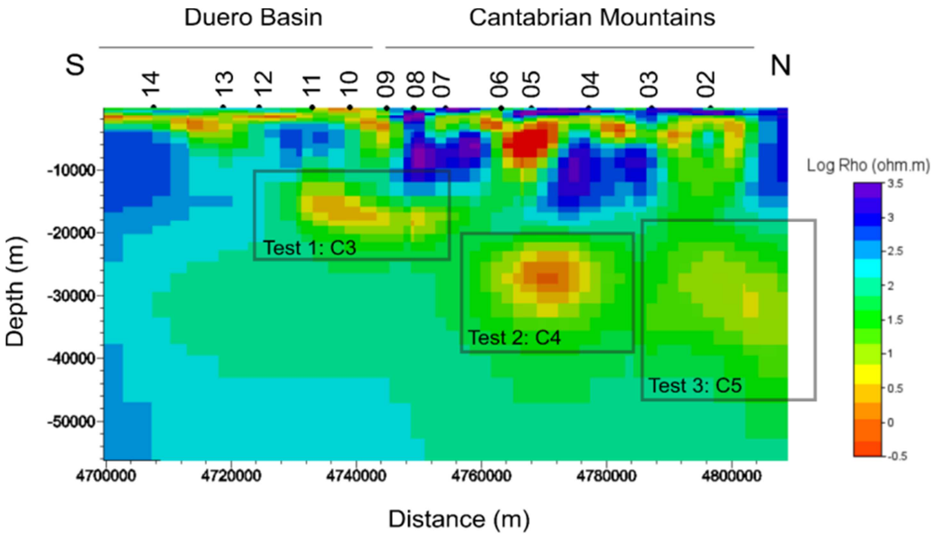

Figure 4-23: Left: Model used for testing the conductor C3. Right: Model used for testing the conductor C4.

Test of conductor C3. Removing the anomaly the global misfit passed from 1.94 to 2.22. Figure 4-24 shows the responses of the perturbed model for two sites located above the anomaly, along with the responses of the final model. This test principally affects the sites located in the south part of the survey. Differences appear in the XY component although the YX is also affected, mainly in site 11.The conclusion is that C3 is a robust feature.

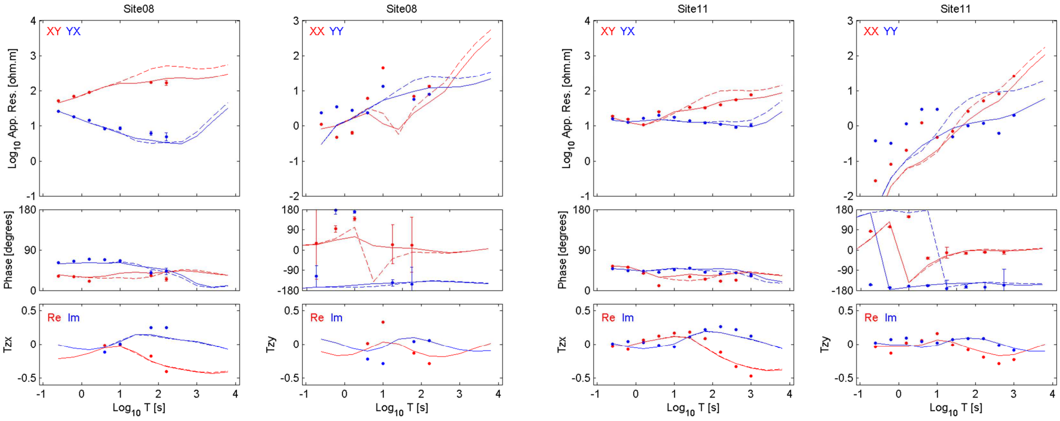

Figure 4-24: Data fitting for the test of the conductor C3. Points: observed data. Continuous line: responses of the final 3-D model. Dashed line: Responses of the perturbed model.

Test of conductor C4. The RMS passed from 1.94 to 2.44 for the perturbed model. Figure 4-25 shows the responses of the perturbed model for two sites, along with the responses of the final model. This test mainly affected the sites located in the central part of the survey at long period. Both the XY and YX polarizations were affected, showing higher apparent resistivity values at long periods. The conclusion is that conductor C4 is a robust feature.

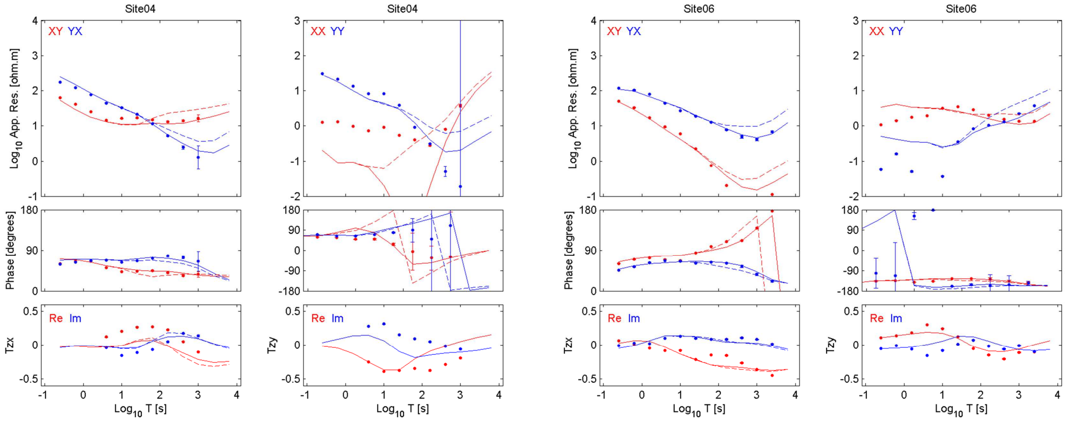

Figure 4-25: Data fitting for the test of conductor C4. Points: observed data. Continuous line: responses of the final 3-D model. Dashed line: Responses of the perturbed model.

Test for the conductor C5. The RMS passed from 1.94 to 2.11 for the perturbed model. Figure 4-26 shows the responses of the perturbed model for two sites, along with the responses of the final model for comparison. This test mainly affected the long periods at sites located in the northern part of the profile. The XY component was more affected than the YX. It shows higher apparent resistivity values at long periods. The Tzx data was also affected, when the Tzy showed no differences.

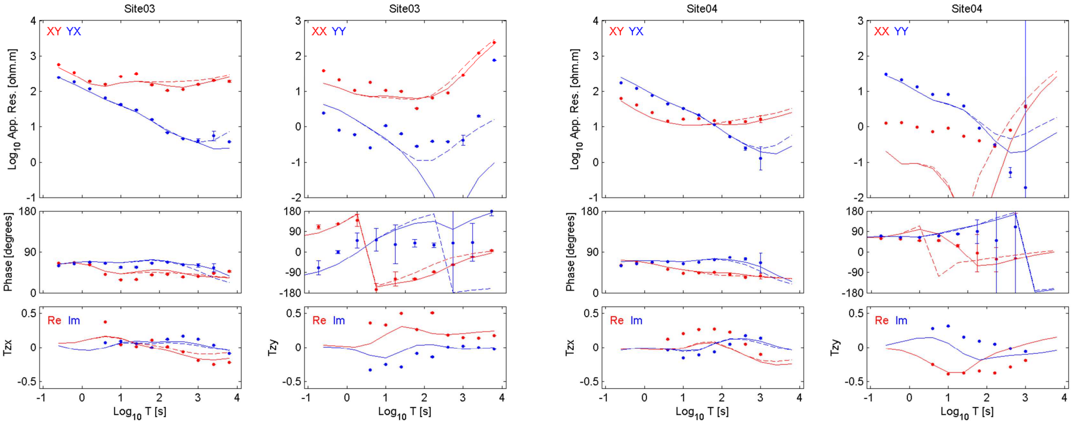

Figure 4-26: Data fitting for the test of the conductor C5. Points: observed data. Continuous line: responses of the final 3-D model. Dashed line: Responses of the perturbed model.

In conclusion these tests show that C3, C4 and C5 features are robust and required by the data.

4.5.7 Comparison of the 2-D and 3-D inversion models

The 3-D inversion was run in order to account for the 3-D effects present in the data. The model obtained from 2-D inversion is compared with the cross section N10ºE of the 3-D model (Figure 4-27). Both cross sections are oriented N10°E and are geographically consistent between each other. The locations of the main anomalies of the 3-D models are identified in the 2-D model to better illustrate the differences.

The upper part of the model, until10 km depth, shows similar results. The Duero Basin sediments are well depicted and several north dipping conductors are visible in both models. Because of the higher discretization of the 2-D model and the use of higher frequencies a better resolution is achieved in the 2-D model for the shallower part. These similarities are not surprising since the dimensionality analysis points out a 1-D to 2-D behaviour of the data at high frequency, and a consistent strike of N10°E for all the sites. Both inversion schemes are then able to model the data in a similar way.

The anomaly C3 visible in the final 3-D model (Figure 4-27) is slightly deeper with regard to the 2-D model (few kilometres) at approximatively the same position. Therefore we consider this anomaly to be consistent between both models. The conductive anomalies C4 and C5 are characterized by moderately conductive bodies in the 2-D model, even if not well depicted.

The main difference is the presence of a conductive region in the 2-D model beneath sites 05, 06 and 07 between 10 and 20 km depth. In the 3-D model the resistive anomalies R1 and R2 are partially located in the position of this conductor. This observation is not surprising since the data analysis (section 4.3) showed several 3-D effects in this area (phase tensor and Bahr analysis, figures 4-6 and 4-7). The current orientation and shape of the anomalies observed in the 3-D model is not reproducible using a 2-D approach considering a unique strike. Also the 3-D inversion inverted for the whole VTF data, when the 2-D inversion only inverted for the projection of the tipper on the Tzx axis. Therefore, the location of those anomalies in the 2-D model is misplaced when 3-D effects have to be considered. We conclude that the 3-D inversion, which is able to fit the full dataset is more robust than the 2-D approach.

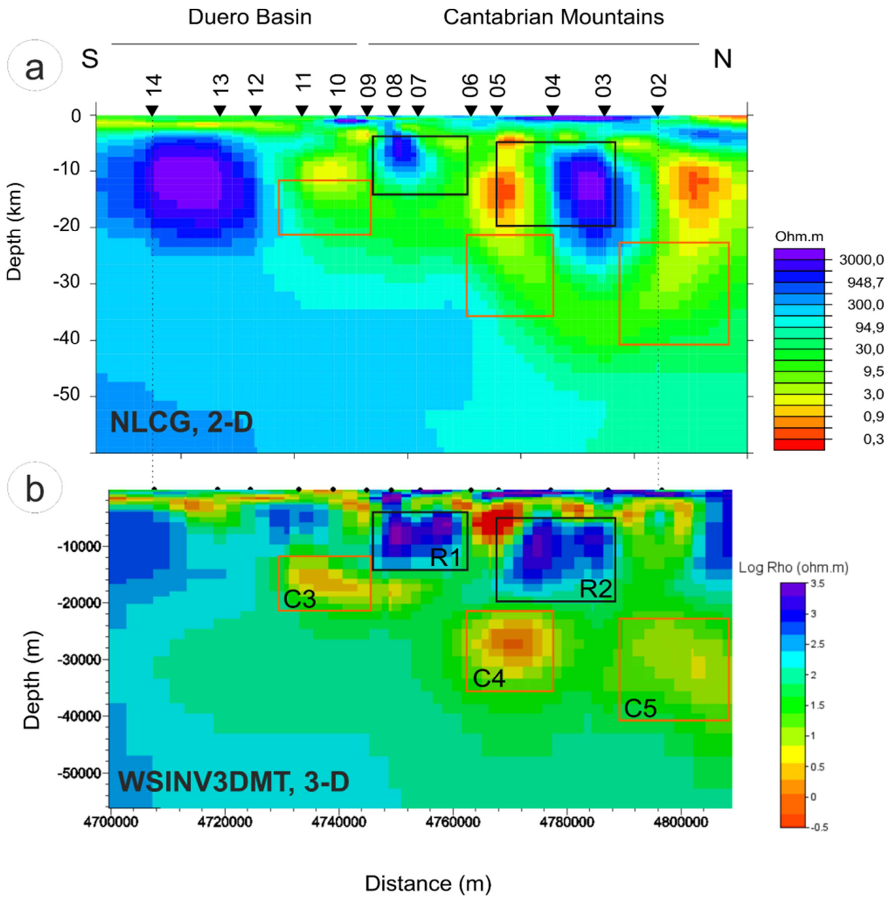

Figure 4-27: Top: 2-D inverse model. Bottom: 3-D inverse model.

4.5.8 Model interpretation

Figure 4-28 shows the N10ºE cross section of the 3-D inverse model. The geological model of the Cantabrian Mountains from Gallastegui (2000), based on the seismic results is superimposed to the MT model. The geological map of the area is also shown. This integrated image allows to see correlations between geological structures observed on surface, their continuation at depth according to the seismic interpretation and their geoelectrical signature.

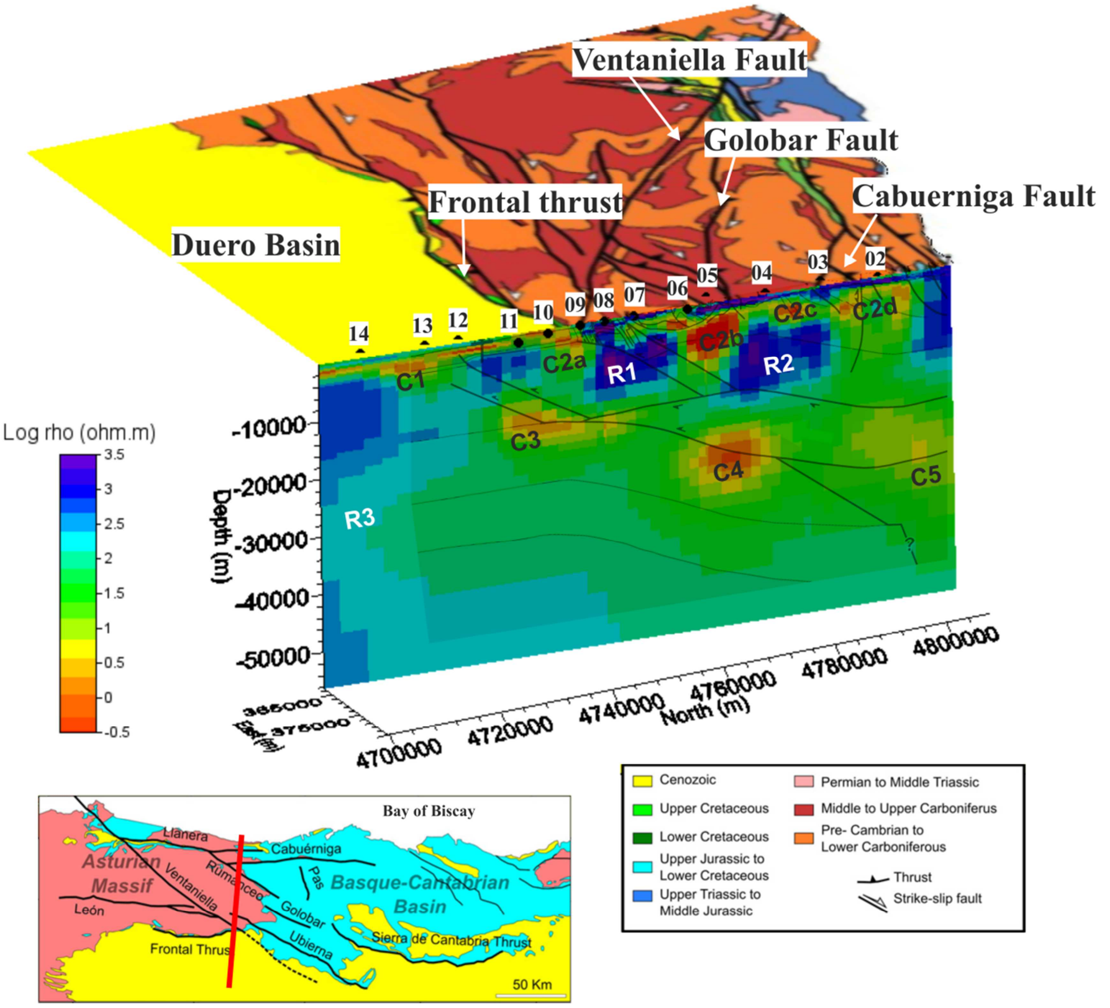

Figure 4-28: Top: Cross section across the 3-D model. Geological map from Tavani et al. (2012), and geological interpretation from Gallastegui (2000). Bottom: Geological legend and tectonic map of the area (Tavani et al., 2012). Red line corresponds to the 3-D cross section on the top of the figure.

4.5.8.1 Duero Basin sediments (C1)

This shallow conductive anomaly is located in the southern part of the profile, below sites 14 to 10 (Figure 4-29). This anomaly is observed on surface, having thicknesses ranging from 3500m beneath site 13 to 2500 m beneath sites12 and 11. Resistivity values between 2 and 30 Ωm define this feature. This conductive anomaly overlies the resistive body R3.

MT sites 14 to 10 are located on the Duero Basin. The Duero Basin is constituted by Tertiary sediments with variable thicknesses deposited upon the Palaeozoic Basement. The conductive anomaly is the signature of these sediments. Porous, permeable and water saturated rocks are responsible for the high electrical conductivity of these formations. In comparison, the unaltered Palaeozoic basement lying below is highly resistive because of its low porosity and thus very low water content. Sediments thickness inferred from the MT image varies, having a maximum thickness of 3500 m thick beneath site 13 and 2500 m beneath site 11. "El Campillo" exploration well, located 5 km west of the MT sites reaches the basement 2584 m below the surface (Lanaja, 1987). The depth-to-basement at well location is well estimated by the electrical resistivity image, the resistivity transition being estimated around 60 Ωm (Figure 4-29). The higher sediment thickness beneath site 13, is related to a local depocenter located in the footwall of a north dipping Alpine thrust (El Campillo thrust), which merges in depth with the horizontal conductor C3. The presence of this fault can be inferred from the MT model, although its signature is not very conductive beneath the MT sites. This thrust is detected by the seismic reflection, and is shown in Gallastegui geological model (Figure 4-16) Gallastegui, 2000).

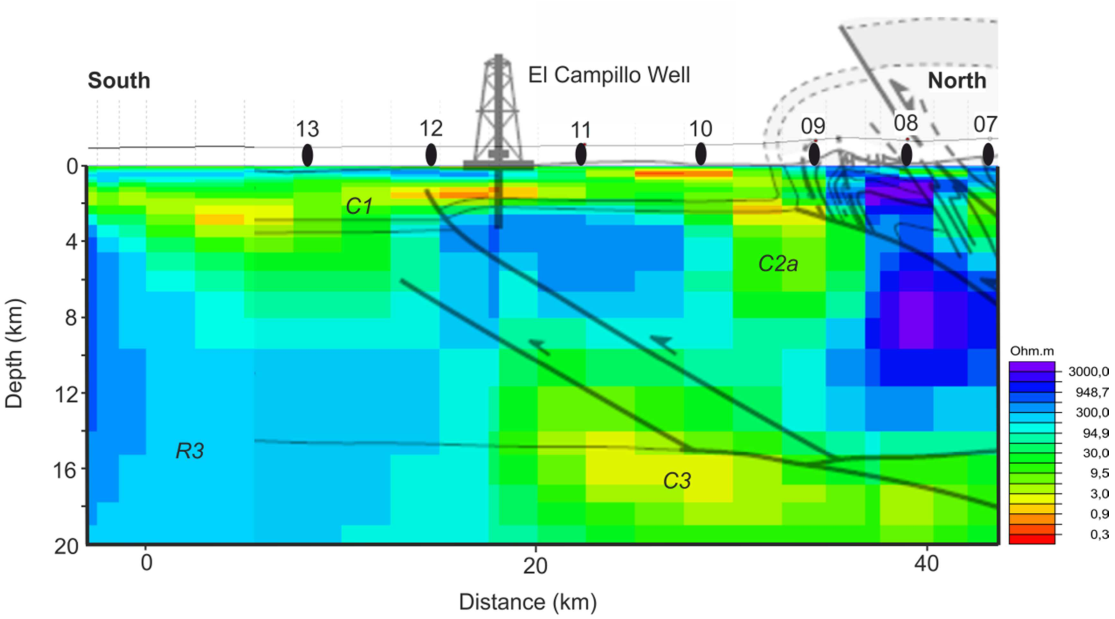

Figure 4-29: Cross section extracted from the final 3-D model. The "El Campillo" well is shown, along with the geological interpretation of Gallastegui, 2000 (black lines). Anomalies C1, C2a, C3 and R3 are labelled.

4.5.8.2 Conductive feature C2a: Estafaniense formation

This feature is depicted as a conductor reaching 6 km depth (Figure 4-28 and Figure 4-29). It is located at the intersection between the frontal thrust and the Venteniella fault. Even if fluids into the faulted area could be invoked, the presence of the Estefaniense formation, which is discordant onto the Variscan basement, could be responsible for this conductive anomaly. The Estefaniense formation has a high porosity and permeability, and contains carbon (Pulgar et al., 1999). According to the MT model this formation would reach more than 6 km depth, what is in accordance with the geological models presented more to the west in Pulgar et al. (1999; Figure 3, cross sections I-I’ and II-II’).

4.5.8.3 Major Alpine structures (C2b/C2c/C2d/R1/R2)

The interpreted conductive anomalies discussed below (C2b, C2c and C2d) are located in the upper crust, and their conductive behavior is due to presence of fluids in the fractured areas of the Palaeozoic basement.

Conductive feature C2b

This conductive anomaly is well marked and is oriented E-W to NE-SW. At depth this anomaly reaches 8 km. This anomaly is interpreted as the signature of the several faults with different orientation located in that area (Figure 4-15).

Conductive feature C2c

The C2c conductor dips north until a depth of 5 km, being consistent with the trace of minor north dipping thrusts located between the Golobar and Cabuerniga faults (Figure 4-28).

Conductive feature C2d

This anomaly is subvertical, reaching a depth of 15 km beneath the trace in surface of the Cabuerniga fault.

Resistive features R1 and R2

The R1 resistive anomaly is located NE of the Ventaniella transpressive fault, and is oriented NW-SE (Figure 4-28 and Figure 4-22). It reaches a maximum depth of 13 km. The resistive feature R2 reaches a maximum depth of 16 km and is roughly oriented E-W (Figure 4-22, slice 24). It is limitated by the Golobar fault to the SW and by the Cabuerniga fault to the north. They correspond to areas of the Palaeozoic basement not affected by the Tertiary contraction, being located between major Alpine/Mesozoic thrusts.

4.5.8.4 Conductor C3

The connection of this subhorizontal conductor with the Alpine faults (El Campillo thrust) (Figure 4-29) suggests that that its conductivity is due to infiltrated fluids of the Duero Basin that reach the base of the superior Iberian crust at 15-16 km depth.

4.5.8.5 Conductor C4

This high conductive feature is oriented roughly E-W (Figure 4-22, slice 32) and is approximately coincident with the tip of the mantle wedge of the Cantabrian Margin, on top of the subducting Iberian crust. Pedreira et al. (2015) have interpreted anomalous seismic velocities as a consequence of mantle wedge hydration. The presence of a conductive feature C4 at the same location supports this hypothesis.

4.5.8.6 Conductor C5

This deep conductor has low resistivities and is located between 20 and 30 km depth. This anomaly is located at the transition between the Cantabrian Margin lower crust and the Cantabrian Margin mantle. Pedreira et al. (2015) interpret that the mantle is still hydrated at this position. Conductor C5, which is practically connected with the above conductor C4 (Figure 4-28), would be the conductivity signature of this mantle hydration. The water required to hydrate/serpentinize the mantle wedge and the upper mantle would have been percolated from the seafloor during the formation of the Margin in the Mesozoic (Pedreira et al., 2015). Electrical conductivity of serpentinized rocks is 3-4 orders of magnitude higher than common upper mantle rocks (peridotites). The enhanced conduction is due to an increase of the porosity (Stesky and Brace, 1973). Enhanced conductivity due to serpentinization has been reported, e.g. in the Costa Rican subduction zone (Worzewski et al., 2010).

4.5.8.7 Iberian subducted crust (R3)

This anomaly dips north following the shape of the Iberian subducting crust.

4.5.9 Conclusions

Thirteen magnetotelluric soundings of broad-band and long period were acquired along an N-S profile crossing the Cantabrian Mountains and the Duero Basin. Main conclusions of this study are:

- A 3-D resistivity model was obtained from a 3-D joint inversion of the full impedance tensor and the magnetic transfer functions.

- The correlation between the geoelectric image, the existing geophysical models and the surface geology provided a deeper understanding of the lithospherical processes.
- The Duero Basin sediments are clearly imaged, the resistivity image being consistent with the well data.
- Conductive zones in the Palaeozoic basement are related to enhanced permeability along the main Alpine faults. These conductive zones detected in the model do not reach more than 10 km in the southern part of the Cantabrian Mountains and 15 km in the northern part, and are therefore concentrated in the upper crust.
- The hydration/serpentinization of the upper mantle within the mantle wedge and beneath the Moho of the Cantabrian Margin is imaged as a zone of low resistivities.

5 Crustal structure of an intraplate thrust belt: the Iberian Chain

5.1 Magnetotelluric data

5.1.1 Data acquisition and processing

The MT data acquired consists of 37 broad-band magnetotelluric sites along two NE-SW profiles crossing the tectonic structures and the main geological units of the Iberian Chain (Figure 5-1).

These data were acquired during three campaigns between 2011 and 2013 in the framework of the TOPOIBERIA project. Space between MT sites along the two profiles is approximately 5 to 7 km. The five components were measured at all sites: two horizontal electric and magnetic field components recorded in N-S (x axis) and E-W (y axis) directions and the vertical magnetic field component. Acquisition system used was the ADU-07 (Metronix Geophysics).

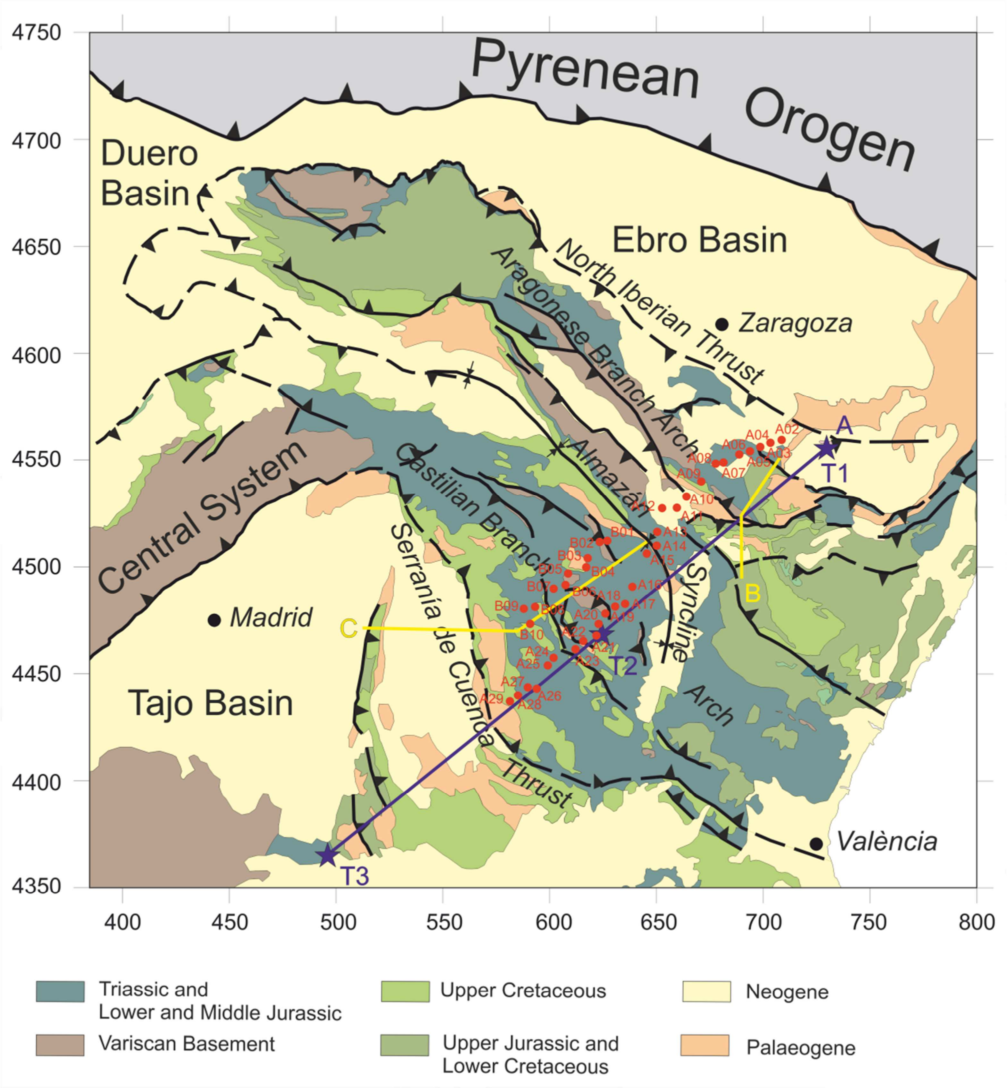

Figure 5-1: Simplified geological map of the Iberian Chain and surrounding Tertiary basins (modified after Guimerà, 2004, 2013). A: seismic line (Figure 2-16); B and C: geological cross sections of Figure 2-15. Magnetotelluric sites (red dots), seismic shots (blue stars) and the major geological units are shown. UTM coordinates (30T, ED50) are also shown in km.

Recording time was between 24 h and 48 hours at each site, and the transfer functions obtained have periods that range from 0.001s to 1000s. The estimates of the MT impedance and the geomagnetic transfer functions were obtained using a standard robust processing method (Egbert and Booker, 1986).

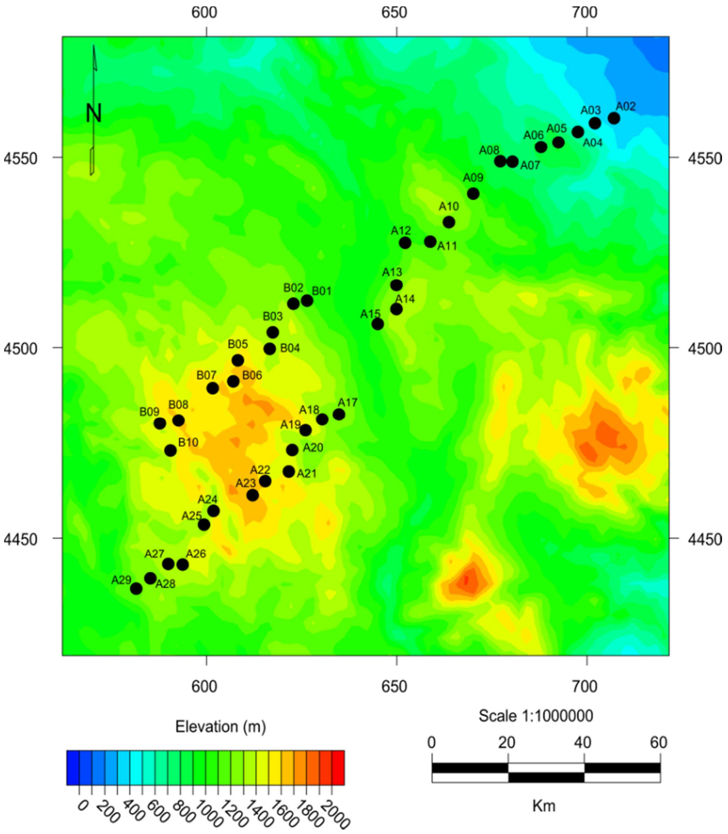

Figure 5-2: Elevation map. Magnetotelluric sites (black dots). UTM coordinates in km.

After data processing, the data was edited to remove noisy behaviours prior to the dimensionality analysis. In spite of the good quality of the data, we noticed some distortions of the impedance tensor at some sites, which are typical of near field effects, as characterized by Junge (1994) (see Chapter 3.6).

5.1.2 Data analysis

The majority of sites have good quality data between 0.001s and 1000 s. Appendix 2 shows the apparent resistivity and phases for all the sites. Consistency between apparent resistivity and phases was checked using the D+ algorithm (Parker and Booker, 1986). Figure 5-3 shows the apparent resistivity and phase at four representative sites over the survey area, along with the smoothed curve obtained using the D+ algorithm. Apparent resistivity and phases are generally consistent across the whole survey.

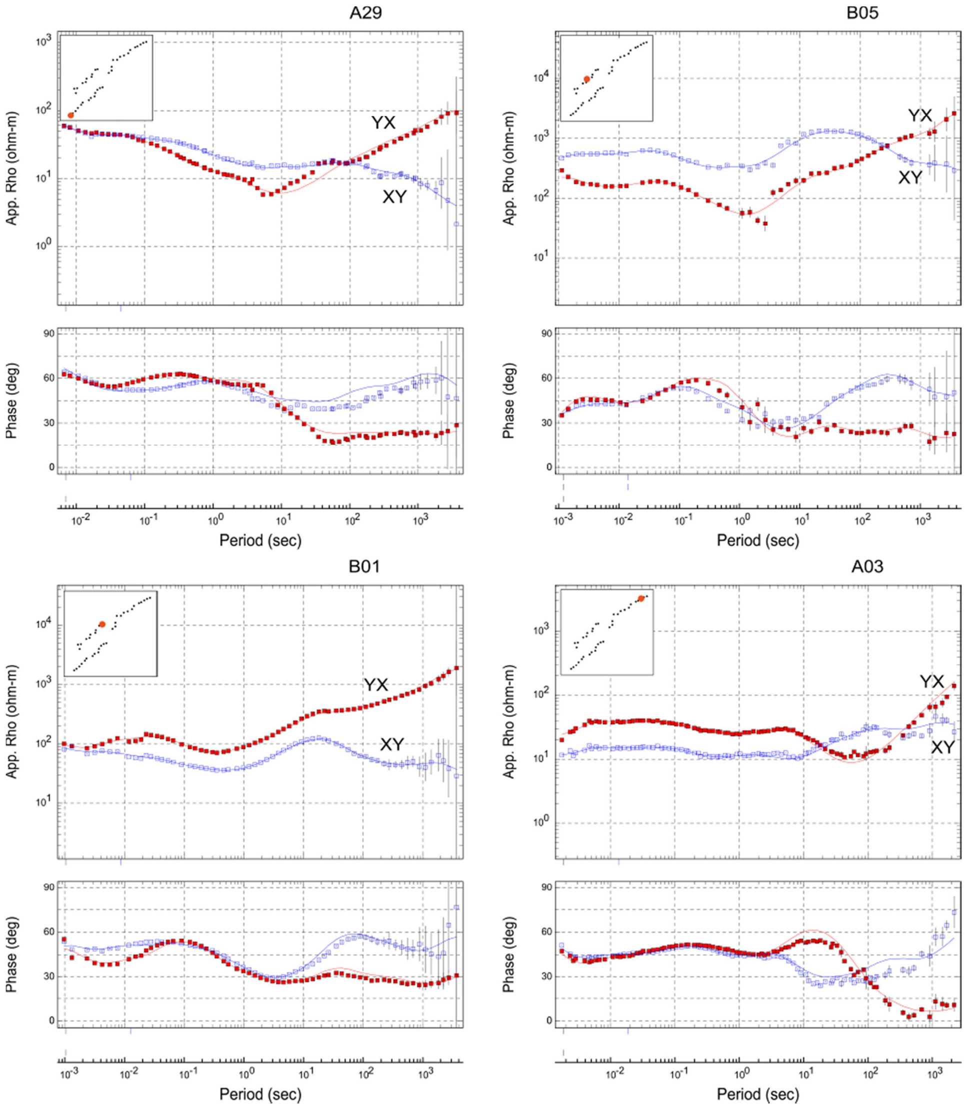

Figure 5-3: Apparent resistivity, phases and D+ smoothed curves for four representative sites. Data rotation: N40°E. Blue points: XY component. Red points: YX component. Location of each site is represented by a red dot on the MT sites map on the top left corner of each plot.

The data shown in Figure 5-3 and Figure 5-4 have been rotated to a direction of N40ºE. This rotation has been made in base of the dimensionality analysis that will be carried out in section 5.1.3.

As indicated by the curves shown in Figure 5-3 and the apparent resistivity maps shown in Figure 5-4, the YX component generally tends to resistive values at long periods, indicating clearly a resistive crust. On the SW and NE part of the survey (sites A29 and A03 respectively), the YX component tends to lower resistive values. Depending on the location of each site respect to the geological settings, some characteristics of the data can be outlined. For example, site A03, located in Neogene sediments, has conductive values at high frequencies (around 10 Ωm at 1000 Hz). Splitting of the two modes at 10 s suggests the presence of multi-dimensional structures at depth. Site B05, located upon Palaeozoic outcrops, exhibits resistive behaviour at high frequencies. At longer periods (around 10 s) multidimensional behaviour is indicated by the split of both polarizations.

In Figure 5-4 the orientation of the anomalies and the different behaviour of the XY and YX components when the period increases suggests a multidimensional behaviour of the impedance tensor as confirmed by the dimensionality analysis carried out in section 5.1.3.

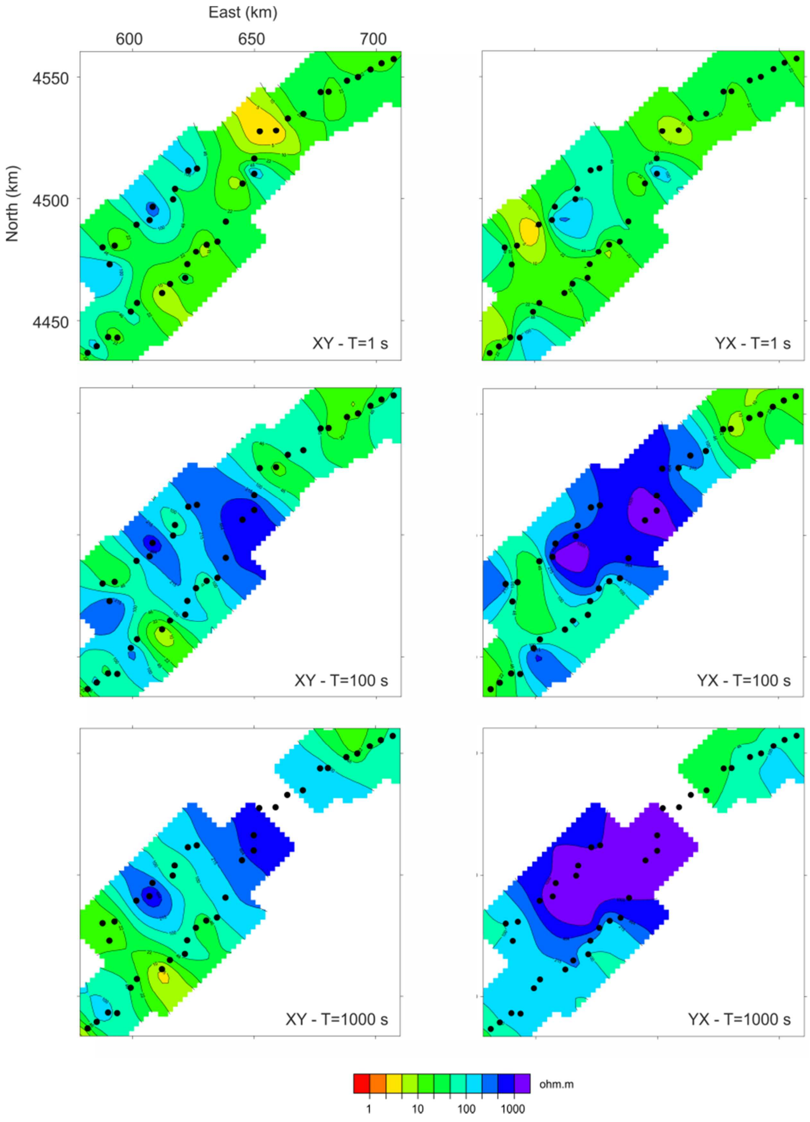

Figure 5-4: Apparent resistivity maps for three selected periods, T=1 s, T=100s and T=1000s. XY (left) and YX (right) components for a rotation of N40ºN.

5.1.3 Dimensionality analysis and induction vectors

The dimensionality for the two profiles was studied using two approaches: (1) the multi-site/multiperiod analysis (McNeice and Jones, 2001) based on the Groom and Bailey (1989) tensor decomposition and (2) the phase tensor analysis (Caldwell et al., 2004).

Following the multisite/multiperiod analysis, the strike direction was calculated in a period range for all sites by minimizing the global χ^2 misfit between experimental and theoretical Groom-Bailey impedance tensor. For the analysis of both profiles an error floor of 13% had to be applied to the data in order to obtain a χ^2 error within the 95% confidence interval for a period range of 1-1000s. A strike direction of N130° for the profile A and N125° for the profile B were obtained. The necessary high error floor was a consequence of: 1- some of the sites were still affected by noise although the suspicious data were removed prior to this analysis; 2- clear 3-D effects in a number of sites.

The phase tensor is defined by the relation $\varphi = X^{-1} Y$, between the real (X) and imaginary (Y) part of the impedance tensor, respectively. As any second rank tensor, the phase tensor can be represented graphically as an ellipse, which is defined by three invariants of the phase tensor: the principal axes φ_{max}, φ_{min}, showing the maximum and minimum phase difference between the magnetic and electric fields and a third coordinate invariant parameter $|\beta|$ (the *skew* angle) that represents the asymmetry of the phase response. The skew angle $|\beta|$ provides a measure of the significance of 3-D effects in the MT phase response. Figure 5-5 shows the phase tensor ellipses of the observed data as pseudosections for both profiles.

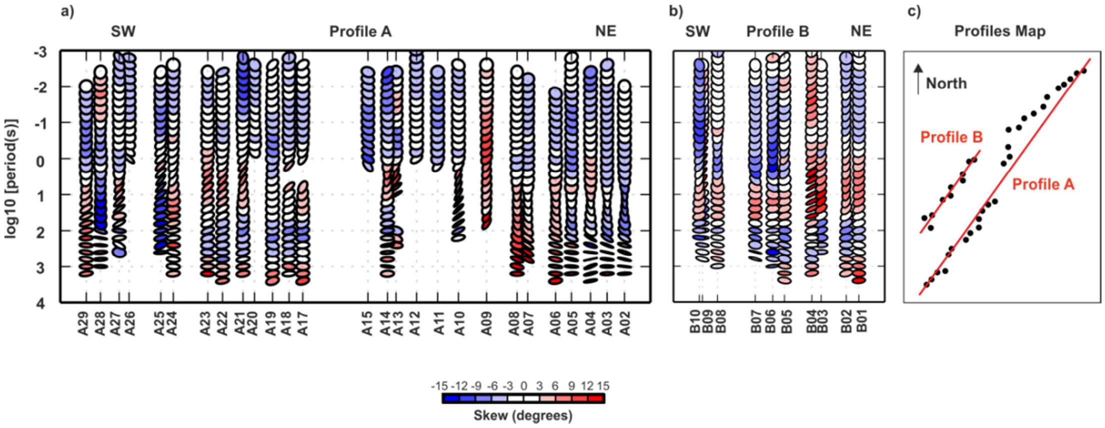

Figure 5-5: Phase tensor ellipses of the observed data. The ellipses are normalized by φ_{max} and filled with the skew angle β. The ellipses are plotted so that the vertical axis is N40°E oriented. a) Phase tensor ellipses of the observed data for profile A. b) Phase tensor ellipses of the observed data for profile B. c) Location of two profiles, black dots are the MT sites.

They were drawn using the MTpy python toolbox (Krieger and Peacock, 2014). The colour used to fill the ellipses shows that low $|\beta|$ values (< 6°) are generally present at high frequencies (<1 s) but increases at long periods, and at sites/areas where data quality is lower. Some sites present great $|\beta|$ values (> 10°) at high frequencies. The criterion for which the data are considered to be affected by 3-D structures is reached when $|\beta| > 3°$ (Caldwell et al., 2004). This complex behaviour suggests a regional multidimensional character.

Induction arrows, that represent the ratio between vertical and horizontal magnetic fields, can be used to infer lateral conductivity variations. In a 2-D case, the induction arrows should be perpendicular to the geoelectric strike. We show the real induction arrows in the Wiese convention (pointing away from the conductor). At long periods (100 s and 1000 s) the vectors in the southern part of the profile point to a NW-SE direction which is parallel to the supposed strike direction. This is an indication of off-profile conductivity variations that could not be considered using a 2-D inversion scheme. The presence of the Mediterranean Sea to the SE of the profile, at a distance between 90 km and 130 km from the sites, was tested through 3-D forward modelling (see section 5.1.4.1) and resulted not to be responsible for the behaviour affecting the inductions arrows, i.e. arrows pointing to the NW with high magnitudes.

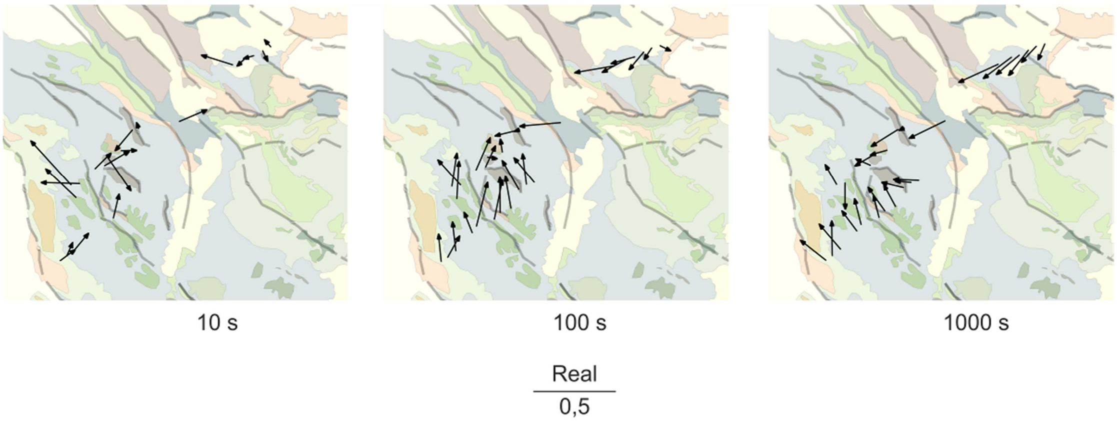

Figure 5-6: Real induction vectors for 3 selected periods (Wiese convention) superimposed to the geological map (same legend as figure 5-1).

In conclusion, the dimensionality analysis carried out shows that both profiles present 3-D effects. In this context the 3-D inversion of the data was thought to be more suitable, in order to accurately model 3-D effects that could bias a 2-D inversion of the profiles. Accordingly, we proceed with 3-D inversion of the whole dataset.

5.1.4 3-D Magnetotelluric inversion

The 3-D inversion was carried out using the 3-D non-linear conjugate gradient (NLCG) algorithm (Rodi and Mackie, 2001, 2012). The algorithm minimizes the misfit between observed and computed data using a regularization operator to produce a smoothly varying resistivity volume.

5.1.4.1 Starting model description

We performed first several forward modelling tests in order to optimize the starting model and the mesh used in the inversion. The influence of the topography and the Mediterranean Sea to the SE were tested. The effect of the sea consists in a small split of both polarizations for the phases at long periods (around 1000 s) and small real induction arrows pointing to the NW (see Figure 5-7). Accordingly, it can be concluded that the Mediterranean Sea is not responsible for the behaviour of the observed real induction arrows, Although responses also point to the NW, the observed data have a much higher amplitude and only for the sites located in the southern part of the survey area point to the NW (Figure 5-6 and Figure 5-7).

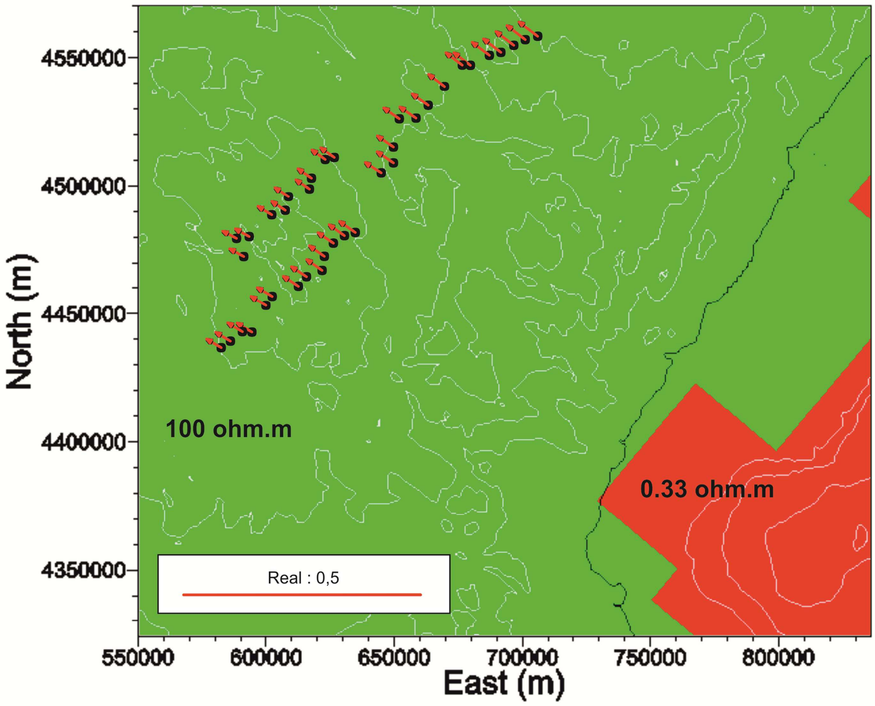

Figure 5-7: Real Induction arrows at 1000 s (Wiese convention: pointing away from conductive areas) for the homogeneous starting model (100 Ωm) including the Mediterranean Sea to the south east. Contour lines represent the topography every 400 m.

The mesh was rotated to N40°E in order to align with the profiles, to reduce the cells number of the mesh and to align it more closely to the strike of the Iberian Chain. The data were accordingly reproduced for a co-ordinate system with the x-axis oriented in direction N40°E.

The cell size in the central part of the mesh has horizontal dimensions of 2000 m x 2000 m and a thickness of 100 m in the superficial area to define the topography. The mesh was designed in order to have 1-3 cells between neighbouring sites. Outside of the central area, the mesh extends long enough laterally and in depth to respect the boundary and continuity conditions. The mesh has a dimension of 1324 km x 717 km x 742 km in the *x*, *y* and *z* directions respectively (as mentioned before, the mesh was rotated so that the *x* direction is oriented N40°E). The total number of cells of the mesh is 483,084 cells (126x54x71).

The starting model of the inversion was a homogeneous model of 100 Ωm that includes topography and the Mediterranean Sea to the East defined by a resistivity value of 0.33 Ωm. The sea was kept fixed during the inversion. The full impedance tensor (all four complex components) and the magnetic transfer function tensor with sixteen frequencies between 0.01 s and 1000 s were used in the 3D inversion.

5.1.4.2 Inversion parameters

Several inversions were carried out with different error floors and regularizers. Small error bars in the data and exclusion of the data affected by noise allowed us to set low error floors, without provoking data overfitting or noise fitting. Rotating the data to N40ºE we noticed that the YX component was to some extent more affected by error propagation than the XY component, accordingly, we decided to give it a slightly higher error floor. Thus the final model was obtained using error floors of 2% for the Z_{xy} component of the impedance tensor and 3% for the Z_{yx} component. For the magnitude of the diagonal elements of the impedance tensor an error floor of 10% was used and for the magnetic transfer function tensor the absolute error floor was 0.05.

5.1.4.3 Inversion results

The last inversion was started using a Lagrange multiplier tau equal to 0.1. In a second step we followed with the inversion reducing tau to 0.05. Reducing the Lagrange multiplier permitted to improve the data fit in the final iterations. Several inversions with different tau values were tested, and this workflow resulted to be the one that was giving the best RMS obtaining a smooth model that was geologically plausible. The inversion using a tau equal to 0.1 converged after 52 iterations. In the second step using a Lagrange multiplier equal to 0.05 the convergence occurred after 13 more iterations. In total after 65 iterations the inversion reached a RMS of 1.88.

All sites present a good RMS, without having any region poorly fitted. Figure 5-8 shows separately the RMS maps of the final inversion for the impedance and vertical transfer function (VTF). The impedance tensor Z is well fitted, with the exception of some sites at long period (site B09 in Figure 5-10, which has a total RMS of 2.68). The tipper data generally shows a very low RMS values, close to 1.

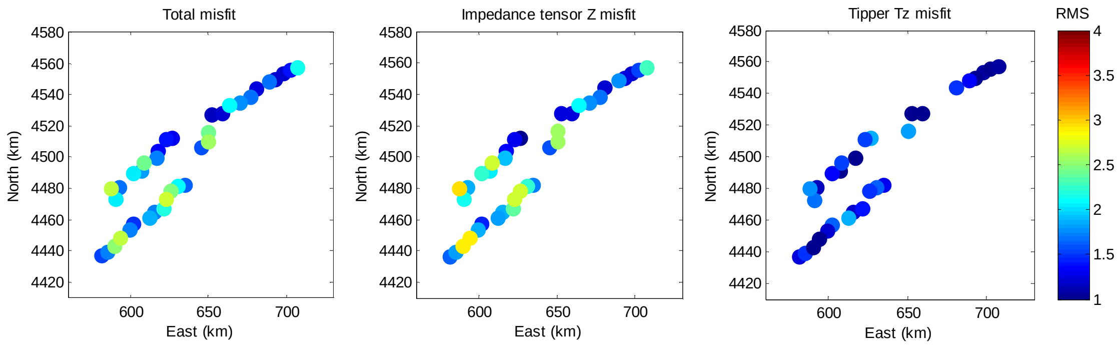

Figure 5-8: RMS values for each site. Left: Total misfit. Centre: Misfit of the impedance tensor Z. Right: Misfit of the magnetic vertical transfer function.

The mesh discretization and the strength of smoothness constraints used during the inversion allowed to obtain a resistivity distribution in the shallow part of the model that was able to fit well the data, having no shift between apparent resistivity responses and the data.

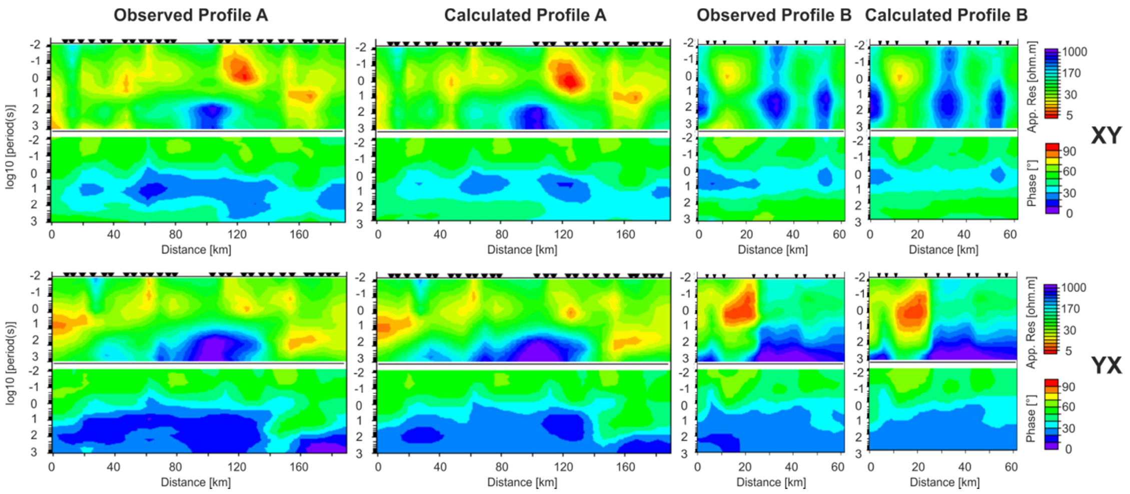

Figure 5-9: Pseudosections (data and responses of the 3-D inverse model) of the off diagonal components along the two profiles A and B shown in Figure 5-5c.

Figure 5-9 shows the data and model responses pseudosections of the off-diagonal components along two profiles A and B grouping the sites (Figure 5-5c). It can be seen that the main characteristics of the data are reproduced by the model, for both polarizations. In Figure 5-10 we show the fitting of four sites, showing both the diagonal and the off-diagonal components of the impedance tensor. In appendix 2 all the observed data along with the responses of the 3-D model are shown. All the components of the impedance tensor are well fitted, with the exception of the diagonal components at high frequencies. The data have values in general lower than the off-diagonal elements, but not as low as the responses. In general phases of the diagonal elements show a good fitting.

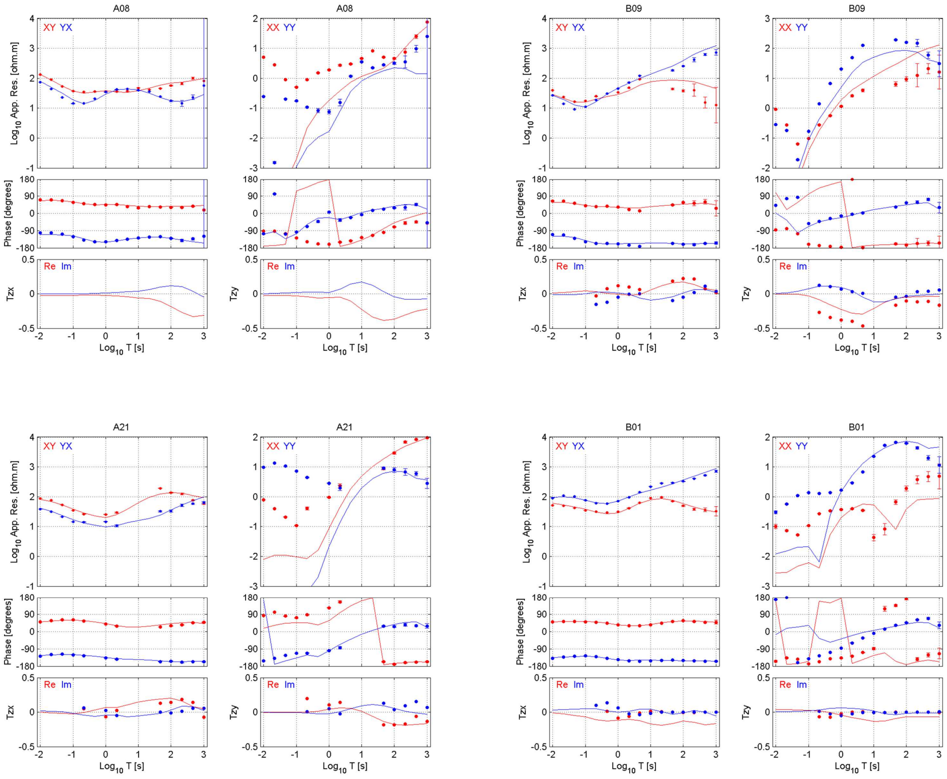

Figure 5-10: The four components of the impedance tensor at four selected MT sites. Data (points) and 3-D model responses (continuous line). The components are rotated to N40°E (see text for explanation). RMS values: A08=1.70; A21=2.40; B01=1.29; B10=2.17.

The calculated induction arrows (Figure 5-11) fit the behaviour of the magnetic transfer function, especially the deflection of the induction arrows from the profile lines in the southern part of the profiles.

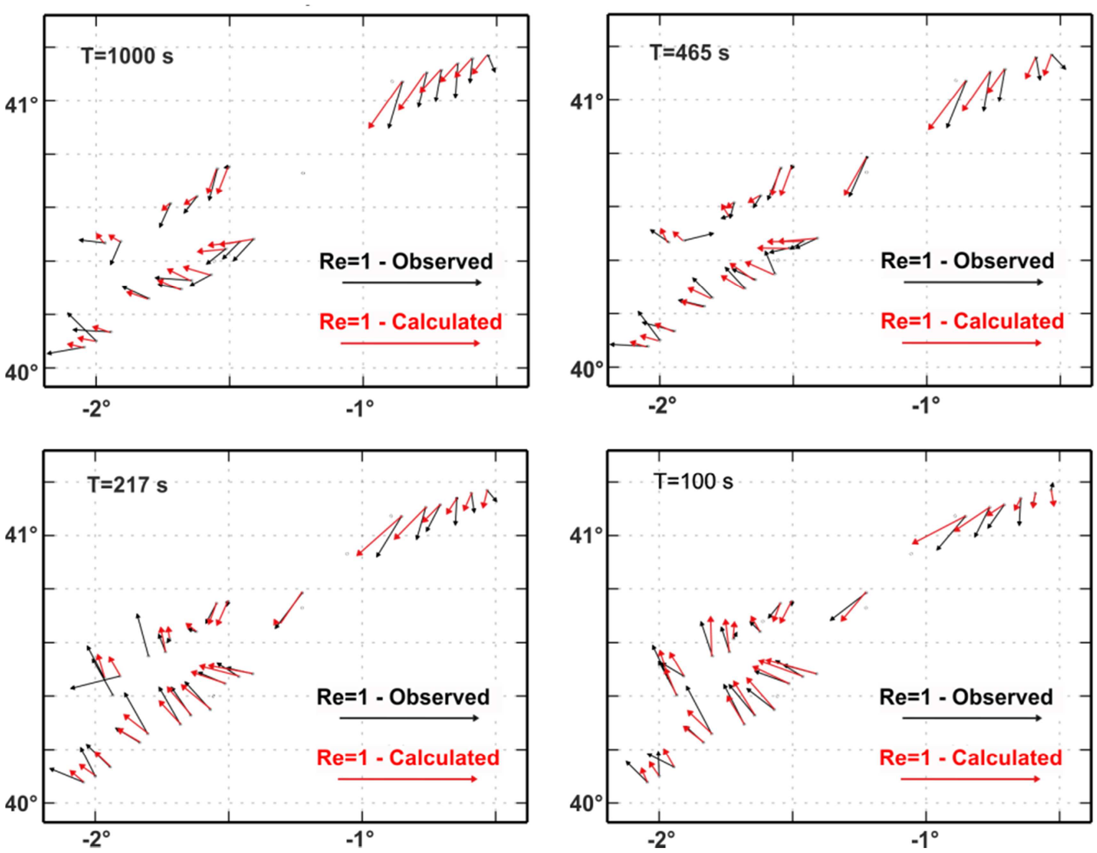

Figure 5-11: Real induction arrows for 4 selected periods (Wiese convention). Data (black) and responses of the 3-D inverse model (red).

5.1.5 3-D resistivity model

The 3-D inverse model is shown in Figure 5-12 and Figure 5-13. Figure 5-12 shows depth slices at selected depths, superimposed with the tectonic structures observed in surface. In Figure 5-13 cross sections from the 3-D mesh, oriented NW-SE (X sections) and NE-SW (Y sections), are shown along with their location on the geological map of the area. In the first kilometres depth, several conductors and resistors coincide with geological features such as Tertiary basins (low resistivities), Palaeozoic basement outcrops (high resistivities) and known fault zones (elongated conductors). At greater depths, from SW to NE, the model is divided into three zones. Horizontally, from 0 to 50 km, beneath de Serranía de Cuenca Thrust, the mid-lower crust is moderately conductive (less than 100 Ωm). The central zone, from 50 to 150 km, the middle-lower crust is homogeneous and highly resistive (higher than 1000 Ωm) and in the northern zone, from 150 km to the NE edge, beneath the Aragonese Branch Arc and the North Iberian Thrust, the crust is moderately conductive (less than 100 Ωm). The causes usually invoked for the high conductivity at mid-lower crust are the presence of aqueous fluids, partial melting and conductive mineralization. In the Iberian Chain no evidences for other causes than fluids occur. Therefore, the homogeneously high resistive mid-lower crust in the central zone reveals low porosities and no fluids circulation. By contrast in the northeast and in the southwest zones the main faults (the North Iberian thrust in the NE and the Serranía de Cuenca Thrust in the SW) are characterized by moderately conductive areas where fluid circulation probably occurs. These faults dominate the structure of the Iberian Chain and reach depths between 8 and 15 km.

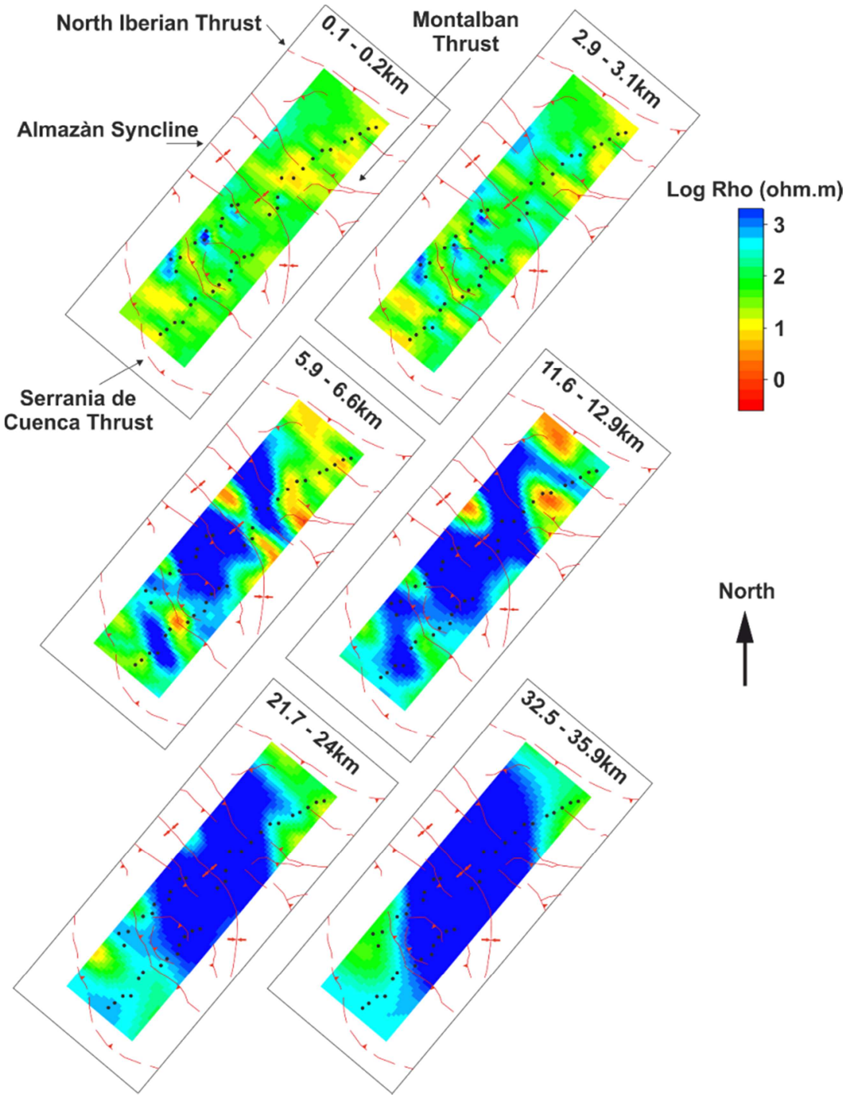

Figure 5-12: Depth slices of the 3-D model at different depths. Superimposed in red are the main faults and structures observed in surface. Black points are the MT sites.

Depth slices at selected depths shown in Figure 5-12 show a good agreement between the orientation of the geological structures and the electrical anomalies (full geological map in Figure 5-1). In the SW part of the model the faults are mainly oriented NNW-SSE, while the NE part of the model is characterized by NW-SE oriented structures. This behaviour is confirmed by the MT model where the main anomalies follow faithfully these orientations. This suggests a slightly change in the dominant direction from north to south, which was recovered through the 3-D inversion.

Main conductive features identified in the cross sections (Figure 5-13) are indicated by letters and correlated to the geological structures present in surface (Figure 5-13).

- A is a mid-crustal conductor located at 25km depth, which fades towards the SE.
- B is an upper crustal conductor dipping southwestwards and reaching a depth of 10 km, as shown in the Y16 to Y35 cross sections. It correlates with the southwest dipping thrust fault located above sections Y35, Y32 and Y29, the latter coinciding with a change in the thrust orientation as it appears on the surface over section Y22.
- C is a shallow conductive anomaly present in all the Y sections reaching 6 km depth. This conductor correlates with the core of the Almazán Syncline (see also Figure 5-12).
- D has been subdivided into two different conductors, D1 and D2. Conductor D1, located in section Y29, dips southwestwards reaching 10 km depth and correlates well with the southwestwards dipping thrust observed on surface. More to the east, on sections Y32 and Y35, this conductor changes and dips northeastwards (conductor D1) coinciding with the dipping of the thrust observed on surface which dips northeastwards (Montalbán thrust) in this eastern part of the geological map (Figure 5-13). This D2 conductor reaches a depth of 10 km. Section X89, located in the north part of the model, shows that the set of both conductors (D1-D2) is also extending (dipping) eastwards, revealing a complex 3-D behaviour of the volume with fluid content related to the complex system faults in this area. Note in Figure 5-1over sites A9 to A12 there is a convergence of a number of thrusts dipping in different directions.
- Conductor E, in the north-eastern part of the model, is visible in sections Y29 to Y35. It dips southwestwards reaching a depth of 10 km probably being the signature at depth of the North Iberian thrust, located north of the studied area (Figure 5-13). The mid crustal conductor F located at 15-20 km depth is present in section Y35. This conductor merges with the northeastwards dipping conductor D2 and the southwestwards dipping conductor E suggesting the branching of the Montalbán thrust to the North Iberian Thrust.

Several others resistive and conductive features correlate with the surface geology (Figure 5-13). The Palaeozoic outcrops (Variscan basement) observed in the geological map are characterized by shallow resistive bodies. Their outcropping is generally a consequence of thrusts, dipping north or south. The Neogene sediments are characterized by shallow conductive bodies. The correlation between the surface geology and the MT conductive/resistive features gives us confidence on the reliability of the anomalies and their structures at depth, allowing us to interpret the shape and extension of the faults in the crust.

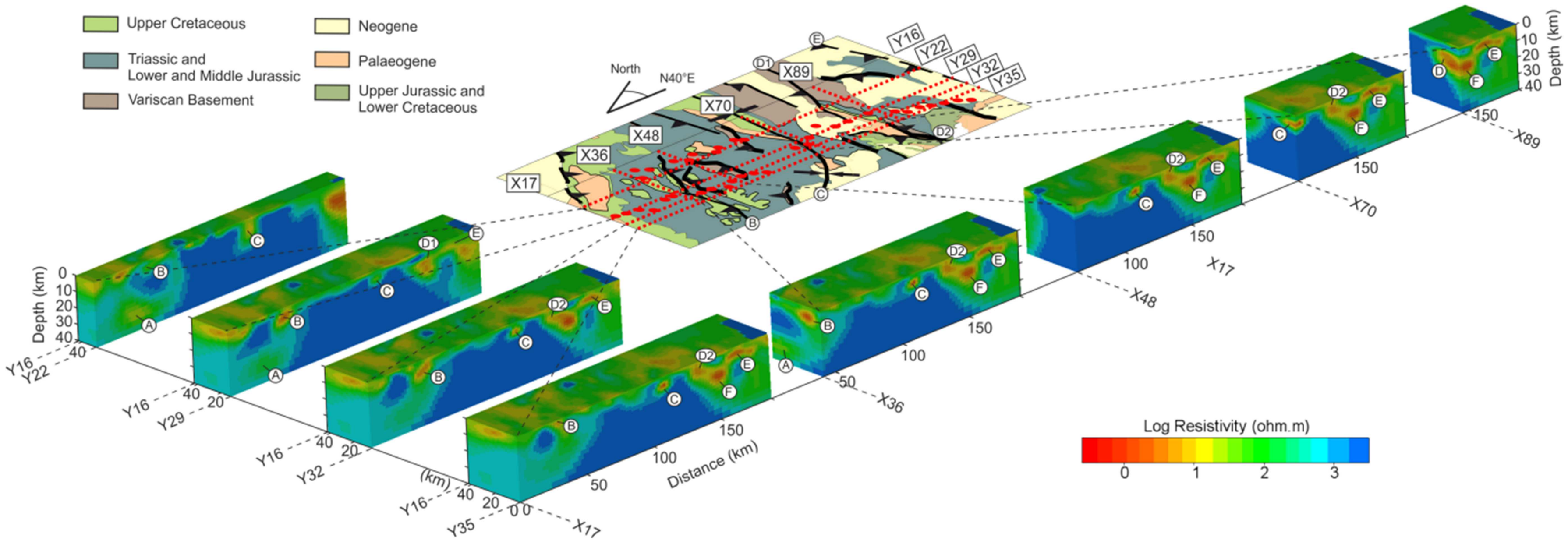

Figure 5-13: 3-D resistivity model: Y are NE-SW sections and X are NW-SE sections. Dashed lines link the corner of each section to its position on the geological map. Red dots are the MT sites, letters indicate the main conductors.

5.1.6 Sensitivity tests

Inversion of the full impedance tensor jointly with the magnetic transfer function constrains the model at shallow and intermediate depths. Using small error floors and having reached a very good fitting for all the sites give us confidence on the sensitivity of the data to the features found in the deeper parts of the model. However, the main features presented at depth need to be tested, in order to conclude that our data are sensitive to those structures, and that they are not due to artefact of the inversion process or to data noise fitting. Testing the sensitivity of the structures was done removing separately the conductors appearing in the model and substituting them by resistivity values surrounding the conductors. To account for their presence we ran the forward modelling and compared the responses.

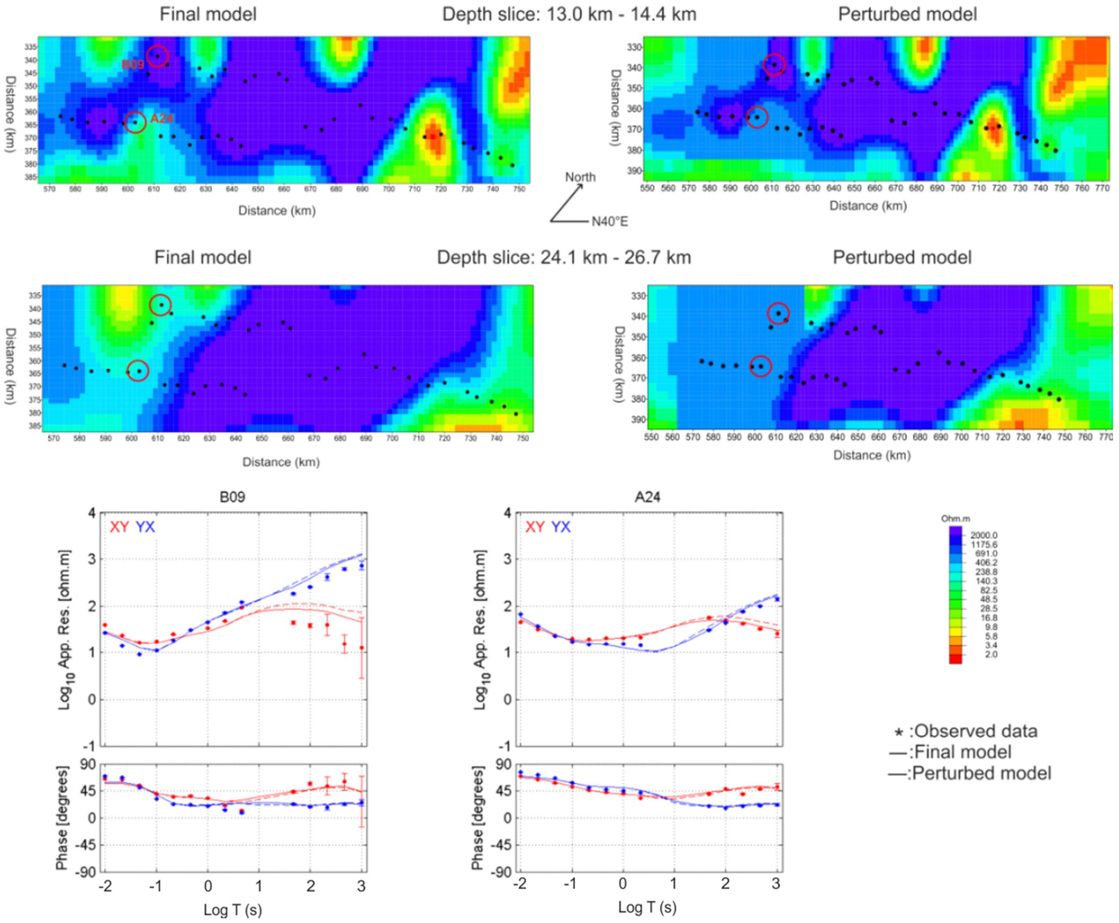

Figure 5-14: Sensitivity test to determine the robustness of the conductor A. Top: 2 depth slices of the 3-D final model (left) and the perturbed model (right). Bottom: Responses of the final model (solid lines) compared with the perturbed model (dashed lines), for sites B09 and A24.

Here we show the test carried out to check the robustness of conductor A (Figure 5-14), which given its location at deeper part of the model and the resistivity contrast with the surrounding areas is the most relevant to show. From 13 km depth until a depth of 40 km this conductor located in the SW part of the model was changed by resistivity values of 500 Ωm. Responses of the perturbed model are slightly changed respect to the original model. However, the change in the responses is too small to consider that this conductor is required by the data. Then the conductor A located at a depth of 25 km is not well resolved given that it is located beneath a shallow conductor (the one at 8-10 km depth), it is located out of the profile area and it presents an average resistivity of 100 Ωm in front of 1000Ωm of the surrounding areas.

The others tests carried out allow us to conclude that: 1- the model loses resolution beneath a depth of 30 km; 2- all the other features at middle shallow depths are well resolved.

5.2 Discussion

5.2.1 Interpretation of the integrated model at crustal scale

The magnetotelluric method provides the electrical conductivity distribution at depth. The 3-D MT inversion images the subsurface from shallow to middle-lower crust, taking into account the sensitivity test and the period range used. The orientation and depth of the main faults imaged are consistent with the geological structures observed at surface.

After the resistivity model, the Mesozoic and Cenozoic cover (e.g., the Calatayud-Montalbán Tertiary basin, with resistivity values from 1 to 50 Ωm) can be distinguished from the Variscan Basement (with resistivity greater than 200 Ωm). Variscan rock outcrops (Montalbán-Variscan Basement) and Cenozoic basins are clearly depicted. The North Iberian thrust, which bounds to the north the basement involved areas of the Iberian Chain, can be recognized by a low resistivity zone emerging at the northern end of the profiles (Figure 5-15 and Figure 5-15 conductors E and F). This major thrust reaches more than 15 km depth and merges with the conductor D2 (Figure 5-15) suggesting the branching of the Montalbán thrust to the North Iberian Thrust as shown in Figure 5-15. The Serranía de Cuenca Thrust, which bounds to the south the basement involved areas, crops out south of the MT sites and it is not well recognized in the resistivity model. However, the conductor beneath sites A29 (Figure 5-15) can be attributed to this thrust, then reaching 7 km depth. The Almazán Syncline megastructure appears clearly depicted (Figure 5-15and Figure 5-15), correlating with the maximum thickness of the shallow conductive area C (Figure 5-15).

At greater depths the Moho discontinuity is not resolved by MT since the Moho does not have a significant change in the electrical conductivity (e.g. Jones, 2013). By contrast, seismic refraction method has detected the discontinuity between crust and upper mantle. The Moho transition is generally very clear, marked by a notable increase in the seismic velocity. However, the low sensitivity of the seismic refraction technique to lateral variations does not constraint the shallow structures. Therefore, the integration of seismic refraction and magnetotellurics is, in this case, optimal in order to obtain a complete image of the Iberian Chain at crust and upper mantle depths (Seillé et al., 2015). Figure 5-15 superimposes the Y-32 section of the 3D resistivity inverse model with the seismic velocity model (Figure 2-16) to illustrate a direct comparison between both models. The crustal thickening observed in the seismic model is mostly concentrated in the upper crust, and the main faults detected by the MT do not reach depths greater than 15 km, thus, being consistent between each other. This shows that the Cenozoic thrusts involve only the upper crust as was previously proposed by Guimerà and Alvaro (1990), who considered a thrust system detachment at 10-12 km depth.

Srivastava et al. (1990) proposed that the Iberian plate, acting as an independent plate during late Eocene and Oligocene, had its north and south boundaries (Pyrenees and Betic Chain respectively) active simultaneously, leading Guimerà et al. (2004) to propose that the deformation of the Iberian Range could be related to either of them, or both. A recent study by Quintana et al. (2015) suggests the presence of a mid-crustal detachment involving the whole Iberian Plate, allowing the displacement transfer from the borders to the intraplate ranges. The MT image shows that the faults are concentrated in the first 15 km depth and probably merge to a common level in the upper crust, but a detachment level linked to the Pyrenees, the Betics or both of them cannot be inferred, mainly because it would have a signature that is outside of the coverage of the MT soundings.

.

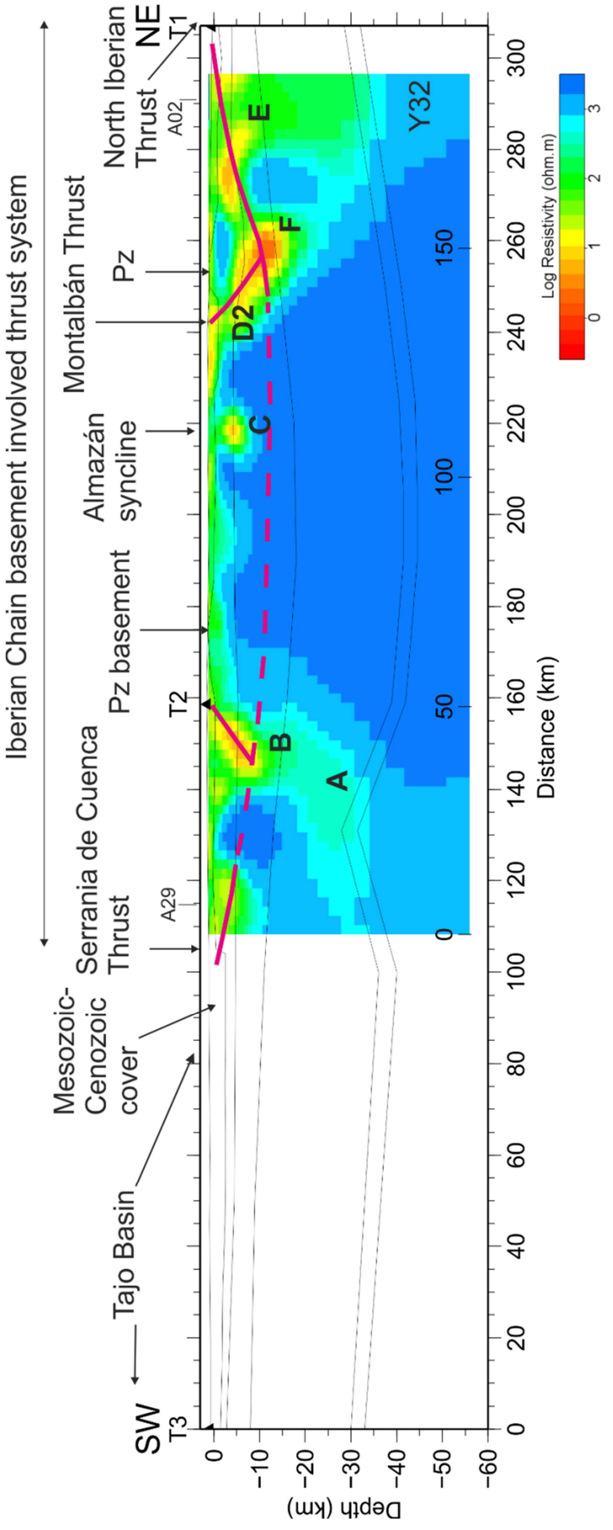

Figure 5-15: Contours of the seismic velocity model superimposed on the Y32 section of the 3-D resistivity model. Red lines are the interpreted faults. Letters represents the anomalies discussed in the text.

5.2.2 Discussion on the origin of the Moho high

The local rise of the Moho boundary (30 km deep) detected by the seismic refraction wide angle reflexion profile (Seillé et al, 2015) at distances of 110-150 km from the SW edge (Figure 2-16) of the profile is a surprising feature. This feature does not have any topographic expression, nor in the superficial geological structure. Interpretation of this enigmatic local rise of the Moho is problematic. Here, two possibilities are analysed. First, the possible tectonic relation with the Serranía de Cuenca thrust, and second the hypothetical correlation of the Moho high with the deep conductor A.

5.2.2.1 Hypothesis 1: Link to the Serranía de Cuenca thrust

One of the hypotheses that arose observing this Moho high was its possible link to the Serranía de Cuenca thrust which is the southern boundary of the Iberian Chain.

A previous study (Guimerà and Alvaro, 1990) suggests that the Cenozoic thrusts involve only the upper crust and considers a thrust system detachment at 7-11 km deep. In order to check the possible relation of this thrust system to the Moho high we realized several forward modelling tests on the topographic expression produced by different geometry and detachment depth faults taking into account their associated horizontal displacement on surface. The Move software was used.

The following geological constraints were imposed in each of the modelling tests:

- The current relief in this part of the Iberian Chain (Castillan Branch) has a maximum close to 2 km.
- The sediments deposited during the Mesozoic have a thickness up to 5 km, and are outcropping in the Castillan Branch. The contractive tectonic context tested here forms a fault-bend fold. This suggests that the expected tectonic relief caused by the contraction along this fault should not be greater than few kilometres.
- A minimum horizontal displacement caused by this thrust has been estimated to 10 km by Guimerà and Alvaro (1990), and it could be greater. This fault goes from the Central Iberian Peninsula to the Mediterranean Sea, more than 200 km long.

The link with the Serranía de Cuenca thrust was tested considering three different cases:

(1) Direct relation between the Serranía de Cuenca thrust and the Moho High, which would imply a dipping angle of 45°.
(2) A thrust system detachment based on Guimerà and Alvaro (1990) hypothesis, where the Serranía de Cuenca thrust would gently dip to the north with a dipping angle of 10°.

(3) An hybrid case based on the geoelectric signature of the Serranía de Cuenca fault inferred from the magnetotelluric model, which implies a thrust system detachment as in case (2) but with a greater dipping angle of 20°. Figure 5-16 shows the three cases tested.

The horizontal displacements tested for the three cases were: 0 km (initial state), 10 km, 15 km and 20 km.

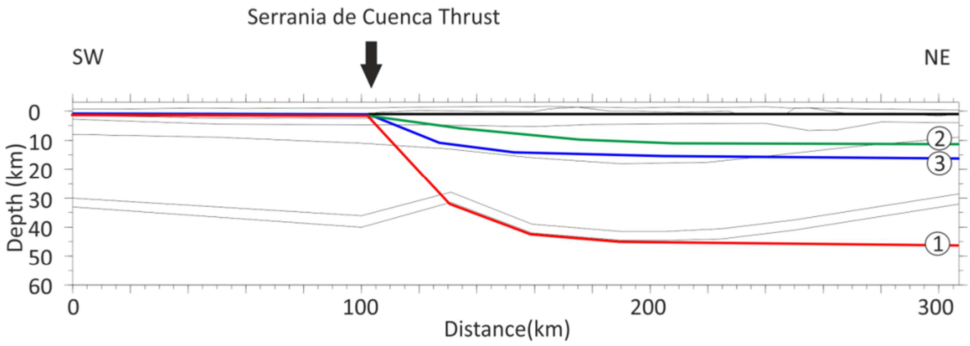

Figure 5-16: Seismic model (Seillé et al., 2015). Thick red line represents the case 1, in which a crustal fault raising the Moho high is assumed. Green line represents the detachment fault, based on Guimerà and Alvaro (1990) (case 2). Blue line represents a detachment fault in which the dipping of the Serranía de Cuenca thrust was inferred from the MT resistivity model (case 3).

Case 1 considers that the Serranía de Cuenca Thrust connects with the Moho high observed at a depth of 30 km. This hypothesis implies a dipping angle of 45 degrees. Figure 5-17 shows the different topographic expressions observed for the different horizontal displacements. The tectonic relief observed for displacement of 10 km and more is too high to fulfil the conditions previously posed. That test can ensure that the Serranía de Cuenca cannot be linked to this Moho high.

In case 2, the gentle ramp scenario gave much more plausible results, where tectonic reliefs between 1.7 and 2.2 km are calculated for horizontal displacements of 10 and 15 km respectively (Figure 5-17). These results are in agreement with the geological constraints explained earlier.

The case 3 is an intermediate case between case 1 and 2. As for case 2 the context is a thrust system detachment but with a detachment located deeper, having a frontal thrust that dips more than in case 2. In this case results show that for possible horizontal displacements (>10 km) the tectonic relief expected is high (>3 km) (Figure 5-17). This suggests that the Serranía de Cuenca thrust dip inferred from the MT results could be taken as an upper bound to account for the actual topography.

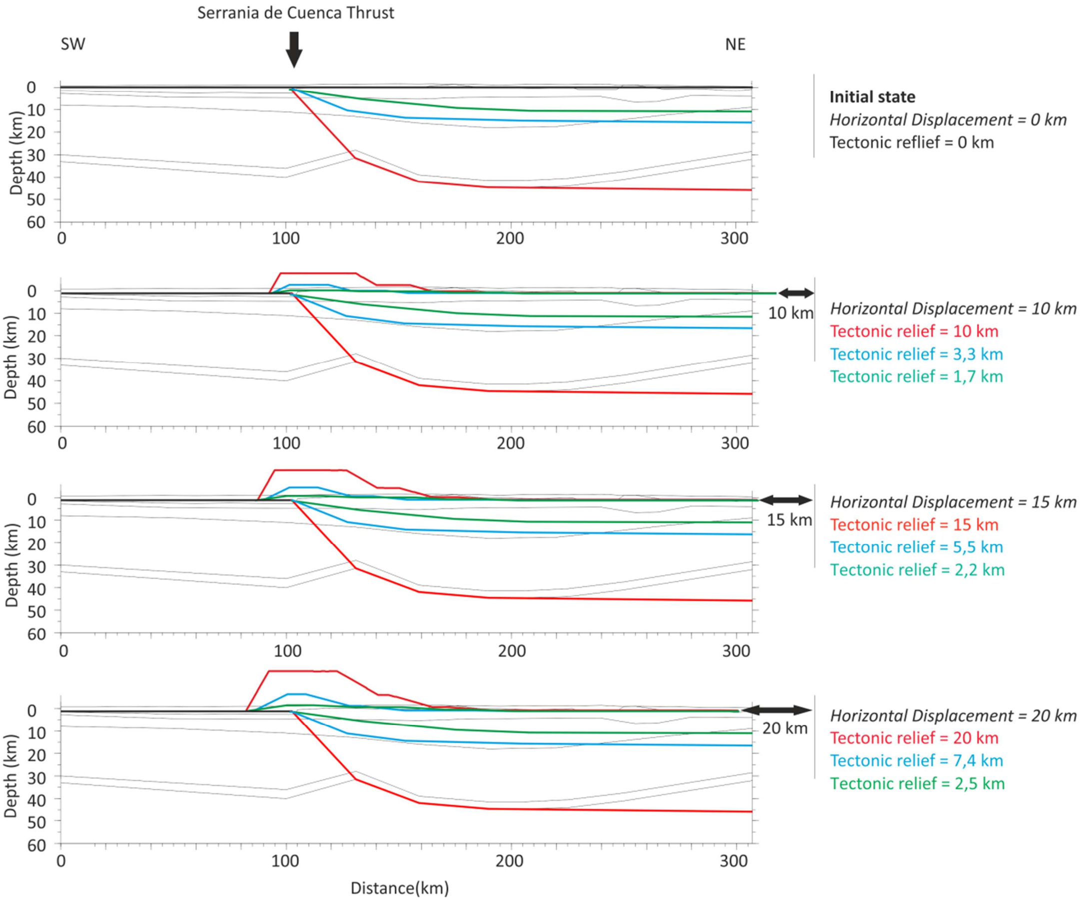

Figure 5-17: Modelling of the tectonic relief obtained applying various horizontal displacements for case 1. Red line represents the fault assumed and the blue line the topographic expression resulting to the horizontal displacement.

These considerations allow only a thrust that would be gently dipping to the north, discarding the possibility that the Moho high is linked to any major surface structure, in particular the Serranía de Cuenca thrust. The Serranía de Cuenca thrust is then likely to be linked to the thrust system detachment located at depth between 10 and 15 km, as suggested by Guimerà and Alvaro (1990) and indicated by the magnetotelluric data. The horizontal displacement related to the low-dipping Serranía de Cuenca thrust and responsible for the tectonic relief of the Castillan Branch could be estimated between 10 km and 15 km, as pointed out by Guimerà and Alvaro (1990).

5.2.2.2 Hypothesis 2: Relation with the deep conductor A

Figure 5-15 and Figure 5-18 show a plan view with the conductor A detected at a depth around 25 km matching the Moho high.

The Sierra de la Demanda Range, located NW of the survey area, is the northern extreme of the Iberian Chain. Pous et al. (2000) have carried out in 1999 a MT profile across the Sierra de la Demanda Range detecting a conductive anomaly located 25 km depth in the southern part of the profile (Figure 5-18). The conductor A located at a depth around 25-30 km in the SW part of the Iberian Chain profiles, which is coincident with the Moho high, is located at the same depth as the anomaly observed below the Sierra de la Demanda Range. Even if not deeply discussed because of the low robustness of this conductor and the distance among surveys, this correlation should be taken into account for future investigations.

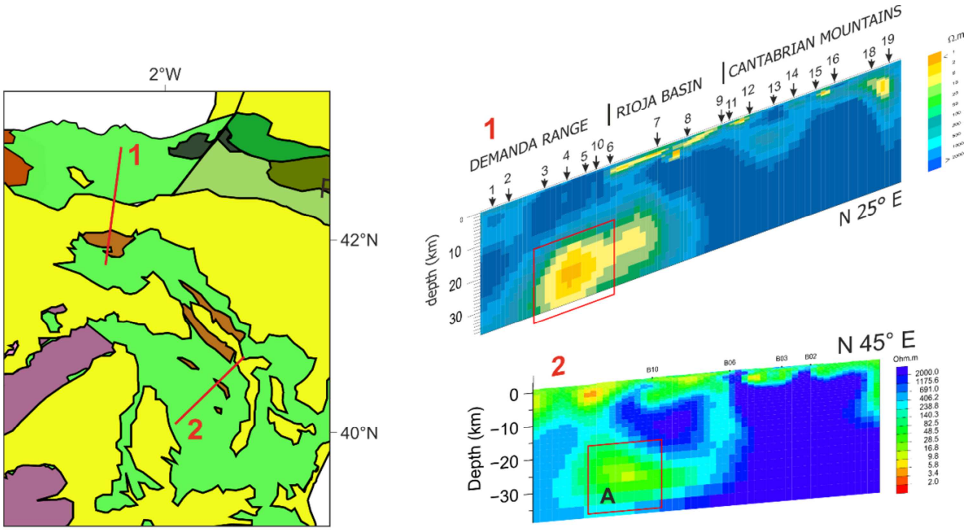

Figure 5-18: (left) Geological map with the location of the profiles 1 and 2. Red circles represent the location of the anomaly shown by a red square in the models. (right) ***1****: 2-D MT model beneath Sierra de la Demanda, modified from Pous et al. (2000).* ***2****: Section Y22 (western section) of the 3-D resistivity model in the Iberian Chain.*

5.2.2.3 Conclusion on the origin of the Moho high

We can conclude that the Moho high is not related to any crustal scale thrust and therefore that the crustal thickening is concentrated in the upper crust.

Abrupt changes and prominent Moho local topography are also observed in other places, e.g. Western Carpathians (Hrubcová and Sroda, 2015). These authors suggest an origin related to the plate convergence that lead to creation of the Western Carpathian mountain chain, i.e., with collisional/transpressional processes during and after the Tertiary subduction. Although the Iberian Chain area does not compare with the Carpathians, we cannot rule out a relict origin either related with the late Jurassic-Early Cretaceous extension or with the Variscan orogeny.

5.2.3 Correlation of resistivity and seismic velocity for the upper crust

5.2.3.1 Introduction

The physical properties of the subsurface can be measured using several geophysical techniques, each of them being sensitive to different physical parameters. A reliable geophysical/geological model can be obtained by integrating independent geophysical datasets having different physical meaning, different resolution capabilities and different resolution scale. In this way the non-uniqueness inherent to each geophysical method is reduced and a lithological model satisfying the behaviour of each physical parameter can be obtained. However, the relationships between different physical parameters are not well defined. The great variations in the physical processes occurring within the Earth can be explained by empirical relationships, usually based on well log data, but are hardly applicable to every geological context. While elastic and density properties are likely easier to be linked, elastic properties and electrical conductivities empirical links are not universal. Porosity is usually used to link them, but it depends much on the geological context (Marquis and Hyndman 1992, Hacikoylu et al. 2006). The most recurrent observation is a trend of increasing velocities with increasing resistivities, as observed by Dell’Aversana (2001) on well log data analysis.

Several approaches have been used to integrate different geophysical parameters. Bedrosian et al., (2007) introduced a joint statistical interpretation methodology that performs structural classification based on correlation between electrical and seismic parameters. Compared to a classic qualitative interpretation of multiple physical properties, this methodology gives structural information not easily identifiable in individual models. Another approach is the cooperative inversion of different datasets, in which the result of a single inversion of one dataset is used to constrain the other inversion. Then, the roles are iteratively switched until a satisfactory result is achieved (Hu et al., 2009). Dell’Aversana (2001) used integration between seismic, MT and gravity data through an iterative process. The seismic model is transformed into a resistivity model using empirical relationship from borehole data. The resulting resistivity model is used as a starting model for the MT inversion and back-converted into a new velocity section using the same relationship. Another approach is a joint inversion (SJI) of different datasets using a link between the model domains. This link can be structural (Gallardo and Meju, 2004; De Stefano et al., 2011) or petrophysical (De Stefano et al., 2011), when relationships between the different parameters are available. The resulting models satisfy each data domain and are mutually constrained, structurally or petrophysically.

Here we present a correlation between seismic velocity and resistivity models analysed through a statistical approach. A statistical correlation of both physical properties in a joint parameter space was used to compare these two independent datasets. In order to compare both models (resistivity and velocity) we chose in the 3-D MT model the cross section Y32 (Figure 5-13) which is the closest to the seismic profile. The first 10 kilometres of the models were analysed given the more uniform velocity distribution at greater depths delineated by the seismic refraction-wide angle reflection data.

5.2.3.2 Analysis and models correlation

The MT and the seismic models are defined on two different grids. The MT mesh is built on a non-uniform grid, where the cell size increases with depth. However, the seismic mesh was defined on a regular grid with an equal horizontal and vertical discretization of 0.5 km. In order to proceed with the cross plot analysis both parameters need to be defined on the same grid.

Since both original grids are different, we chose to interpolate both grids in a common mesh with cell size increasing with depth. The horizontal spacing of the common grid was chosen to coincide with the original MT grid (2 km). Vertically the common grid is discretized using a step of 0.25 km between 0 and 3 km depth and a step of 0.5 km between 3 km and 10 km depth.

Figure 5-19 and Figure 5-20 show how the interpolation on the common grid for the p-wave velocity Vp and the resistivity models was performed. In both figures the upper panel represents the original model (left) and its data distribution in form of a histogram (right). The middle panel shows the interpolated model on the common grid. Data interpolation was done using the natural neighbour gridding algorithm which was more suitable because of the discrete distribution of the MT data. Data distribution in form of a histogram (on the right) allows to compare the original data histogram with the interpolated. For both, the resistivity (Figure 5-19) and the seismic velocity parameters (Figure 5-20) the original and interpolated histograms show the same distribution. The lower panel represents the differences between the original and interpolated values for each node of the grid (residuals). Both models present very low values (around 0) of residuals, indicating that the interpolated models reproduce faithfully the original ones.

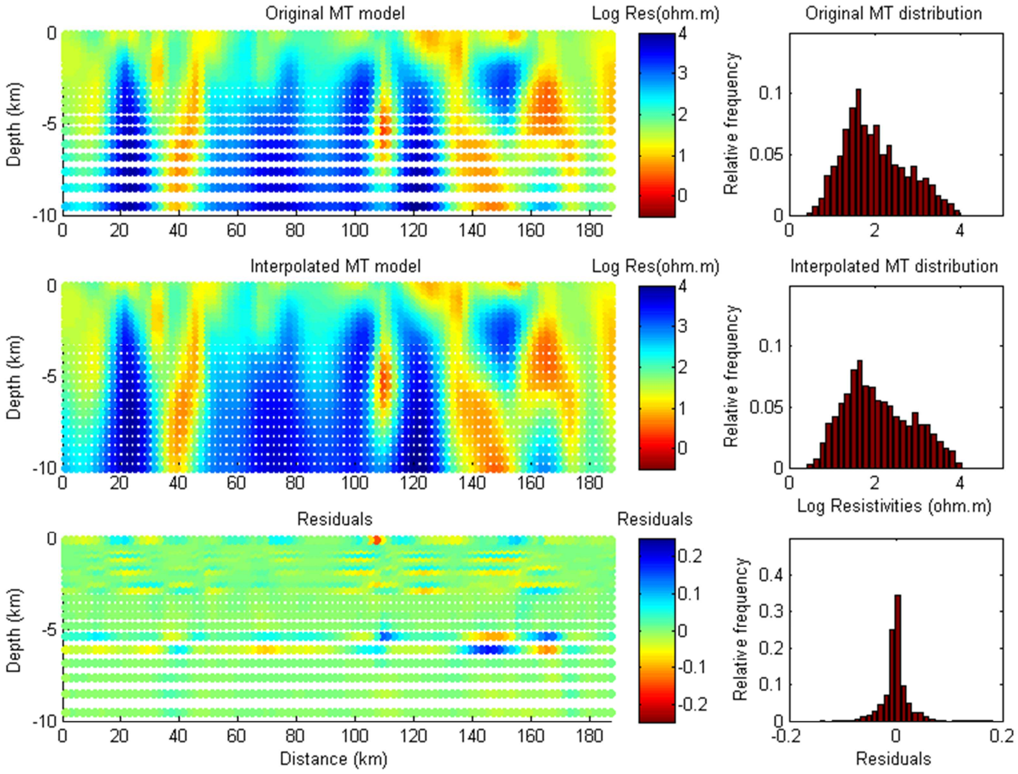

Figure 5-19: Interpolation of the resistivity MT model on the common grid. The original model, the interpolated model and the residuals are shown on the model space on the left and on the data space (relative frequency of each resistivity value) on the right.

Differences occur when abrupt changes (in velocity or electrical resistivity) are present in the original model. The interpolation process smoothes the interpolated data across these boundaries, resulting in slightly underestimated or overestimated values. However, histograms of the distribution of the residuals (shown on the right) are centred on zero.

This analysis ensures us that the interpolation process was able to reproduce the original distribution of resistivity and velocity on the common grid, without introducing any artificial structures.

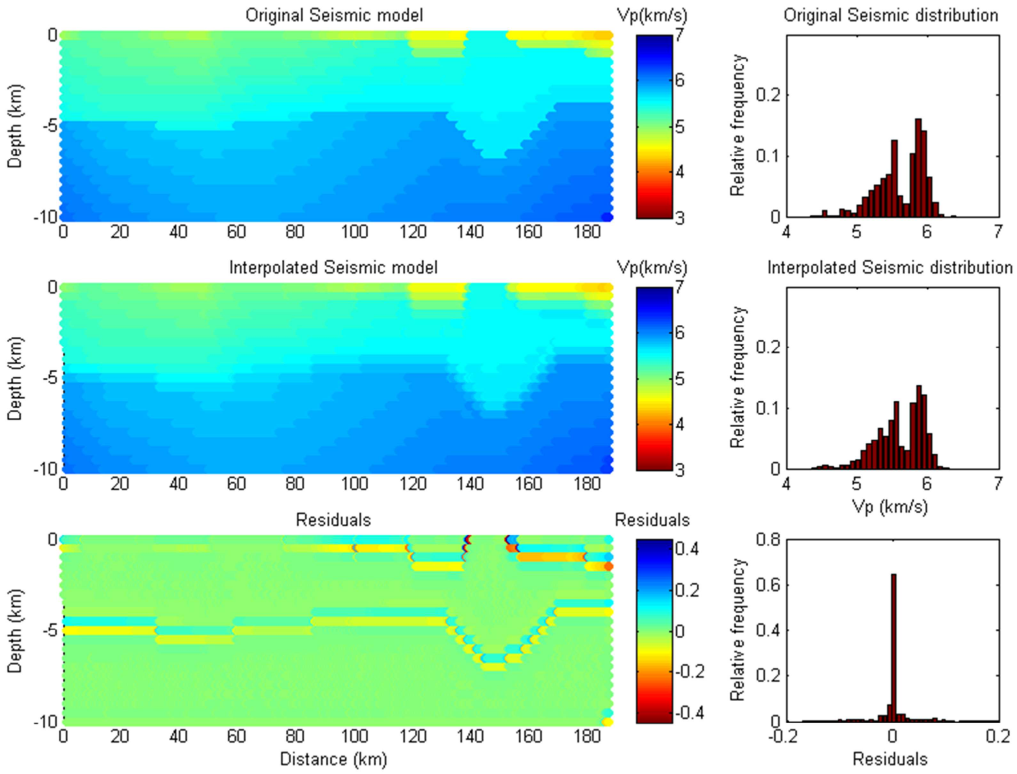

Figure 5-20: Interpolation of the seismic model on the common grid. The original model, the interpolated model and the residuals are shown on the model space on the left and on the data space on the right.

Having defined a common grid in which each cell is described by a resistivity and a velocity value, a crossplot was generated. Figure 5-21a shows a histogram of the correlation between electrical resistivity and seismic velocity (Vp). This crossplot allows us to identify areas of high occurrences. Five zones are manually identified. Figure 5-21b shows the spatial region from which these zones derive.

Zones 1 to 4 follow are grouped following a clear trend, with a general increase in apparent resistivity with increasing seismic velocity. Choice of zone 5 is conditioned by user’s criteria. They are grouped according to their resistivity: low resistivity data covering a wide range of velocities. This is why the red zone in the resulting image (Figure 5-21b) follows the trend of the resistivity model.

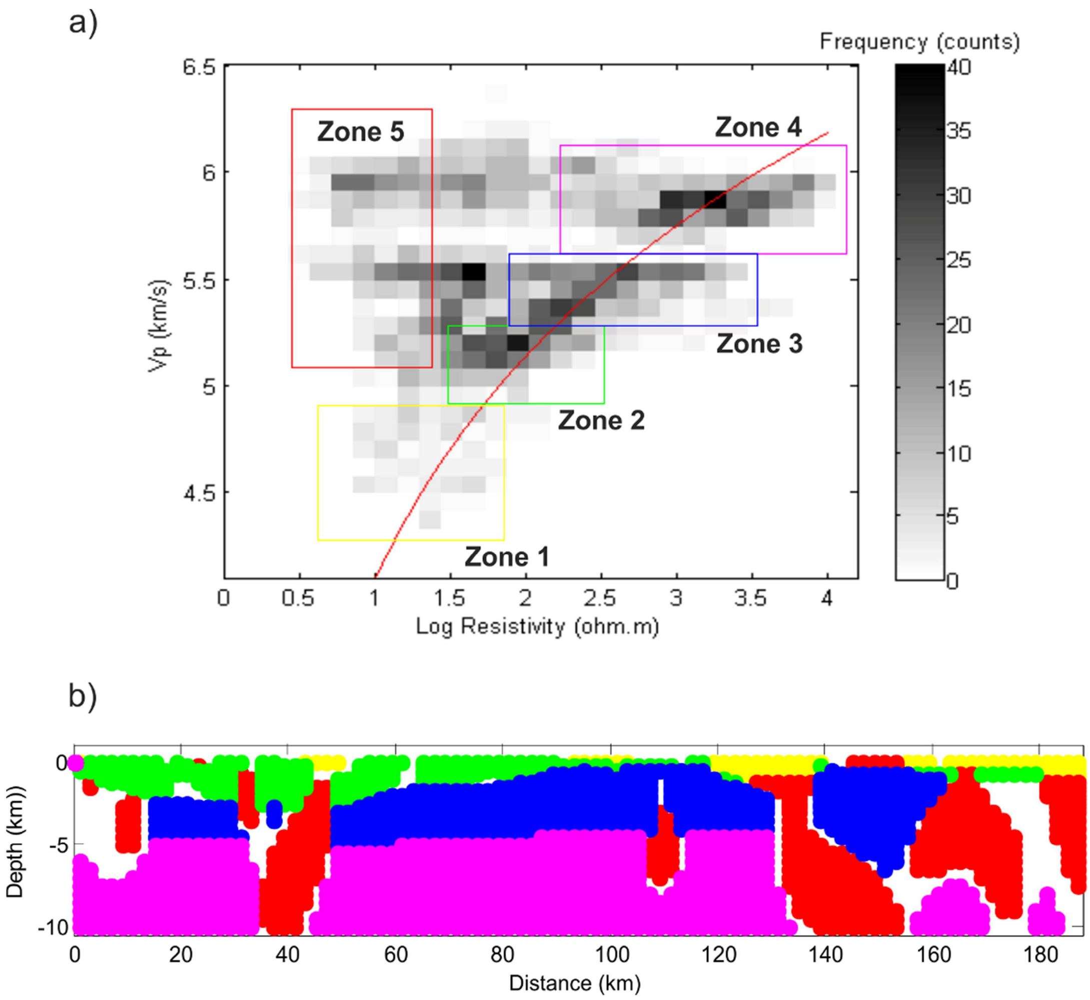

Figure 5-21: a) Cross plot resistivity-velocity. Coloured ellipses show the groups selected. Red line indicates the resistivity/velocity relationship modified from Dell'Aversana (2001). b) Spatial distribution of the groups identified in a). White areas indicate regions not belonging to any of the groups identified. Vertical exaggeration 4:1.

Results

Figure 5-21b shows the location in the spatial domain of the areas identified in the crossplot. White areas correspond to data that did not belong to any of the guessed zones.

Zone 1, in yellow, characterized by low velocity and low resistivity is assimilated to the Tertiary infill of the sedimentary basins (Ebro basin and Catalayud basin). This formation is located mainly on the uppermost parts of the model, with moderate thickness (up to 1.5 km thick). Low rock compaction and reasonable fluid content are responsible for this behaviour.

Zone 2, in green, has conductive to moderately resistive values and low velocity values. This area was interpreted to be related to the Mesozoic cover, which is mainly composed by dolomites, gypsum, shales, marine limestones and dolostones and continental and marine deposits. Mesozoic rocks are mainly visible SW of the Almazán syncline, having thickness ranging from few hundred meters to several kilometers. In the NE it is also possible to see some Mesozoic materials beneath the Tertiary Ebro Basin. In the Castillan Branch the less amount of Mesozoic sediments could be explained by the strongest erosion that affected this part of the Iberian Chain.

Zone 3, in blue, has resistive values and moderate velocity values. This zone was attributed to the Palaeozoic basement, mainly formed by metamorphic shales, sandstones and limestones. The basement has a slightly variable thickness along the studied profile, from 4 km at km 120 on the NE (Figure 5-21b) to 5 km thick at kilometre 0 on the SW.

Zone 4, in purple, has the highest resistivity and velocities found in this analysis. We interpret this zone as the upper crust, constituted by highly metamorphized and intruded rocks.

As pointed out, zones 1 to 4 follow a trend that points towards an increase of both the velocity and the resistivity. This trend has been observed for different rock formations (both sedimentary and igneous) by several authors (Bedrosian et al., 2004; Bernard et al., 2009; Munoz et al., 2010). Dell´Aversana (2001) proposed the following empirical relationship, obtained from well log analysis:

$$V_p = 1.63 \log\big(\log(\rho)\big) + 3.12 \qquad \text{in km}/s$$

Because of the large scatter observed to build this relationship, we introduce a modified relationship that fit our observation and still is in the confidence limits of the well log analysis carried out by Dell'Aversana (2001):

$$V_p = 1.5 \log\big(\log(\rho)\big) + 4.1 \qquad \text{in km}/s$$

This trend is pictured on top of the Figure 5-21a and follows the zones of most occurrences in the histogram.

This correlation depicts the effect of rock compaction with depth. A decrease in porosity and permeability produces an increase in electrical resistivity and seismic velocity. Older rocks were buried deeper with time and compacted or metamorphized, decreasing porosity and expelling fluids.

Zone 5, in red, is defined because of its low resistivity content with a broad range of velocities. While zones 1 to 4 define uniform material properties representing different geological units, zone 5 represents a hydrologic contrast within the same geological unit separating areas with different water content. The areas have been interpreted as fractured and faulted zones. Because of its resolution the refraction seismic model is not expected to detect changes in velocities related to dipping faults, and is laterally homogeneous. On the other hand the MT detects the presence of the fluids distributed along the fault planes. The preferred explanation for the origin of the enhanced fault zone conductivity is the presence of aqueous fluids in the fault zone and its fractured surrounding areas (e.g. Unsworth et al., 2001).

An integrated geophysical model for the upper crust is presented in Figure 5-22. Five distinct zones are evidenced:

Zone 1- The Tertiary infill
Zone 2- The Mesozoic cover
Zone 3- The Palaeozoic basement
Zone 4- The Upper Crust
Zone 5- Fluid saturated regions

The resistivity and velocity of these regions are summarised in Table 5-1, which includes the interpreted lithological and geological types. The zone 5 is not included in this table as it represents a hydrologic contrast and could belong to several lithologies.

Zone	ρ (Ωm)	V_p (km/s)	Lithology	Geol. classification
1	3 - 40	4.2 – 5.1	continental deposits	Tertiary filling
2	30 - 300	5.1 – 5.3	dolomites, gypsum, shales, marine limestones / dolostones and continental / marine deposits	Mesozoic cover
3	70 - 3000	5.3 – 5.5	metamorphic shales, sandstones and limestones	Palaeozoic basement
4	100 - 10^4	5.5 - 6	metamorphic	Upper crust

Table 5-1: Resistivity, velocity of the regions shown in Figure 5-21. Velocity values from Seillé et al. (2015).

The seismic events shown in the Figure 5-22 were taken from the *Intituto Geografico National* (http://www.ign.es). Relation between the recorded seismicity and the detected fractured areas seems to be divided into two patters: seismicity observed in the vicinity of the interpreted faulted areas and seismicity beneath the Almazán syncline where no conductive anomalies were detected. The first one shows a correlation between the hypocentre locations and the orientation of the interpreted faults. The second pattern is characterized by a high seismicity of low magnitude beneath the Almazán syncline (magnitude below 3 in the Richter scale) without any clear orientation, and with most of the earthquakes concentrated in the brittle upper crust. This indicates that in the Iberian Chain the main intraplate tectonic stress currently existing in the upper crust could be released beneath the Almazán Syncline, which separates the two crustal-scale anticlinoria structures, the Aragonese Branch Arch in the NE and the Castilian Branch Arch in the SW.

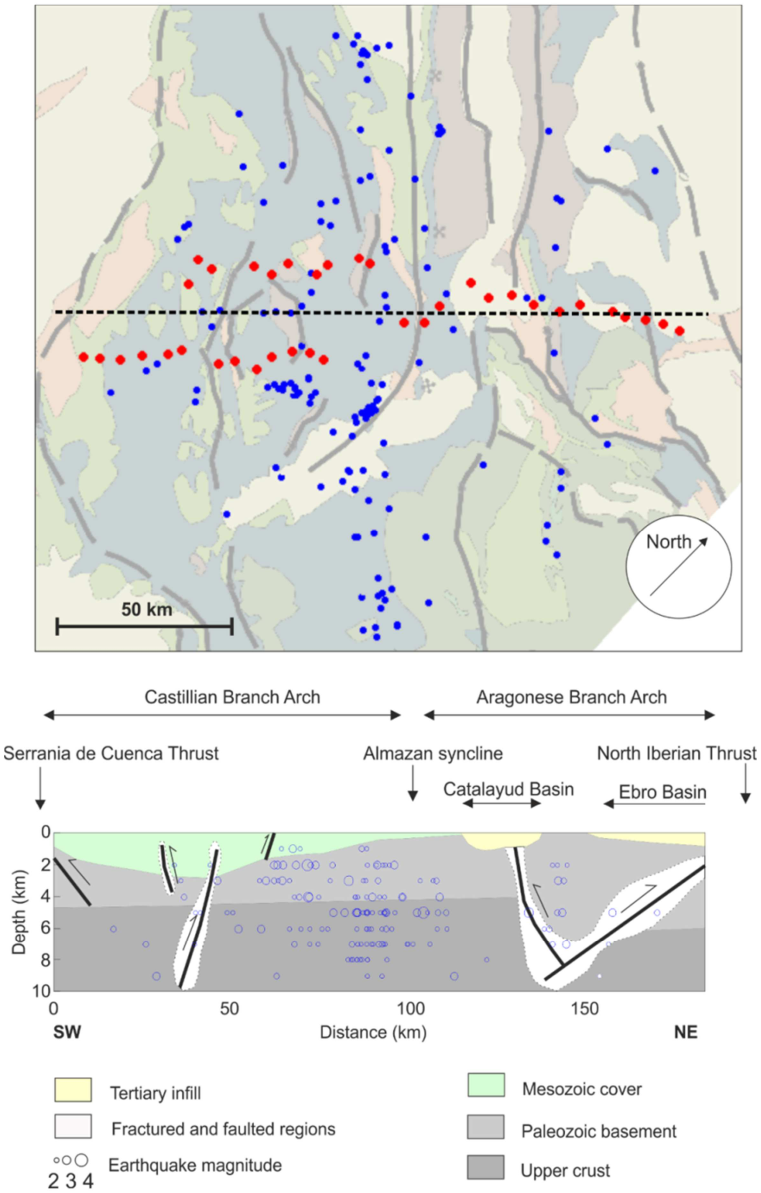

Figure 5-22: Top) geological map. Red points: MT sites. Blue points: earthquakes epicentres (http://www.ign.es). Dashed line represents the cross section shown in the bottom figure. Bottom: Interpreted model. Blue circles are the projected earthquakes hypocentres. Vertical exaggeration 1:5.

5.3 Conclusions:

Thirty-seven new magnetotelluric soundings were acquired along two profiles oriented NE-SW across the Iberian Chain, coincident with a wide-angle seismic profile. An integrated interpretation of the 3D resistivity model and the seismic velocities was carried out, leading to these main conclusions:

- A 3-D resistivity model was obtained from a 3D joint inversion of the full impedance tensor and the magnetic transfer functions. This is the first image of the crustal structure of the Iberian Chain.
- The major thrusts depicted after MT data reach a maximum depth of 15 km which agree with seismic data in that the crustal thickening is concentrated in the upper crust. This is consistent with the hypothesis of a Cenozoic thrust system involving only the upper crust proposed by Guimerà and Alvaro (1990). The Serranía de Cuenca Thrust located in the SW and the North Iberian Thrust located in the NE have been evidenced to be linked to the thrust system detachment at 10–15 km deep.
- Analysis of the correlation between electrical resistivity and seismic velocity permitted to map the distribution of the main geological formations of the first 10 kilometres along a SW-NE profile. Attribution of electrical resistivity and seismic velocity for each geological unit was performed. Aqueous fluids present in the fractured areas are responsible for the enhanced conductivity observed in the fault areas.
- We explored various hypotheses to explain the origin of the Moho High. None of them were satisfactorily. Tentative interpretations include an origin related to a relict feature of the Variscan crust or with the late Jurassic–Early Cretaceous extension. Further research is required to provide a satisfying interpretation for the enigmatic local rise of the Moho and its possible connection with conductor A.

6 Discussion and Conclusions

6.1 Discussion

Geophysics is a geoscience discipline used to sense the physical properties of the subsurface using non-invasive technologies. The physical fields are measured on surface to infer the subsurface characteristics. The forward problem determines the responses that would be measured in the surface on top of a given Earth model, following theoretical physical equations. The forward problem has a unique solution. However, the inverse problem suffers from ambiguity, or non-uniqueness, meaning that several different geological configurations can reproduce the observed measurements. Furthermore, the experimental errors associated to the data acquisition add some uncertainty. Since a unique solution cannot be directly determined from a set of field measurements, the geophysicist needs to reduce the number of possible solutions, using a priori information (geological, geophysical) or logical criteria, such as finding the simplest possible model able to explain the data.

The magnetotelluric inverse problem suffers from this non-uniqueness. The experience derived from this thesis showed several ways to undertake this uncertainty and to reduce the possible solutions.

Errors affecting the field measurements increase the uncertainty dramatically. This is especially true for the MT method and a good data acquisition is the base in obtaining a robust inverse model. Discarding noisy data into the inversion was found a good procedure, otherwise the fitting of highly noisy data produce unrealistic models.

Dimensionality analysis is crucial in order to choose the appropriate modelling approach. When using a 2-D approach not including data with 3-D characteristics resulted to be the most suitable procedure to obtain reliable models.

Knowing the resolvability of the targets by means of forward modelling tests is of crucial importance. This allows building adequate meshes for adequate frequency ranges, prior to the inversion. It can also reveal the limitations inherent to the proper MT method in certain geological environments. This allows to understand the data, its contribution on the interpretation and the uncertainties associated to the model.

The inclusion of a priori information during the modelling can guide the inversion process towards a solution that will satisfy other geological or geophysical measurements, discarding models that equally fit the data.

Finally, the experience acquired during the course of this thesis highlighted the importance of the integration of multiple datasets (geological, geophysical) during the interpretation stage of the geoelectrical models. This integration can be performed qualitatively to spot similarities between several observations (as it has been done for the Cantabrian Mountains and the Iberian Chain) or statistically to obtain unified Earth model satisfying each observable (as it has been done for the Iberian Chain). Each geosciences discipline and results have to be taken as a contribution to build unified Earth models in order to obtain a better understanding of the structure and processes happening in the Earth.

It has been shown during this thesis that the MT method resulted to be a powerful tool to study the Earth at crustal scale, but also at shallower depths. Determination of the transition between conductive basin sediments and a resistive basement can be done accurately, as it has been done in the Duero Basin, confirmed by well data. At crustal scale presence of fluids in the fractured areas permit to reveal the shape, depth and orientation of the faults. Other geophysical techniques, especially the seismic reflection, cannot directly sense the presence of vertical faults. In this case, the MT method reveals them, even if the faults cross homogeneous geological formations. Another example of the added value of the MT method is the behaviour of the EM waves in some geological environments where the seismic method has a poor resolution. For example in subsalt or subbasalts environments the seismic waves are easily scattered, which prevent the geophysicist to obtain reliable images of the subsurface. In these cases the use of the MT method (or other EM methods) undertakes those difficulties being sensitive to another physical parameter, the electrical conductivity.

However, the MT method suffers from inherent difficulties. The most important one is the influence of the near surface static distortions that affect the data and can influence the interpretation of the whole model, even in its deeper parts. Several advances were recently made and a way to by-pass this issue can be found when large dataset are acquired and inverted using advanced inversion algorithms. Other limitation of the MT method that was outlined in this thesis is the resolvability of the high resistive features. Because of the behaviour of the EM waves in electrically resistive mediums, the MT method cannot easily detect changes related to thin or deep high resistive anomalies. In these cases the use of active EM methods (Constable and Weiss, 2006) or inclusion of a-priori information (Matsuno et al., 2010; McGary et al., 2014) is necessary.

6.2 Conclusions

6.2.1 Cantabrian Mountains

In the Cantabrian Mountains the thirteen sites acquired along an N-S line crossing the Cantabrian Mountains and the Duero Basin permitted to construct a 3-D resistivity model, from which a resistivity profile was extracted and interpreted.

The main conclusions regarding the analysis and the inversion of this MT dataset are:

- Detailed analysis of the data showed the presence of numerous 3-D effects, as expected from the geology of the area. Part of the data ($T < 300$s) was found to be compatible with a 2-D approach, with a dominant strike estimated in N10°E.
- 2-D inversion of apparent resistivity, phases and tipper of this limited data set was carried out.
- However, to account for the 3-D behaviour of the data a 3-D inversion of the whole dataset was carried out. Experience with this dataset led us to follow the following strategy for the 3D inversion: first, the off-diagonal components of the impedance tensor were inverted. Second the model obtained was used as the initial model for the joint inversion of the off-diagonal components of the impedance tensor and the vertical transfer function data (VTF). Finally the diagonal of the impedance tensor were included in a last inversion to obtain the final model. The final 3-D model achieved a good fitting having a RMS=1.94.
- Main differences between the 2-D and 3-D models were attributed to the different data ranges and to the 3-D effects that biased the location of the anomalies on the 2-D image.

The tectonic interpretations of the main structures imaged with the 3-D resistivity model are:

- The correlation between the geoelectrical image, the existing geophysical models and the surface geology provided a deeper understanding of the lithospherical processes.
- The final 3-D inverse model shows excellent correlation with the superficial geology, depicting the main faults and lithologies at depth.
- The Duero Basin sediments are well delineated. A thickness of 2.5 to 3.5 km was deduced, and is in agreement with the seismic studies and well log data.
- Conductive zones in the Palaeozoic basement are related to enhanced permeability along the main Alpine faults. These conductive zones detected in the model do not reach more than 10 km in the southern part of the Cantabrian Mountains and 15 km in the northern part, and are therefore concentrated in the upper crust.
- The hydration/serpentinization of the upper mantle within the mantle wedge and beneath the Moho of the Cantabrian Margin is imaged as a zone of low resistivities.

6.2.2 Iberian Chain

The first magnetotelluric data acquired through the Iberian chain has been described and interpreted in this thesis. The MT data consists in thirty-seven broad band magnetotelluric soundings acquired along two profiles oriented NE-SW across the orogen.

The main conclusions related to the analysis and inversion of this MT dataset are summarized as follows:

- The dimensionality analysis indicates a dominant strike direction for short-medium periods, however, it shows clearly a 3-D regional resistivity structure at long periods ($T > 500$s). Real induction arrows are deflected parallel to this strike direction in the southern part of the studied area. Accordingly, a 3-D inversion was carried out.
- A joint inversion of the full impedance tensor and the vertical transfer function was performed and a very good fitting of all the data was obtained. RMS = 1.88.

The tectonic interpretations of the main structures imaged by the 3-D resistivity model are:

- The main geological structures observed in surface are well imaged in the resistivity model. The Mesozoic and Cenozoic covers are depicted as low resistivity features well distinguished from the high resistivity of the Variscan basement. The Almazán Syncline megastructure is characterized by a conductive structure.
- The middle and lower crust in the central part of the Iberian Chain is highly resistive, suggesting the absence of major crustal faults.

- Several alpine thrusts are imaged as dipping conductors, which are limited to the upper crust. Two of them are the North Iberian Thrust and the Serranía de Cuenca Thrust, which bound to the north and to the south respectively the basement involved areas of the Iberian Chain. Both faults do not reach more than 15 km depth, suggesting that they are linked to the thrust system detachment at 10–15 km deep. This indicates that the Cenozoic thrust system causing the crustal thickening of the Iberian Chain is concentrated in the upper crust, which confirms the previous geological hypothesis proposed by Guimerà and Alvaro (1990).
- The resistivity model was integrated with an existing seismic velocity model. Because of the different sensitivities and depth resolution of both methods their integration allowed to obtain a complete image of the Iberian Chain at crust and upper mantle depths. The seismic velocity model shows a thickening of the upper crust consistent with the base of the conductors associated to the thrust system detachment, confirming that the Cenozoic thrust system causing the crustal thickening of the Iberian Chain is concentrated in the upper crust.
- The statistical analysis of the correlation between seismic velocity and electrical resistivity along a NE-SW profile showed a clear correlation between both parameters. An increase in both seismic velocity and electrical resistivity is observed and is related to the depth at which those formations are located. A geological classification of the main lithologies of the upper crust based on their physical characteristics was realized.

6.3 Future works:

This study allowed us to characterize the crustal structure in the two Alpine orogens of the Iberian Peninsula by means of the interpretation of geoelectrical models. From this study new questions arose related to the geodynamics of both areas.

- In the Cantabrian Mountains the resistivity image obtained took into account the 3-D effects observed in the data. However, a more precise image of lateral structures could be achieved including more MT sites on each side of the current profile. The characterization of the continuity of the deep conductor to the north beneath the Bay of Biscay could only be achieved if MT sites could be acquired in sea.
- In the Iberian Chain the presence of a deep conductor close but outside of the survey area was evidenced. This conductor is correlated with the Moho high evidenced in the seismic image and is similar with another conductor found at the same depth in another MT study located NW, in the Sierra de la Demanda. Acquisition of new MT sites NW of the present study area would lead to a broader 3-D electrical resistivity image of the crust beneath the Iberian Chain. Another remaining question is the ge-

oelectrical characterization of the whole lithosphere, especially the geometry of the lithosphere asthenosphere boundary (LAB) beneath the Iberian Chain. In that case new long period magnetotellurics (LMT) would be required.

Bibliography

Almeida, E., Monteiro Santos, F., Mateus, A., Heise, W., & Pous, J. (2005). Magnetotelluric measurements in SW Iberia: New data for the Variscan crustal structures. *Geophysical Research Letters*, *32*(8).

Alonso, J., Pulgar, J., García-Ramos, J., & Barba, P. (1996). W5 Tertiary basins and Alpine tectonics in the Cantabrian Mountains (NW Spain). *Tertiary Basins of Spain: The Stratigraphic Record of Crustal Kinematics*.

Amante, C., & Eakins, B. W. (2009). *ETOPO1 1 arc-minute global relief model: procedures, data sources and analysis*. US Department of Commerce, National Oceanic and Atmospheric Administration, National Environmental Satellite, Data, and Information Service, National Geophysical Data Center, Marine Geology and Geophysics Division Colorado.

Anadón, P., & Roca, E. (1996). Geological setting of the Tertiary basins of Northeast Spain. *Tertiary Basins of Spain, the Stratigraphic Record of Crustal Kinematics. Cambridge University Press, Cambridge*, 43–48.

Archie, G. E. (1942). The electrical resistivity log as an aid in determining some reservoir characteristics. *Transactions of the AIME*, *146*(1), 54–62.

Ayala, C. (2013). A new compilation of gravity data over the Iberian Peninsula and surrounding areas.

Bahr, K. (1988). Interpretadon of the magnetotelluric impedance tensor: regional induction and local telluric distortion. *J. Geophys*, 119–127.

Banda, E., Suriñach, E., Aparicio, A., Sierra, J., & De La Parte, E. R. (1981). Crust and upper mantle structure of the central Iberian Meseta (Spain). *Geophysical Journal International*, *67*(3), 779–789.

Bedrosian, P., Maercklin, N., Weckmann, U., Bartov, Y., Ryberg, T., & Ritter, O. (2007). Lithology-derived structure classification from the joint interpretation of magnetotelluric and seismic models. *Geophysical Journal International*, *170*(2), 737–748.

Berdichevsky, M. N., & Dmitriev, V. I. (2010). *Models and methods of magnetotellurics*. Springer Science & Business Media.

Boillot, G., & Malod, J. (1988). The north and north-west Spanish continental margin: a review. *Rev. Soc. Geol. España*, *1*(3–4), 295–316.

Booker, J. R. (2014). The magnetotelluric phase tensor: a critical review. *Surveys in Geophysics*, *35*(1), 7–40.

Boonchaisuk, S., Siripunvaraporn, W., & Ogawa, Y. (2013). Evidence for middle Triassic to Miocene dual subduction zones beneath the Shan–Thai terrane, western Thailand from magnetotelluric data. *Gondwana Research*, *23*(4), 1607–1616.

Brasse, H., Schäfer, A., Díaz, D., Alvarado, G. E., Muñoz, A., & Mütschard, L. (2015). Deep-crustal magma reservoirs beneath the Nicaraguan volcanic arc, revealed by 2-D and semi 3-D inversion of magnetotelluric data. *Physics of the Earth and Planetary Interiors*, *248*, 55–62.

Cagniard, L. (1953). Basic theory of the magneto-telluric method of geophysical prospecting. *Geophysics*, *18*(3), 605–635.

Caldwell, T. G., Bibby, H. M., & Brown, C. (2004). The magnetotelluric phase tensor. *Geophysical Journal International*, *158*(2), 457–469.

Campanyà, J., Ledo, J., Queralt, P., Marcuello, A., Liesa, M., & Muñoz, J. A. (2012). New geoelectrical characterisation of a continental collision zone in the West-Central Pyrenees: Constraints from long period and broadband magnetotellurics. *Earth and Planetary Science Letters*, *333*, 112–121.

Carballo, A., Fernandez, M., Jiménez-Munt, I., Torne, M., Vergés, J., Melchiorre, M., Díaz, J. (2015). From the North-Iberian Margin to the Alboran Basin: A lithosphere geo-transect across the Iberian Plate. *Tectonophysics*, *663*, 399–418.

Carbonell, R., Simancas, F., Juhlin, C., Pous, J., Pérez-Estaún, A., González-Lodeiro, F., Ayarza, P. (2004). Geophysical evidence of a mantle derived intrusion in SW Iberia. *Geophysical Research Letters*, *31*(11).

Carlson, R. L., & Miller, D. J. (2003). Mantle wedge water contents estimated from seismic velocities in partially serpentinized peridotites. *Geophysical Research Letters*, *30*(5).

Chave, A. D., & Jones, A. G. (2012). *The magnetotelluric method: Theory and practice*. Cambridge University Press.

Choukroune, P. (1989). The ECORS Pyrenean deep seismic profile reflection data and the overall structure of an orogenic belt. *Tectonics*, *8*(1), 23–39.

Christensen, N. I., & Mooney, W. D. (1995). Seismic velocity structure and composition of the continental crust: A global view. *Journal of Geophysical Research: Solid Earth*, *100*(B6), 9761–9788.

Daignières, M., Gallart, J., Banda, E., & Hirn, A. (1982). Implications of the seismic structure for the orogenic evolution of the Pyrenean range. *Earth and Planetary Science Letters*, *57*(1), 88–100.

Dañobeitia, J., Arguedas, M., Gallart, J., Banda, E., & Makris, J. (1992). Deep crustal configuration of the Valencia trough and its Iberian and Balearic borders from extensive refraction and wide-angle reflection seismic profiling. *Tectonophysics*, *203*(1), 37–55.

De Stefano, M., Golfré Andreasi, F., Re, S., Virgilio, M., & Snyder, F. F. (2011). Multiple-domain, simultaneous joint inversion of geophysical data with application to subsalt imaging. *Geophysics*, *76*(3), R69–R80.

De Vicente, G., Vegas, R., Martín, A. M., Silva, P., Andriessen, P., Cloetingh, S., … Carbó, A. (2007). Cenozoic thick-skinned deformation and topography evolution of the Spanish Central System. *Global and Planetary Change*, *58*(1), 335–381.

De Vicente, G. de, Cloetingh, S., Muñoz-Martín, A., Olaiz, A., Stich, D., Vegas, R., … Fernández-Lozano, J. (2008). Inversion of moment tensor focal mechanisms for active stresses around the microcontinent Iberia: Tectonic implications. *Tectonics*, *27*(1).

Dell‘Aversana, P. (2001). Integration of seismic, MT and gravity data in a thrust belt interpretation. *First Break*, *19*(6), 335–341.

Dercourt, J. et al, Zonenshain, L., Ricou, L.-E., Kazmin, V., Le Pichon, X., Knipper, A., … Lepvrier, C. (1986). Geological evolution of the Tethys belt from the Atlantic to the Pamirs since the Lias. *Tectonophysics*, *123*(1), 241–315.

Díaz, J., & Gallart, J. (2009). Crustal structure beneath the Iberian Peninsula and surrounding waters: A new compilation of deep seismic sounding results. *Physics of the Earth and Planetary Interiors*, *173*(1), 181–190.

Egbert, G. D., & Booker, J. R. (1986). Robust estimation of geomagnetic transfer functions. *Geophysical Journal International*, *87*(1), 173–194.

Ehsan, S. A., Carbonell, R., Ayarza, P., Martí, D., Pérez-Estaún, A., Martínez-Poyatos, D. J., Mansilla, L. (2014). Crustal deformation styles along the reprocessed deep seismic reflection transect of the Central Iberian Zone (Iberian Peninsula). *Tectonophysics*, *621*, 159–174.

Ehsan, S. A., Carbonell, R., Ayarza, P., Martí, D., Poyatos, D. M., & Pérez-Estaún, A. (2015). The structure and nature of the Moho beneath Central Iberia. *Tectonophysics*, *663*, 275–289.

Evans, R. L., Wannamaker, P. E., McGary, R. S., & Elsenbeck, J. (2014). Electrical structure of the central Cascadia subduction zone: the EMSLAB Lincoln line revisited. *Earth and Planetary Science Letters*, *402*, 265–274.

Fernández-Viejo, G. (1997). Estructura cortical de la Cordillera Cantábrica y su transición a la Cuenca del Duero a partir de datos de sísmica de refracción/reflexión de gran ángulo.

Fernéndez-Viejo, G., Gallart, J., Pulgar, J., Gallastegui, J., Dañobeitia, J., & Córdoba, D. (1998). Crustal transition between continental and oceanic domains along the North Iberian margin from wide angle seismic and gravity data. *Geophysical Research Letters*, *25*(23), 4249–4252.

Fernández-Viejo, G., Gallart, J., Pulgar, J. A., Córdoba, D., & Dañobeitia, J. J. (2000). Seismic signature of Variscan and Alpine tectonics in NW Iberia: Crustal structure of the Cantabrian Mountains and Duero basin. *Journal of Geophysical Research: Solid Earth*, *105*(B2), 3001–3018.

Franke, W. (1989). Tectonostratigraphic units in the Variscan belt of central Europe. *Geological Society of America Special Papers*, *230*, 67–90.

Gallardo, L. A., & Meju, M. A. (2004). Joint two-dimensional DC resistivity and seismic travel time inversion with cross-gradients constraints. *Journal of Geophysical Research: Solid Earth*, *109*(B3).

Gallart, J., Banda, E., & Daignières, M. (1981). Crustal structure of the paleozoic-axial-zone of the pyrenees and transition to the north-pyrenean-zone (vol. 37, pp. 457–480). presented at the annales de geophysique, editions cnrs 20/22 rue st. amand, 75015 Paris, France.

Gallart, J., Vidal, N., Estévez, A., Pous, J., Sábat, F., Santisteban, C., & Suriñach, E. (1995). The ESCI-Valencia Trough vertical reflection experiment: a seismic image of the crust from the NE Iberian Peninsula to the Western Mediterranean. *Rev Soc Geol Espana*, *8*(4), 405–415.

Gallart, J., Salas, R., Guimerá, J., Mas, R., Diaz, J., & Ruiz, M. (2004). A refraction/wide-angle reflection seismic profile through the Iberian Chain: preliminary report. *Gen*, *6*, 2.

Gallastegui Suárez, J. (2000). Estructura cortical de la cordillera y margen continental cantábricos: perfiles ESCI-N.

Gamble, T., Goubau, W. M., & Clarke, J. (1979). Magnetotellurics with a remote magnetic reference. *Geophysics*, *44*(1), 53–68.

Garcia, X., Seillé, H., Elsenbeck, J., Evans, R., Jegen, M., Hölz, S., … Marcuello, A. (2015). Structure of the mantle beneath the Alboran Basin from magnetotelluric soundings. *Geochemistry, Geophysics, Geosystems*.

Gómez-Ortiz, D., Tejero-López, R., Babín-Vich, R., & Rivas-Ponce, A. (2005). Crustal density structure in the Spanish Central System derived from gravity data analysis (Central Spain). *Tectonophysics*, *403*(1), 131–149.

Groom, R. W., & Bailey, R. C. (1989). Decomposition of magnetotelluric impedance tensors in the presence of local three-dimensional galvanic distortion. *Journal of Geophysical Research: Solid Earth*, *94*(B2), 1913–1925.

Guimerà, J., & Alvaro, M. (1990). Structure et évolution de la compression alpine dans la Chaîne Ibérique et la Chaîne côtière catalane (Espagne). *Bull. Soc. Géol. Fr*, *8*, 339–348.

Guimerà, J., Alonso, Á., & Mas, J. R. (1995). Inversion of an extensional-ramp basin by a newly formed thrust: the Cameros basin (N. Spain). *Geological Society, London, Special Publications*, *88*(1), 433–453.

Guimerà, J., & González, A. (1998). El relieve de la Cadena Ibérica como producto de la compresión alpina. *Geogaceta*, *24*, 163–166.

Guimerà, J., Mas, R., & Alonso, Á. (2004). Intraplate deformation in the NW Iberian Chain: Mesozoic extension and Tertiary contractional inversion. *Journal of the Geological Society*, *161*(2), 291–303.

Guimerà, J. (2013). Estructura y evolución tectónica de la Cadena Ibérica. In *XLVII Curso de Geología Práctica. Teruel 15-20 de Jul. 2013* (pp. 1–9). Universidad de Verano de Teruel.

Hacikoylu, P., Dvorkin, J., & Mavko, G. (2006). Resistivity-velocity transforms revisited. *The Leading Edge*, *25*(8), 1006–1009.

Heise, W., & Pous, J. (2001). Effects of anisotropy on the two-dimensional inversion procedure. *Geophysical Journal International*, *147*(3), 610–621.

Heise, W., & Pous, J. (2003). Anomalous phases exceeding 90 in magnetotellurics: anisotropic model studies and a field example. *Geophysical Journal International*, *155*(1), 308–318.

Heise, W., Bibby, H. M., Caldwell, T. G., Bannister, S. C., Ogawa, Y., Takakura, S., & Uchida, T. (2007). Melt distribution beneath a young continental rift: the Taupo Volcanic Zone, New Zealand. *Geophysical Research Letters*, *34*(14).

Heise, W., Caldwell, T., Bibby, H. M., & Bannister, S. (2008). Three-dimensional modelling of magnetotelluric data from the Rotokawa geothermal field, Taupo Volcanic Zone, New Zealand. *Geophysical Journal International*, *173*(2), 740–750.

Hu, W., Abubakar, A., & Habashy, T. M. (2009). Joint electromagnetic and seismic inversion using structural constraints. *Geophysics*, *74*(6), R99–R109.

Hrubcová, P., Środa, P., (2015). Complex local Moho topography in the Western Carpathians: Indication of the ALCAPA and the European Plate contact. *Tectonophysics*, 638, 63-81.

Ichihara, H., & Mogi, T. (2009). A realistic 3-D resistivity model explaining anomalous large magnetotelluric phases: the L-shaped conductor model. *Geophysical Journal International*, *179*(1), 14–17.

Jones, A. G. (1988). Static shift of magnetotelluric data and its removal in a sedimentary basin environment. *Geophysics*, *53*(7), 967–978.

Jones, A. G. (2013). Imaging and observing the electrical Moho. *Tectonophysics*, *609*, 423–436.

Junge, A. (1996). Characterization of and correction for cultural noise. *Surveys in Geophysics*, *17*(4), 361–391.

Krieger, L., & Peacock, J. R. (2014). MTpy: A Python toolbox for magnetotellurics. *Computers & Geosciences*, *72*, 167–175.

Ledo, J., Ayala, C., Pous, J., Queralt, P., Marcuello, A., & Muñoz, J. A. (2000). New geophysical constraints on the deep structure of the Pyrenees. *Geophysical Research Letters*, *27*(7), 1037–1040.

Lezaeta, P., & Haak, V. (2003). Beyond magnetotelluric decomposition: induction, current channeling, and magnetotelluric phases over 90. *Journal of Geophysical Research: Solid Earth*, *108*(B6).

Lister, G., Forster, M., & Rawling, T. (2001). Episodicity during orogenesis. *Geological Society, London, Special Publications*, *184*(1), 89–113.

Mackie, R. L., & Madden, T. R. (1993). Three-dimensional magnetotelluric inversion using conjugate gradients. *Geophysical Journal International*, *115*(1), 215–229.

Malod, J.-A., Boillot, G., Lepvier, C., Mascle, G., Taugourdeau-Lantz, J., Capdevila, R., Müller, C. (1982). Subduction and tectonics on the continental margin off northern

Spain: observations with the submersible Cyana. *Geological Society, London, Special Publications*, *10*(1), 309–315.

Malod, J., & Mauffret, A. (1990). Iberian plate motions during the Mesozoic. *Tectonophysics*, *184*(3), 261–278.

Mancilla, F., & Diaz, J. (2015). High resolution Moho topography map beneath Iberia and Northern Morocco from receiver function analysis. *Tectonophysics, 663,* 203–211.

Marquis, G., & Hyndman, R. D. (1992). Geophysical support for aqueous fluids in the deep crust: seismic and electrical relationships. *Geophysical Journal International*, *110*(1), 91–105.

Martí, A., Queralt, P., Roca, E., Ledo, J., & Galindo-Zaldivar, J. (2009). Geodynamic implications for the formation of the Betic-Rif orogen from magnetotelluric studies. *Journal of Geophysical Research: Solid Earth*, *114*(B1).

Matsuno, T., Seama, N., Evans, R. L., Chave, A. D., Baba, K., White, A., Yoneda, A. (2010). Upper mantle electrical resistivity structure beneath the central Mariana subduction system. *Geochemistry, Geophysics, Geosystems*, *11*(9).

Matte, P. (2001). The Variscan collage and orogeny (480–290 Ma) and the tectonic definition of the Armorica microplate: a review. *Terra Nova*, *13*(2), 122–128.

McGary, R. S., Evans, R. L., Wannamaker, P. E., Elsenbeck, J., & Rondenay, S. (2014). Pathway from subducting slab to surface for melt and fluids beneath Mount Rainier. *Nature*, *511*(7509), 338–340.

McNeice, G. W., & Jones, A. G. (2001). Multisite, multifrequency tensor decomposition of magnetotelluric data. *Geophysics*, *66*(1), 158–173.

Meju, M. A. (1996). Joint inversion of TEM and distorted MT soundings: Some effective practical considerations. *Geophysics*, *61*(1), 56–65.

Metronix (http://www.geo-metronix.de/)

Monteiro Santos, F. A. M., Pous, J., Almeida, E. P., Queralt, P., Marcuello, A., Matias, H., & Victor, L. A. M. (1999a). Magnetotelluric survey of the electrical conductivity of the crust across the Ossa Morena Zone and South Portuguese Zone suture. *Tectonophysics*, *313*(4), 449–462.

Muñoz, G., Mateus, A., Pous, J., Heise, W., Monteiro Santos, F., & Almeida, E. (2008). Unraveling middle-crust conductive layers in Paleozoic Orogens through 3D modeling of magnetotelluric data: The Ossa-Morena Zone case study (SW Iberian Variscides). *Journal of Geophysical Research: Solid Earth*, *113*(B6).

Muñoz Martín, A., & Muñoz, V. (1998). Cuantificación del acortamiento alpino y estructura en profundidad del extremo sur-occidental de la Cordillera Ibérica (Sierras de Altomira y Bascunana). *Revista de La Sociedad Geológica de España*, *11*(3–4), 233–252.

Muñoz-Jiménez, A., & Casas-Sainz, A. (1997). The Rioja Trough (N Spain): tectosedimentary evolution of a symmetric foreland basin. *Basin Research*, *9*(1), 65–85.

Parker, R. L., & Booker, J. R. (1996). Optimal one-dimensional inversion and bounding of magnetotelluric apparent resistivity and phase measurements. *Physics of the Earth and Planetary Interiors*, *98*(3), 269–282.

Patro, P. K., & Egbert, G. D. (2011). Application of 3D inversion to magnetotelluric profile data from the Deccan Volcanic Province of Western India. *Physics of the Earth and Planetary Interiors*, *187*(1), 33–46.

Pedreira, D., Pulgar, J., Gallart, J., & Díaz, J. (2003). Seismic evidence of Alpine crustal thickening and wedging from the western Pyrenees to the Cantabrian Mountains (north Iberia). *Journal of Geophysical Research: Solid Earth*, *108*(B4).

Pedreira, D., Pulgar, J., Gallart, J., & Torné, M. (2007). Three-dimensional gravity and magnetic modeling of crustal indentation and wedging in the western Pyrenees-Cantabrian Mountains. *Journal of Geophysical Research: Solid Earth*, *112*(B12).

Pedreira, D., Afonso, J. C., Pulgar, J. A., Gallastegui, J., Carballo, A., Fernàndez, M., … García-Moreno, O. (2015). Geophysical-petrological modeling of the lithosphere beneath the Cantabrian Mountains and the North-Iberian margin: geodynamic implications. *Lithos*, *230*, 46–68.

Pérez-Estaún, A., & Bea, F. (2004). Macizo Ibérico. *Geología de España*, 19–230.

Pous, J., Ledo, J., Marcuello, A., & Daignières, M. (1995). Electrical resistivity model of the crust and upper mantle from a magnetotelluric survey through the central Pyrenees. *Geophysical Journal International*, *121*(3), 750–762.

Pous, J., Queralt, P., Ledo, J., & Roca, E. (1999). A high electrical conductive zone at lower crustal depth beneath the Betic Chain (Spain). *Earth and Planetary Science Letters*, *167*(1), 35–45.

Pous, J.; Queralt, P.; Marcuello, A.; Heise, W. (2000). Magnetotelluric signature of northern Iberian Peninsula: Crustal of the Cantabrian Mountains and associated foreland basins *15th Workshop on Electromagnetic Induction in the Earth.*

Pous, J., Queralt, P., & Marcuello, A. (2001). Magnetotelluric signature of the western Cantabrian Mountains. *Geophysical Research Letters*, *28*(9), 1795–1798.

Pous, J., Muñoz, G., Heise, W., Melgarejo, J. C., & Quesada, C. (2004). Electromagnetic imaging of Variscan crustal structures in SW Iberia: the role of interconnected graphite. *Earth and Planetary Science Letters*, *217*(3), 435–450.

Pous, J., Martínez Poyatos, D., Heise, W., Santos, F. M., Galindo-Zaldívar, J., Ibarra, P., Gonçalves, R. (2011). Constraints on the crustal structure of the internal Variscan Belt in SW Europe: A magnetotelluric transect along the eastern part of Central Iberian Zone, Iberian Massif. *Journal of Geophysical Research: Solid Earth*, *116*(B2).

Pueyo, E. L., Izquierdo-Llavall, E., Rodríguez-Pintó, A., Rey-Moral, C., Oliva-Urcia, B., Casas, A. M., del Rio, P. (2015). Petrophysical properties in the Iberian Range and surrounding areas (NE Spain): 1-density. *Journal of Maps*, 1–9.

Pulgar, J., Gallart, J., Fernández-Viejo, G., Pérez-Estaún, A., Álvarez-Marrón, J., & ESCIN Group. (1996). Seismic image of the Cantabrian Mountains in the western extension of the Pyrenees from integrated ESCIN reflection and refraction data. *Tectonophysics*, *264*(1), 1–19.

Pulgar, J., Pérez-Estaún, A., Gallart, J., Álvarez-Marrón, J., Gallastegui, J., Alonso, J., & ESCIN Group. (1997). The ESCI-N2 deep seismic reflection profile: a traverse across the Cantabrian Mountains and adjacent Duero basin. *Rev. Soc. Geol. España*, *8*(4), 383–394.

Pulgar, J., Alonso, J., Espina, R., & Marín, J. (1999). La deformación alpina en el basamento varisco de la Zona Cantábrica. Trabajos de Geologia, 21(21), 283–295.

Qian, W., & Pedersen, L. (1991). Industrial interference magnetotellurics: an example from the Tangshan area, China. *Geophysics*, *56*(2), 265–273.

Quintana, L., Pulgar, J., & Alonso, J. (2015). Displacement transfer from borders to interior of a plate: A crustal transect of Iberia. *Tectonophysics*, *663*, 378–398.

Roca, E., Muñoz, J. A., Ferrer, O., & Ellouz, N. (2011). The role of the Bay of Biscay Mesozoic extensional structure in the configuration of the Pyrenean orogen: Constraints from the MARCONI deep seismic reflection survey. *Tectonics*, *30*(2).

Rodi, W., & Mackie, R. L. (2001). Nonlinear conjugate gradients algorithm for 2-D magnetotelluric inversion. *Geophysics*, *66*(1), 174–187.

Rodi, W. L., & Mackie, R. L. (2012). The inverse problem. *The Magnetotelluric Method: Theory and Practice*, 347–414.

Romero-Ruiz, I. (2015). Tensor de impedencias magnetotelúrico en álgebras de Clifford. *PhD thesis*, Universitat de Barcelona.

Rosell, O., Martí, A., Marcuello, À., Ledo, J., Queralt, P., Roca, E., & Campanyà, J. (2011). Deep electrical resistivity structure of the northern Gibraltar Arc (western Mediterranean): evidence of lithospheric slab break-off. *Terra Nova*, *23*(3), 179–186.

Rosenbaum, G., Lister, G. S., & Duboz, C. (2002). Relative motions of Africa, Iberia and Europe during Alpine orogeny. *Tectonophysics*, *359*(1), 117–129.

Ruiz-Constán, A., Pedrera, A., Galindo-Zaldívar, J., Pous, J., Arzate, J., Roldán-García, F., Anahnah, F. (2012). Constraints on the frontal crustal structure of a continental collision from an integrated geophysical research: The central-western Betic Cordillera (SW Spain). *Geochemistry, Geophysics, Geosystems*, *13*(8).

Salas, R., & Casas, A. (1993). Mesozoic extensional tectonics, stratigraphy and crustal evolution during the Alpine cycle of the eastern Iberian basin. *Tectonophysics*, *228*(1–2), 33–55.

Salas, R., Guimerà, J., Mas, R., Martín-Closas, C., Meléndez, A., & Alonso, A. (2001). Evolution of the Mesozoic central Iberian Rift System and its Cainozoic inversion (Iberian chain). *Peri-Tethys Memoir*, *6*, 145–185.

Seillé, H., Salas, R., Pous, J., Guimerà, J., Gallart, J., Torne, M., Carbonell, R. (2015). Crustal structure of an intraplate thrust belt: the Iberian Chain revealed by wide-angle seismic, magnetotelluric soundings and gravity data. *Tectonophysics*, *663*, 339–353.

Sibuet, J., Srivastava, S. P., & Spakman, W. (2004). Pyrenean orogeny and plate kinematics. *Journal of Geophysical Research: Solid Earth*, *109*(B8).

Simancas, J., Carbonell, R., González Lodeiro, F., Pérez Estaún, A., Juhlin, C., Ayarza, P., Almodovar, G. R. (2003). Crustal structure of the transpressional Variscan orogen of SW Iberia: SW Iberia deep seismic reflection profile (IBERSEIS). *Tectonics*, *22*(6).

Simpson, F., & Bahr, K. (2005). *Practical magnetotellurics*. Cambridge University Press.

Siripunvaraporn, W., & Egbert, G. (2000). An efficient data-subspace inversion method for 2-D magnetotelluric data. *Geophysics*, *65*(3), 791–803.

Siripunvaraporn, W., Egbert, G., & Uyeshima, M. (2005a). Interpretation of two-dimensional magnetotelluric profile data with three-dimensional inversion: synthetic examples. *Geophysical Journal International*, *160* (3), 804–814.

Siripunvaraporn, W., Egbert, G., Lenbury, Y., & Uyeshima, M. (2005b). Three-dimensional magnetotelluric inversion: data-space method. *Physics of the Earth and Planetary Interiors*,*150*(1), 3–14.

Siripunvaraporn, W., & Egbert, G. (2009). WSINV3DMT: vertical magnetic field transfer function inversion and parallel implementation. *Physics of the Earth and Planetary Interiors*, *173*(3), 317–329.

Srivastava, S., Roest, W., Kovacs, L., Oakey, G., Levesque, S., Verhoef, J., & Macnab, R. (1990). Motion of Iberia since the Late Jurassic: results from detailed aeromagnetic measurements in the Newfoundland Basin. *Tectonophysics*, *184*(3–4), 229–260.

Stesky, R., & Brace, W. (1973). Electrical conductivity of serpentinized rocks to 6 kilobars. *Journal of Geophysical Research*, *78*(32), 7614–7621.

Stich, D., Serpelloni, E., de Lis Mancilla, F., & Morales, J. (2006). Kinematics of the Iberia–Maghreb plate contact from seismic moment tensors and GPS observations. *Tectonophysics*, *426*(3), 295–317.

Szarka, L. (1988). Geophysical aspects of man-made electromagnetic noise in the earth—A review. *Surveys in Geophysics*, *9*(3–4), 287–318.

Tavani, S. (2012). Plate kinematics in the Cantabrian domain of the Pyrenean orogen. *Solid Earth*, *3*(2), 265.

Tikhonov, A. (1950). On determining electrical characteristics of the deep layers of the Earth’s crust (Vol. 73, pp. 295–297). Presented at the Doklady, Citeseer.

Tikonov, A. N., & Arsenin, V. Y. (1977). Solutions of ill-posed problems. *New York: Winston.*

Torné, M., Pascal, G., Buhl, P., Watts, A., & Mauffret, A. (1992). Crustal and velocity structure of the Valencia trough (western Mediterranean), Part I. A combined refraction/wide-angle reflection and near-vertical reflection study. *Tectonophysics*, *203*(1), 1–20.

Torne, M., Fernàndez, M., Vergés, J., Ayala, C., Salas, M. C., Jimenez-Munt, I., … Díaz, J. (2015). Crust and mantle lithospheric structure of the Iberian Peninsula deduced from potential field modeling and thermal analysis. *Tectonophysics*, *663*, 419–433.

Unsworth, M., Jones, A. G., Wei, W., Marquis, G., Gokarn, S., Spratt, J., Clarke, G. (2005). Crustal rheology of the Himalaya and Southern Tibet inferred from magnetotelluric data. *Nature*, *438*(7064), 78–81.

Varentsov, I. M. (2006). Arrays of simultaneous electromagnetic soundings: design, data processing and analysis. *Electromagnetic Sounding of the Earth’s Interior*, *40*, 259–273.

Vergés, J., & Fernàndez, M. (2006). Ranges and basins in the Iberian Peninsula: their contribution to the present topography. *Geological Society, London, Memoirs*, *32*(1), 223–234.

Vergés, J., & Fernàndez, M. (2012). Tethys–Atlantic interaction along the Iberia–Africa plate boundary: The Betic–Rif orogenic system. *Tectonophysics*, *579*, 144–172.

Vozoff, K. (1972). The magnetotelluric method in the exploration of sedimentary basins. *Geophysics*, *37*(1), 98–141.

Watts, A., Torné, M., Buhl, P., Mauffret, A., Pascal, G., & Pinet, B. (1990). Evidence for reflectors in the lower continental crust before rifting in the Valencia trough. *Nature*, *348*(6302), 631–635.

WDC-SILSO, Royal Observatory of Belgium, Brussels (http://www.sidc.be/silso/datafiles)

Worzewski, T., Jegen, M., Kopp, H., Brasse, H., & Castillo, W. T. (2011). Magnetotelluric image of the fluid cycle in the Costa Rican subduction zone. *Nature Geoscience*, *4*(2), 108–111.

Xiao, Q., Zhang, J., Wang, J., Zhao, G., & Tang, J. (2012). Electrical resistivity structures between the Northern Qilian Mountains and Beishan Block, NW China, and tectonic implications. *Physics of the Earth and Planetary Interiors*, *200*, 92–104.

Zeyen, H., Banda, E., Gallart, J., & Ansorge, J. (1985). A wide angle seismic reconnaissance survey of the crust and upper mantle in the Celtiberian Chain of eastern Spain. *Earth and Planetary Science Letters*, *75*(4), 393–402.

Ziegler, A. (1990). Phytogeographic patterns and continental configurations during the Permian Period. *Geological Society, London, Memoirs*, *12*(1), 363–379.

Appendix 1

Cantabrian Mountains: MT data and 3-D model responses

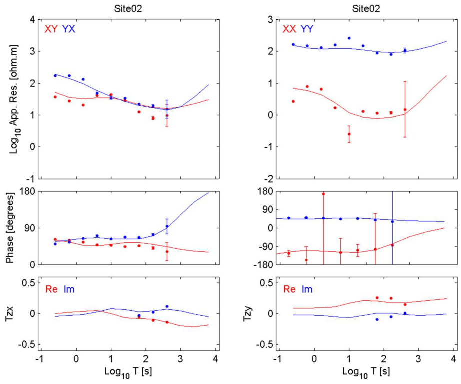
Site02
Site02
XY YX
XX YY
Log10 App. Res. [ohm.m]
Phase [degrees]
Re Im
Tzx
Tzy
Log10 T [s]
Log10 T [s]

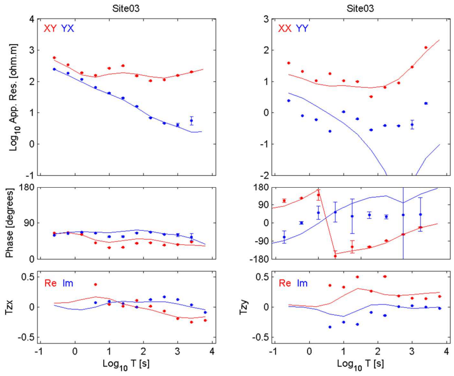
Site03
Site03
XY YX
XX YY
Log10 App. Res. [ohm.m]
Phase [degrees]
Re Im
Tzx
Tzy
Log10 T [s]
Log10 T [s]

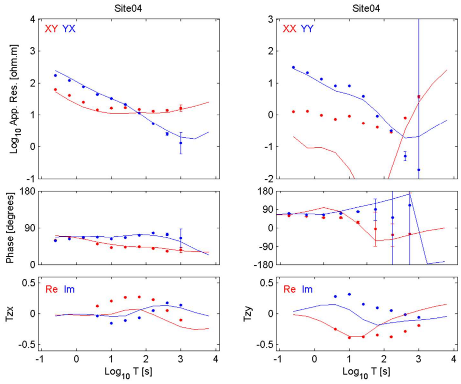
Site04
Site04
XY YX
XX YY
Log10 App. Res. [ohm.m]
Phase [degrees]
Re Im
Tzx
Tzy
Log10 T [s]
Log10 T [s]

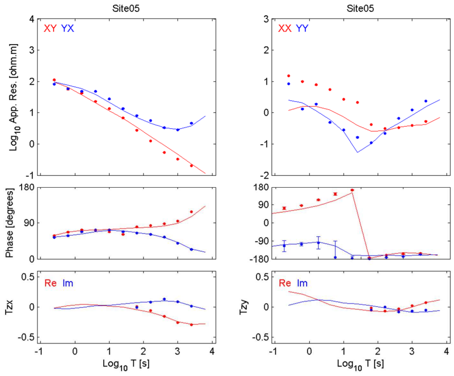
Site05
Site05
XY YX
XX YY
Log10 App. Res. [ohm.m]
Phase [degrees]
Re Im
Tzx
Tzy
Log10 T [s]
Log10 T [s]

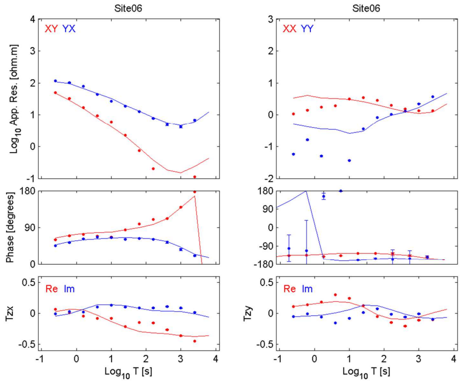
Site06
Site06
XY YX
XX YY
Log10 App. Res. [ohm.m]
Phase [degrees]
Re Im
Tzx
Tzy
Log10 T [s]
Log10 T [s]

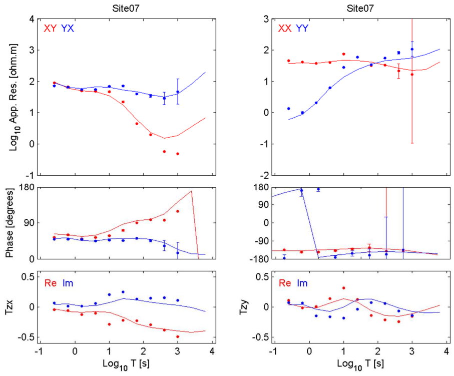
Site07
Site07
XY YX
XX YY
Log10 App. Res. [ohm.m]
Phase [degrees]
Re Im
Tzx
Tzy
Log10 T [s]
Log10 T [s]

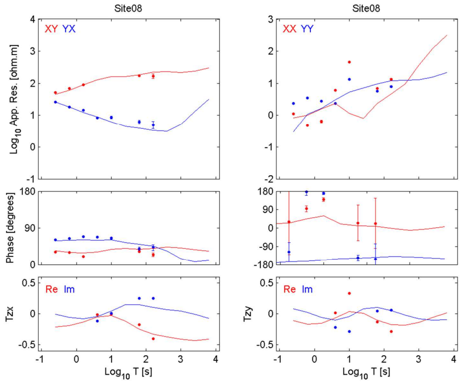
Site08
Site08
XY YX
XX YY
Log10 App. Res. [ohm.m]
Phase [degrees]
Re Im
Tzx
Tzy
Log10 T [s]
Log10 T [s]

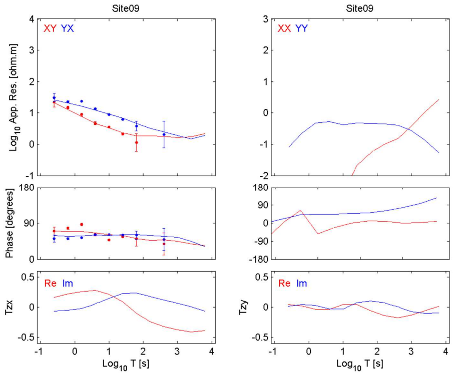
Site09
Site09
XY YX
XX YY
Log10 App. Res. [ohm.m]
Phase [degrees]
Re Im
Tzx
Tzy
Log10 T [s]
Log10 T [s]

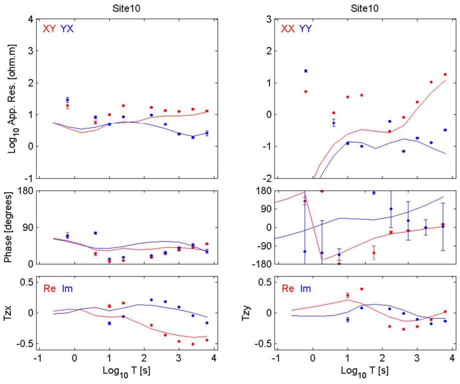
Site10
Site10
XY YX
XX YY
Log10 App. Res. [ohm.m]
Phase [degrees]
Re Im
Tzx
Tzy
Log10 T [s]

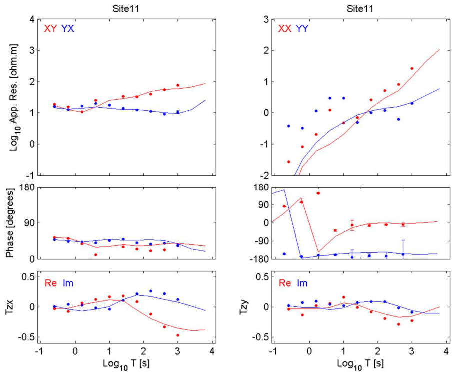
Site11
Site11
XY YX
XX YY
Log10 App. Res. [ohm.m]
Phase [degrees]
Re Im
Tzx
Tzy
Log10 T [s]

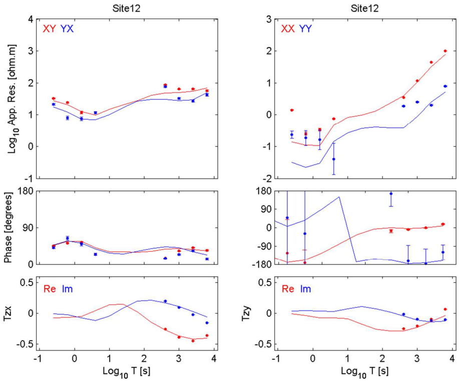
Site12
Site12
XY YX
XX YY
Log10 App. Res. [ohm.m]
Phase [degrees]
Re Im
Tzx
Tzy
Log10 T [s]

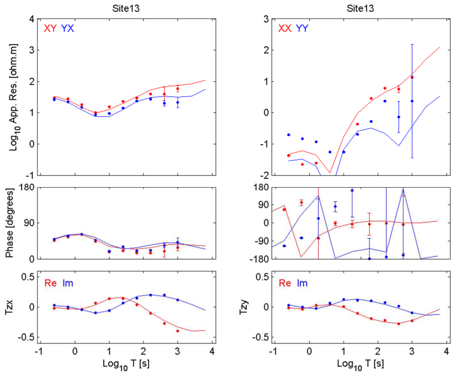
Site13
Site13
XY YX
XX YY
Log10 App. Res. [ohm.m]
Phase [degrees]
Re Im
Tzx
Tzy
Log10 T [s]

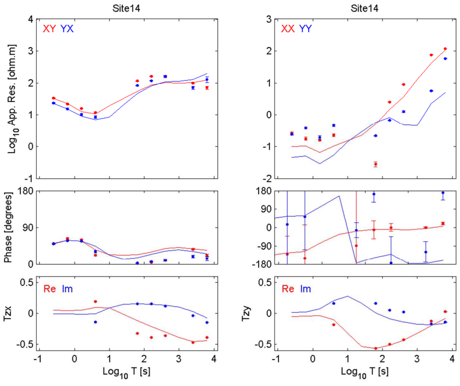
Site14
Site14
XY YX
XX YY
Log10 App. Res. [ohm.m]
Phase [degrees]
Re Im
Tzx
Tzy
Log10 T [s]

Appendix 2

Iberian Chain: MT data and 3-D model responses

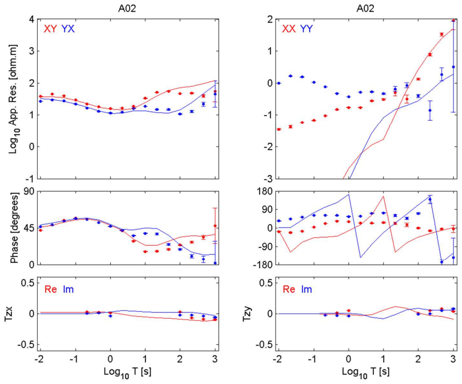
A02
XY YX
Log10 App. Res. [ohm.m]
4
3
2
1
0
-1
Phase [degrees]
90
45
0
Re Im
Tzx
0.5
0
-0.5
-2 -1 0 1 2 3
Log10 T [s]
A02
XX YY
2
1
0
-1
-2
-3
180
90
0
-90
-180
Re Im
Tzy
0.5
0
-0.5
-2 -1 0 1 2 3
Log10 T [s]

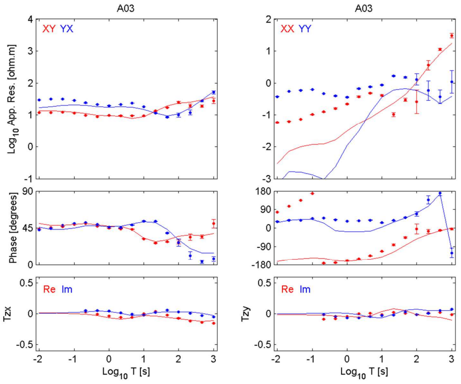
A03
XY YX
Log10 App. Res. [ohm.m]
4
3
2
1
0
-1
Phase [degrees]
90
45
0
Re Im
Tzx
0.5
0
-0.5
-2 -1 0 1 2 3
Log10 T [s]
A03
XX YY
2
1
0
-1
-2
-3
180
90
0
-90
-180
Re Im
Tzy
0.5
0
-0.5
-2 -1 0 1 2 3
Log10 T [s]

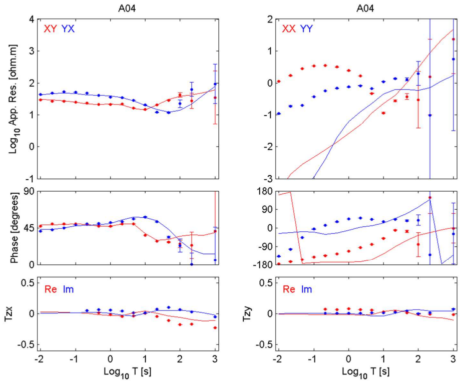
A04
XY YX
Log10 App. Res. [ohm.m]
4
3
2
1
0
-1
Phase [degrees]
90
45
0
Re Im
Tzx
0.5
0
-0.5
-2 -1 0 1 2 3
Log10 T [s]
A04
XX YY
2
1
0
-1
-2
-3
180
90
0
-90
-180
Re Im
Tzy
0.5
0
-0.5
-2 -1 0 1 2 3
Log10 T [s]

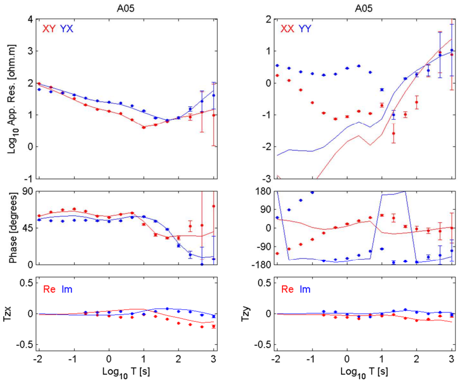
A05
XY YX
Log10 App. Res. [ohm.m]
4
3
2
1
0
-1
Phase [degrees]
90
45
0
Re Im
Tzx
0.5
0
-0.5
-2 -1 0 1 2 3
Log10 T [s]
A05
XX YY
2
1
0
-1
-2
-3
180
90
0
-90
-180
Re Im
Tzy
0.5
0
-0.5
-2 -1 0 1 2 3
Log10 T [s]

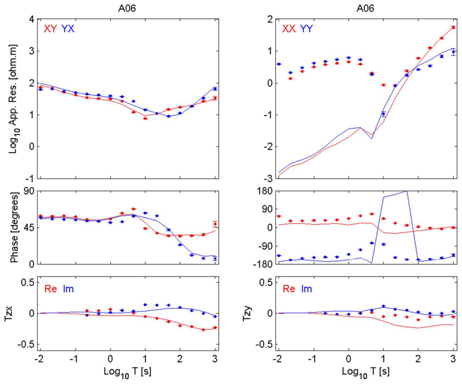
A06
XY YX
Log10 App. Res. [ohm.m]
4
3
2
1
0
-1
Phase [degrees]
90
45
0
Re Im
Tzx
0.5
0
-0.5
-2 -1 0 1 2 3
Log10 T [s]
A06
XX YY
2
1
0
-1
-2
-3
180
90
0
-90
-180
Re Im
Tzy
0.5
0
-0.5
-2 -1 0 1 2 3
Log10 T [s]

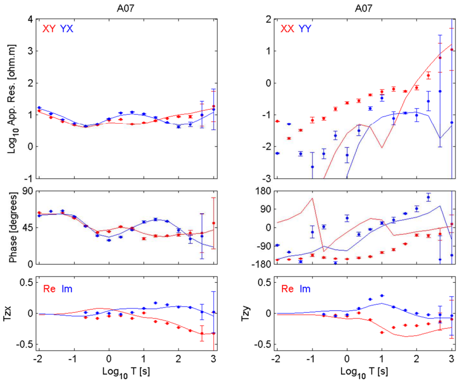
A07
XY YX
Log10 App. Res. [ohm.m]
4
3
2
1
0
-1
Phase [degrees]
90
45
0
Re Im
Tzx
0.5
0
-0.5
-2 -1 0 1 2 3
Log10 T [s]
A07
XX YY
2
1
0
-1
-2
-3
180
90
0
-90
-180
Re Im
Tzy
0.5
0
-0.5
-2 -1 0 1 2 3
Log10 T [s]

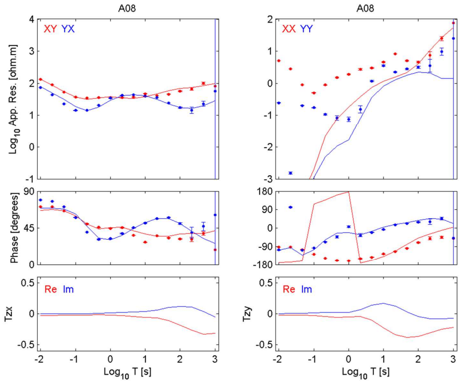
A08
XY YX
Log10 App. Res. [ohm.m]
4
3
2
1
0
-1
Phase [degrees]
90
45
0
Re Im
Tzx
0.5
0
-0.5
-2 -1 0 1 2 3
Log10 T [s]
A08
XX YY
2
1
0
-1
-2
-3
180
90
0
-90
-180
Re Im
Tzy
0.5
0
-0.5
-2 -1 0 1 2 3
Log10 T [s]

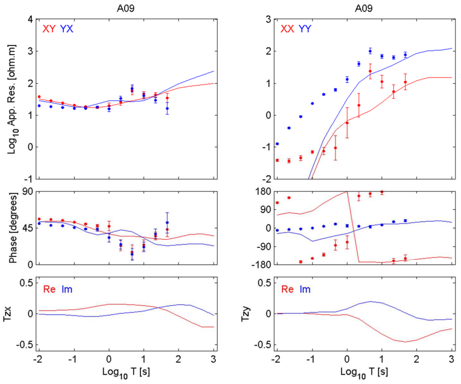
A09
XY YX
Log10 App. Res. [ohm.m]
4
3
2
1
0
-1
Phase [degrees]
90
45
0
Re Im
Tzx
0.5
0
-0.5
-2 -1 0 1 2 3
Log10 T [s]
A09
XX YY
3
2
1
0
-1
-2
180
90
0
-90
-180
Re Im
Tzy
0.5
0
-0.5
-2 -1 0 1 2 3
Log10 T [s]

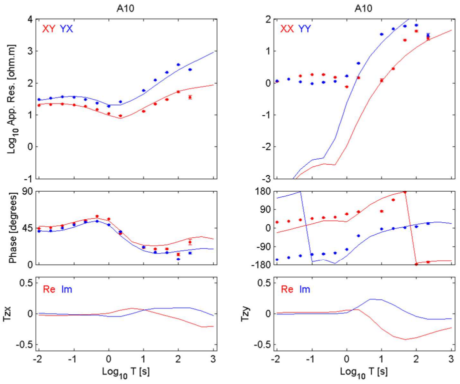
A10
XY YX
Log$_{10}$ App. Res. [ohm.m]
Phase [degrees]
Re Im
Tzx
Log$_{10}$ T [s]
A10
XX YY
Tzy
Log$_{10}$ T [s]

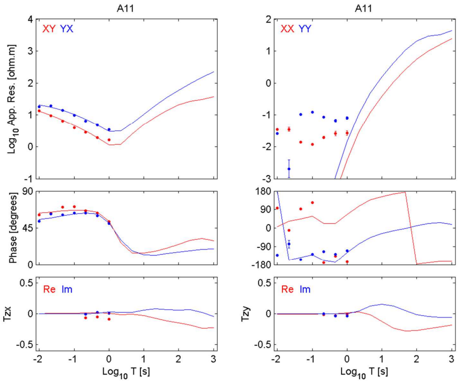
A11
XY YX
Log$_{10}$ App. Res. [ohm.m]
Phase [degrees]
Re Im
Tzx
Log$_{10}$ T [s]
A11
XX YY
Tzy
Log$_{10}$ T [s]

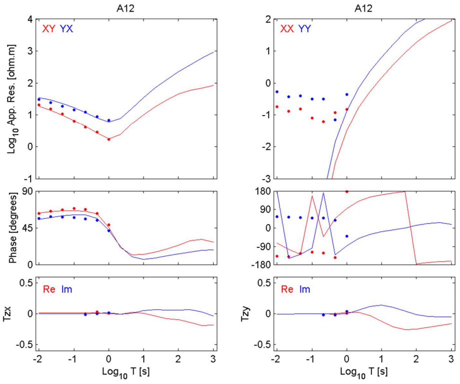
A12
XY YX
Log$_{10}$ App. Res. [ohm.m]
Phase [degrees]
Re Im
Tzx
Log$_{10}$ T [s]
A12
XX YY
Tzy
Log$_{10}$ T [s]

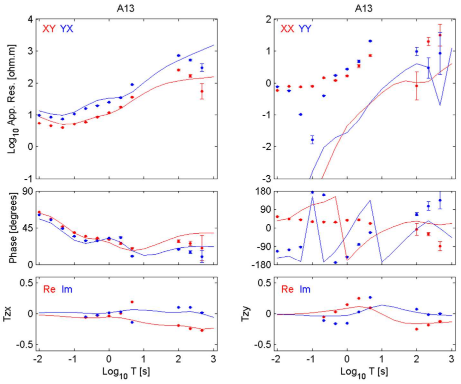
A13
XY YX
Log$_{10}$ App. Res. [ohm.m]
Phase [degrees]
Re Im
Tzx
Log$_{10}$ T [s]
A13
XX YY
Tzy
Log$_{10}$ T [s]

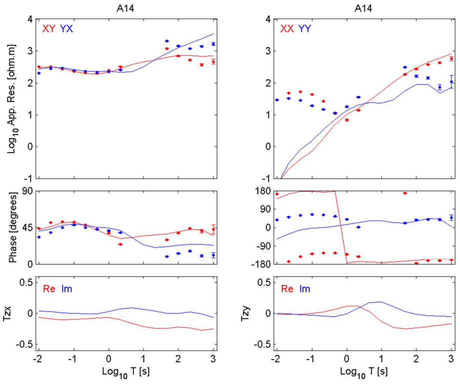
A14
XY YX
Log$_{10}$ App. Res. [ohm.m]
Phase [degrees]
Re Im
Tzx
Log$_{10}$ T [s]
A14
XX YY
Tzy
Log$_{10}$ T [s]

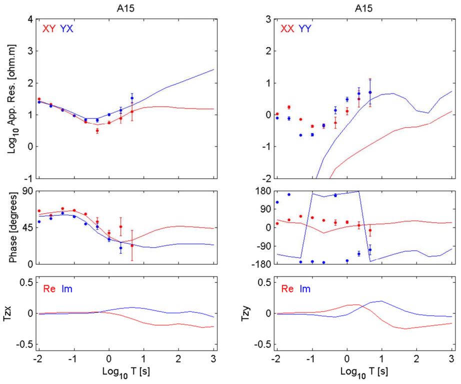
A15
XY YX
Log$_{10}$ App. Res. [ohm.m]
Phase [degrees]
Re Im
Tzx
Log$_{10}$ T [s]
A15
XX YY
Tzy
Log$_{10}$ T [s]

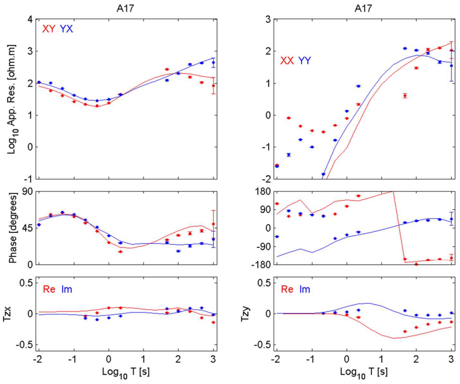
A17
XY YX
Log$_{10}$ App. Res. [ohm.m]
Phase [degrees]
Re Im
Tzx
Log$_{10}$ T [s]
A17
XX YY
Tzy
Log$_{10}$ T [s]

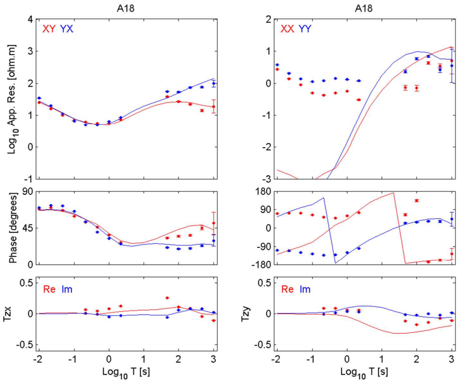
A18
XY YX
Log$_{10}$ App. Res. [ohm.m]
Phase [degrees]
Re Im
Tzx
Log$_{10}$ T [s]
A18
XX YY
Tzy
Log$_{10}$ T [s]

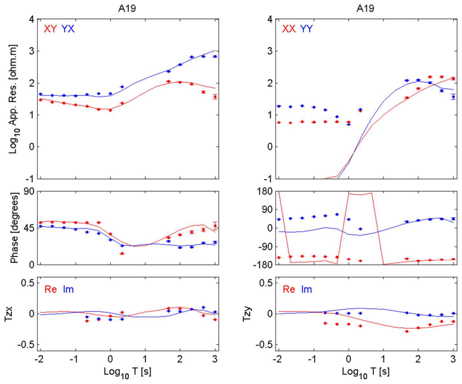
A19
A19
XY YX
XX YY
Log10 App. Res. [ohm.m]
Phase [degrees]
Re Im
Tzx
Tzy
Log10 T [s]

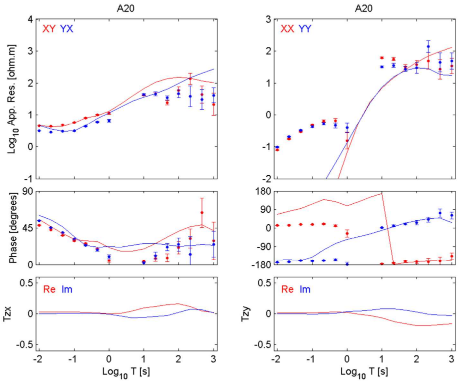
A20
A20
XY YX
XX YY
Log10 App. Res. [ohm.m]
Phase [degrees]
Re Im
Tzx
Tzy
Log10 T [s]

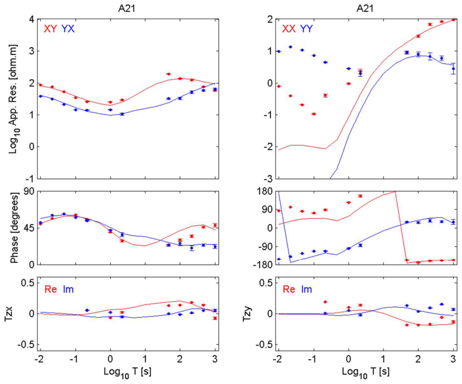
A21
A21
XY YX
XX YY
Log10 App. Res. [ohm.m]
Phase [degrees]
Re Im
Tzx
Tzy
Log10 T [s]

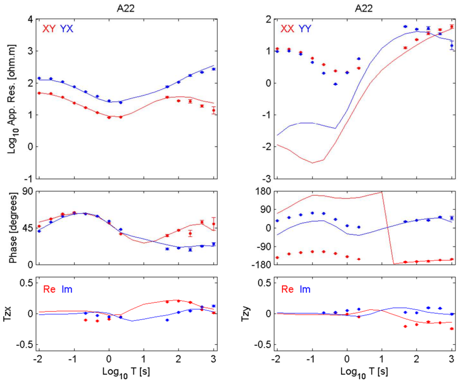
A22
A22
XY YX
XX YY
Log10 App. Res. [ohm.m]
Phase [degrees]
Re Im
Tzx
Tzy
Log10 T [s]

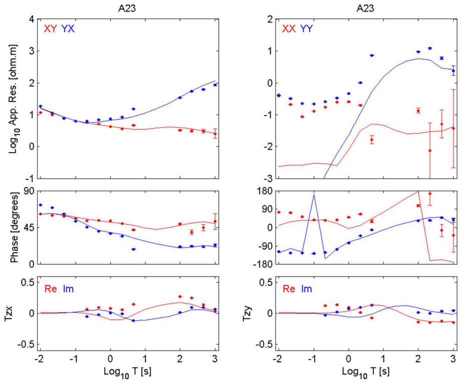
A23
A23
XY YX
XX YY
Log10 App. Res. [ohm.m]
Phase [degrees]
Re Im
Tzx
Tzy
Log10 T [s]

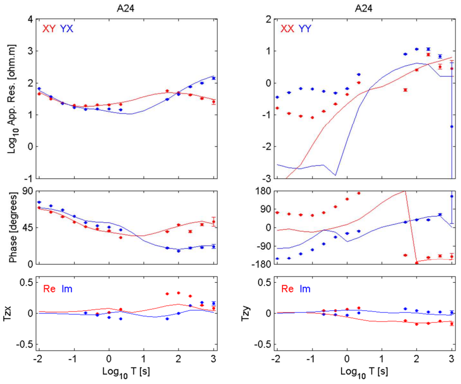
A24
A24
XY YX
XX YY
Log10 App. Res. [ohm.m]
Phase [degrees]
Re Im
Tzx
Tzy
Log10 T [s]

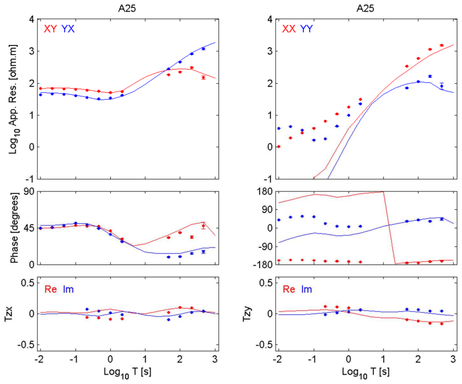
A25
A25
XY YX
XX YY
Log10 App. Res. [ohm.m]
Phase [degrees]
Re Im
Tzx
Tzy
Log10 T [s]

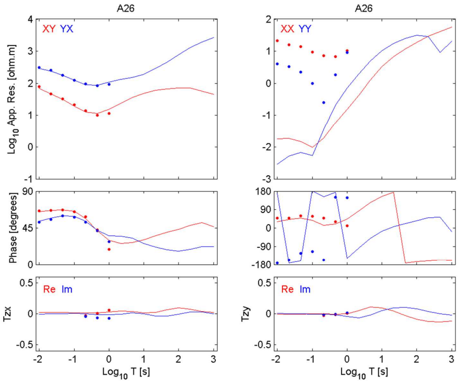
A26
A26
XY YX
XX YY
Log10 App. Res. [ohm.m]
Phase [degrees]
Re Im
Tzx
Tzy
Log10 T [s]

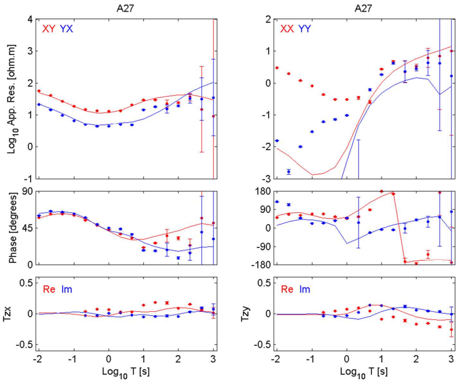
A27
XY YX
Log10 App. Res. [ohm.m]
Phase [degrees]
Re Im
Tzx
Log10 T [s]
A27
XX YY
Tzy
Log10 T [s]

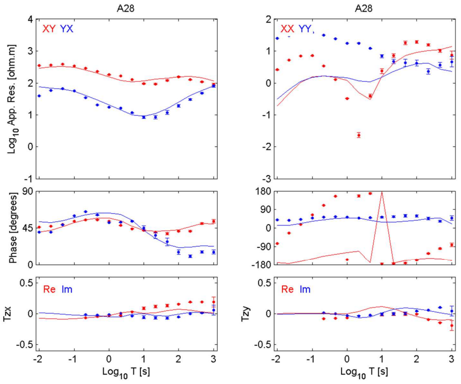
A28
XY YX
Log10 App. Res. [ohm.m]
Phase [degrees]
Re Im
Tzx
Log10 T [s]
A28
XX YY
Tzy
Log10 T [s]

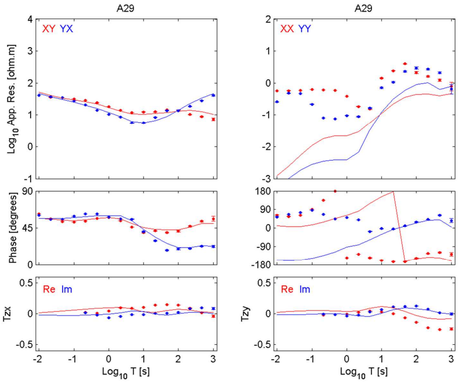
A29
XY YX
Log10 App. Res. [ohm.m]
Phase [degrees]
Re Im
Tzx
Log10 T [s]
A29
XX YY
Tzy
Log10 T [s]

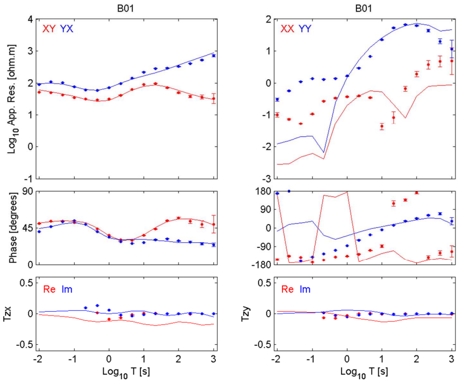
B01
XY YX
Log10 App. Res. [ohm.m]
Phase [degrees]
Re Im
Tzx
Log10 T [s]
B01
XX YY
Tzy
Log10 T [s]

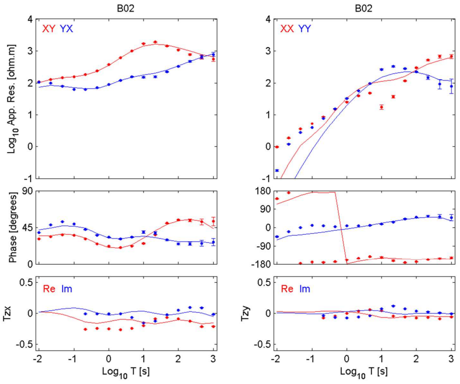
B02
XY YX
Log10 App. Res. [ohm.m]
Phase [degrees]
Re Im
Tzx
Log10 T [s]
B02
XX YY
Tzy
Log10 T [s]

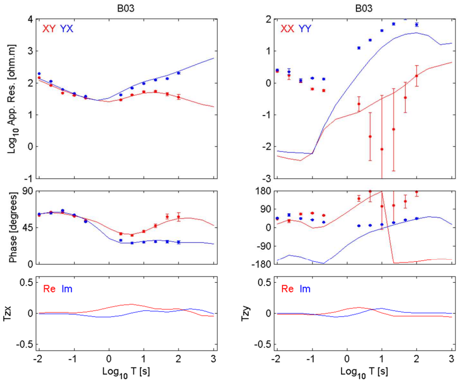
B03
XY YX
Log10 App. Res. [ohm.m]
Phase [degrees]
Re Im
Tzx
Log10 T [s]
B03
XX YY
Tzy
Log10 T [s]

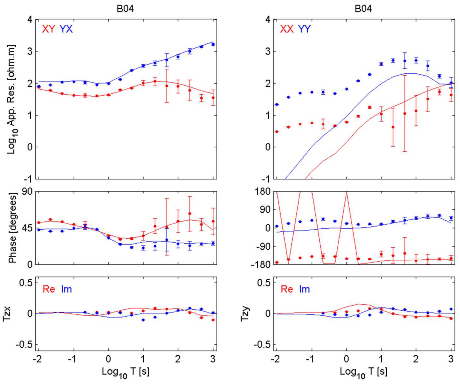
B04
XY YX
Log10 App. Res. [ohm.m]
Phase [degrees]
Re Im
Tzx
Log10 T [s]
B04
XX YY
Tzy
Log10 T [s]

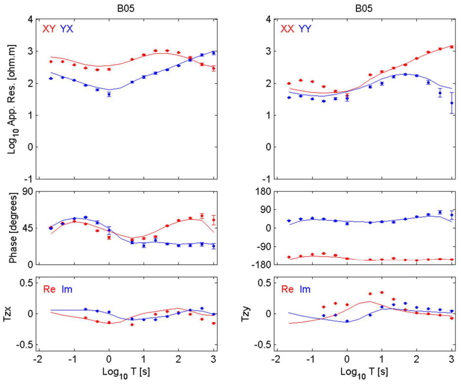
B05
XY YX
Log10 App. Res. [ohm.m]
Phase [degrees]
Re Im
Tzx
Log10 T [s]
B05
XX YY
Tzy
Log10 T [s]

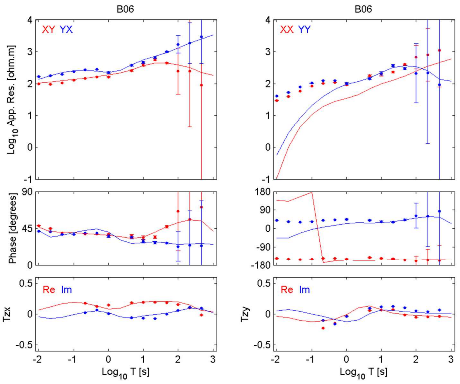
B06
XY YX
Log10 App. Res. [ohm.m]
Phase [degrees]
Re Im
Tzx
Log10 T [s]
B06
XX YY
Tzy
Log10 T [s]

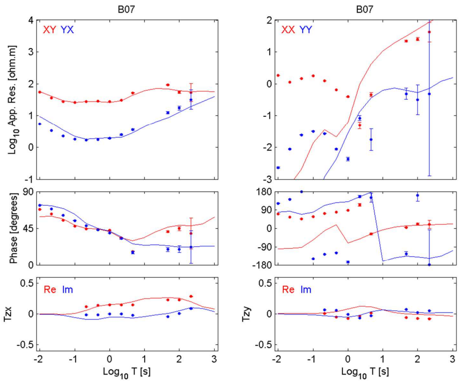
B07
XY YX
Log10 App. Res. [ohm.m]
Phase [degrees]
Re Im
Tzx
Log10 T [s]
B07
XX YY
Tzy
Log10 T [s]

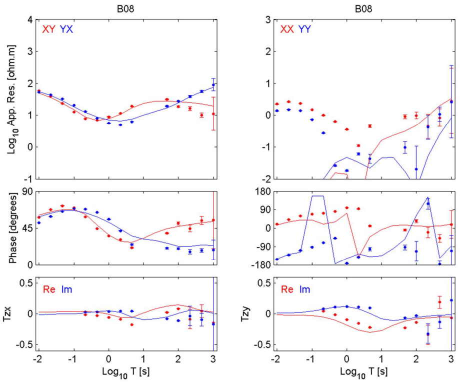
B08
XY YX
Log10 App. Res. [ohm.m]
Phase [degrees]
Re Im
Tzx
Log10 T [s]
B08
XX YY
Tzy
Log10 T [s]

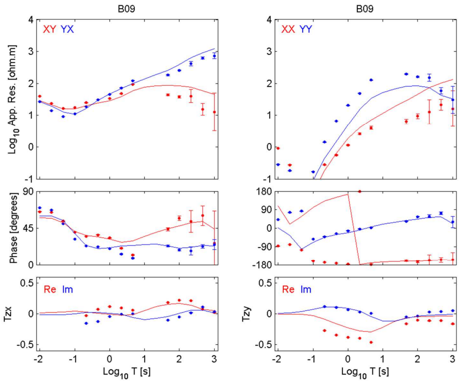
B09
XY YX
Log10 App. Res. [ohm.m]
Phase [degrees]
Re Im
Tzx
Log10 T [s]
B09
XX YY
Tzy
Log10 T [s]

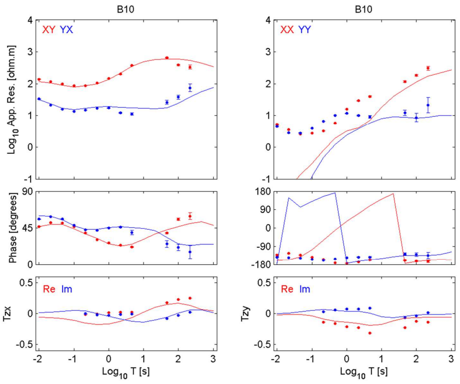
B10
XY YX
Log10 App. Res. [ohm.m]
Phase [degrees]
Re Im
Tzx
Log10 T [s]
B10
XX YY
Tzy
Log10 T [s]